

Similarity Conditions for Modal Sound Propagation in Turbomachinery Test Rigs

Von der Fakultät für Maschinenbau
der Gottfried Wilhelm Leibniz Universität Hannover
zur Erlangung des akademischen Grades
Doktor-Ingenieurin
genehmigte Dissertation

von
Carolin Mandanna Hurfar, M.Sc.

2021

Schlagwörter:

Ähnlichkeitskennzahlen, Akustische Moden, Gruppengeschwindigkeit, Turbomaschinen

Keywords:

Similarity Parameters, Acoustic Modes, Group Velocity, Turbomachinery

Vorsitzende: Prof. Dr.-Ing. Annika Raatz

1. Referent: Prof. Dr.-Ing. Jörg Seume

2. Referent: Prof. Stéphane Moreau

Tag der Promotion: 18. Dezember 2020

Abstract

Psychoacoustic studies show that the level of perceived annoyance with respect to noise emitted by aircrafts engine positively depends on the sound pressure level of the tonal components in the frequency spectrum. Acoustic modes generated by the rotation of the rotor and the periodic interaction of the stationary and rotating blades in the turbomachinery parts of the aircraft engine are the main contributors to the emitted tonal noise. In order to develop mitigation measures for these modal sound fields, experimental investigations are carried out on turbomachinery test rigs. For high quality research data, similarity between measurements has to be accomplished, as even minor changes to reference conditions might impair the significance of measurements. For time-harmonic sound propagation in an inviscid and ideal flow, the Helmholtz number and the Mach number establish similarity conditions.

This work addresses the establishment of similarity of modal sound propagation on test rigs where equality of the Mach number and / or the Helmholtz number cannot be met reliably between measurements. The investigation focuses on individual acoustic modes propagating in a circular duct carrying an axial uniform flow.

Experimental investigations are carried out on a low-pressure air turbine test rig. The test rig is equipped with a so-called sound generator for the controlled excitation of acoustic modes of arbitrary order and at specific frequencies. Similarity of the propagation of excited modes is evaluated by analyzing the modal response function. Based on an analytical analysis of the collected measurement data and a post-hoc scaling approach, it is shown that the axial angle of the group velocity vector is a suitable parameter to establish partial similarity with respect to modal sound propagation in cases where similarity of the Helmholtz number and / or the Mach number cannot be achieved. A similarity relation between the three parameters is derived. A sensitivity analysis shows that the impact of variations in the Helmholtz number and the Mach number can differ considerably depending on the operating point. For the two operating points investigated here, it is found accordingly that the variations in the modal response strongly correlate with the axial angle of the group velocity vector and the Helmholtz number, but only moderately or even negligible with the Mach number.

A reduced frequency is introduced which, similar to the reduced rotational speed and reduced mass flow rate, can be used as an acoustic operating parameter to establish similarity of modal sound propagation. For test rigs equipped with a sound generator, partial similarity can thus be established between measurements even though equality of the parameters, Helmholtz number and Mach number, is not met.

Zusammenfassung

Psychoakustische Studien zeigen, dass die empfundene Belästigung durch Fluglärm von dem Anteil der tonalen Komponenten im emittierten Frequenzspektrum des Triebwerks abhängig ist. Durch den Rotor und die Interaktion von rotierenden und stehenden Schaufeln im Triebwerk werden modale Schallfelder, so genannte akustisch Moden, generiert, welche als diskrete Frequenzen im abgestrahlten Spektrum auftreten. Experimentelle Versuche an Triebwerkskomponenten dienen der Entwicklung von Maßnahmen zur Reduzierung dieser modalen Anteile. Die Qualität der Messdaten ist dabei maßgeblich von der Einhaltung der Ähnlichkeit zwischen den einzelnen Messungen abhängig, da bereits minimale Änderungen in den Messbedingungen zu unterschiedlichen Ergebnissen führen können. Für die in dieser Arbeit betrachtete harmonische Schallausbreitung in einem angenommenen idealen nicht-viskosen Fluid, sind die Helmholtz-Zahl und die Mach-Zahl die bestimmenden Ähnlichkeitsparameter.

In dieser Arbeit wird eine Methode zur Einhaltung von Ähnlichkeit in Bezug auf die modale Schallausbreitung vorgestellt. Die Methode konzentriert sich auf Prüfstände, bei denen bei veränderten Eintrittsbedingungen die Helmholtz-Zahl und die Mach-Zahl zwischen zwei Messungen nicht zuverlässig konstant gehalten werden können. Der Fokus liegt dabei auf der Ausbreitung einzelner Moden in einem axial durchströmten Rohr.

Experimentelle Untersuchungen werden auf einem Niederdruck-Luftturbinenprüfstand durchgeführt. Im Eintritt ist ein Schallgenerator eingebaut, der die Anregung spezifischer akustischer Moden bei ausgewählten Frequenzen ermöglicht. Die Ähnlichkeit zwischen Messungen wird anhand der modalen Antwortfunktion bestimmt. Analytische Betrachtungen und eine nachträglich durchgeführte Skalierung der Messergebnisse zeigen, dass der Winkel zwischen dem modalen Gruppengeschwindigkeitsvektor und der Rohrachse geeignet ist, partielle Ähnlichkeit in Bezug auf die modale Schallausbreitung herzustellen. Eine Analyse der Ähnlichkeitsbeziehung zwischen diesem Winkel und der Helmholtz-Zahl und der Mach-Zahl ergibt, dass der Einfluss von Schwankungen der beiden zuletzt genannten Parameter auf den Winkel stark vom gewählten Betriebspunkt abhängig ist. Für die hier betrachteten Betriebspunkte ist eine starke lineare Korrelation zwischen der modalen Antwort und dem Gruppenausbreitungswinkel sowie der Helmholtz-Zahl zu beobachten. Gleichzeitig aber nur eine moderate oder vernachlässigbare Korrelation mit der Mach-Zahl.

Für die Einhaltung von Ähnlichkeit der modalen Schallausbreitung im Versuchsbetrieb wird, in Anlehnung an die Betriebsgrößen reduzierte Drehzahl und reduzierter Massenstrom, eine reduzierte Frequenz eingeführt. Mittels dieser Frequenz kann bei Nicht-Einhaltung einer konstanten Helmholtz-Zahl und / oder Mach-Zahl partielle Ähnlichkeit hergestellt werden.

Acknowledgments

The thesis on hand was written during my time as research associate at the Institute of Turbomachinery and Fluid Dynamics at Gottfried Wilhelm Leibniz University in Hanover, Germany. I would like to thank various individuals for the successful conclusion of my doctorate.

I am very grateful to Professor Dr.-Ing. Joerg Seume for his assistance and the faith vested in me while working on this topic at his institute. The autonomy I was granted as well as a supportive work environment enabled me to dedicate myself intensely to scientific research in the field of sound propagation in turbomachinery, both theoretically and experimentally. Many thanks to Professor Stéphane Moreau for showing great interest in my thesis as well as proofreading it. Also, I would like to thank Professor Dr.-Ing. Annika Raatz for chairing the examination board.

I would like to thank particularly all research associates at the institute, the colleagues at the test rigs and the workshop as well as those in the administration and IT departments. I especially often think of my former comrades-in-arms of the aeroacoustics and aeroelasticity research group. I want to thank them for their close and friendly cooperation, the intense discussions we had and the valuable clues they gave me for my research. My express gratitude also goes to all individuals who assisted me in the preparation and execution of the measurements. Furthermore, I would like to thank the students whose dedicated efforts in various areas have provided so much support and whose help has always given me great pleasure.

I would be remiss if I did not use this opportunity to appreciate all my dear friends who backed me up over many years and accompanied me through ups and downs. In particular, I want to thank my parents who were always by my side. I am especially grateful to my dear mother for the many hours and days of the most intense topical discussions of my work and her incredible moral support during those long months of evaluating measurements and putting the results in writing. I would certainly never have concluded this task without all of you.

Hanover, 2021

Mandanna Hurfar

Danksagung

Die vorliegende Arbeit entstand während meiner Zeit als wissenschaftliche Mitarbeiterin am Institut für Turbomaschinen und Fluid-Dynamik der Gottfried Wilhelm Leibniz Universität Hannover. Für das erfolgreiche Abschließen der Promotion möchte ich an dieser Stelle verschiedenen Personen danken.

Mein großer Dank gilt Herrn Prof. Dr.-Ing. Jörg Seume für seine Unterstützung und für das mir entgegengebrachte Vertrauen bei der Bearbeitung dieser Themenstellung an seinem Institut. Die von ihm gewährten Freiräume sowie das fördernde Arbeitsumfeld haben mir die Möglichkeit gegeben, mich intensiv der wissenschaftlichen Forschung im Bereich der akustischen Schallausbreitung in Turbomaschinen sowohl theoretisch als auch experimentell zu widmen. Herrn Prof. Stéphane Moreau danke ich vielmals für die Übernahme des Koreferats sowie das meiner Arbeit entgegengebrachte Interesse. Weiterhin danke ich Frau. Prof. Dr.-Ing. Annika Raatz für die Übernahme des Vorsitzes der Prüfungskommission.

Insbesondere möchte ich auch allen wissenschaftlichen Mitarbeiter und Mitarbeiterinnen des Instituts, den Kollegen und Kolleginnen im Versuchsfeld und der Werkstatt sowie in der Verwaltung und der IT danken. Besonders oft denke ich an meine ehemaligen Mitstreiter der Fachgruppe Aeroakustik und Aeroelastik. Ihnen danke ich für die enge freundschaftliche Zusammenarbeit, den intensiven Austausch und den wertvollen Hinweisen zu meiner Forschungsarbeit. Auch allen Personen, die mich bei der Vorbereitung und Durchführung der Messkampagnen an den verschiedenen Prüfständen unterstützt und diese damit erst ermöglicht haben, danke ich ausdrücklich. Weiterhin danke ich den Studenten und Studentinnen, die mich engagiert in den verschiedenen Bereichen unterstützt haben und deren Zusammenarbeit mir immer große Freude bereitet hat.

Bei dieser Gelegenheit möchte ich auch nicht versäumen, meinen lieben Freunden und Freundinnen zu danken, die mich in den vielen Jahren unterstützt haben und mich durch die Hochs und Tiefs begleitet haben. Im Speziellen möchte ich mich auch bei meinen Eltern bedanken, die mir jederzeit zur Seite gestanden haben. Insbesondere danke ich meiner lieben Mutter für die Stunden und Tage intensivster inhaltlicher Diskussion zu meiner Arbeit und die unglaubliche moralische Unterstützung in den langen Monaten der Auswertung der Messungen und der Verschriftlichungen der Ergebnisse. Ohne euch hätte ich die Arbeit sicherlich nicht zu Ende gebracht.

Contents

List of Figures	iii
List of Tables	xv
List of Symbols	xvii
1 Introduction	1
1.1 Motivation	1
1.2 Objectives	4
2 Theory of Similarity	5
2.1 Establishment of Similarity	5
2.2 Similarity Conditions for Fluid Flows and Turbomachinery	8
2.3 Approximation of Aeroacoustic Similarity Conditions in the LPT	11
2.4 Partial Similarity	15
3 Similarity of Modal Sound Propagation	19
3.1 Modal Sound Propagation in Circular Ducts	20
3.1.1 Solutions to the wave equation	20
3.1.2 Velocities of modal propagation	25
3.2 Hypothesis of this Work	32
3.3 Similarity Approach	34
3.4 Modal similarity map	37
4 Acoustic Measurements in a Low-Pressure Turbine	43
4.1 Measurement Setup	43
4.1.1 Test rig	43
4.1.2 Turbine configuration and test conditions	44
4.1.3 Instrumentation and Data Acquisition	47
4.2 Synthetic Sound Field Excitation	50
4.2.1 Sound generator design and excitation method	50
4.2.2 Preliminary investigations in an aeroacoustic wind tunnel	52
4.3 Cut-off Analysis	55
5 Signal Processing Methods	61
5.1 Spectral Analysis and Modal Decomposition	61
5.1.1 Decomposition methods	61
5.1.2 Two-dimensional discrete Fourier Transform	63

5.1.3	Approximation errors	67
5.1.4	Validation of the 2D-DFT	69
5.2	Statistical Analysis	72
5.2.1	Overlapped-segmented DFT	72
5.2.2	Statistical measures	76
5.3	Background Noise	77
6	Experimental validation	83
6.1	Non-compliance with Similarity	83
6.1.1	Test case 1: Part-load operation	85
6.1.2	Test case 2: Design-point operation	92
6.1.3	Findings	95
6.2	Procedure of Post-hoc Scaling	98
6.3	Discussion of the Results	101
6.3.1	Test case 1: Results of post-hoc scaling	104
6.3.2	Test case 2: Results of post-hoc scaling	106
6.3.3	Alteration of the modal response function	109
6.3.4	Findings	114
6.4	Limits of post-hoc scaling	115
6.5	Summary of the Experimental Validation	118
7	Conclusions and Outlook	121
	Bibliography	125
A	Appendix	133
A.1	Derivation of the Dispersion Relation	134
A.2	Radial Dependency of the Group Velocity Vector	135
A.3	Derivation of the Similarity Relation for the Axial Angle of the Group Velocity Vector	140
A.4	Similarity Map for Mode (2,0)	142
A.5	Aerodynamic Characteristics of the LPT	145
A.5.1	Design Parameter	145
A.6	Test Measurements in the AWT	146
A.7	Validation of the 2D-DFT: Further test cases	148
A.8	Correlation Analysis	150
A.9	Results of Post-hoc Scaling for Test Case 1	152
A.10	Results of Post-hoc Scaling for Test Case 2	174
	Wissenschaftlicher Werdegang	197

List of Figures

3.1	Left: Geometry of the observed problem and definition of the flow direction. Right: Exemplary pressure pattern of the acoustic mode (2, 0). The illustration is based on Fig. 1 in the publication of Hurfar et al. (2015).	22
3.2	Left: Wave vector normal to the wave front. Right: Geometrical construction of the group velocity vector in the presence of flow. Both illustrations are based on Fig. 2 in the publication of Hurfar et al. (2015).	28
3.3	Properties of the group velocity vector relative to cut-off ratio. Top left: Magnitude and axial component of the vector normalized to the speed of sound represented by the solid and dashed lines, respectively. Top right: Axial angle of the group velocity vector. Bottom left: Geometric relations at cut-off condition. Bottom right: Geometric relations at high cut-off ratios.	30
3.4	Similarity map for modal sound propagation. The map is characteristic of the mode (1,0) and a hub-to-tip ratio of $\sigma = 0$. The solid lines represent constant values of the axial angle of the group velocity vector $\phi_{gr,x}$. The dashed lines represent the boundaries of selected values of sensitivity of $\phi_{gr,x}$ with respect to the Mach number ($\Xi_{\phi_{gr,x} M_x}$).	40
3.5	Similarity map for modal sound propagation. The map is characteristic of the mode (1,0) and a hub-to-tip ratio of $\sigma = 0$. The solid lines represent constant values of the axial angle of the group velocity vector $\phi_{gr,x}$. The dashed lines represent the boundaries of selected values of sensitivity of $\phi_{gr,x}$ with respect to the Helmholtz number ($\Xi_{\phi_{gr,x} He}$).	41
4.1	Panoramic view of the instrumented turbine test rig with a sound generator installed in the inlet. (Source: TFD)	44
4.2	Schematic sectional view of the turbine test rig with the 1.5-stage LPT configuration and installed sound generator. Acoustic measurement planes are marked red. Aerodynamic measurements planes are marked green.	46
4.3	Synthetic sound field excitation of the mode $m = 1$ in the AWT. The solid and dashed lines represent a spin in (mathematical) positive and negative direction, respectively.	54
4.4	Synthetic sound field excitation of the mode $m = 2$ in the AWT. The solid and dashed lines represent a spin in (mathematical) positive and negative direction, respectively.	54

4.5	Cut-off conditions for different acoustic modes (m,n) in the measurement planes of the LPT for part-load operation. The areas marked grey give the range of suitable excitation frequencies for the validation measurements with respect to the resolvable modes.	58
4.6	Cut-off conditions for different acoustic modes (m,n) in the measurement planes of the LPT for design-point operation. The areas marked grey give the range of suitable excitation frequencies for the validation measurements with respect to the resolvable modes.	59
5.1	Concept of the 2D-DFT modal decomposition method for J equally-spaced circumferential measurement positions / microphones and N data points / time steps.	64
5.2	Validation of the 2D-DFT using numerically generated test cases considering the mode $m = 1 $ and 20 sensors equally distributed in circumferential direction. Left: Complex vectors of the temporal DFT $F_{k,j}$. Center: Complex vector(s) of the spatial DFT $A_{k,m}$. Right: Temporal amplitude and phase characteristic.	71
5.3	Concept of segmenting of the discrete-time signal $p'_{n,j}$ of length N sampled at the circumferential position j	73
5.4	Concept of overlapping segmenting of the discrete-time signal $p'_{n,j}$ of length N sampled at the circumferential position j	74
5.5	Concept of segment-specific application of the 2D-DFT modal decomposition method.	75
5.6	Noise analysis of the LPT test rig for part-load operation in Sec A and Sec B. Top: Frequency spectrum. Bottom: Relative standard deviation of the spectral amplitudes (RSD).	81
5.7	Noise analysis of the LPT test rig for design-point operation in Sec A and Sec B. Top: Frequency spectrum. Bottom: Relative standard deviation of the spectral amplitudes (RSD).	82
6.1	Acoustic characterization of the measurement section Sec A. Left: Measured modal response subject to the excitation frequency. Right: Measured modal response function to the calculated axial angle of the group velocity vector. [Test case 1 part-load operation $m = -1$ Data set No. 1]	85
6.2	Variations in the aerodynamic data and in the similarity parameters for measurement Sec A. Top left: Ambient temperature. Top right: Total flow temperature. Center left: Total flow pressure. Center right: Reduced mass flow rate. Bottom left: Helmholtz number. Bottom right: Mach number. [Test case 1 part-load operation $m = -1$ $f_{exc} = 520$ Hz]	87

List of Figures

6.3	Correlation Analysis for test case 1. Top left: Variations in the modal response. Top right: Variations in the angle of the group velocity vector. Bottom: Correlation of the modal response with the angle of the group velocity vector. [Test case 1 part-load operation $m = -1$ $f_{\text{exc}} = 520$ Hz]	89
6.4	Relation between linear dependencies and the similarity relation. Top left: Relative change of the Helmholtz number. Top right: Relative change of the Mach number. Center left: Correlation of the modal response with the Helmholtz number. Center right: Correlation of the modal response with the axial Mach number. Bottom left: Extract of the similarity map ($\Xi_{\phi_{\text{gr},x} \text{He}}$). Bottom right: Extract of the similarity map ($\Xi_{\phi_{\text{gr},x} M_x}$). The square marks the operating point. [Test case 1 part-load operation $m = -1$ $f_{\text{exc}} = 520$ Hz]	90
6.5	Acoustic characterization of the measurement section Sec A. Left: Measured modal response subject to the excitation frequency. Right: Measured modal response subject to the calculated axial angle of the group velocity vector. [Test case 2 design-point operation $m = 2$ Data set No. 1]	92
6.6	Variations in the aerodynamic data and in the similarity parameters for measurement Sec A. Top left: Ambient temperature. Top right: Total flow temperature. Center left: Total flow pressure. Center right: Reduced mass flow rate. Bottom left: Helmholtz number. Bottom right: Mach number. [Test case 2 design-point operation $m = 2$ $f_{\text{exc}} = 813$ Hz]	94
6.7	Correlation analysis for test case 2. Top left: Variations in the modal response. Top right: Variations in the angle of the group velocity vector. Bottom: Correlation of the modal response with the angle of the group velocity vector. [Test case 2 design-point operation $m = 2$ $f_{\text{exc}} = 813$ Hz]	96
6.8	Relation between linear dependencies and the similarity relation. Top left: Relative change of the Helmholtz number. Top right: Relative change of the Mach number. Center left: Correlation of the modal response with the Helmholtz number. Center right: Correlation of the modal response with the axial Mach number. Bottom left: Extract of the similarity map ($\Xi_{\phi_{\text{gr},x} \text{He}}$). Bottom right: Extract of the similarity map ($\Xi_{\phi_{\text{gr},x} M_x}$). The square marks the operating point. [Test case 2 design-point operation $m = 2$ $f_{\text{exc}} = 813$ Hz]	97
6.9	Schematic illustration of the process of applied post-hoc scaling for approximation of modal sound propagation similarity.	100
6.10	Surface plots of results of post-hoc scaling. Top: Normalized modal amplitudes before and after post-hoc scaling. Bottom: Absolute relative difference of the modal amplitudes relative to reference before and after post-hoc scaling. [Test case 1 part-load operation $m = -1$]	102

6.11	Results of post-hoc scaling. Top left: Modal amplitude. Top right: Relative change of the modal amplitude with respect to reference data set No.1. Center left: Group velocity angle. Center right: Excitation frequency and calculated reduced frequency. Bottom: Helmholtz number (the lines and markers colored in black and magenta refer to the left and the right ordinate, respectively). [Test case 1 part-load operation $m = -1$ $f_{\text{exc}} = 520$ Hz]	103
6.12	Surface plots of results of post-hoc scaling. Top: Normalized modal amplitudes before and after post-hoc scaling. Bottom: Absolute relative difference of the modal amplitudes relative to the reference before and after post-hoc scaling. [Test case 2 design-point operation $m = 2$]	107
6.13	Results of post-hoc scaling. Top left: Modal amplitude. Top right: Relative change of the modal amplitude with respect to reference data set No.1. Center left: Group velocity angle. Center right: Excitation frequency and calculated reduced frequency. Bottom: Helmholtz number (the lines and markers colored in black and orange refer to the left and the right ordinate, respectively). [Test Case 2 design-point operation $m = 2$ $f_{\text{exc}} = 813$ Hz]	108
6.14	Alteration of the modal response function. Top: Modal frequency-response function relative to the excitation frequency and relative to the angle of the group velocity vector for data Set No. 5. Bottom: Modal frequency-response function relative to the excitation frequency and relative to the angle of the group velocity vector for data Set No. 11. [Test case 1 part-load operation $m = -1$ different data sets]	110
6.15	Alteration of the modal response function. Top: Modal frequency-response function relative to the excitation frequency and relative to the angle of the group velocity vector for data Set No. 15. Bottom: Modal frequency-response function relative to the excitation frequency and relative to the angle of the group velocity vector for data Set No. 28. [Test case 2 design-point operation $m = 2$ different data sets]	113
6.16	Schematic illustration of the impact of varying similarity conditions on the modal response function. Left: Modal response function with a pronounced peak. Right: Modal response function with a flat plateau.	114
6.17	Change of the cut-off condition throughout the LPT. The line colored in magenta and the line colored in orange give the cut-off frequencies for part-load operation and design-point operation, respectively. The marked areas show the range of excited frequencies.	117
A.1	Dependency of the radius r^* on the circumferential mode order m and the hub-to-tip ratio σ for $n = 0$	138

List of Figures

A.2	Similarity map for modal sound propagation. The map is characteristic of the mode (2,0) and a hub-to-tip ratio of $\sigma = 0$. The solid lines represent constant values of the axial angle of the group velocity vector $\phi_{gr,x}$. The dashed lines represent the boundaries of selected values of sensitivity of $\phi_{gr,x}$ with respect to the Mach number ($\Xi_{\phi_{gr,x} M_x}$).	143
A.3	Similarity map for modal sound propagation. The map is characteristic of the mode (2,0) and a hub-to-tip ratio of $\sigma = 0$. The solid lines represent constant values of the axial angle of the group velocity vector $\phi_{gr,x}$. The dashed lines represent the boundaries of selected values of sensitivity of $\phi_{gr,x}$ with respect to the Helmholtz number ($\Xi_{\phi_{gr,x} He}$).	144
A.4	Test measurements of the synthetic modal sound field excitation method. The figure is taken from Bartelt (2015).	146
A.5	Validation of the 2D-DFT using numerically generated test cases considering the mode $m = 2 $ and 20 sensors equally distributed in circumferential direction. Left: Complex vectors of the temporal DFT $F_{k,j}$. Center: Complex vector(s) of the spatial DFT $A_{m,k}$. Right: Temporal amplitude and phase characteristic.	149
A.6	Correlation analysis for all excitation frequencies. Left: Test case 1, part-load operation, and $m = -1$. Right: Test case 2, design-point operation, and $m = 2$	150
A.7	Results of post-hoc scaling. Top left: Modal amplitude. Top right: Relative change of the modal amplitude with respect to reference data set No.1. Center left: Group velocity angle. Center right: Excitation frequency and calculated reduced frequency. Bottom: Helmholtz number (the lines and markers colored in black and magenta refer to the left and the right ordinate, respectively). [Test case 1 part-load operation $m = -1$ $f_{exc} = 505$ Hz]	153
A.8	Results of post-hoc scaling. Top left: Modal amplitude. Top right: Relative change of the modal amplitude with respect to reference data set No.1. Center left: Group velocity angle. Center right: Excitation frequency and calculated reduced frequency. Bottom: Helmholtz number (the lines and markers colored in black and magenta refer to the left and the right ordinate, respectively). [Test case 1 part-load operation $m = -1$ $f_{exc} = 506$ Hz]	154
A.9	Results of post-hoc scaling. Top left: Modal amplitude. Top right: Relative change of the modal amplitude with respect to reference data set No.1. Center left: Group velocity angle. Center right: Excitation frequency and calculated reduced frequency. Bottom: Helmholtz number (the lines and markers colored in black and magenta refer to the left and the right ordinate, respectively). [Test case 1 part-load operation $m = -1$ $f_{exc} = 507$ Hz]	155

A.10 Results of post-hoc scaling. Top left: Modal amplitude. Top right: Relative change of the modal amplitude with respect to reference data set No.1. Center left: Group velocity angle. Center right: Excitation frequency and calculated reduced frequency. Bottom: Helmholtz number (the lines and markers colored in black and magenta refer to the left and the right ordinate, respectively).
 [Test case 1 | part-load operation | $m = -1$ | $f_{exc} = 508$ Hz] 156

A.11 Results of post-hoc scaling. Top left: Modal amplitude. Top right: Relative change of the modal amplitude with respect to reference data set No.1. Center left: Group velocity angle. Center right: Excitation frequency and calculated reduced frequency. Bottom: Helmholtz number (the lines and markers colored in black and magenta refer to the left and the right ordinate, respectively).
 [Test case 1 | part-load operation | $m = -1$ | $f_{exc} = 509$ Hz] 157

A.12 Results of post-hoc scaling. Top left: Modal amplitude. Top right: Relative change of the modal amplitude with respect to reference data set No.1. Center left: Group velocity angle. Center right: Excitation frequency and calculated reduced frequency. Bottom: Helmholtz number (the lines and markers colored in black and magenta refer to the left and the right ordinate, respectively).
 [Test case 1 | part-load operation | $m = -1$ | $f_{exc} = 510$ Hz] 158

A.13 Results of post-hoc scaling. Top left: Modal amplitude. Top right: Relative change of the modal amplitude with respect to reference data set No.1. Center left: Group velocity angle. Center right: Excitation frequency and calculated reduced frequency. Bottom: Helmholtz number (the lines and markers colored in black and magenta refer to the left and the right ordinate, respectively).
 [Test case 1 | part-load operation | $m = -1$ | $f_{exc} = 511$ Hz] 159

A.14 Results of post-hoc scaling. Top left: Modal amplitude. Top right: Relative change of the modal amplitude with respect to reference data set No.1. Center left: Group velocity angle. Center right: Excitation frequency and calculated reduced frequency. Bottom: Helmholtz number (the lines and markers colored in black and magenta refer to the left and the right ordinate, respectively).
 [Test case 1 | part-load operation | $m = -1$ | $f_{exc} = 512$ Hz] 160

A.15 Results of post-hoc scaling. Top left: Modal amplitude. Top right: Relative change of the modal amplitude with respect to reference data set No.1. Center left: Group velocity angle. Center right: Excitation frequency and calculated reduced frequency. Bottom: Helmholtz number (the lines and markers colored in black and magenta refer to the left and the right ordinate, respectively).
 [Test case 1 | part-load operation | $m = -1$ | $f_{exc} = 513$ Hz] 161

List of Figures

- A.16 Results of post-hoc scaling. Top left: Modal amplitude. Top right: Relative change of the modal amplitude with respect to reference data set No.1. Center left: Group velocity angle. Center right: Excitation frequency and calculated reduced frequency. Bottom: Helmholtz number (the lines and markers colored in black and magenta refer to the left and the right ordinate, respectively).
 [Test case 1 | part-load operation | $m = -1$ | $f_{exc} = 514$ Hz] 162
- A.17 Results of post-hoc scaling. Top left: Modal amplitude. Top right: Relative change of the modal amplitude with respect to reference data set No.1. Center left: Group velocity angle. Center right: Excitation frequency and calculated reduced frequency. Bottom: Helmholtz number (the lines and markers colored in black and magenta refer to the left and the right ordinate, respectively).
 [Test case 1 | part-load operation | $m = -1$ | $f_{exc} = 515$ Hz] 163
- A.18 Results of post-hoc scaling. Top left: Modal amplitude. Top right: Relative change of the modal amplitude with respect to reference data set No.1. Center left: Group velocity angle. Center right: Excitation frequency and calculated reduced frequency. Bottom: Helmholtz number (the lines and markers colored in black and magenta refer to the left and the right ordinate, respectively).
 [Test case 1 | part-load operation | $m = -1$ | $f_{exc} = 516$ Hz] 164
- A.19 Results of post-hoc scaling. Top left: Modal amplitude. Top right: Relative change of the modal amplitude with respect to reference data set No.1. Center left: Group velocity angle. Center right: Excitation frequency and calculated reduced frequency. Bottom: Helmholtz number (the lines and markers colored in black and magenta refer to the left and the right ordinate, respectively).
 [Test case 1 | part-load operation | $m = -1$ | $f_{exc} = 517$ Hz] 165
- A.20 Results of post-hoc scaling. Top left: Modal amplitude. Top right: Relative change of the modal amplitude with respect to reference data set No.1. Center left: Group velocity angle. Center right: Excitation frequency and calculated reduced frequency. Bottom: Helmholtz number (the lines and markers colored in black and magenta refer to the left and the right ordinate, respectively).
 [Test case 1 | part-load operation | $m = -1$ | $f_{exc} = 518$ Hz] 166
- A.21 Results of post-hoc scaling. Top left: Modal amplitude. Top right: Relative change of the modal amplitude with respect to reference data set No.1. Center left: Group velocity angle. Center right: Excitation frequency and calculated reduced frequency. Bottom: Helmholtz number (the lines and markers colored in black and magenta refer to the left and the right ordinate, respectively).
 [Test case 1 | part-load operation | $m = -1$ | $f_{exc} = 519$ Hz] 167

- A.22 Results of post-hoc scaling. Top left: Modal amplitude. Top right: Relative change of the modal amplitude with respect to reference data set No.1. Center left: Group velocity angle. Center right: Excitation frequency and calculated reduced frequency. Bottom: Helmholtz number (the lines and markers colored in black and magenta refer to the left and the right ordinate, respectively).
[Test case 1 | part-load operation | $m = -1$ | $f_{exc} = 520$ Hz] 168
- A.23 Results of post-hoc scaling. Top left: Modal amplitude. Top right: Relative change of the modal amplitude with respect to reference data set No.1. Center left: Group velocity angle. Center right: Excitation frequency and calculated reduced frequency. Bottom: Helmholtz number (the lines and markers colored in black and magenta refer to the left and the right ordinate, respectively).
[Test case 1 | part-load operation | $m = -1$ | $f_{exc} = 521$ Hz] 169
- A.24 Results of post-hoc scaling. Top left: Modal amplitude. Top right: Relative change of the modal amplitude with respect to reference data set No.1. Center left: Group velocity angle. Center right: Excitation frequency and calculated reduced frequency. Bottom: Helmholtz number (the lines and markers colored in black and magenta refer to the left and the right ordinate, respectively).
[Test case 1 | part-load operation | $m = -1$ | $f_{exc} = 522$ Hz] 170
- A.25 Results of post-hoc scaling. Top left: Modal amplitude. Top right: Relative change of the modal amplitude with respect to reference data set No.1. Center left: Group velocity angle. Center right: Excitation frequency and calculated reduced frequency. Bottom: Helmholtz number (the lines and markers colored in black and magenta refer to the left and the right ordinate, respectively).
[Test case 1 | part-load operation | $m = -1$ | $f_{exc} = 523$ Hz] 171
- A.26 Results of post-hoc scaling. Top left: Modal amplitude. Top right: Relative change of the modal amplitude with respect to reference data set No.1. Center left: Group velocity angle. Center right: Excitation frequency and calculated reduced frequency. Bottom: Helmholtz number (the lines and markers colored in black and magenta refer to the left and the right ordinate, respectively).
[Test case 1 | part-load operation | $m = -1$ | $f_{exc} = 524$ Hz] 172
- A.27 Results of post-hoc scaling. Top left: Modal amplitude. Top right: Relative change of the modal amplitude with respect to reference data set No.1. Center left: Group velocity angle. Center right: Excitation frequency and calculated reduced frequency. Bottom: Helmholtz number (the lines and markers colored in black and magenta refer to the left and the right ordinate, respectively).
[Test case 1 | part-load operation | $m = -1$ | $f_{exc} = 525$ Hz] 173

List of Figures

- A.28 Results of post-hoc scaling. Top left: Modal amplitude. Top right: Relative change of the modal amplitude with respect to reference data set No.1. Center left: Group velocity angle. Center right: Excitation frequency and calculated reduced frequency. Bottom: Helmholtz number (the lines and markers colored in black and orange refer to the left and the right ordinate, respectively).
[Test Case 2 | design-point operation | $m = 2$ | $f_{\text{exc}} = 797$ Hz] 175
- A.29 Results of post-hoc scaling. Top left: Modal amplitude. Top right: Relative change of the modal amplitude with respect to reference data set No.1. Center left: Group velocity angle. Center right: Excitation frequency and calculated reduced frequency. Bottom: Helmholtz number (the lines and markers colored in black and orange refer to the left and the right ordinate, respectively).
[Test Case 2 | design-point operation | $m = 2$ | $f_{\text{exc}} = 798$ Hz] 176
- A.30 Results of post-hoc scaling. Top left: Modal amplitude. Top right: Relative change of the modal amplitude with respect to reference data set No.1. Center left: Group velocity angle. Center right: Excitation frequency and calculated reduced frequency. Bottom: Helmholtz number (the lines and markers colored in black and orange refer to the left and the right ordinate, respectively).
[Test Case 2 | design-point operation | $m = 2$ | $f_{\text{exc}} = 799$ Hz] 177
- A.31 Results of post-hoc scaling. Top left: Modal amplitude. Top right: Relative change of the modal amplitude with respect to reference data set No.1. Center left: Group velocity angle. Center right: Excitation frequency and calculated reduced frequency. Bottom: Helmholtz number (the lines and markers colored in black and orange refer to the left and the right ordinate, respectively).
[Test Case 2 | design-point operation | $m = 2$ | $f_{\text{exc}} = 800$ Hz] 178
- A.32 Results of post-hoc scaling. Top left: Modal amplitude. Top right: Relative change of the modal amplitude with respect to reference data set No.1. Center left: Group velocity angle. Center right: Excitation frequency and calculated reduced frequency. Bottom: Helmholtz number (the lines and markers colored in black and orange refer to the left and the right ordinate, respectively).
[Test Case 2 | design-point operation | $m = 2$ | $f_{\text{exc}} = 801$ Hz] 179
- A.33 Results of post-hoc scaling. Top left: Modal amplitude. Top right: Relative change of the modal amplitude with respect to reference data set No.1. Center left: Group velocity angle. Center right: Excitation frequency and calculated reduced frequency. Bottom: Helmholtz number (the lines and markers colored in black and orange refer to the left and the right ordinate, respectively).
[Test Case 2 | design-point operation | $m = 2$ | $f_{\text{exc}} = 802$ Hz] 180

- A.34 Results of post-hoc scaling. Top left: Modal amplitude. Top right: Relative change of the modal amplitude with respect to reference data set No.1. Center left: Group velocity angle. Center right: Excitation frequency and calculated reduced frequency. Bottom: Helmholtz number (the lines and markers colored in black and orange refer to the left and the right ordinate, respectively).
[Test Case 2 | design-point operation | $m = 2$ | $f_{exc} = 803$ Hz] 181
- A.35 Results of post-hoc scaling. Top left: Modal amplitude. Top right: Relative change of the modal amplitude with respect to reference data set No.1. Center left: Group velocity angle. Center right: Excitation frequency and calculated reduced frequency. Bottom: Helmholtz number (the lines and markers colored in black and orange refer to the left and the right ordinate, respectively).
[Test Case 2 | design-point operation | $m = 2$ | $f_{exc} = 804$ Hz] 182
- A.36 Results of post-hoc scaling. Top left: Modal amplitude. Top right: Relative change of the modal amplitude with respect to reference data set No.1. Center left: Group velocity angle. Center right: Excitation frequency and calculated reduced frequency. Bottom: Helmholtz number (the lines and markers colored in black and orange refer to the left and the right ordinate, respectively).
[Test Case 2 | design-load operation | $m = 2$ | $f_{exc} = 805$ Hz] 183
- A.37 Results of post-hoc scaling. Top left: Modal amplitude. Top right: Relative change of the modal amplitude with respect to reference data set No.1. Center left: Group velocity angle. Center right: Excitation frequency and calculated reduced frequency. Bottom: Helmholtz number (the lines and markers colored in black and orange refer to the left and the right ordinate, respectively).
[Test Case 2 | design-point operation | $m = 2$ | $f_{exc} = 806$ Hz] 184
- A.38 Results of post-hoc scaling. Top left: Modal amplitude. Top right: Relative change of the modal amplitude with respect to reference data set No.1. Center left: Group velocity angle. Center right: Excitation frequency and calculated reduced frequency. Bottom: Helmholtz number (the lines and markers colored in black and orange refer to the left and the right ordinate, respectively).
[Test Case 2 | design-point operation | $m = 2$ | $f_{exc} = 807$ Hz] 185
- A.39 Results of post-hoc scaling. Top left: Modal amplitude. Top right: Relative change of the modal amplitude with respect to reference data set No.1. Center left: Group velocity angle. Center right: Excitation frequency and calculated reduced frequency. Bottom: Helmholtz number (the lines and markers colored in black and orange refer to the left and the right ordinate, respectively).
[Test Case 2 | design-point operation | $m = 2$ | $f_{exc} = 808$ Hz] 186

List of Figures

- A.40 Results of post-hoc scaling. Top left: Modal amplitude. Top right: Relative change of the modal amplitude with respect to reference data set No.1. Center left: Group velocity angle. Center right: Excitation frequency and calculated reduced frequency. Bottom: Helmholtz number (the lines and markers colored in black and orange refer to the left and the right ordinate, respectively).
[Test Case 2 | design-point operation | $m = 2$ | $f_{\text{exc}} = 809$ Hz] 187
- A.41 Results of post-hoc scaling. Top left: Modal amplitude. Top right: Relative change of the modal amplitude with respect to reference data set No.1. Center left: Group velocity angle. Center right: Excitation frequency and calculated reduced frequency. Bottom: Helmholtz number (the lines and markers colored in black and orange refer to the left and the right ordinate, respectively).
[Test Case 2 | design-point operation | $m = 2$ | $f_{\text{exc}} = 810$ Hz] 188
- A.42 Results of post-hoc scaling. Top left: Modal amplitude. Top right: Relative change of the modal amplitude with respect to reference data set No.1. Center left: Group velocity angle. Center right: Excitation frequency and calculated reduced frequency. Bottom: Helmholtz number (the lines and markers colored in black and orange refer to the left and the right ordinate, respectively).
[Test Case 2 | design-point operation | $m = 2$ | $f_{\text{exc}} = 811$ Hz] 189
- A.43 Results of post-hoc scaling. Top left: Modal amplitude. Top right: Relative change of the modal amplitude with respect to reference data set No.1. Center left: Group velocity angle. Center right: Excitation frequency and calculated reduced frequency. Bottom: Helmholtz number (the lines and markers colored in black and orange refer to the left and the right ordinate, respectively).
[Test Case 2 | design-point operation | $m = 2$ | $f_{\text{exc}} = 812$ Hz] 190
- A.44 Results of post-hoc scaling. Top left: Modal amplitude. Top right: Relative change of the modal amplitude with respect to reference data set No.1. Center left: Group velocity angle. Center right: Excitation frequency and calculated reduced frequency. Bottom: Helmholtz number (the lines and markers colored in black and orange refer to the left and the right ordinate, respectively).
[Test Case 2 | design-point operation | $m = 2$ | $f_{\text{exc}} = 813$ Hz] 191
- A.45 Results of post-hoc scaling. Top left: Modal amplitude. Top right: Relative change of the modal amplitude with respect to reference data set No.1. Center left: Group velocity angle. Center right: Excitation frequency and calculated reduced frequency. Bottom: Helmholtz number (the lines and markers colored in black and orange refer to the left and the right ordinate, respectively).
[Test Case 2 | design-point operation | $m = 2$ | $f_{\text{exc}} = 814$ Hz] 192

A.46 Results of post-hoc scaling. Top left: Modal amplitude. Top right: Relative change of the modal amplitude with respect to reference data set No.1. Center left: Group velocity angle. Center right: Excitation frequency and calculated reduced frequency. Bottom: Helmholtz number (the lines and markers colored in black and orange refer to the left and the right ordinate, respectively).
 [Test Case 2 | design-point operation | $m = 2$ | $f_{\text{exc}} = 815$ Hz] 193

A.47 Results of post-hoc scaling. Top left: Modal amplitude. Top right: Relative change of the modal amplitude with respect to reference data set No.1. Center left: Group velocity angle. Center right: Excitation frequency and calculated reduced frequency. Bottom: Helmholtz number (the lines and markers colored in black and orange refer to the left and the right ordinate, respectively).
 [Test Case 2 | design-point operation | $m = 2$ | $f_{\text{exc}} = 816$ Hz] 194

A.48 Results of post-hoc scaling. Top left: Modal amplitude. Top right: Relative change of the modal amplitude with respect to reference data set No.1. Center left: Group velocity angle. Center right: Excitation frequency and calculated reduced frequency. Bottom: Helmholtz number (the lines and markers colored in black and orange refer to the left and the right ordinate, respectively).
 [Test Case 2 | design-point operation | $m = 2$ | $f_{\text{exc}} = 817$ Hz] 195

List of Tables

4.1	Calculated cut-off frequencies f_{cut} for the test measurements in the AWT. The given frequencies are restricted to the modes which are cut-on in the given range of excited frequencies from $f_{\text{exc}} = 400$ Hz to $f_{\text{exc}} = 1200$ Hz.	53
5.1	Analysis of the (noise) frequency spectra of the LPT test rig. 2D-DFT processing parameters and properties.	79
6.1	Mean aerodynamic operating parameters for part-load operation and design-point operation.	83
6.2	2D-DFT processing parameters and properties. The Nyquist mode m_{Nyquist} refers to the highest mode resolvable with respect to both directions of spinning. The frequency resolution $\Delta f^{[s]}$ is valid for the segmented data sequences.	84
A.1	Test conditions at design-point operation and blade characteristics as given by Biester et al. (2011).	145
A.2	Test measurements of the synthetic modal sound field excitation method: 2D-DFT processing parameters and properties. The Nyquist mode refers to the highest mode resolvable with respect to both directions of spinning.	147

List of Symbols

Latin Symbols

Symbol	Unit	Description	Definition
a	–	Integer	Π theorem
\mathbf{A}	–	Modal frequency-response function	Eq. (6.1), Eq. (6.2)
A	Pa	Pressure amplitude	
A_m	Pa	Modal pressure amplitude	
$\underline{A_{k,m}}$	–	(Forward) Spatial DFT with respect to the discrete frequency f_k^*	Eq. (5.3), DFT
B	–	Number of rotor blades	
c	$\frac{\text{m}}{\text{s}}$	Speed of sound or velocity of sound propagation	
\mathbf{c}	$\frac{\text{m}}{\text{s}}$	Velocity vector of sound propagation	Fig. 3.2
c_x	$\frac{\text{m}}{\text{s}}$	Axial velocity of sound propagation	Eq. (3.18)
\mathbf{c}_x	$\frac{\text{m}}{\text{s}}$	Vector of the axial velocity of sound propagation	Fig. 3.2
c_{gr}	$\frac{\text{m}}{\text{s}}$	Group velocity	i.a. Eq. (3.20)
\mathbf{c}_{gr}	$\frac{\text{m}}{\text{s}}$	Vector of the group velocity	Eq. (3.19), Fig. 3.2
$c_{\text{gr},x}$	$\frac{\text{m}}{\text{s}}$	Axial group velocity	i.a. Eq. (3.21)
$\mathbf{c}_{\text{gr},x}$	$\frac{\text{m}}{\text{s}}$	Vector of the axial group velocity	Fig. 3.2
C	–	Cauchy number	Eq. (2.9)
D	m	Diameter	
e	Pa	Bulk modulus	
\mathbf{e}_x	–	Coordinate vector	
E	–	Euler number	Eq. (2.7)
f	–	Function or functional relation	
f	Hz	Frequency	
f_{cut}	Hz	Cut-off frequency	Eq. (3.10), Eq. (4.3)
f_{exc}	Hz	Excitation frequency	
f_k	Hz	Continuous-time frequency	Eq. (5.5), DFT
f_k^*	–	Discrete temporal frequency	Eq. (5.4), DFT
f_{red}	Hz	Reduced frequency	Eq. (3.42)

f_s	Hz	Sampling frequency	
F	–	Function or functional relation	II theorem
$F_{k,j}$	–	(Forward) Temporal DFT with respect to the microphone j	Eq. (5.3), DFT
Fr	–	Froude number	Eq. (2.6)
g	$\frac{\text{m}}{\text{kg s}^2}$	Acceleration of gravity	
$g(r)$	–	Radial function or solution	Eq. (3.5)
h	–	Harmonic of BPF	
\mathbf{h}	–	Vector describing a helicoid	Eq. (A.14)
He	–	Helmholtz number	Eq. (2.24)
He _{red}	–	Reduced Helmholtz number	Eq. (3.44)
i	–	Integer	II theorem
j	–	Integer, circumferential position (microphone)	DFT
J	–	Number of microphones	
J_m	–	m -th order Besselfunction of the first kind	
k	–	Integer	II theorem, DFT
k	$\frac{1}{\text{m}}$	Wave number	
\mathbf{k}	$\frac{1}{\text{m}}$	Wave vector	Fig. 3.2
k^0	$\frac{1}{\text{m}}$	Free-field wave number	Eq. (3.9)
k_i	$\frac{1}{\text{m}}$	Wave number in the i -th direction	
k_m	$\frac{1}{\text{m}}$	Continuous spatial frequency	Eq. (5.9), DFT
k_m^*	–	Discrete spatial frequency	Eq. (5.8), DFT
k_x	$\frac{1}{\text{m}}$	Axial wave number	Eq. (3.8), Eq. (4.4)
k_θ	$\frac{1}{\text{m}}$	Circumferential wave number	Eq. (3.12)
$k_{r\theta}$	$\frac{1}{\text{m}}$	Combined radial and circumferential wave number	
l	–	Integer	DFT
L	m	Length	
L	–	Number of data points in segment s (without overlapping)	DFT
m	–	Circumferential mode order ($m = \dots - 2, -1, 0, 1, 2, \dots$)	
\dot{m}	$\frac{\text{kg}}{\text{s}}$	Mass flow rate	
M	–	Mach number	Eq. (2.10)
M_x	–	Mach number in axial direction	Eq. (2.19)
\mathbf{M}_x	–	Vector of the axial Mach number	Fig. 3.2

List of Symbols

M_θ	–	Mach number in circumferential direction	
n	–	Integer	II theorem, DFT
n	–	Radial mode order ($n = 0, 1, 2, \dots$)	
\mathbf{n}	–	Unit space vector	Fig. 3.2
N	$\frac{1}{min}$	Rotational speed	
N	–	Number of data points	DFT
p	–	Pitch of helicoid	Eq. (A.15)
p'	Pa	Acoustic pressure	
p	Pa	Pressure	
$p_{n,j}$	–	Discrete-time sequence with respect to microphone j	2D-DFT
P	–	Dependent quantity	II theorem
q	–	Arbitrary quantity	
Q	–	Independent quantity	II theorem
$Q_{(m,n)}$	–	Weighting factor	
r	–	Pearson correlation coefficient	Eq. (5.20)
r	m	Radial coordinate	Fig. 3.1
r'	–	Specific ratio, e.g. ratio of length	II theorem
r^*	m	Caustic radius	Eq. (3.30)
R	–	Number of overlapping data points	DFT
R	m	Duct radius	Fig. 3.1
R_h	m	Radius at the hub	Fig. 3.1
R_s	$\frac{J}{kgK}$	Specific gas constant	
Re	–	Reynolds number	Eq. (2.5)
s	–	Integer	i.a. DFT
s	$\frac{J}{K}$	Entropy	
S	–	Number of segments or samples	DFT
St	–	Strouhal number	Eq. (2.11)
t	s	Time variable	
T	s	Measurement time	
T	K	Temperature	
u_i	$\frac{m}{s}$	Flow velocity in the i -th direction	
$u_{(m,n)}$	–	Characteristic eigenvalue	
U^0	$\frac{m}{s}$	Flow velocity in the axial direction	
\mathbf{U}	$\frac{m}{s}$	Vector of the flow velocity in the axial direction	
V	–	Number of stator blades	

V	$\frac{\text{m}}{\text{s}}$	Flow velocity	
w	–	Hanning-function	Eq. (5.11), DFT
We	–	Weber number	Eq. (2.8)
x	–	Arbitrary variable	
x	m	Axial coordinate	Fig. 3.1
x_i	m	Vector of the spatial coordinate	
x_n	–	Discrete time-signal	
\underline{X}_k	–	Forward DFT	Eq. (5.1)
y	–	Arbitrary variable	
Y_m	–	m -th order Besselfunction of the second kind	

Greek Symbols

Symbol	Unit	Description	Definition
$\beta_{(m,n)}$	–	Argument of the Bessel function	Eq. (3.6)
ϵ	–	Relative modal amplitude	Eq. (3.14)
ϕ	rad	Propagation angle	
ϕ_x	rad	Propagation angle relative to the duct axis	Fig. 3.2
$\phi_{\text{gr},x}$	rad	Axial angle of the group velocity vector	i.a. Eq. (3.22)
φ	rad	Modal phase	
φ^0	rad	Initial modal phase	
γ	$\frac{\text{N}}{\text{m}}$	Surface tension	
η	–	Arbitrary variable	
κ	–	Ratio of specific heats	
λ	m	Wavelength	
λ_x	m	Axial wavelength	
λ_θ	m	Circumferential wavelength	
μ	$\frac{\text{kg}}{\text{ms}}$	Dynamic viscosity	
Π	–	Dimensionless product	Π theorem
θ	rad	Circumferential coordinate	Fig. 3.1
ρ	$\frac{\text{kg}}{\text{m}^3}$	Density	
σ	–	Hub-to-tip ratio	Eq. (2.30)
σ	–	Standard deviation	Eq. (5.16)
ω	$\frac{\text{rad}}{\text{s}}$	Angular (acoustic) frequency	Eq. (3.2)

List of Symbols

ξ	–	Cut-off ratio	Eq. (3.11)
Ξ	–	Sensitivity	
ψ	–	Function or functional relation	II theorem
Ψ	–	Function or functional relation	

Subscripts

Symbol	Description
$(\cdot)_{\text{amb}}$	With respect to ambient condition
$(\cdot)_{\text{cut}}$	Matching cut-off condition
$(\cdot)_{\text{max}}$	Maximum value
$(\cdot)_{\text{min}}$	Minimum value
$(\cdot)_{(m,n)}$	With respect to the mode (m, n)
$(\cdot)_{\text{Nyquist}}$	Nyquist frequency or Nyquist mode
$(\cdot)_{\text{red}}$	Reduced quantity, e.g. reduces mass flow rate
$(\cdot)_{\text{ref}}$	Reference or relative to reference
$(\cdot)_{\text{tot}}$	Total quantity

Superscripts

Symbol	Description
$(\cdot)'$	Acoustic quantity
$(\cdot)^0$	Quantity of the undisturbed steady state
$(\cdot)^+$	Modal propagation in the direction of the flow
$(\cdot)^-$	Modal propagation opposite to the direction of the flow
$(\cdot)^*$	Dimensionless variable (cf. Sec. 2.3), or conjugate symmetric (DFT), or radial-dependent (cf. Sec. A.2)
$\overline{(\cdot)}$	Mean of a quantity
$(\cdot)^{[s]}$	With respect to segment s of the overlapped-segmented DFT
$(\cdot)^{(\sigma)}$	With respect to the hub-to-tip ratio

Mathematical Symbols and Operators

Symbol	Description
$\frac{D}{Dt}$	Total derivative as defined in Eq. (2.17)
Re	Real part of a complex number
Im	Imaginary part of a complex number
\mathbb{N}	Natural numbers 0, 1, 2 ...
\mathbb{Z}	Set of integers ... -2, -1, 0, 1, 2 ...
∂	Partial derivative
(\cdot)	Complex value
\angle	Angle of a complex value
$ (\cdot) $	Absolute value

Mathematical Constants

Symbol	Description
π	Pi constant ($\pi = 3.14159\dots$)
e	Euler's constant ($e = 0.57721\dots$)
i	Imaginary unit ($i^2 = -1$)

Abbreviations

Symbol	Description
AWT	Aeroacoustic Wind Tunnel
BPF	Blade-passing frequency
CI	Confidence interval
Cov	Covariance
DC	Direct current
DFT	Discrete Fourier Transform
2D-DFT	Two-dimensional discrete Fourier Transform

List of Symbols

FPGA	Field programmable gate array chips
LPT	Low-pressure turbine
MP	Measurement plane
RMA	Radial mode analysis
RSD	Relative standard deviation
Sec	(Acoustic measurement) Section
TFD	Institute of Turbomachinery and Fluid Dynamics
WHO	World Health Organization

1 Introduction

This work is concerned with the establishment of similarity of modal sound propagation in turbomachinery test rigs. In the first section of this chapter, the social responsibility and general motivation to carry out research on the propagation of acoustic modes is outlined (cf. Sec. 1.1). Furthermore, the challenges of experimental investigations with respect to the achievement of similarity between individual measurements are described. Based on this introduction to the topic, the objectives of this work and the procedures selected to achieve these objectives are presented in Sec. 1.2.

1.1 Motivation

In a free space, sound propagates as a simple plane wave. However, in enclosed or partly enclosed spaces, as in the different sections of a turbomachine, sound propagates in complex forms of higher order called *acoustic modes*. These sound fields are characterized by specific patterns which are formed by multiple reflections at the boundaries of the confined area. Such patterns depend, among other factors, on the acoustic impedance at the boundaries and the geometry of the confined area, the propagation medium, ambient conditions, the acoustic oscillation frequency, and, of course, on the sound source itself.

The major sources of acoustic modes in the turbomachinery components of an aircraft engine, such as the compressor or the turbine, are the rotor, on the one hand, and the periodic interaction of the stationary blades and the rotating blades, on the other hand. In their classic work on sound generation and propagation in the early 1960's, Tyler and Sofrin (1962) showed that the acoustic modes appear as distinct peaks in the sound pressure spectrum of the turbomachines at frequencies matching the blade-passing frequency or its harmonics. Acoustic modes radiate from the inlet and exhaust nozzle of an aircraft engine to the environment and are a strong contributor to the emitted sound pressure level, and thus to the perceived noise exposure of the population affected. As the modes appear at specific frequencies, they are referred to as the tonal noise components.

Long-term and short-term exposure to unwelcome sound as transportation noise or aircraft noise may result in various health impairments both physical as well as psychological. Possible health consequences of exposure to elevated noise levels include hearing damage, cardiovascular disease, insomnia, cognitive impairment, stress, and annoyance response, to name but a few (cf. Kaltenbach et al. (2016), WHO Regional Office for Europe (2011), or WHO Regional Office for Europe (2018)). Results of empirical studies carried out, for example, by Hellman (1982), Angerer et al. (1991), Landström et al. (1995), and Berckmans et al. (2008) demonstrate that the presence of one or more

tonal components in a frequency spectrum increases annoyance perception and has a negative impact on cognitive performance. Thus, the perceived level of exposure not only depends on the overall sound pressure level but on specific characteristics of the tone-noise-complex, as for example the tone-to-noise ratio, the frequency of the tone(s), the relative location of the tone(s) in the spectrum, the spectral shape of the noise, and the number of tonal components. Fundamental works on these characteristics have been carried out by R. P. Hellmann in the 1980's (cf. Hellman (1982), Hellman (1984), and Hellman (1985)). But Hellmann concentrated - in line with most studies - not on specific noise sources but on community noise in general. Tonal components in aircraft noise in particular, have been only scarcely addressed, but for example by Angerer et al. (1991) and Berckmans et al. (2008). Recently, White et al. (2017) and White (2018) investigated the relationship between the tonal components in the radiated noise spectrum of an aircraft and the level of perceived annoyance. For this purpose, the researchers played different sound samples to participants of an empirical study while they were working on mentally demanding tasks. Subsequently, the participants were asked to quantify their annoyance by each sample. Among other things, an original recording of a flyover of a descending A320 aircraft as well as a processed version of the same recording were used. In the processed version, the tonal components of the original sample were filtered out, but the overall sound pressure level was maintained. For different overall noise levels, the original sample with specific tonal components was always rated as being more annoying than the sample from which the major tonal components had been removed. This observation confirms that the relation between perceived annoyance and tonal components also applies to the noise emitted by an aircraft engine.

The World Health Organization (WHO) reviewed available scientific work and identified noise pollution as a "threat to public health". The organization derived guidelines and recommendations to support community institutions and political bodies in their decision-making on noise control legislation (cf. WHO (1999), WHO Regional Office for Europe (2009), and WHO Regional Office for Europe (2018)). Nowadays, the noise emissions of an aircraft are strictly regulated and limited. Continuous tightening of the statutory noise certification requirements puts pressure on aircraft and engine designers and facilitates further development of sound abatement technologies to reduce the overall noise level of an aircraft engine. The study of White et al. (2017) demonstrates the importance of concentrating on the reduction of specific tonal noise components as part of the reduction of the overall noise level in accordance with psychoacoustic results. Thus, it is necessary to develop effective measures to attenuate the tonal acoustic modes which are generated in the turbomachinery components and propagate throughout the engine. In order to determine the dominant frequencies and modes and accordingly develop highly efficient noise reduction technologies, it is mandatory to fully understand the modal sound field propagation throughout the turbomachinery components and ducts of an aircraft engine.

Turbomachinery research in general and research on modal sound propagation in turbomachines in particular are carried out either analytically, numerically, or experimentally. Since analytical studies are restricted to simple conditions and numerical analyses are

1.1 Motivation

limited by calculation capacities and the simplifications of the implemented models, experimental investigations are an essential tool in scientific research. For economic reasons, experiments are mostly carried out on scale models rather than on the actual machines (cf. Murphy (1950)). Thus, turbomachinery test rigs often differ from the machines eventually in use in terms of geometric size, material, and operating conditions such as temperature, pressure, or working medium. In order to observe similar physical effects in both systems, the *theory of similarity* is considered in the design and operation of test rigs. *Similarity conditions* are established when certain non-dimensional parameters, which control the behavior of the system, are numerically equal (cf. Bridgman (1922)). These quantities are also referred to as *similarity parameters*. Depending on the research objectives, measurement setups might be designed either to satisfy the requirements for *complete similarity* or for *partial similarity*. For complete similarity, all known similarity parameters have to be adhered to. On the contrary, partial similarity refers to the establishment of similarity with respect to one specific physical effect or discipline while accepting non-compliance with similarity with respect to other aspects as pointed out by e.g. Spurk (1992) or Schlichting (2016).

For high-quality research data, the values of the similarity parameters have to be accurately met during the time of measurements. For this purpose, the operating parameters of the test rigs have to be continuously evaluated and, if necessary, adjusted, to compensate for changes in the inlet conditions of the respective measurement volume. Especially for turbomachinery test rigs with an open cycle configuration, where the medium is continuously collected at ambient conditions, compliance with the exact values of defined similarity parameters in two consecutive measurements is challenging. In open cycle test rigs, variations in the inlet conditions like, for example, inlet temperature, inlet pressure, or humidity of the fluid frequently occur. Eventually, these changes might impair similarity conditions if not compensated by an adjustment of the operating parameters.

This work now focuses on the establishment of aeroacoustic similarity during turbomachinery test rig operation. For aeroacoustic similarity, both aerodynamic similarity and (aero)acoustic similarity have to be accounted for. By non-dimensionalization of the convective wave equation, the *Helmholtz number* and the *Mach number* can be identified to establish similarity conditions for time-harmonic sound propagation in an ideal and inviscid flow (cf. Sec. 2.3). Hence, similar operating conditions for sound propagation investigations require that these similarity parameters are numerically equal. In the last years, the application of so-called *sound generators* has become more and more established. Installed in the setup of a test rig, these sound generators can be used to synthetically excite rotor-synchronous as well as non-rotor synchronous sound fields of an arbitrary modal order. Enghardt et al. (2002) for example analyzed the application of loudspeakers for active noise control in turbomachinery. Bartelt (2015) extensively made use of this methodological tool to investigate the propagation properties of acoustic modes through a low-pressure turbine configuration. The application of such a sound generator presumed, the Helmholtz number can then be accurately controlled by adjusting the frequency of the excited modal sound field. The Mach number

can be controlled by adjusting the mass flow rate and the rotor speed of the turbomachinery test rig (Braeunling (2015)). However, control of these operating parameters is restricted by the resolution and constancy of the controls of the test rig's periphery. As a result, similarity of the Mach number is not always met and similarity conditions often cannot be achieved. When observing narrow frequency-band sensitive phenomena like, for example, acoustic resonances as reported by Hellmich and Seume (2008), even small variations in the similarity parameters might change modal propagation characteristics and consequently impair the comparability of measurements, and in the end research results. Despite the possibly severe impact of non-compliance with similarity, reported research on this topic in general and on methods for the establishment of (partial) similarity in particular are not published in open sources to the knowledge of the author.

1.2 Objectives

This work addresses similar operating conditions for research on modal sound propagation in turbomachinery test rigs equipped with a sound generator for synthetic sound field excitation. The investigation focuses on individual acoustic modes with a specific mode order propagating in a circular duct carrying an axial uniform flow. Furthermore, the investigation focuses on test rig operations where equality of the Helmholtz number and / or the Mach number between measurements is not met. The objective of this work is to define the requirement for similarity, on the one hand, and to develop an approach for establishing similarity conditions of modal sound propagation under the aforementioned conditions, on the other hand. Impact of non-compliance with similarity on measurement results is investigated with the objective to assess possible impairment of research results. Essential fundamentals of the approach developed have already been published by the author of this work (cf. Hurfar et al. (2015)).

To achieve the work's objectives, the first part of this work is concerned with an analytical investigation of modal sound propagation properties. Based on this analysis and in consideration of the theory of similarity, the hypothesis is developed that with respect to the propagation of one specific acoustic mode, the modal *axial angle of the group velocity vector* can be used to establish partial similarity conditions in case of varying Helmholtz number and / or the Mach number (cf. Sec. 3.2). The second part of this work concentrates on the experimental validation of the hypothesis introduced. For this purpose, measurements are carried out on the low-pressure air turbine test rig (LPT) of the Institute of Turbomachinery and Fluid Dynamics (TFD). A sound generator is installed in the inlet duct of the test rig upstream of the first turbine stage for controlled excitation of specific acoustic modes. Similarity is evaluated by considering the modal response function measured in the circular inlet duct for a specified frequency range for two different test cases and under varying aerodynamic boundary conditions.

2 Theory of Similarity

In this chapter, an overview of the theory of similarity and of the similarity parameters used for turbomachinery research is given. Furthermore, the similarity conditions for the propagation of sound fields in the inlet duct upstream of the first stage of the LPT are derived for an approximate flow model.

In Sec. 2.1, general definitions are introduced and common procedures for the derivation of similarity parameters are described. Section 2.2 then focuses on the establishment of similarity conditions in turbomachines. Chosen similarity parameters are presented. Subsequently, in Sec. 2.3, the requirements for similarity of sound propagation in the LPT are determined for simplified assumptions of the flow. For this purpose, the convective wave equation and the corresponding boundary conditions are non-dimensionalized. The chapter closes with a discussion of the achievement of complete similarity conditions and the possibilities and limits of concentrating on the achievement of partial similarity conditions (cf. Sec. 2.4).

2.1 Establishment of Similarity

"In modern engineering practice, scarcely any new type of structure or machine, whether it be a long-span bridge, a canal, a jet engine, or a supersonic speed airplane, is constructed until a model of it has been built, tested, redesigned, and retested, often several times. Frequently, for reasons of economy, the models are smaller than the final structure or machine. Those principles which underlie the proper design and construction, operation, and interpretation of the test results of these models comprise the theory of similitude. That is, the theory of similitude includes a consideration of the conditions under which the behavior of two separate entities or systems will be similar ..."

The citation above is quoted from Murphy (1950) and captures the reasons but also the restricting conditions for carrying out conclusive research on scaled models well. For predicting the performance of the full-scale machine eventually in use from observations on a model, it is mandatory that similar physical effects develop in both machines. In literature, the full-scale machine is thereby often referred to as the *prototype*. Now, the *theory of similarity* or *theory of similitude* is concerned with the establishment of *similarity conditions* between the prototype or scale model and the full-scale machine¹. Generally, two systems are understood to be physical similar, if certain non-dimensional parameters, which describe the governing physical relations of the considered problem,

¹In literature, both the term *similitude* as well as the term *similarity* are common. In most contexts, both expressions are interchangeable. In this work, the latter is favored.

are numerically equal (cf. Bridgman (1922)). These non-dimensional parameters thus characterize similarity and are referred to as *similarity parameters*. Furthermore, as similarity parameters often present a combination of the different physical quantities involved, the number of variables of a problem in question decreases. This has the advantage that the complexity of experimental investigations or analytical studies can be significantly reduced as pointed out, for example, by Spurk (1992)).

Due to their practical usefulness, a large number of similarity parameters have been derived either experimentally or analytically in all fields of scientific and technical research. Generally, two widely applied procedures exist for the derivation of similarity parameters for a particular problem. Generally, the requirements for similarity conditions can either be determined by

- (1) *Dimensional analysis* or by
- (2) *Non-dimensionalization* of the governing equations,

where the latter also includes the non-dimensionalization of the governing boundary conditions. The first procedure is of great practical use as it is solely based on theoretical consideration of the identified quantities involved. However, dimensional analysis is also susceptible to application errors and depends on the expertise of the researcher. Verification of the results is either carried out by critical evaluation by others or by experimental verification. In contrast, the second approach provides reliable results, but it requires exact knowledge of the governing system's equations, which are mostly of complex differential type and therefore difficult to analyze or to determine if not known. Below, both procedures are briefly introduced. For an extensive evaluation of the advantages and disadvantages of the different methods it is referred to Kline (1986).

Reported applications of dimensional analysis, nowadays often equated with and consequently referred to as the Π *theorem*, the *Buckingham Method* or the *Bridgman Method*, go back to studies carried out at the end of the 19th century. Initial applications of dimensional analysis mainly concentrated on aerodynamics-related problems and results were presented by e.g. Strouhal (1878), Reynolds (1883), and Prandtl (1910). The first in-depth treatise of this topic was published by Bridgman (1922). However, it was Lord Rayleigh (1915) who strongly advocated the use of dimensional analysis referred to by himself and others as the *principle of similitude*. Lord Rayleigh (1915) extensively applied this method and analyzed, for example, Boussinesq's problem of heat transfer. The latter considers the problem of a solid body immersed in a moving incompressible and inviscid fluid.

Dimensional analysis is a theoretical tool generally applied to deduce the functional physical relations between the quantities associated with a particular problem by analyzing the fundamental dimensions of these quantities. For this purpose, the quantities involved are identified and grouped in dependent and independent fundamental quantities². The dimensions of the latter are the fundamental dimensions of the problem and

²These are also referred to as *primary* and *secondary* quantities, respectively. A detailed definition and a discussion of their identification of those is given by Bridgman (1922).

2.1 Establishment of Similarity

often include the dimensions of mass, length, and time. In fluid dynamics, the mass dimension, however, is often substituted by the dimension of force (cf. Murphy (1950)). The dimensions of the dependent quantities can then be expressed as a sum of products of powers of the chosen fundamental dimensions. Knowing these *dimensional formulas*, the desired functional relations can then be deduced by combining the quantities involved in such a way that the numerical magnitude of the quantity considered only depends on the size of the fundamental units used in the respective dimensional formula (cf. Bridgman (1922)).

Following the basics of dimensional analysis as described above, Buckingham (1914) developed the famous Π theorem. Denoting the total number of quantities involved by n and the number of independent fundamental quantities by k , Buckingham (1914) found that $i = n - k$ non-dimensional products of the n quantities involved can be theoretically deduced. In formal terms, any function

$$F(Q_1, Q_2, \dots, Q_n) = 0, \quad (2.1)$$

which describes the physical relation between the quantities of a problem correctly, can be reduced to the form

$$\psi(\Pi_1, \Pi_2, \dots, \Pi_i) = 0, \quad (2.2)$$

where Q_1, Q_2, \dots, Q_n represent the n involved quantities and $\Pi_1, \Pi_2, \dots, \Pi_i$ represent the i dimensionless products. For the dimension of the latter, the condition

$$[\Pi_1] = [\Pi_2] = \dots [\Pi_i] = [1] \quad (2.3)$$

applies. With Q_1, Q_2, \dots, Q_k representing the fundamental quantities, and P_1, P_2, \dots, P_i representing the i dependent quantities $Q_{k+1}, Q_{k+2}, \dots, Q_n$, then the dimensionless products are obtained by the set of equations

$$\begin{aligned} [\Pi_1] &= [Q_1^{a_{1,1}} Q_2^{a_{1,2}} \dots Q_k^{a_{1,k}} P_1] \\ [\Pi_2] &= [Q_1^{a_{2,1}} Q_2^{a_{2,2}} \dots Q_k^{a_{2,k}} P_2] \\ &\dots \\ [\Pi_i] &= [Q_1^{a_{i,1}} Q_2^{a_{i,2}} \dots Q_k^{a_{i,k}} P_i], \end{aligned} \quad (2.4)$$

where the exponents $a_{1,1}, a_{1,2}, \dots, a_{k,k}$ must be such that Eq. (2.3) is satisfied (cf. Buckingham (1914)). The non-dimensional products respective similarity parameters on the left side of the equations then fully describe the physical relations, and thus determine similarity conditions.

Dimensional analysis is a powerful and comparatively simple tool to apply in cases where the governing differential equations of a problem are not known. However, misapplication easily occurs. The major challenges of this method lie in the accurate identification of the parameters involved and the grouping of these parameters. Both choices are crucial as different results are obtained if different parameters or groups are used. The uncertainties of the dimensional analysis became prominently evident already a century ago in the analysis of *Boussinesq's problem* of heat transfer. Here, the treatment of

temperature as an independent parameter or as a dependent parameter was intensely and publicly discussed (cf. Lord Rayleigh (1915) and Riabouchinsky (1915))³. In the end, a certain expertise is mandatory for the right classification of the parameters, as also stressed by Bridgman (1922). As mentioned earlier, the most accurate way of determining the requirements for similarity conditions for a particular problem is by non-dimensionalization of the governing equations. Precondition for this approach is that the complete set of the governing equations and boundary conditions are known and that these equations are *dimensional homogeneous*. In dimensional theory equations are classified in *dimensional homogeneous* and *dimensional non-homogeneous* equations. An equation with more than one term is said to be dimensionally homogeneous if all terms have or can be reduced to the same dimension (cf. Murphy (1950) or Spurk (1992))⁴. If the governing equations and the boundary conditions of a problem are known and dimensional homogeneity is met, the similarity parameters can be identified by non-dimensionalization of the given relations. Interestingly and conveniently, this approach can be pursued even in cases in which the equations cannot be analytically solved. A prominent example in fluid mechanics is the non-dimensionalization of the *Navier-Stokes equations*, which yields among others the *Reynolds number*, the *Froude number*, and the *Mach number* for an ideal gas (cf. Traupel (2001) or Schlichting (2016)).

For the problem of modal sound propagation analyzed here, the situation is more convenient as the governing equation is known. The latter is given by the convective wave equation (as defined in Eq. (2.15)) and the requirements for similarity can be deduced by non-dimensionalization of the respective relations as shown in Sec. 2.3. However, before turning to this analysis in detail, similarity of flow in turbomachines in general is briefly addressed in the section below.

2.2 Similarity Conditions for Fluid Flows and Turbomachinery

Similarity of flow between two different machines (e.g. model and prototype) is established if *geometric similarity*, *kinematic similarity*, and *dynamic similarity* are satisfied (cf. Kline (1986) or Dick (2015)). Generally, dynamic and kinematic similarity cannot be achieved if geometric similarity is not maintained⁵. Geometric similarity exists when the model is a scaled geometric version of the prototype. In practice, reduced scale

³Where in the end it has been found that the temperature indeed represents an independent quantity of this problem of heat transfer (cf. Buckingham (1915)).

⁴Buckingham (1914) refers to these kind of equations as *complete equations* and the theorem according to Eq. (2.1) to Eq. (2.4) holds.

⁵Geometric similarity is also assumed in the application of the Π theorem, although not explicitly mentioned in the previous discussion. In fact, Buckingham (1914) also expresses the Π theorem in the more general form where $F(Q_1, Q_2, \dots, Q_n, r', r'', \dots) = 0$ is reduced to an equation of the form $\psi(\Pi_1, \Pi_2, \dots, \Pi_i, r', r'', \dots) = 0$, with r', r'', \dots denoting to specific ratios of the observed system as for example the ratios of different basic lengths. In Eq. (2.1) similar geometries are understood to be provided.

2.2 Similarity Conditions for Fluid Flows and Turbomachinery

models are usually employed. Thus, the model differs from the full-scale machine in size but not in shape. For kinematic similarity, motion of the fluid has to be similar. The ratio of velocity at two points in the machines must be equal while the respective velocity vectors at each point must be parallel. Regarding, for example, a turbine stage, the velocity triangles at the leading edge of the stator blades and at the trailing edge of the rotor blades of the model and the prototype must be similar in shape and direction, while the ratios of the magnitudes have to be proportional. Dynamic similarity refers to the forces acting on the machines or, more specifically, the forces acting on each fluid element. In line with the requirement for kinematic similarity, the ratio of forces at two points in the model and the prototype must be equal for dynamic similarity and the direction of force has to be the same.

Dynamic similarity often inherently comprises kinematic similarity as the velocity field results from the acting forces, for example for steady incompressible flows (cf. Dick (2015)). Therefore, for a good number of problems, the three described types of similarity automatically exist, if the geometry as well as the forces are similar. Kline (1986), respectively, postulated that "*Two systems will exhibit similar behavior if geometric, kinematic, and dynamic similarity are all guaranteed; furthermore these conditions will be fulfilled if the two systems are made geometrically similar and if the ratios of all the pertinent forces are made the same in the two problems*". As described in the previous section, the governing similarity parameters for turbomachinery flow can be determined by dimensional analysis or non-dimensionalization of the governing equations and boundary conditions. Kline (1986) suggested an alternative fast-forward way to determine the requirements for similarity conditions. According to Kline (1986), the similarity parameters can be obtained from the ratio of forces acting on the fluid elements in a moving medium. Eventually, this approach can be understood to be a special form of the dimensional analysis⁶. Also pointed out by Kline (1986), this approach does not cover all phenomena (like, for example, heat transfer or electromagnetic effects) but still presents a smart approach for problems which are (predominantly) governed by mechanical forces. Therefore, this approach shall be used below to introduce a selection of important similarity parameters for fluid flows. The definitions in Eq. (2.5) to Eq. (2.11) are taken from Kline (1986), if not specified otherwise.

The approach of similarity of forces results in the deduction of a considerable number of important similarity parameters when applied to fluid mechanics⁷. According to Kline (1986), inertia forces, viscous forces, pressure forces, compressive or elastic forces, surface tension forces, and gravity forces can be determined as the governing common forces for fluid flows. These forces may be expressed in terms of pressure p , velocity V , length L , density ρ , dynamic viscosity μ , bulk modulus e , surface tension γ , and acceleration of gravity g . From the ratio of the listed forces, fifteen dimensionless parameters can be derived where especially *the Reynolds number, the Froude number, the Euler number, the Weber number, and the Cauchy number or Mach number*, respectively, are of particular

⁶Kline (1986) himself referred to this approach as the *Method of Similitude* and introduced the procedure as an alternative to the dimensional analysis and the approach of non-dimensionalization.

⁷The whole set of parameters needed to establish similarity is eventually given by the Pi theorem or by the number of parameters deduced from the governing relations.

interest for most physical problems. The Reynolds number denotes the ratio of the inertia forces to viscous forces and was introduced in 1883 by O. Reynolds (Reynolds (1883)). This parameter is therefore relevant for problems where viscous forces are dominant and is defined as

$$\text{Re} = \frac{\rho V L}{\mu}. \quad (2.5)$$

Commonly, the Reynolds number is used to characterize the flow condition and to assess the conditions when the flow changes from laminar to turbulent. The Froude number is defined as the ratio of inertia forces to gravitational forces and is an important parameter for characterizing open channel flows (free-surface flows) and hydraulic machines, namely where gravity develops forces of significant influence. The Froude number is expressed by the relation

$$\text{Fr} = \frac{V^2}{gL}. \quad (2.6)$$

The pressure coefficient and eventually the Euler number can be derived from the ratio of pressure forces to inertia forces yielding

$$\text{E} = \frac{\Delta p}{\rho V^2}. \quad (2.7)$$

Alternative to the definition above, the Euler number is also found to be defined with the factor 1/2 in the denominator to emphasize the link to dynamic pressure. The Euler number thus quantifies the importance of pressure forces in the flow. However, as pointed out for example by White (2011), the Euler number only becomes significant in liquid fluids when pressure drops, causing local cavitation.

The fourth dimensionless parameter deducible from the identified forces, the Weber number, is associated with surface tension effects and is defined as

$$\text{We} = \frac{\rho V^2 L}{\gamma}. \quad (2.8)$$

The Weber number denotes the ratio of inertia forces to surface tension forces and becomes an important parameter when investigating problems involving two fluid interfaces or free-surface flows. Finally, the Cauchy number expressed by

$$\text{C} = \frac{V^2 \rho}{e}. \quad (2.9)$$

is equivalent to the ratio of inertia forces to compressibility forces. Thus, this parameter is of minor importance when considering incompressible fluids but becomes relevant when compressible flows are considered. Implementing the relation $e = \kappa p$ in Eq. 2.9, where κ is the ratio of specific heats, it can be shown that, for an ideal gas, the Cauchy number is simply the square of the Mach number

$$\text{C} = \text{M}^2 = \frac{V^2}{c^2}, \quad (2.10)$$

2.3 Approximation of Aeroacoustic Similarity Conditions in the LPT

where c denotes the speed of sound (cf. Murphy (1950)). Both parameters can be used when compressibility effects have to be taken into account. The Mach number, however, is normally used and appears in most equations rather than the Cauchy number (cf. Kline (1986)). In the interest of completeness, it is noted that in case of relevant compressibility effects, in addition to the equality of the Mach number, the equality of the ratio of specific heats of the fluid has to be considered to meet similar conditions (cf. Kline (1986)).

Beside the force-based similarity parameters introduced here, multiple others exist and are frequently used in turbomachinery applications. Explicitly, the Strouhal number

$$\text{St} = \frac{fL}{V}, \quad (2.11)$$

shall be mentioned here. This dimensionless parameter becomes important when characterizing flows which are unsteady but oscillating at a specific frequency f (cf. Landau and Lifshitz (1959)). A prominent example is the periodic vortex shedding of a body emerged in a moving fluid. The occurrence of the so-called *Karman vortex street* also depends on the Reynolds number, and thus similar motion can be only observed when both parameters have the same value (cf. Landau and Lifshitz (1959)).

2.3 Approximation of Aeroacoustic Similarity Conditions in the LPT

In this section, the requirements for similarity conditions in the considered measurement volume of the turbine test rig, namely the inlet duct, are analyzed. For the particular case of a test rig equipped with a sound generator as given here, the sound propagation mechanisms can be investigated completely separate from the physical mechanisms of sound generation. Therefore, the scope of similarity investigation in this work focuses on the requirements for similarity of sound propagation only.

For the experimental validation, aerodynamic and acoustic data collected in the circular inlet duct of the LPT test rig are used. In order to analyze sound propagation analytically, approximations for the flow have to be made. The validity of these are discussed in Sec. 4.1.2. First of all, viscous effects and thus, boundary layers, are neglected. Furthermore, it is assumed that there are neither internal or external sources nor any internal or external forces acting on the fluid particles. Considering these conditions, the motion of the inviscid fluid is then determined by *Euler's equation*

$$\rho \frac{Du_i}{Dt} = -\frac{\partial p}{\partial x_i}, \quad (2.12)$$

the *continuity equation*

$$\rho \frac{D\rho}{Dt} = -\rho \frac{\partial u_i}{\partial x_i}, \quad (2.13)$$

and the *energy or entropy equation*

$$\rho \frac{Ds}{Dt} = 0, \quad (2.14)$$

where s denotes the entropy (cf. Landau and Lifshitz (1959) or Schlichting (2016)). In Eq. (2.12), Eq. (2.13), and Eq. (2.14), the flow variables are thereby a function of time t and space x_i . The flow velocity profile in the chosen measurement volume is assumed to be steady and uniform over the cross-section with only one flow component aligned with the duct axis. Assuming further an isentropic and ideal flow with the mean velocity U^0 in the direction of the x-coordinate, a constant mean density ρ^0 , and a constant mean pressure p^0 , the homogeneous *convective wave equation* according to

$$\frac{1}{c^2} \frac{(D^0)^2 p'}{Dt^2} - \frac{\partial^2 p'}{\partial x_i^2} = 0 \quad (2.15)$$

governs the propagation of small time-varying pressure perturbations p' of the constant (steady-state) pressure p^0 . The derivation of the wave equation is given in detail, for example, in the work by Goldstein (1976).

The perturbations p' in Eq. (2.15) are a function of time and space, thus $p' := p'(x_i, t)$. Linear effects are provided and only those perturbations which satisfy the inequality $\hat{p}' \ll p^0$ are considered. If the amplitude exceeds a magnitude of approx. $20 \cdot 10^{-6}$ Pa, the pressure perturbations can be perceived by the human ear as sound. Then, p' represents the sound pressure. The variable c in Eq. (2.15) gives the speed of sound in an ideal gas, namely the propagation velocity of the acoustic perturbations. The speed of sound is defined in quadratic terms by $c^2 = \kappa R_s T^0$, where κ denotes the ratio of specific heats, R_s the specific gas constant, and T^0 the steady-state temperature (cf. for example Goldstein (1976)).

The convective aerodynamic effect due to the motion of the fluid is captured in the total derivative of second order (cf. the first term of Eq. (2.15)), which is given for $U^0 = f(x)$ by

$$\frac{(D^0)^2 p'}{Dt^2} = \frac{\partial^2 p'}{\partial t^2} + 2U^0 \frac{\partial^2 p'}{\partial t \partial x} + (U^0)^2 \frac{\partial^2 p'}{\partial x^2}, \quad (2.16)$$

with

$$\frac{D^0}{Dt} := \frac{\partial}{\partial t} + U^0 \frac{\partial}{\partial x}. \quad (2.17)$$

According to Eq. (2.17), the total derivative combines the derivative of the pressure perturbation with respect to time and the derivative with respect to space (cf. Schlichting (2016)). Inserting the expanded form of the total derivative (cf. Eq. (2.16)) in the wave equation yields

$$\frac{1}{c^2} \frac{\partial^2 p'}{\partial t^2} + 2 \frac{M_x}{c} \frac{\partial^2 p'}{\partial t \partial x} + M_x^2 \frac{\partial^2 p'}{\partial x^2} - \frac{\partial^2 p'}{\partial x_i^2} = 0, \quad (2.18)$$

where the Mach number

$$M_x = \frac{U^0}{c} \quad (2.19)$$

2.3 Approximation of Aeroacoustic Similarity Conditions in the LPT

for the flow in axial direction has been introduced (cf. Fig 3.1).

Hence, the governing equation for the considered problem is known, and similarity of sound propagation can be investigated by non-dimensionalization of the wave equation. A precondition is that the equation is dimensionally homogeneous as described in Sec. 2.1. For this to be verified, the dimensions of each term of the convective wave equation according to Eq. (2.18) are expressed in the dimensions of mass (kg), time (s), and length (m) so that

$$\begin{aligned}
 \left[\frac{1}{c^2} \frac{\partial^2 p'}{\partial t^2} \right] &= \left[\frac{\text{s}^2}{\text{m}^2} \frac{\text{kg}}{\text{ms}^2} \frac{1}{\text{s}^2} \right] = \left[\frac{\text{kg}}{\text{m}^3 \text{s}^2} \right], \\
 \left[\frac{M_x}{c} \frac{\partial^2 p'}{\partial t \partial x} \right] &= \left[\frac{\text{s}}{\text{m}} \frac{\text{kg}}{\text{ms}^2} \frac{1}{\text{s}} \frac{1}{\text{m}} \right] = \left[\frac{\text{kg}}{\text{m}^3 \text{s}^2} \right], \\
 \left[M_x^2 \frac{\partial^2 p'}{\partial x^2} \right] &= \left[\frac{\text{kg}}{\text{ms}^2} \frac{1}{\text{m}^2} \right] = \left[\frac{\text{kg}}{\text{m}^3 \text{s}^2} \right], \\
 \left[\frac{\partial^2 p'}{\partial x_i^2} \right] &= \left[\frac{\text{kg}}{\text{ms}^2} \frac{1}{\text{m}^2} \right] = \left[\frac{\text{kg}}{\text{m}^3 \text{s}^2} \right].
 \end{aligned} \tag{2.20}$$

It is found that each term has the same dimension, where mass enters with the power of one, while length and time are reciprocal with the power of three and two, respectively. This check of dimensions confirms that the wave equation satisfies the requirement of homogeneity and can be reduced to a dimensionless form.

In the formulation of the convected wave equation according to Eq. (2.18), the flow velocity has already been scaled by the speed of sound introducing the dimensionless Mach number in the equation. Now, to further analyze the equation, it is convenient to scale the spatial dimensions with a characteristic length. With respect to the geometry of the turbine test rig, the spatial coordinates are non-dimensionalized with the duct radius R according to

$$x_i^* := \frac{x_i}{R} \Rightarrow \frac{\partial}{\partial x_i} := \frac{\partial}{R \partial x_i^*}, \tag{2.21}$$

where x_i^* is then a dimensionless numerical value. Furthermore, as suggested by Rienstra and Hirschberg (2017), the time scale

$$t^* := t\omega \Rightarrow \frac{\partial}{\partial t} := \omega \frac{\partial}{\partial t^*} \tag{2.22}$$

with the angular frequency ω is introduced. Inserting x_i^* and t^* in the convected wave equation yields

$$\frac{\omega^2}{c^2} \frac{\partial^2 p'}{\partial (t^*)^2} + 2 \frac{M_x \omega}{c} \frac{\partial^2 p'}{\partial t^* \partial x^*} + M_x^2 \frac{1}{R^2} \frac{\partial^2 p'}{\partial (x^*)^2} - \frac{1}{R^2} \frac{\partial^2 p'}{\partial (x_i^*)^2} = 0. \tag{2.23}$$

Subsequently, multiplying all terms with the square of the radius and introducing a second non-dimensional parameter, namely the *Helmholtz number*

$$\text{He} = \frac{\omega}{c} R = \frac{2\pi f}{c} R, \tag{2.24}$$

then Eq. (2.23) becomes

$$\text{He}^2 \frac{\partial^2 p'}{\partial (t^*)^2} + 2\text{He}M_x \frac{\partial p'}{\partial t^* \partial x^*} + M_x^2 \frac{\partial^2 p'}{\partial (x^*)^2} - \frac{\partial^2 p'}{\partial (x_i^*)^2} = 0, \quad (2.25)$$

where only the dimension of pressure remains in each term. The complete dimensionless equation can be found by scaling the pressure p' with an arbitrary reference pressure p_{ref} so that

$$p^* := \frac{p'}{p_{\text{ref}}} \quad \text{with} \quad \frac{p'}{p_{\text{ref}}} \leq 1. \quad (2.26)$$

With this non-dimensionalization, the complete dimensionless form of the convective wave equation is given by

$$\text{He}^2 \frac{\partial^2 p^*}{\partial (t^*)^2} + 2\text{He}M_x \frac{\partial p^*}{\partial t^* \partial x^*} + M_x^2 \frac{\partial^2 p^*}{\partial (x^*)^2} - \frac{\partial^2 p^*}{\partial (x_i^*)^2} = 0. \quad (2.27)$$

According to Kline (1986), for example, a dimensionless equation is generally defined as an equation which contains only dimensionless variables (dependent or independent) and dimensionless parameters. The dimensionless variables are identified by the superscript star $(.)^*$ in the equations above. In the final deduced form of Eq. (2.27), p^* is the dimensionless dependent variable and the coordinates x_i^* and the time variable t^* are the dimensionless independent variables defining the system's boundaries. The dimensionless parameters He and M_x evidently present the searched for similarity parameters.

As outlined in Sec. 2.1, the requirements for similarity are fully defined by analyzing the governing equations as well as the boundary conditions of the problem under consideration. Here, acoustically hard-walled ducts are assumed. For an annular duct, this condition requires that the pressure gradient in radial direction is zero at the hub and at the outer duct wall⁸. Formally, it can be written

$$\left. \frac{\partial p'}{\partial r} \right|_{r=R_h} = 0 \quad \text{and} \quad \left. \frac{\partial p'}{\partial r} \right|_{r=R} = 0. \quad (2.28)$$

As pointed out in Sec. 2.2, geometric similarity is mandatory for establishing similarity conditions between two turbomachines. Following the definition of geometric similarity, all ratios of characteristic length of the system considered have to be identical. With respect to the geometry of the circular- or annular-shaped duct at hand, a respective dimensionless parameter or ratio can be found by non-dimensionalization of the hard-walled boundary conditions with the outer duct radius R . Equation (2.28) is then expressed by

$$\left. \frac{\partial p'}{\partial r^*} \right|_{r^* = \frac{R_h}{R} = \sigma} = 0 \quad \text{and} \quad \left. \frac{\partial p'}{\partial r^*} \right|_{r^*=1} = 0, \quad (2.29)$$

where the radial coordinate is scaled. Through the surface condition at the hub, the hub-to-tip ratio

$$\sigma = \frac{R_h}{R} \quad (2.30)$$

⁸For details of the geometry under consideration, please refer to Fig. 3.1 in Sec. 3.1.1.

2.4 Partial Similarity

is found to determine geometric similarity.

For simplified assumptions of the flow and geometry, the requirements for similarity of sound propagation in the inlet duct of the LPT can thus be explicitly defined. In summary, it is found by non-dimensionalization of the convective wave equation that a triad of similarity parameters, namely the Helmholtz number, the Mach number, and the hub-to-tip ratio, determine similarity of sound propagation in an annular duct carrying an one-dimensional inviscid and isentropic homogeneous flow. At this point, it needs to be emphasized that this observation refers to the propagation of the complete sound field which might be decomposed in different wave components, the so-called acoustic modes. The latter are introduced in Sec. 3.1 of the following chapter.

For the sake of completeness, note that in a medium at rest, similarity is only defined by the Helmholtz number and the hub-to-tip ratio. For $M_x = 0$, the wave equation according to Eq. (2.18) reduces to

$$\frac{1}{c^2} \frac{\partial^2 p'}{\partial t^2} - \frac{\partial^2 p'}{\partial x_i^2} = 0, \quad (2.31)$$

and correspondingly the dimensionless form according to Eq. (2.27) reduces to

$$\text{He}^2 \frac{\partial^2 p^*}{\partial (t^*)^2} - \frac{\partial^2 p^*}{\partial (x_i^*)^2} = 0. \quad (2.32)$$

The boundary conditions defined in Eq. (2.29) remain unaffected.

2.4 Partial Similarity

In many cases, it is not possible or economical to completely meet all requirements for establishing similarity conditions between model and prototype (cf. Murphy (1950), Spurk (1992), or Traupel (2001)). Technical and economical reasons may simply impose limitations on the design of models and test rigs.

Geometric similarity, for example, is often not met with respect to the surface roughness or tip clearance, as pointed out by both Spurk (1992) and Dick (2015). Whereas the quantitative reproduction of surface roughness is often easily achieved when considering models of the same scale (since similar machines or techniques are normally used for the production), for geometrically reduced models the achievement of similarity of roughness is technically often limited to a certain degree. The same holds true for the achievement of similarity with respect to the clearance between blade tip and shroud in reduced models. To avoid these problems of geometric scale altogether, it is convenient to simply use turbomachinery models that are of the same size and have the same material properties as the prototypes. In fact, turbomachinery test rigs more often differ from the prototype regarding the working medium rather than the geometry. The turbine test rig used for research in this work, for example, is operated by air instead of the air-gas mixture used in the combustion chambers of an aircraft engine. This not only

permits a substantial reduction in the test rig periphery and fewer design requirements e.g. for instrumentation and material in general, but also has considerable advantages regarding safety, health, and environmental aspects.

For cases in which not all similarity requirements can be met, so-called *partial similarity* can still be achieved (Schlichting (2016))⁹. While all similarity parameters governing the system's behaviour have to be met for *complete similarity*, partial similarity focuses on equality of the parameters describing a specific effect. Partial similarity can be established, for example, with respect to geometry, material properties, acting forces and energies, or with respect to a combination of those.

Studies with models satisfying partial similarity still allow reliable prediction of the behaviour of the prototype. One possible solution is the implementation of an estimate of error if the impact of non-fulfillment of the respective similarity requirements is quantifiable and predictable, as suggested by Schlichting (2016) and discussed by Murphy (1950)¹⁰. Dick (2015) followed this approach and suggested the application of certain model laws to take the variations in the geometric features mentioned in the examples above into account. In other cases, the non-fulfillment of a certain similarity parameter (or requirement) simply has no or only a negligibly minor influence on the effect considered. Deviations in the surface roughness or the tip clearance can be accepted in cases where the physical effect under consideration is not influenced by the boundary layer or the secondary flows near the tip clearance region, for example.

Furthermore, in most cases not all fluid flow forces mentioned in Sec. 2.2 have a significant impact on the considered problem and most often it is sufficient to satisfy similarity of the dominant forces only. Regarding viscosity effects, for example, Dick (2015) and Traupel (2001) point out that in some turbomachines, the Reynolds number will be mostly so high in magnitude that the parameter is no longer of practical importance as long as the order of magnitude is met. Vice versa, the equality of the Reynolds number becomes important where viscous forces are a factor. This is the case, when considering friction effects, for example (cf. Murphy (1950)). For the problem at hand, an approximate flow model is used in order to analytically investigate the requirements for similarity of modal sound propagation. This flow model does not consider most of the forces described in Sec. 2.2 as these are assumed to be unimportant for the problem considered. Accordingly, following the assumptions of the flow and the problem at hand, the viscous forces, the surface tension forces, and the gravity forces are neglected, and thus the corresponding similarity parameters meaning the Reynolds number, the Froude number, and the Weber number, are not considered. The pressure gradient and the inertia forces enter via Euler's equation and are summarized in the Euler number. The

⁹Here it is convenient to point out that no common term has developed in the scientific community to refer to non-complete similarity. Dick (2015), for example, uses the expression *imperfect similitude*, Spurk (1992) the expression *complete similarity (in german: vollstaendige Aehnlichkeit)* and *non-complete similarity (in german: unvollstaendige Aehnlichkeit)*, and Schlichting (2016) uses the term *partial similarity (in german: partielle Aehnlichkeit)*. In this work, the expressions *complete similarity* and *partial similarity* are used.

¹⁰In literature, works addressing this approach are often found under the keywords *theory of models* or *model laws*.

2.4 Partial Similarity

latter is also unimportant here as no significant pressure drop is to be expected. Hence, with respect to the parameters discussed in Sec. 2.2, similarity of flow here reduces to the consideration of the Mach number only.

In summary, the key statement is that sufficient similarity may be achieved even though numerical equality of one or more similarity parameters is not met. In this case of partial similarity, an assessment has to be made whether non-compliance with similarity of certain parameters is acceptable, thus has negligible impact on the considered physical effect, or if correction measures like, for example, introducing a correction factor, have to be taken into account.

With respect to the objectives of this work, these findings can be transferred to the establishment of similarity conditions during the operation of test rigs for research on modal sound propagation. Non-dimensionalization of the convective wave equation, as carried out in the previous section, has shown that the Helmholtz number and the Mach number establish similarity of sound propagation between two measurements. This work now focuses explicitly on operating conditions under which the Mach number and / or the Helmholtz number cannot be kept equal between two measurements. Thus, complete similarity as defined above is not achieved in these case.

In Chap. 3, the properties of the propagation of the individual components of sound fields, namely the acoustic modes, are investigated. This investigation aims to assess the possible application of the approach of partial similarity when considering not the complete sound field but only modal components, on the one hand, and to analytically exploit the impact of variations in the before-mentioned similarity parameters on modal sound propagation, on the other hand.

3 Similarity of Modal Sound Propagation

This chapter addresses the development of a hypothesis to define the requirements for similarity of modal sound propagation for the geometry, the flow conditions and the operating conditions under consideration. Based on this hypothesis, an approach for establishing similar conditions for modal sound propagation is developed and tested in this work.

In a first step, solutions to the convective wave equation for the approximate flow model considered in this work are introduced in Sec. 3.1 of this chapter. Relations for the most important propagation properties are provided. A focus is on the group velocity, which governs the propagation of sound fields in general and the propagation of modal sound fields in particular. The hypothesis of this work is developed under consideration of the theory of similarity and based on the findings of the analytical investigation (cf. Sec. 3.2). Following in Sec. 3.3, a functional relation between the axial angle of the group velocity vector and the triad of similarity parameters, the Helmholtz number, the Mach number, and the hub-to-tip ratio, is derived. This so-called *similarity relation* presents the basis of the similarity approach. Furthermore, a *similarity map* for analyzing and identifying similar operating conditions is developed and discussed in Sec. 3.4.

In this chapter, references are made to several publications of importance for this work. A few of these shall be shortly addressed: In the 1960s, research on sound propagation focused on the group velocity of sound waves and findings were published by Lighthill and Whitham (1955), Landau and Lifshitz (1959), or Whitham (1960). Some years later, Lighthill (1965) summarized these works and published an extensive and illustrative treatise on the propagation properties of sound waves. In 1962, Tyler and Sofrin (1962) pioneered research in the field of sound generation mechanism in turbomachines by experimentally determining the well-known relation between the generation of acoustic modes and rotor-stator interaction or rotation of the rotor alone. Furthermore, Tyler and Sofrin (1962) derived a harmonic solution to describe the propagation of these modes in rectangular or cylindrical ducts and their radiation from the duct's end. Until that point in time, modal sound fields had received comparatively little attention. Following Tyler and Sofrin (1962), however, research focused on the modal components of sound fields. With the objective of studying modal sound transmission through turbomachinery blade rows, modal sound attenuation or radiation, the propagation properties of acoustic modes have been addressed in several analytical works. For example, Rice et al. (1979), Rice (1979), Farassat and Myers (1996), and Farassat and Myers (1997) de-

rived and analyzed analytical relations to describe modal sound propagation properties in ducts for investigating modal attenuation in acoustically treated ducts and radiation from the intake of aircraft engines. Farassat and Myers (1996) and Farassat and Myers (1997) concentrated especially on the properties of energy propagation. The geometric approach used for these analytical works are also followed in this work. More recently, Bartelt (2015) presented results from sound measurements carried out on the same test rig as used for the experimental investigations in this work. His work comprises a detailed analytical study of the modal solutions of the wave equation for an equivalent approximate model assumed here.

Beside references to the before-mentioned works, references are also made to a publication of the author of this work that also addresses similarity of modal sound propagation. Essential parts of the analytical basis of the similarity approach developed in the scope of the research carried out for this treatise have been presented by Hurfar et al. (2015).

3.1 Modal Sound Propagation in Circular Ducts

3.1.1 Solutions to the wave equation

Landau and Lifshitz (1959) define sound waves as "... an oscillatory motion of small amplitude in a compressible fluid...". These waves induce small variations or perturbations of the steady-state quantities as the mean pressure or the mean density of the fluid. A *plane wave* describes the propagation of a sound wave in which the perturbations are only a function of one coordinate (cf. Landau and Lifshitz (1959)). In contrast, acoustic modes are generally sound waves of higher order depending on two or more coordinates. The research field of *duct acoustics* is concerned with the analytical description of these modes in rectangular and circular ducts in undisturbed or moving media. As shown in Sec. 2.3 for an one-dimensional inviscid and isentropic flow, which is completely homogeneous over the cross section, the propagation of sound waves can be satisfactorily approximated by the convective wave equation already introduced

$$\frac{1}{c^2} \frac{(D^0)^2 p'}{Dt^2} - \frac{\partial^2 p'}{\partial x_i^2} = 0$$

with

$$\frac{(D^0)^2 p'}{Dt^2} = \frac{\partial^2 p'}{\partial t^2} + 2U^0 \frac{\partial^2 p'}{\partial t \partial x} + (U^0)^2 \frac{\partial^2 p'}{\partial x^2}.$$

Considering a continuous time- and space-harmonic propagation of the acoustic perturbations, then

$$p'(x_i, t) = \operatorname{Re} \{ A e^{i(\omega t - k_i x_i)} \} \quad (3.1)$$

presents a general solution to Eq. (2.15) or Eq. (2.18), respectively (cf. Goldstein (1976) or Rienstra and Hirschberg (2017)). Here, the constant A is the amplitude of the pressure perturbation p' , ω is the angular acoustic frequency in radians per second, and

3.1 Modal Sound Propagation in Circular Ducts

k_i represents the spatial wave number. With

$$\omega = 2\pi f \quad (3.2)$$

the angular frequency is related to the frequency f , given in Hertz (Hz), with which the steady-state quantities oscillate around their mean due to the propagation of the acoustic perturbations.

With respect to the geometry of the LPT it is convenient to analyze the sound propagation in a cylindrical coordinate system with x , r , and θ being the axial, radial, and circumferential coordinate, respectively. Equation (2.15) then specifies to

$$\frac{1}{c^2} \frac{(D^0)^2 p'}{Dt^2} - \frac{1}{r} \frac{\partial p'}{\partial r} \left(r \frac{\partial p'}{\partial r} \right) - \frac{1}{r^2} \frac{\partial^2 p'}{\partial \theta^2} - \frac{\partial^2 p'}{\partial x^2} = 0 \quad (3.3)$$

as shown by Bartelt (2015). The total derivative as given in Eq. (2.17) remains unchanged. Considering the harmonic description introduced in Eq. (3.1), a particular solution to the wave equation of the form

$$p'_{(m,n)}{}^{\pm x}(r, x, \theta, t) = \operatorname{Re} \left\{ A_{(m,n)}^{\pm x} \cdot e^{i(\omega t - k_x^{\pm x} x - m\theta + \varphi^0)} \cdot g(r) \right\} \quad (3.4)$$

for $m \in \mathbb{Z}$ and $n \in \mathbb{N}$,

can be found by using, for example, the method of separation of variables (cf. Bartelt (2015)). This type of solution is referred to as a *mode* (cf. Goldstein (1976)), and describes the propagation of higher order sound fields specified by the integer circumferential mode order m and the integer radial mode order n in a circular duct. The circumferential order thereby corresponds to the number of wavelengths in circumferential direction, whereas the value of the radial mode order corresponds to the number of lines of zero pressure in radial direction. For the experimental validation, however, only pure circumferential modes with $n = 0$ as the mode (2,0) shown in Fig. 3.1 are considered. Different modal solutions exist for the propagation in the direction of the flow and the propagation opposite to the flow direction. This is taken into account by the superscripts $(\cdot)^{+x}$ and $(\cdot)^{-x}$, respectively.

According to Eq. (3.4), each acoustic mode (m, n) is characterized by a complex amplitude represented by the absolute modal amplitude $A_{(m,n)}^{\pm x}$, and the modal phase $\varphi_{(m,n)}^{\pm x}$ specified by the complex exponent $(\omega t - k_x^{\pm x} x - m\theta + \varphi^0)$. The exponent depends on the time variable t and on the spatial coordinates x and θ , thus expressing the harmonic character of the propagation. In the axial direction, the mode propagation is determined by the (axial) wave number $k_x^{\pm x}$. In the circumferential direction, the pressure pattern of the propagating mode is determined by the mode order m . The angle φ^0 denotes the initial phase. The radial propagation is expressed by the function $g(r)$. Both, the axial wave number and the radial function are associated with the mode orders and have to be defined with respect to the boundary conditions of the regarded problem.

Tyler and Sofrin (1962) referred to the acoustic modes observed in the different sections of a turbomachine as *spinning modes*. Thereby, the authors made reference to the

spiral or helical type of propagation of these pressure patterns. Below, the propagation properties of acoustic modes in the different directions (x, r, θ) are further specified and respective relations are detailed regarding the geometry and the flow conditions of the problem at hand.

The problem at hand can be specified making the assumption of an infinite annular axis-symmetric duct with a constant outer radius R and a constant hub-to-tip ratio $\sigma = R_h/R$ as illustrated in Fig. 3.1. The duct surface is assumed to be acoustically hard-walled requesting a local maximum of the sound pressure at the hub and at the outer duct radius. According to the assumption for the flow used for the derivation of the wave equation, the duct carries a unidirectional steady flow U^0 in x-direction expressed in the axial Mach number $M_x = U^0/c$, where $M_x < 1$. By choosing to analyze an annular geometry, both the cylindrical inlet duct as well as the annular duct sections of the turbine stage are taken into account. The solutions can subsequently be easily be reduced to the case of $\sigma = 0$.

Having defined the geometry with respect to the sections of the LPT, the radial solution $g(r)$ can be determined. Tyler and Sofrin (1962) describe the radial propagation by a sum of Bessel function of the form

$$g(r) = J_m \left(\beta_{(m,n)}^{(\sigma)} r \right) + Q_{(m,n)}^{(\sigma)} Y_m \left(\beta_{(m,n)}^{(\sigma)} r \right). \quad (3.5)$$

Here, the functions J_m and Y_m denote the m -th order Bessel function of the first and second kind, respectively. The latter is also known as the Neumann function and is multiplied with the weighting factor $Q_{(m,n)}^{(\sigma)}$. The argument of the Bessel functions is defined as

$$\beta_{(m,n)}^{(\sigma)} := \frac{u_{(m,n)}^{(\sigma)}}{R}, \quad (3.6)$$

where $u_{(m,n)}^{(\sigma)}$ is the characteristic eigenvalue of the problem of radial sound propagation

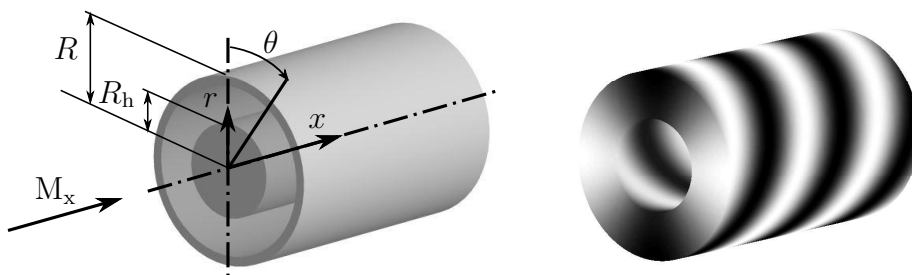


Figure 3.1: Left: Geometry of the observed problem and definition of the flow direction. Right: Exemplary pressure pattern of the acoustic mode $(2,0)$. The illustration is based on Fig. 1 in the publication of Hurfar et al. (2015).

3.1 Modal Sound Propagation in Circular Ducts

specified by the acoustically hard-walled boundary condition. The superscript $(\cdot)^{(\sigma)}$ thereby indicates a dependency on the hub-to-tip ratio. Hence, $u_{(m,n)}^{(\sigma)}$ is the (m,n) th-solution to the surface conditions

$$\frac{\partial g}{\partial r}\Big|_{r=R_h} = 0 \quad \text{and} \quad \frac{\partial g}{\partial r}\Big|_{r=R} = 0. \quad (3.7)$$

and depends on the hub-to-tip ratio. The eigenvalue depends on the radial as well as on the circumferential mode order, and thus connects the propagation in the respective directions as pointed out by Tyler and Sofrin (1962) and Rice et al. (1979). In fact, Rice et al. (1979) interpreted $\beta_{(m,n)}^{(\sigma)}$ as the combined *radial-circumferential wave number* $k_{r\theta}$. Now, for the cylindrical inlet of the LPT, only the surface condition at the outer duct radius holds, and Eq. (3.5) reduces to $g(r) = J_m(\beta_{(m,n)}r)$ as also given by Tyler and Sofrin (1962).

In the axial direction, the propagation of acoustic modes is determined by the modal *axial wave number* given by

$$k_x^{\pm x} = \frac{-k^0 M_x \pm \sqrt{(k^0)^2 - (1 - M_x^2) \left(\beta_{(m,n)}^{(\sigma)}\right)^2}}{(1 - M_x^2)}, \quad (3.8)$$

where

$$k^0 = \frac{\omega}{c} \quad (3.9)$$

denotes the *free-field wave number* (cf. Rice et al. (1979)). Equation (3.8) shows that the axial propagation depends on the mode order through the scaled eigenvalue $\beta_{(m,n)}^{(\sigma)}$. Furthermore, it follows that the axial wave number can become complex ($\text{Im}(k_x^{\pm x}) \neq 0$). In that case, the amplitude of the mode attenuates exponentially along the duct axis. This mathematical special case defines the *cut-off condition* of the mode, and arises when the radicand in Eq. (3.8) becomes negative as also observed by Tyler and Sofrin (1962). From the condition $\text{Im}(k_x^{\pm x}) = 0$, the *cut-off-frequency*

$$f_{(m,n),\text{cut}} = \frac{c\sqrt{(1 - M_x^2)}\beta_{(m,n)}^{(\sigma)}}{2\pi} \quad (3.10)$$

is obtained. This frequency defines the limit of propagation, where $f > f_{(m,n),\text{cut}}$ is the condition for propagation. Cut-off condition depends on the flow velocity, the speed of sound, the duct radius, and - through the characteristic eigenvalue - on the radial and circumferential mode order as well as on the hub-to-tip ratio. Consequently, each mode has its own characteristic cut-off-frequency subject to the boundary conditions. Hence, f_{cut} can be understood to be the natural (characteristic) frequency of the duct. The fundamental zeroth-order mode $(0,0)$, which corresponds to a plane wave, presents an exception. With $u_{(m,n)} = 0$, the plane wave has no limiting frequency, and is thus not bound by the boundary conditions. Modes satisfying the propagation condition are referred to as *cut-on* modes, and, vice versa, modes not meeting the condition are *cut-off*.

Here, it is convenient to introduce the dimensionless *cut-off ratio*

$$\xi_{(m,n)} = \frac{f}{f_{(m,n),\text{cut}}} = \frac{k^0}{\beta_{(m,n)}^{(\sigma)} \sqrt{(1 - M_x^2)}}, \quad (3.11)$$

which gives the ratio of the mode's oscillation frequency to the respective cut-off frequency. A cut-off-ratio with the value of one ($\xi = 1$) thus indicates cut-off-condition, whereas a high value indicates that the mode is well cut-on. The cut-off ratio is frequently used to describe modal sound propagation, e.g. by Rice et al. (1979).

Having specified the pressure distribution of an acoustic mode for the axial and radial directions, the propagation in the circumferential direction still has to be defined. In θ -direction, the pressure distribution has to satisfy the demand for periodicity $p'(\theta_1) = p'(\theta_1 + 2\pi)$. A simple harmonic solution found to fulfil this condition is expressed in the complex notation $e^{-im\theta}$ (cf. Eq. (3.4)). The latter constrains the circumferential mode order m to be an integer. As the circumferential mode order is chosen to adopt positive as well as negative values, the direction of spin depends on the sign of m . Here, positive values of m correspond to modes spinning in the direction of the rotor, and, vice versa, negative values to modes spinning in the direction opposite to the rotation of the rotor. It follows that the circumferential wave number at an arbitrary radius r of the duct is given by

$$k_\theta = \frac{2\pi}{\lambda_\theta} = \frac{m}{r}, \quad (3.12)$$

where $\lambda_\theta = 2\pi r/m$ denotes the circumferential wavelength.

With Eq. (3.4), Eq. (3.5), and Eq. (3.8), the up- and downstream propagation of an arbitrary modal sound field (m, n) throughout the inlet duct of the LPT and the annular flow path upstream of the first stage for a unidirectional and uniform flow can be uniquely described.

For the sake of completeness, note that modes are orthogonal solutions of the wave equation. The linearity of the wave equation implies that any linear combination of the modal solutions is a solution to Eq. (2.15) as well. With

$$p'(r, x, \theta, t) = \sum_{m=-\infty, n=0}^{\infty} p'_{(m,n)}{}^{\pm x}(r, x, \theta, t) \quad (3.13)$$

the sound field is described as a superposition of an arbitrary number of acoustic modes. This formulation takes into account that practical applications often demand the considering of not only one but multiple acoustic modes, which may differ in the mode order as well as in the oscillation frequency. A good example for this is the generation of acoustic modes by rotor-rotation or rotor-stator interaction as postulated by Tyler and Sofrin (1962).

A special case to be addressed briefly, is the superposition of two acoustic modes which have the same order and frequency but are traveling in opposite directions. If the

3.1 Modal Sound Propagation in Circular Ducts

modal amplitudes are numerically equal, this superposition results in a sound field with standing character in the respective spatial direction. This applies to a standing circumferential mode, a standing axial mode, or a combination of both. Different amplitudes of the superposed modes yield to sound fields with partial spinning or partial standing character, respectively, as demonstrated by Bartelt (2015). With

$$\epsilon = \frac{A_1}{A_2} \quad (3.14)$$

denoting the relative modal amplitude of two superposed modes with opposite propagation directions, $\epsilon = 1$ holds true for the case of a standing mode. Vice versa, $\epsilon = 0$ describes a pure spinning mode.

3.1.2 Velocities of modal propagation

This section is concerned with the propagation velocities of modal sound fields. Beside the well-known speed of sound, *group velocity* and *phase velocity* are commonly used to describe sound propagation. This section therefore starts with a short analysis of the differences between group velocity and phase velocity. Subsequently, relations for determining the different velocities are presented.

Group velocity is the velocity with which an acoustic wave carries energy in space (cf. Whitham (1960) or Lighthill (1965)). Hence, group velocity governs sound propagation in general and modal sound propagation in particular. Contrary to this key physical fact, phase velocity is often considered instead of group velocity, as also pointed out by Lighthill (1965). Phase velocity is the velocity with which the fronts of constant phase of a sound wave travel in space. In comparison to group velocity, phase velocity can be comparatively easily be determined experimentally by the rise and fall of the pressure amplitude of the wave. Physically, a differentiation between both velocities becomes mandatory if considering sound propagation in a moving medium. While the magnitude of group velocity and the magnitude of phase velocity are the same and equal to the speed of sound if the medium is at rest (cf. Landau and Lifshitz (1959)), the *convective effect* by flow yields a change of the propagation properties in the presence of a flow. The two velocities no longer match, neither in magnitude nor in direction. This effect accompanies the effect of *dispersion*. The latter describes the situation where sound waves do not travel at the same speed in space (cf. Lighthill (1965)). In that case, it is mandatory to differentiate between phase velocity and group velocity.

The review above considers sound propagation in general. With respect to the propagation of sound within the ducted parts of turbomachinery, it is found that group velocity also governs the characteristic of sound transmission through blade cascade as well as radiation characteristics. In a detailed analytical study of the transmission of sound waves through non-rotating blade cascades, Kaji and Okazaki (1970) showed that the amplitudes of the transmitted and reflected waves depend on the angle with which the sound waves impinge upon the blade row. This incident angle depends on the convection

of the sound wave by flow as pointed out by Kaji and Okazaki (1970). Thus, although not explicitly stated by the authors, it is the angle of group velocity which determines the sound transmission and reflection characteristics. Considering radiation characteristics of a sound wave from the open end of a duct, Rice (1979) showed analytically that the angle which the group velocity vector forms with the axial direction corresponds to the maximum noise peak of the far-field radiation pattern.

Based on the analysis outlined above, it can be concluded that group velocity governs the propagation of (modal) sound fields. Therefore, the following analysis concentrates on this propagation velocity.

The derivations of the propagation velocities of sound fields of modal character given below are mainly based on the works of Rice et al. (1979) and Rice (1979) that were published in the late 1970s. The authors derived equations for the propagation velocities of acoustic modes by following a geometric approach approximating the modal phase fronts locally by plane waves. This procedure is common in *geometrical acoustics*, and, according to Landau and Lifshitz (1959), applies to sound waves where the amplitude and direction of propagation vary only slightly as a function of the wavelength. In addition, the works of Farassat and Myers (1996) and Farassat and Myers (1997) are referred to here. The authors also followed the suggested geometric approach.

The geometric relations have been recently analyzed by Hurfar et al. (2015) with respect to similarity conditions of modal sound propagation. The equations and geometrical relations presented here can be understood to be taken from Rice et al. (1979) or from Hurfar et al. (2015), if not stated otherwise. For the sake of ease of notation, the superscripts $(\pm x)$ and (σ) used in the previous expressions and indicating the dependence on the axial direction of propagation and the dependence on the hub-to-tip ratio, respectively, are omitted. In line with the focus of this work, the description concentrates on the analysis of the propagation of individual modes. A detailed study of the sound field properties for multiple-mode propagation has been carried out by Bartelt (2015). Furthermore, as the experimental investigation sound field excitation is carried out upstream of the LPT, the following analysis concentrates on waves or modes propagating in the direction of flow. Results can, however, be easily adapted to an upstream propagation.

Starting point of the following analysis is the sketch of a propagating sound wave shown on the top left side of Fig. 3.2. Here, the wave vector $\mathbf{k} := k \mathbf{n}$ points in the direction of the unit space vector \mathbf{n} , which is perpendicular to the assumed locally planar phase fronts of the mode. For the magnitude k of the wave vector the geometric relation

$$k^2 = k_x^2 + k_r^2 + k_\theta^2 \quad (3.15)$$

holds. With the approximation $k_{r\theta}^2 \approx k_r^2 + k_\theta^2 = \beta_{(m,n)}^2$ as stated by Rice et al. (1979), the root of each side of the so-called *dispersion relation* defined by

$$(k^0 - M_x k_x)^2 = (k_x)^2 + \beta_{(m,n)}^2 \quad (3.16)$$

3.1 Modal Sound Propagation in Circular Ducts

gives the magnitude k of the wave vector. Equation (3.16) shows that k only corresponds to the free-field number k^0 for modal propagation in a medium at rest. With $k^0 = \frac{\omega}{c}$, the wave number then depends linearly on the frequency. In the presence of a mean flow, however, this non-linear relation no longer holds and the effect of dispersion occurs. Accordingly, the relation above is often addressed as the *dispersive relation*. Generally, this relation can be either obtained by inserting the modal solution of Eq. (3.4) in the wave equation according to Eq. (3.3) as suggested by Rice et al. (1979), or by rearranging the equation for the axial wave number (cf. Eq. (3.8)) as proposed by Farassat and Myers (1996) and Farassat and Myers (1997) and described in the appendix in Sec. A.1.

The phase fronts propagate through the duct at an angle ϕ_x with the duct axis as illustrated in Fig. 3.2. With the axial component of the wave vector given by Eq. (3.8), this propagation angle between the wave vector and the coordinate vector \mathbf{e}_x parallel to the duct axis can be calculated from

$$\begin{aligned} \cos(\phi_x) &= \frac{\mathbf{k} \cdot \mathbf{e}_x}{|\mathbf{k}| |\mathbf{e}_x|} \\ &= \frac{k_x}{(k^0 - M_x k_x)} \\ &= \frac{k_x}{\sqrt{(k_x)^2 + \beta_{(m,n)}^2}}. \end{aligned} \tag{3.17}$$

As the problem is axis-symmetric, the angle holds for any circumferential position θ and the direction of propagation is completely determined. It shall be noted, that ϕ_x can exceed 90° as the axial wave number k_x can also take on negative values, cf. Eq. (3.8). In that case, the wave vector depicted in Fig. 3.2 no longer points in positive direction - which is, according to the definition chosen here, equivalent to the direction of flow - but in the direction opposite to the flow. The same then holds true for the unit space vector. This case will be addressed in detail later in this section.

The respective angles for the radial and circumferential direction can be obtained in accordance with the calculation of the axial propagation angle. As these are of no relevance for this work, the respective relations are not shown here and the reader is referred to the work of Rice et al. (1979).

Locally, the phase fronts can be assumed to travel in space with a propagation speed matching the speed of sound c . The velocity vector of propagation $\mathbf{c} := c \mathbf{n}$ points in the direction of the unit space vector or rather in the direction of the wave vector (cf. drawing on the top right corner of Fig. 3.2). The angle between the vector of propagation and the duct axis thus corresponds to the angle defined by Eq. (3.17), and value of the axial component of \mathbf{c} can be determined by

$$c_x = c \cos(\phi_x). \tag{3.18}$$

Now, as already has been worked out at the beginning of the section, it is group velocity which truly determines the propagation of sound waves. The group velocity

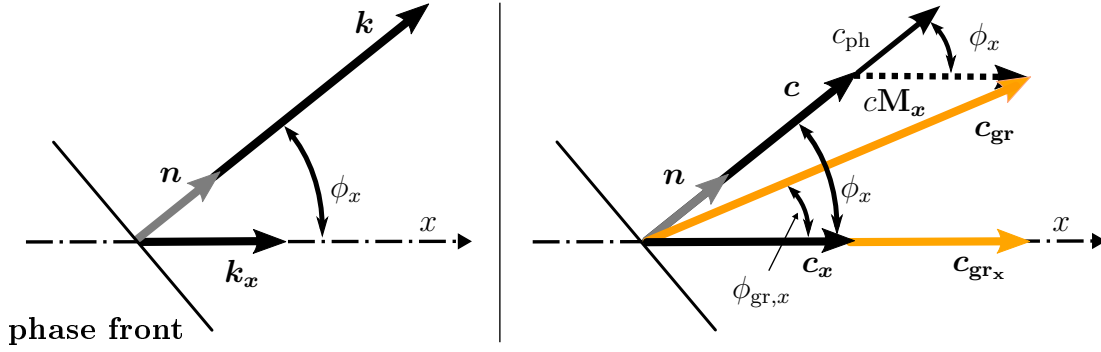


Figure 3.2: Left: Wave vector normal to the wave front. Right: Geometrical construction of the group velocity vector in the presence of flow. Both illustrations are based on Fig. 2 in the publication of Hurfar et al. (2015).

vector gives the direction of the energy propagation, and the magnitude of the vector gives the speed with which the wave transports energy in space (cf. Lighthill (1965)). The group velocity vector of an acoustic mode can be geometrically constructed by adding the flow vector to the velocity vector of propagation

$$\mathbf{c}_{\text{gr}} = \mathbf{c} + \mathbf{U} = c(\mathbf{n} + \mathbf{M}_x) \quad (3.19)$$

(cf. Landau and Lifshitz (1959)). Thus, Eq. 3.19 fully reflects the convective effect of flow. As shown in Fig. 3.2, the resulting group velocity vector is then no longer parallel to the wave vector, and thus not perpendicular to the phase fronts. The sound energy propagates in a different direction than the phase fronts and with a different velocity than the speed of sound. This observation concurs with the statement of Lighthill (1965). Calculated by trigonometry, the magnitude of the modal group velocity vector and the axial component of the vector can be determined according to

$$c_{\text{gr}} = c\sqrt{1 + 2M_x\cos(\phi_x) + M_x^2} \quad (3.20)$$

and

$$c_{\text{gr},x} = c(\cos(\phi_x) + M_x), \quad (3.21)$$

respectively (cf. Hurfar et al. (2015))¹. In line with the determination of the axial angle ϕ_x , the angle of the group velocity vector relative to the duct axis $\phi_{\text{gr},x}$ is given by

$$\cos(\phi_{\text{gr},x}) = \frac{c_{\text{gr},x}}{c_{\text{gr}}}. \quad (3.22)$$

This angle now differs from the angle of the velocity vector of propagation ϕ_x due to the convective effect. The relation between both angles is given by

$$\cos(\phi_{\text{gr},x}) = \cos(\phi_x) + M_x. \quad (3.23)$$

¹Equation (3.20) can be deduced by application of Pythagoras' theorem: $c_{\text{gr}}^2 = (c_x + cM_x)^2 + (c\sin(\phi_x))^2$ with $c_x = c\cos(\phi_x)$.

3.1 Modal Sound Propagation in Circular Ducts

Considering the algebraic difference between the velocity vector \mathbf{c} and the group velocity vector \mathbf{c}_{gr} in Fig. 3.2, it becomes obvious that the group velocity vector approximates the velocity vector in direction as well as in magnitude with decreasing flow Mach number. In a medium at rest, the group velocity vector \mathbf{c}_{gr} eventually points in the direction normal to the phase fronts and equals the propagation velocity vector ($\mathbf{c}_{\text{gr}} = \mathbf{c}$). This is confirmed by Eq. (3.20), if inserting $M_x = 0$.

In the interest of completeness, phase velocity shall be briefly addressed as follows. As already described, phase velocity c_{ph} gives the speed with which the phase fronts of a sound wave travel in space. The phase fronts thereby represent the surfaces of constant phase φ defined by the exponent in Eq. (3.4). Pursuing the geometric approach followed here, the phase velocity of a propagating mode with respect to the direction of the wave vector, thus the direction of the unit space vector, is obtained by

$$c_{\text{ph}} = |c(1 + \mathbf{M}\mathbf{n})| \quad (3.24)$$

as shown by Farassat and Myers (1996) and illustrated here in Fig. 3.2. With a superimposed flow, phase velocity increases or decreases with respect to the speed of sound depending on the propagation direction relative to the flow direction. Furthermore, it can be observed that with $c_{\text{ph}} = \lambda f$, the wavelength also depends on the magnitude and direction of flow. In case of no flow, the velocity of phase propagation in the direction normal to the phase fronts equals the propagation velocity c . As already outlined, in the presence of a mean flow the phase velocity deviates from the propagation speed c and from the group velocity c_{gr} .

The equations (3.20) to (3.22) give the general trigonometric relations for determining the considered quantities. Rice et al. (1979) give the fully developed relations depending on the cut-off-ratio ξ (cf. Eq. (3.11)), yielding

$$c_{\text{gr}} = c \sqrt{\frac{(1 - M_x^2) \left[1 + M_x \sqrt{1 - \frac{1}{\xi^2}} \right]}{1 - M_x \sqrt{1 - \frac{1}{\xi^2}}}}, \quad (3.25)$$

$$c_{\text{gr},x} = c \frac{(1 - M_x^2) \sqrt{1 - \frac{1}{\xi^2}}}{1 - M_x \sqrt{1 - \frac{1}{\xi^2}}}, \quad (3.26)$$

and

$$\cos(\phi_{\text{gr},x}) = \sqrt{1 - M_x^2} \sqrt{\frac{1 - \frac{1}{\xi^2}}{1 - M_x^2 \left(1 - \frac{1}{\xi^2}\right)}} \quad (3.27)$$

for the magnitude, the axial component, and the axial angle of the group velocity vector, respectively. Presented in this form, the equations provide a good basis for analyzing the relation between the group velocity vector and the cut-off ratio.

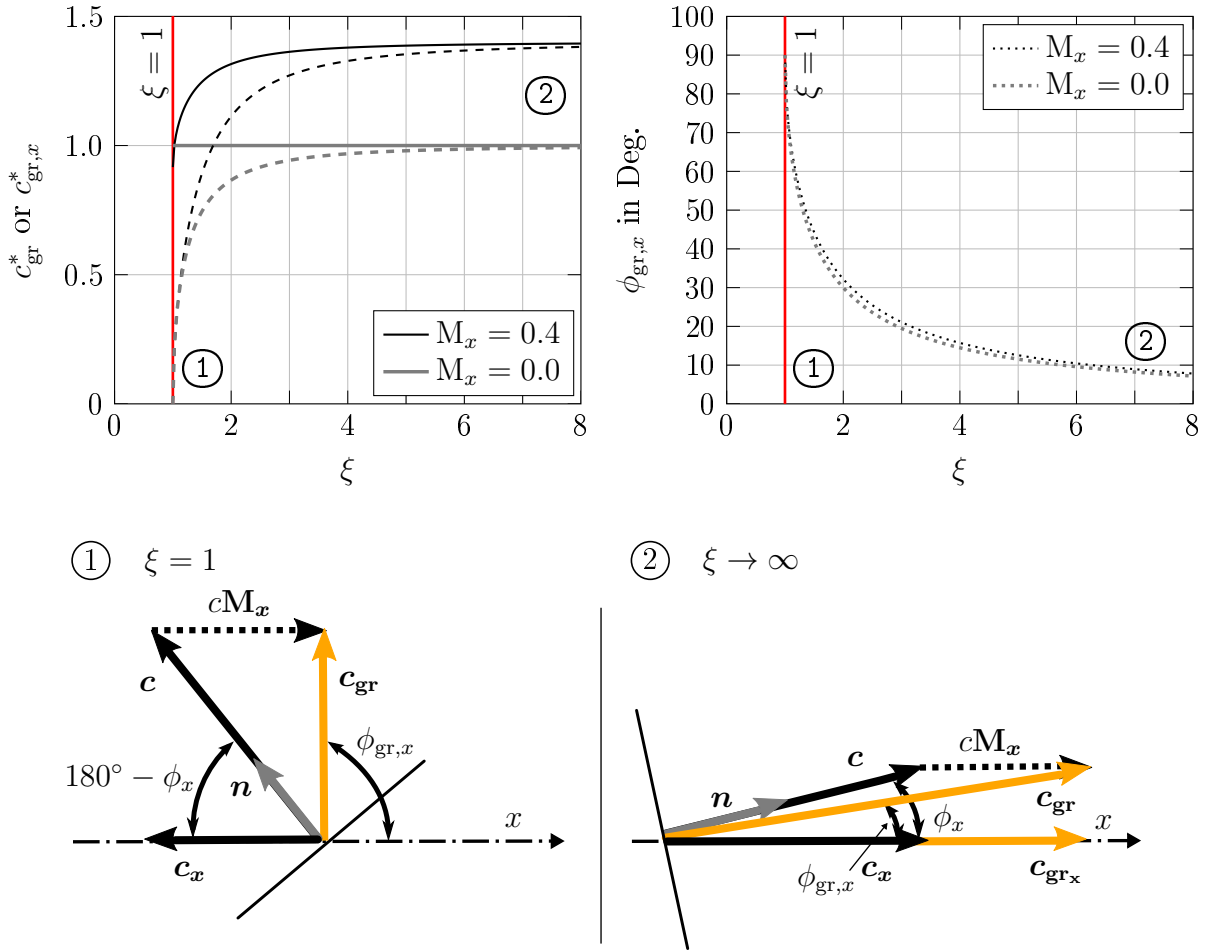


Figure 3.3: Properties of the group velocity vector relative to cut-off ratio. Top left: Magnitude and axial component of the vector normalized to the speed of sound represented by the solid and dashed lines, respectively. Top right: Axial angle of the group velocity vector. Bottom left: Geometric relations at cut-off condition. Bottom right: Geometric relations at high cut-off ratios.

In Fig. 3.3, the components of the group velocity vector are depicted versus the cut-off ratio for an exemplary Mach number of $M_x = 0.4$ and the case of no flow ($M_x = 0$). In the diagram on the left, the solid and the dashed lines represent the magnitude and the axial component of the vector, respectively. Both values are normalized with the speed of sound. In the right diagram, the corresponding axial angles of the vectors are depicted. The vertical lines indicate cut-off condition. At that point, the frequency of the mode just equals the cut-off frequency and the cut-off ratio has the value one ($\xi = 1$). Beneath the two diagrams, the geometric relations between the velocity vectors are schematically illustrated for the limiting cases $\xi = 1$ and $\xi \rightarrow \infty$. These drawings are in line with Fig. 3.2.

3.1 Modal Sound Propagation in Circular Ducts

Approximating cut-off condition, both the axial component and the magnitude of the group velocity vector decrease in value. Correspondingly, the axial angle becomes steeper with increasing cut-off ratio. Eventually, if meeting cut-off condition $\xi = 1$, the axial angle equals 90° and the vector is perpendicular to the duct axis as also pointed out by Rice et al. (1979) or Farassat and Myers (1996). In this case no sound energy is transported along the duct axis and, according to Eq. (3.4), the amplitude of the mode decreases exponentially in axial direction. It shall be stressed, that this observation is independent of the magnitude of flow velocity, and also holds true for propagation in a medium at rest. At cut-off condition the velocity in axial direction takes on a value of zero. However, from Eq. (3.25)

$$\lim_{\xi \rightarrow 1} c_{gr} = c\sqrt{1 - M_x^2}. \quad (3.28)$$

it follows that the group velocity takes on a value smaller than the speed of sound, but other than zero if $M_x > 0$. Consequently, this velocity represents the rotation of the mode in circumferential direction. Interestingly, with $M_x > 0$, the phase fronts of the mode are not parallel to the duct-axis, as can be seen from the geometric construction at the bottom left of Fig. 3.3. The velocity vector \mathbf{c} is thus on the contrary to the group velocity vector not perpendicular to the duct axis at cut-off condition. Also with respect to this observation, Rice et al. (1979) concluded that group velocity governs modal sound propagation. Furthermore, for a mode propagating in downstream direction as observed here, it is evident from the geometric construction that the velocity vector can point in the upstream direction, and thus in the direction opposite to the direction of energy transport. This is in line with the previously described observation that ϕ_x can exceed 90° . For $\xi = 1$, this angle depends on the Mach number only and can be calculated by $\cos(\phi_{x,cut}) = -M_x$ (cf. Rice et al. (1979)). This relation can be obtained from Eq. (3.21), if setting $c_{gr,x} = 0$, as is the case for cut-off condition. Thus, in the presence of flow and at cut-off condition, $\phi_{x,cut}$ is always greater than 90° and the vector points in the direction opposite to the propagation direction. The previously described properties are driven by the presence of flow. It should be kept in mind that in the absence of flow, $\mathbf{c}_{gr} = \mathbf{c}$ and the magnitude of the group velocity vector equals speed of sound for all cut-off ratios, cf. diagram on the top left of Fig. 3.3.

For $\xi \rightarrow \infty$, the axial component and the magnitude of the group velocity vector increase and gradually approximate the same value. In case of no flow, this would be speed of sound. From the illustration on the bottom right, it can be seen that both the axial angle of the group velocity vector as well as the angle of the propagation vector become small. The vectors approach the duct-axis.

In summary, with respect to the axial angle of the group velocity vector, it is found that a mode which is well cut-on has a small angle with $\phi_{gr,x} \rightarrow 0$. Contrary, approximating cut-off condition, the angle becomes steeper until the group velocity vector is eventually perpendicular to the duct axis and points to the duct wall.

Besides the geometric construction of the group velocity vector outlined previously, which, from the author's point of view, allows a very physical interpretation of the modal propagation properties, the relations according to Eq. (3.25) and Eq. (3.26) can be also derived following an analytical approach². Then the group velocity is given by

$$\mathbf{c}_{\text{gr}} = \frac{\partial \omega}{\partial \mathbf{k}} = \left(\frac{\partial \mathbf{k}}{\partial \omega} \right)^{-1} \quad (3.29)$$

(cf. Landau and Lifshitz (1959), Lighthill (1965), and Rienstra and Hirschberg (2017)). For the axial direction Bartelt (2015), for example, deduces the group velocity $c_{\text{gr},x}$ by applying Eq. (3.29) to the axial wave number defined in Eq. (3.8).

Excursus: As already stated, the geometric approach followed is based on an approximation of the three-dimensional mode by a planar one-dimensional wave. In the appendix in Sec. A.2, an excursus on the radial dependency of the group velocity vector is given. It is found that the aforementioned relations are valid at the caustic radius, which is given by

$$r^* = \frac{m}{u_{(m,n)}^{(\sigma)}} R. \quad (3.30)$$

This is contrary to the common understanding that the relations hold true near or at the duct radius. This is discussed in detail in the excursus. Furthermore, an approach is presented that allows the calculation of the propagation velocity vector \mathbf{c} and group velocity vector \mathbf{c}_{gr} at any radial position over the cross-section of the duct.

3.2 Hypothesis of this Work

Following the theory of similarity, similar conditions between two measurements separated in time but carried out on the same test rig are established by certain dimensionless parameters, called similarity parameters, that govern the physical behavior of the system. Hence, in order to carry out conclusive research on test rigs by being able to compare test data obtained several hours or days apart, equality of the numerical values of the similarity parameters has to be achieved between the different measurements. For this purpose, constant conditions in the measurement plane or measurement volume of a research test rig are mandatory. However, even in a laboratory environment, the inlet conditions of the measurement volume may change due to variations in external factors. For open-circuit turbomachinery test rigs where the working medium is collected at ambient conditions - as is the case for the turbine test rig used in this work - changing inlet conditions frequently occur. Therefore, to satisfy similar operating conditions, the operating point of the machine has to be continuously adjusted so that the similarity parameters considered are numerically equal between two measurements.

²Note, that this approach is also based on the assumption of a locally plane wave.

3.2 Hypothesis of this Work

Non-dimensionalization of the convected wave equation shows that in an ideal and inviscid flow with one spatial component, the Mach number and the Helmholtz number establish similarity conditions of sound propagation. Specifying the problem for sound propagation in a circular or annular hard-walled duct, approximate to the flow path in the components of a jet engine or in the different sections of the LPT test rig considered here, the hub-to-tip ratio is found to establish geometric similarity. This triad of dimensionless parameters (Mach number, Helmholtz number, and hub-to-tip ratio) then defines complete similarity conditions for sound propagation in a duct carrying a uniform one-dimensional flow. Geometric similarity provided, similar operating conditions with respect to sound propagation on a test rig are then achieved if Mach number and Helmholtz number are kept identical.

For test rigs equipped with a sound generator - as is the case here - the Helmholtz number can be controlled via the excitation frequency. With control of the frequency, equality of the Helmholtz number can thus be exactly maintained between two measurements. To maintain the identical numerical value of the Mach number, the operating conditions of the considered test rig have to be constantly controlled and the operating parameters have to be adapted if changes in the inlet conditions occur. To ensure equality of the Mach number, the operating points of turbomachines are determined with respect to a reduced mass flow rate and a reduced rotor speed (cf. Braeunling (2015)). However, control of these two operating parameters depends on the constancy of the controls of the test rig's periphery. Therefore, small changes in the Mach number can be expected for some turbomachines. That is also the case for the low-pressure turbine test rig focused on in this work.

One objective of this work is to define the requirements for similarity of modal sound propagation focusing on test rig operations, where constant conditions in the measurement section, and thus complete similarity, meaning equality of both the Mach number and the Helmholtz number, cannot be achieved. Based on a review of the state-of-the-art, it is found that group velocity governs propagation of sound waves in general. Following a geometric approach and approximating the phase fronts of a propagating mode by plane waves, it can be shown that the axial angle of the vector of the group velocity governs propagation of acoustic modes, in particular.

Based on these findings, the hypothesis is developed that the modal axial angle of the group velocity vector can be used to establish partial similarity with respect to the propagation of one specific mode in cases where equality of the Mach number and / or Helmholtz number cannot be achieved. In the section below, an approach for establishing similarity conditions is presented. The approach focuses on test rigs equipped with a sound generator for the controlled excitation of acoustic modes and is applied here for the experimental validation of the suitability of the group velocity angle to establish similarity of modal sound propagation (cf. Chap. 6).

3.3 Similarity Approach

It has been shown in Sec. 2.3 by non-dimensionalization of the wave equation that the Mach number and Helmholtz number establish similarity conditions for sound propagation in an inviscid and ideal flow with one flow component uniform over the cross section of the considered duct. The hub-to-tip ratio complements this duo when referring to sound field propagation in an annular duct. Considering the sound field as a superposition of modal components as described in Eq. (3.13), the triad of similarity parameters (M_x, He, σ) also governs the propagation of each individual mode of the sound field. Following the hypothesis of this work, the axial angle of the group velocity vector is analyzed for dependencies on the aforementioned parameters with the objective to develop an approach for establishing partial similarity conditions.

Essential parts of the findings presented in this section have been already published by Hurfar et al. (2015).

To begin with, it is found - without major effort - that the cut-off-ratio ξ can be expressed in terms of the Helmholtz number, the Mach number, and the hub-to-tip ratio. The latter thereby enters through the characteristic eigenvalue $u_{(m,n)}^{(\sigma)}$. Combining the quantities in Eq. (3.11) yields

$$\xi = \frac{\text{He}}{u_{(m,n)}^{(\sigma)} \sqrt{(1 - M_x^2)}}. \quad (3.31)$$

From Eq. (3.25) and Eq. (3.26) it then follows that the group velocity and the axial group velocity depend on the triad of parameters (M_x, He, σ) as well, and additionally on the speed of sound. In general form it can be written

$$c_{\text{gr}} = c \cdot \Psi(M_x, \text{He}, u_{(m,n)}^{(\sigma)}) \quad (3.32)$$

and

$$c_{\text{gr},x} = c \cdot \Psi_x(M_x, \text{He}, u_{(m,n)}^{(\sigma)}). \quad (3.33)$$

It follows that, without prejudging results, the respective angle to the duct axis depends solely on the Mach number, Helmholtz number, and the characteristic eigenvalue. In general form, this reads

$$\cos(\phi_{\text{gr},x}) = \frac{c_{\text{gr},x}}{c_{\text{gr}}} = \Psi_{\text{gr},x}(M_x, \text{He}, u_{(m,n)}^{(\sigma)}). \quad (3.34)$$

The challenge now is to find an equivalent form of Eq. (3.27) in terms of the Helmholtz number, the Mach number, and the characteristic eigenvalue that is convenient to analyze. Hurfar et al. (2015) investigated this problem and presented a rather long and complex equation. It is found that a significantly simpler form can be deduced which is more convenient to analyze. A detailed description of the derivation is given in the appendix in Sec. A.3. Following a shortened description is given.

3.3 Similarity Approach

In a first step, the cut-off ratio according to Eq. (3.31) is substituted in Eq. (3.27). Rearranging gives

$$\cos(\phi_{\text{gr},x}) = \sqrt{1 - M_x^2} \sqrt{\frac{\text{He}^2 - (u_{(m,n)}^{(\sigma)})^2 (1 - M_x^2)}{\text{He}^2 - M_x^2 [\text{He}^2 - (u_{(m,n)}^{(\sigma)})^2 (1 - M_x^2)]}}. \quad (3.35)$$

Combining the expression $\sqrt{1 - M_x^2}$ with the main root of the equation and further rearranging yields

$$\cos(\phi_{\text{gr},x}) = \sqrt{\frac{\text{He}^2 - (u_{(m,n)}^{(\sigma)})^2 (1 - M_x^2)}{\text{He}^2 + (u_{(m,n)}^{(\sigma)})^2 M_x^2}}. \quad (3.36)$$

Finally, Eq. (3.36) can be transformed so that

$$\cos(\phi_{\text{gr},x}) = \sqrt{1 - \left(\frac{1}{\frac{\text{He}^2}{(u_{(m,n)}^{(\sigma)})^2} + M_x^2} \right)}, \quad (3.37)$$

or

$$\cos(\phi_{\text{gr},x}) = \sqrt{1 - \left(\frac{\text{He}^2}{(u_{(m,n)}^{(\sigma)})^2} + M_x^2 \right)^{-1}}, \quad (3.38)$$

respectively. The relation presented above is an equivalent form to Eq. (3.27), but expressed in terms of the Mach number, the Helmholtz number, and the characteristic eigenvalue $u_{(m,n)}^{(\sigma)}$, where the latter depends on the mode order (m, n) and the hub-to-tip ratio σ . It follows that for a specific mode, an infinite number of combinations of the triad of parameters exist which yield the same axial angle of the group velocity vector. This observation has also been stated by Hurfar et al. (2015). In other words, for a specific mode, equality of the numerical value of the axial angle of the group velocity vector can be achieved by an infinite number of combinations of the Mach number, the Helmholtz number, and the hub-to-tip ratio σ . Geometric similarity provided, the previous statement results in an infinite number of combinations of the Mach number and the Helmholtz number. The functional relation according to Eq. (3.37) is described by the general description

$$\phi_{\text{gr},x} = \Psi_{\phi}(M_x, \text{He}, m), \quad (3.39)$$

which is referred to as the *similarity relation*, hereinafter.

For the sake of completeness, the case for a medium at rest shall be considered. For

$M_x = 0$, Eq. (3.37) reduces to

$$\cos(\phi_{\text{gr},x}) = \sqrt{1 - \left(\frac{u_{(m,n)}^{(\sigma)}}{\text{He}}\right)^2}. \quad (3.40)$$

The axial angle is then determined by a combination of the Helmholtz number and the hub-to-tip ratio, only.

Based on the similarity relation derived, it follows that for a specific test rig with a specific geometry the axial angle of the group velocity vector can be experimentally controlled by the Mach number and the Helmholtz number. That means, any variation in the numerical value of one of the two parameters can be compensated by a respective adaptation of the other parameter in order to meet equality of the group velocity angle, and thus, according to the hypothesis of this work, to establish partial similarity of modal sound propagation between two measurements. As outlined previously, control of the Mach number is limited, but the Helmholtz number can be accurately controlled via the frequency in case of sound propagation research supported by a modal sound generator.

Based on Eq. (3.36), the relation

$$\text{He}^2 = \frac{[M_x^2 (\cos(\phi_{\text{gr},x})^2 - 1) + 1] u_{mn}^2}{(1 - \cos(\phi_{\text{gr},x})^2)} \quad (3.41)$$

for the Helmholtz number can be determined. From Eq. (3.41), a relation for the frequency, henceforth called *reduced frequency*, given by

$$(f_{\text{red}})^2 = \frac{c^2 [M_x^2 (\cos(\phi_{\text{gr},x}^*)^2 - 1) + 1] u_{mn}^2}{(2\pi R)^2 (1 - \cos(\phi_{\text{gr},x}^*)^2)} \quad (3.42)$$

can then be derived. The reduced frequency provides the excitation frequency, which yields the exact same value for the angle of the group velocity vector as the reference angle $\phi_{\text{gr},x}^*$ under any aerodynamic condition characterized here by the axial Mach number M_x and speed of sound c . The reduced frequency is determined for a defined reference data set with the arbitrary reference conditions He^* and M_x^* . As the reduced frequency is dependent on the mode order via the eigenvalue u_{mn} , the calculated frequency only holds for one specific mode. A generalized description of this procedure may be written as

$$\phi_{\text{gr},x}^* = \Psi_\phi(M_x^*, \text{He}^*, m) = \Psi_\phi(M_x, \text{He}_{\text{red}}, m), \quad (3.43)$$

with the *reduced Helmholtz number* given by

$$\text{He}_{\text{red}} = \frac{2\pi f_{\text{red}} R}{c}. \quad (3.44)$$

3.4 Modal similarity map

For sound propagation measurements carried out on a test rig with a sound generator for synthetic sound field excitation, the reduced frequency introduced may serve as an (acoustic) operating parameter comparative to the reduced mass flow rate or the reduced rotor speed.

This work focuses on the establishment of similarity conditions for varying Mach numbers and / or Helmholtz numbers. For completeness, the case of a variation of the Helmholtz number without any changes of the Mach number shall be addressed. In this case, the reduced frequency can be determined on the basis of the Helmholtz number instead of the group velocity angle. With respect to the reference similarity condition He^* , the reduced frequency is then given by

$$f_{\text{red}} = \frac{cHe^*}{2\pi R}. \quad (3.45)$$

In this case, complete similarity is achieved, as both similarity parameter, Mach number and Helmholtz number, are equal.

3.4 Modal similarity map

The similarity relation between the axial angle of the group velocity vector and the triad of similarity parameters (He, M_x, σ) as defined in Eq. (3.37) is analyzed in this section. With respect to the motivation for this work, the analysis strives to assess the impact of changing similarity conditions on the modal sound propagation governing group velocity angle in dependence of the test rig's operating point. For this purpose, the similarity relation derived is displayed for selected values of the Mach number and the Helmholtz number in the form of a contour map. The latter is based on the map presented in Fig. 3 and Fig. 4 in the publication of Hurfar et al. (2015). Considering its intended application to analyze and eventually support the establishment of similarity in the LPT test rig, the map is hereafter referred to as the *similarity map* for modal sound propagation.

Below, the similarity maps are discussed by way of example. With respect to the setup of the validation measurement carried out in the inlet duct of the LPT, the analysis focuses on the geometry of a circular shaped duct with $\sigma = 0$. Furthermore, the analysis concentrates on modes of order $(m,n) = (1,0)$ and $(m,n) = (2,0)$. Generally, the similarity maps can also be derived for $\sigma \neq 0$ and for modes of higher radial order $n > 0$ as shown by Hurfar et al. (2015).

In the similarity maps developed the solid contour lines give constant values of the axial angle of the group velocity vector ($\phi_{\text{gr},x} = \text{constant}$). The contour lines thereby represent all possible combinations of the Mach number and the Helmholtz number which yield the same numerical value of this angle. For a specific value of the angle of

the group velocity vector, the contour lines can be either determined from

$$M_x^2 = \frac{\left(\frac{\text{He}}{u_{(m,n)}^{(\sigma)}}\right)^2 (1 - \cos(\phi_{\text{gr},x})^2) - 1}{(\cos(\phi_{\text{gr},x})^2 - 1)} \quad (3.46)$$

or

$$\text{He}^2 = \frac{[M_x^2 (\cos(\phi_{\text{gr},x})^2 - 1) + 1] (u_{(m,n)}^{(\sigma)})^2}{(1 - \cos(\phi_{\text{gr},x})^2)}. \quad (3.47)$$

Both equations are derived by solving Eq. (3.37) for M_x^2 and He^2 , respectively. The similarity maps presented here are all based on the first equation. In the diagrams the Mach number gives the ordinate and the Helmholtz number the abscissa.

Sensitivity of the group velocity angle with respect to changes in the Mach number and the Helmholtz number is determined here by

$$\Xi_{f(x)|x} = \frac{\partial f(x)}{\partial x} \frac{x}{f(x)}. \quad (3.48)$$

Hence, for an arbitrary functional relation $y = f(x)$, the sensitivity $\Xi_{f(x)|x}$ gives the relative change of y with respect to a fractional change in x . For $|\Xi_{f(x)|x}| > 1$ the change in y is relatively higher than the change in x , and vice versa for $|\Xi_{f(x)|x}| < 1$. From Eq. (3.48) it follows that for a given value of the Helmholtz number, sensitivity with respect to the Mach number is given by

$$\Xi_{\phi_{\text{gr},x}|M_x} = \frac{-1}{\cos(\phi_{\text{gr},x})} \frac{M_x^2}{\left[\left(\frac{\text{He}}{u_{(m,n)}^{(\sigma)}}\right)^2 + M_x^2\right] \sqrt{\left(\frac{\text{He}}{u_{(m,n)}^{(\sigma)}}\right)^2 + M_x^2 - 1}}. \quad (3.49)$$

Analogously, for a given value of the Mach number, the following equation

$$\Xi_{\phi_{\text{gr},x}|\text{He}} = \frac{-1}{\cos(\phi_{\text{gr},x})} \frac{\text{He}^2}{(u_{(m,n)}^{(\sigma)})^2 \left[\left(\frac{\text{He}}{u_{(m,n)}^{(\sigma)}}\right)^2 + M_x^2\right] \sqrt{\left(\frac{\text{He}}{u_{(m,n)}^{(\sigma)}}\right)^2 + M_x^2 - 1}} \quad (3.50)$$

gives the sensitivity with respect to the Helmholtz number.

In Fig. 3.4 and Fig. 3.5, the similarity maps for the acoustic mode of order (1,0) for a hub-to-tip ratio of $\sigma = 0$ are shown³. Thus, the maps are applicable in case of a respective mode propagating through a circular duct, as, for example, the inlet duct of the LPT test rig. The two maps differ in the sensitivity displayed. The first map

³In the appendix in Sec. A.4, the respective similarity maps of the mode (2,0) are given. The characteristics of these maps confirm the findings described here.

3.4 Modal similarity map

shows the sensitivity with respect to changes in the Mach number ($\Xi_{\phi_{gr,x}|M_x}$), whereas the second map displays the sensitivity with respect to changes in the Helmholtz number ($\Xi_{\phi_{gr,x}|\text{He}}$). The Mach number and the Helmholtz number are given for values up to $M_x = 0.8$ and $\text{He} = 5.0$, respectively. For these conditions, the values of the depicted group velocity angle are between $\phi_{gr,x} = 22^\circ$ and $\phi_{gr,x} = 90^\circ$. For the sake of brevity, only selected contour lines are depicted here where a contour interval of 2° is chosen⁴. The difference between the bold lines is 10° . Furthermore, for increasing values of the group velocity angle, the tagging of the contour lines is restricted to the bold lines, again for the sake of brevity. In view of the objective of easily assessing the impact of variations in the similarity conditions on the axial angle of the group velocity vector by means of the similarity map, areas of different levels of sensitivity are colored in different shades of grey. Light colors suggest low values of sensitivity and areas of dark-shaded grey represent higher values of sensitivity. The dashed lines represent the boundaries of selected values of sensitivity. That means that in the area between two dashed lines, sensitivity is within the range of the two values tagged to the respective lines.

The similarity maps visually show the inverse relation between the axial angle of the group velocity vector and the Mach number as well as the Helmholtz number as stated by Eq. (3.37). This inverse relation results in negative values of sensitivity for both similarity parameters. That means that for decreasing values of the Mach number and / or Helmholtz number, the angle of the group velocity vector relative to the duct axis increases and the respective mode approaches cut-off condition. Analyzing the two maps regarding sensitivity of the axial angle of the group velocity vector with respect to the Mach number and the Helmholtz number, it is found that

- (1) the numerical value of sensitivity with respect to the Mach number and the numerical value of sensitivity with respect to the Helmholtz number can differ considerably for the same operating point.
- (2) sensitivity with respect to either Mach number or Helmholtz number is highest when the respective mode approximates cut-off condition, thus $\phi_{gr,x} \rightarrow 90^\circ$.

With respect to finding (1), it is found that especially for high values of the axial angle of the group velocity vector in combination with low values of the Mach number, the level of sensitivity differs most significantly. Considering an angle of $\phi_{gr,x} = 60^\circ$ for $m = 1$ by way of example, it can be seen that for the same operating point sensitivity with respect to the Mach number is much smaller compared with the numerical value of sensitivity with respect to the Helmholtz number (e.g. $\Xi_{\phi_{gr,x}|M_x} < -0.1$ but $-2.0 < \Xi_{\phi_{gr,x}|\text{He}} < -1.0$).

Furthermore it can be observed, that sensitivity with respect to Mach number increases with increasing velocity of flow. Physically, it can be concluded that with higher flow velocity and approximation of cut-off condition the convective effect becomes more significant for the establishment of similarity on a test rig. For the sensitivity with respect to the Helmholtz number an opposing dependency is observed. Here sensitivity decreases with increasing values of the Helmholtz number as the mode leaves the area

⁴The contour interval gives the difference in degree between two adjacent contour lines.

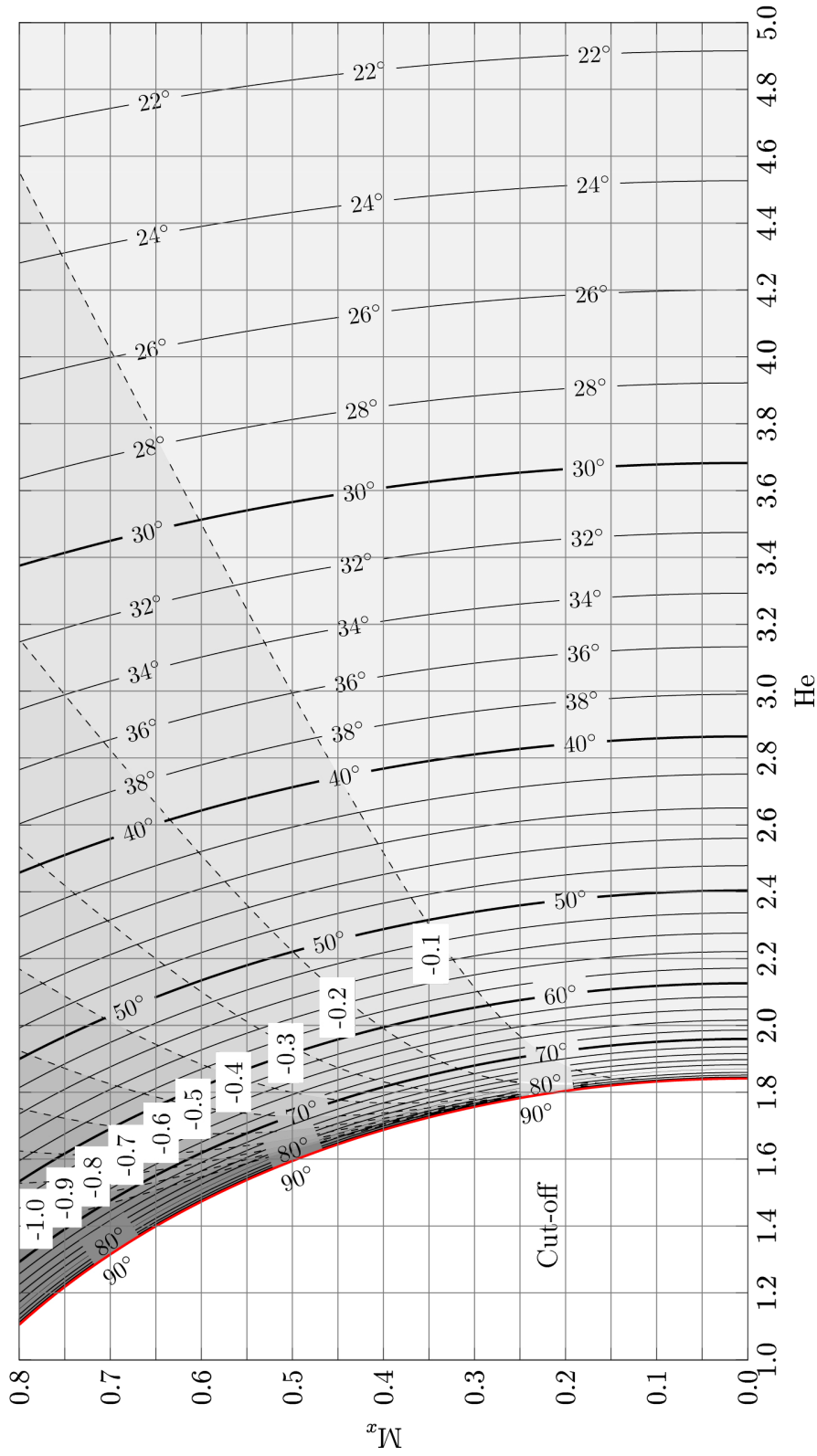


Figure 3.4: Similarity map for modal sound propagation. The map is characteristic of the mode (1,0) and a hub-to-tip ratio of $\sigma = 0$. The solid lines represent constant values of the group velocity vector $\phi_{gr,x}$. The dashed lines represent the boundaries of selected values of sensitivity of $\phi_{gr,x}$ with respect to the Mach number ($\Xi_{\phi_{gr,x}|M_x}$).

3.4 Modal similarity map

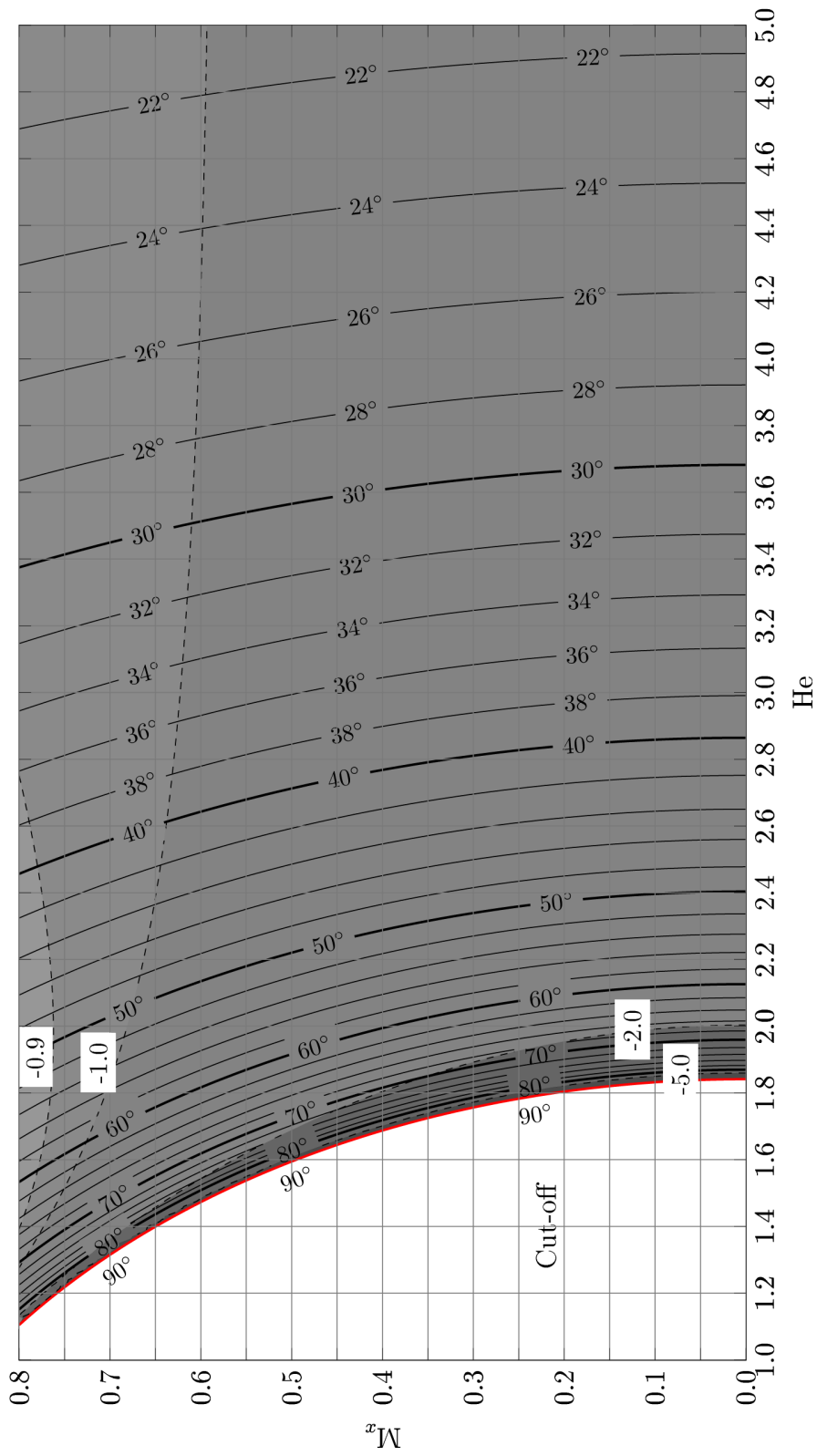


Figure 3-5: Similarity map for modal sound propagation. The map is characteristic of the mode (1,0) and a hub-to-tip ratio of $\sigma = 0$. The solid lines represent constant values of the axial angle of the group velocity vector $\phi_{gr,x}$. The dashed lines represent the boundaries of selected values of sensitivity of $\phi_{gr,x}$ with respect to the Helmholtz number $(\Xi_{\phi_{gr,x}|He})$.

of cut-off condition.

Generally, it is found that sensitivity is highest if the operating point of the test rig is chosen so that the mode is close to cut-off or meeting cut-off condition (cf. finding (2)). At cut-off condition the physical properties of sound propagation change from an axial transport of sound energy to an exponential decay of the sound pressure amplitudes along the duct axis (cf. Sec. 3.1), so that even minor changes in the similarity parameters Mach number and Helmholtz number will significantly change the physical properties of the propagation of the respective mode. Conversely, for operating conditions where the axial angle of the group velocity vector is well below $\phi_{gr,x} = 90^\circ$, the latter is nearly insensitive to changes in the Mach number, and thus propagation properties at that point are not affected if similarity is not achieved during test rig operation. The similarity maps for mode (2,0) are given in the appendix in Sec. A.4. These confirm the findings summarized here.

The sensitivity analysis here is based on an analytical investigation of the numerical equations and on the derived modal sound propagation properties. In order to detect the impact of non-compliance of similarity conditions on measurement results, the modal response function can be taken into account. The response function gives the sound pressure amplitude relative to a chosen acoustic quantity. While in most cases the modal response is given with respect to the acoustic frequency, the response function will be analyzed here also as a function of the axial angle of the group velocity vector. In doing so, the relation between variations in the Mach number and Helmholtz, respective changes in the group velocity angle and the sound pressure amplitude is given. Chapter 6 is concerned with this analysis.

4 Acoustic Measurements in a Low-Pressure Turbine

To validate the suitability of the axial angle of the group velocity vector for the establishment of similarity for modal sound propagation investigations, aerodynamic as well as acoustic measurements carried out on the axial air-turbine test rig of the TFD are analyzed. To show generality of results, two operating points are considered for the experimental validation: a *part-load operating point* and the *design operating point* of the turbine configuration. The first one mentioned is specified by approximately half the mass flow rate and rotor speed compared to operation at design point.

In Sec. 4.1 of this chapter, a general description on the test rig and the low-pressure turbine configuration used is given. Acoustic as well as aerodynamic measurement planes are defined, and the data acquisition chain including the instrumentation employed in the defined measurement planes are described. For controlled variation of the different parameters of the modal sound field (e.g. mode order, direction of spinning, and the oscillation frequency), a sound generator consisting of multiple loudspeakers has been implemented in the inlet of the turbine test rig. The synthetic excitation of modal sound fields is a major methodical tool in this work. The applied excitation method is therefore described in detail, and results of test measurements in the Aeroacoustic Wind Tunnel (AWT) of the TFD are presented in Sec. 4.2. This chapter closes with a discussion of the results of a cut-off analysis of the modal propagation carried out for the operating points considered (cf. Sec 4.3).

4.1 Measurement Setup

4.1.1 Test rig

The air-turbine test rig of the TFD is a research multistage axial-turbine which can be equipped with different turbine configurations of up to seven stages depending on the rotor design. Several configurations and bladings for high-, medium-, and low-pressure gas and steam turbines have been tested since the test rig was first put into operation in the 1960s. The turbine was initially dedicated mostly to aerodynamic studies, research objectives in recent years increasingly include aeroelastic and aeroacoustic studies. Works on the aforementioned fields include the investigations carried out by Meinzer et al. (2015), J. Aschenbruck et al. (2015), Bartelt (2015), Laguna (2016), and Hauptmann et al. (2017).

The air-turbine test rig is operated in an open circuit mode. Compressed air is provided by up to three screw compressors. The air is collected at ambient conditions and

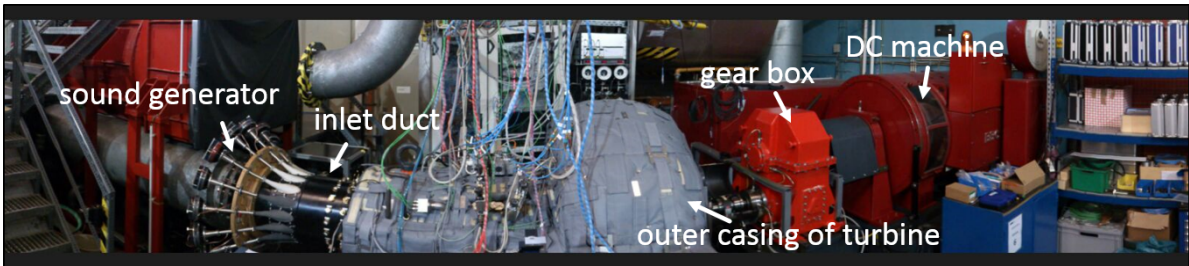


Figure 4.1: Panoramic view of the instrumented turbine test rig with a sound generator installed in the inlet. (Source: TFD)

exits the test rig to ambient pressure. In the current setup, the turbine shaft is coupled to a direct-current pendulum-type machine (DC machine) through a gearbox, which serves either as a generator or motor, depending on the operating conditions. The test rig is equipped with an extensive monitoring system which includes a data acquisition system permitting among other things, an on-time recording of the rotor speed and of the mass flow rate. To ensure (aerodynamic) similarity conditions between two points in time, the operating point is controlled via a reduced mass flow rate and a reduced rotor speed as proposed by Braeunling (2015). A calibrated venturi nozzle is used to measure the mass flow rate of the compressed air according to ISO 5167-4. The inlet duct to the venturi nozzle is straight, ensuring a homogeneous axial flow. The nozzle itself is located approx. 9 m upstream of the turbine's inlet so that the flow enters the turbine fully-developed and undisturbed. Control of the mass flow is achieved by switching the number of the screw compressors in operation and by operating the valve of the bypass, respectively. Control of the rotational speed of the turbine is independent of the mass flow control. The rotor speed is triggered by a capacitive sensor and is adjusted continuously by the DC motor. For further detailed information on the test rig specifications and infrastructure refer to Binner (2011), Henke et al. (2012), or Binner and Seume (2014).

4.1.2 Turbine configuration and test conditions

The experimental study presented here considers acoustic measurements taken within an extensive measurement campaign investigating aerodynamic effects on a 1.5-stage subsonic low-pressure gas-turbine configuration. The turbine stage was designed in cooperation with MTU Aero Engines for unsteady aerodynamic investigations on the influence of blade row interaction on work transfer and loss-effects in the core flow of turbines. To minimize side-wall and secondary flow-field effects in the core flow, the aero-design includes a high aspect ratio blading, tip-shrouded rotor blades, and labyrinth seals. The design process was numerically supported and the results are published in Biester et al. (2011) and Biester et al. (2013a). Experimental results presented by Henke et al. (2016) confirm the numerically-predicted quasi two-dimensional flow in the core flow region. The nominal stage parameters for the design point, as well as the geometric blade characteristics are summarized in Tab. A.1 in the appendix in Sec.

4.1 Measurement Setup

A.5. Biester (2016) characterizes the design as similar to state-of-the-art low-pressure jet engine turbines.

To meet the objectives of the aerodynamic study, three different axial gap configurations were designed. This approach was chosen to clearly differentiate between blade-wake effects and potential field effects. In order to compensate aerodynamic clocking effects due to the axial gap variation, both the first and the second stator vane carrier are specifically designed to allow movement in the circumferential direction. Considering the periodicity of the turbine stage, circumferential rotation over one pitch (20°) with respect to the first vane row can be realized. Details on this design concept are given in Henke et al. (2012) The aerodynamic and acoustic data used in this work are all collected from measurements at the configuration with the largest axial spacing of 80% of the rotor blade's axial chord length. This axial gap configuration is chosen as probe traversing is possible in all inter-row sections and unsteady potential as well as viscous wake effects are smallest within the axial gap and the blade passage, as shown by Biester et al. (2013b). Even though this is not of particular relevance to this work, it still might be of interest to future efforts as a quasi-steady two-dimensional core flow favors the application of simplified analytical sound propagation and transmission models.

The turbine configuration consists of a stator-rotor-stator combination as mentioned above. The blade count of the first stator vane row is $V_1 = 18$. The second stator vane row carries twice the number, so that $V_2 = 36$. The rotor consists of thirty blades ($B = 30$). According to the relation

$$m = hB + sV \quad \text{for } h = 0, 1, 2, \dots \quad \text{and } s = \dots - 1, 0, 1, \dots \quad (4.1)$$

derived by Tyler and Sofrin (1962), acoustic modes of the order $m = \pm 6$ or multiples of this order can be expected to be generated by the interaction of the first stator with the rotor, the interaction of the rotor with the second stator, or by the rotation of the rotor alone. Depending on the operating point, these modes then propagate with the blade-passing frequency (BPF) or its harmonics throughout the turbine (cf. Sec. 4.3).

For the acoustic measurements, a sound generator has been installed in the inlet of the turbine. Figure 4.1 shows a panoramic view of the test rig with the sound generator located on the left, the instrumented outer casing of the turbine with thermal insulation in the middle, and the gear box and DC machine on the far right. The general setup of the test rig is identical to the one used for the acoustic measurements on a one-stage and two-stage turbine configuration, as carried out by Bartelt (2015) and Laguna (2016). A schematic sectional view of the current configuration with an expanded view of the sound generator is depicted in Fig. 4.2. The sound generator's main part is a circular duct with an inner diameter of $D = 0.496$ m, which exactly matches the casing diameter of the turbine's inlet. Figure 4.2 shows that, the inner diameter of the inlet duct of the turbine narrows down in the region of the star-shaped head bearing. The latter consists of six radial struts distributed at regular intervals over the circumference of the rotor shaft. Downstream of the struts the annular flow path of the turbine configuration has a constant hub-to-tip ratio of $\sigma = 0.61$ (with $D_{\text{Rotor}} = 0.270$ m).

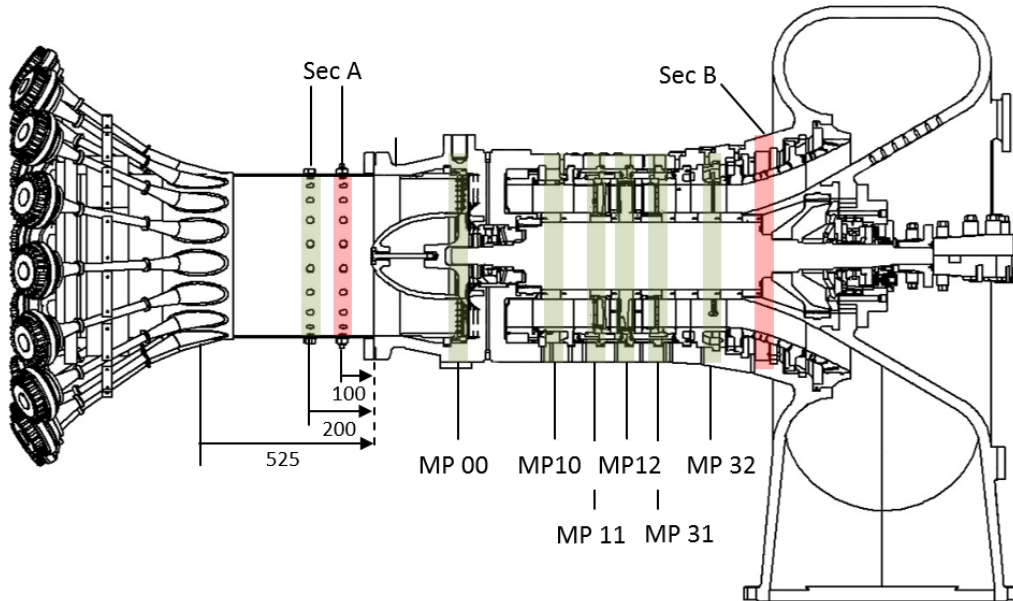


Figure 4.2: Schematic sectional view of the turbine test rig with the 1.5-stage LPT configuration and installed sound generator. Acoustic measurement planes are marked red. Aerodynamic measurements planes are marked green.

The acoustic measurement campaign was planned after the final design. Therefore, the instrumentation is not acoustically optimized, and the acoustic measurement planes differ from the main aerodynamic measurement planes. In Fig. 4.2, the acoustic measurement planes and the aerodynamic measurement planes are marked in red and green, respectively. Acoustic instrumentation is employed in two sections of the test rig: In the cylindrical duct of the sound generator, and in the diffuser part of the turbine behind the second vane row. Hereinafter, these measurement planes are also referred to as *Sec A* and *Sec B*, respectively. Measurement plane *Sec A* is located directly in front of the turbine, thus, in the inlet of the turbine. For the detection and modal decomposition of the sound field, 20 microphones are equidistantly distributed around the circumference in each section at one axial position. The microphones are mounted flush with the wall in order to be non-intrusive. According to the sampling theorem, the number of sensors employed allows the detection of ten wavelengths around the circumference. However, decomposition with respect to both directions of circumferential propagation is only possible up to modes of the circumferential order $|m| = 9$, as shown in Sec. 5.1.2. Radial mode decomposition as well as a differentiation between upstream and downstream propagating modes is not feasible with this setup (cf. Sec. 5.1.1).

Steady measurement data of the flow pressure and the flow temperature are collected, both for the control of the operating point and for the application of analytical models of modal sound propagation. The aerodynamic instrumentation is extensively distributed

4.1 Measurement Setup

throughout all parts of the turbine. The corresponding measurement planes (MP) are specified in Fig. 4.2: MP 00 is thus located at the axial position of the struts, MP 10 in front of the first stator vane row, MP 11 between the first stator and the rotor, MP 12 respectively behind the rotor and in front of the second stator vane row, MP 31 behind the second stator, and MP 32 in front of the diffuser but behind MP 31. The labeling of the aerodynamic measurement planes is in accordance with Henke et al. (2016).

Intrusive radial investigations have been carried out in all measurement planes in the annular flow path of the LPT. In MP 00 and MP 32 built-in rakes are installed. In the other four measurement planes (MP 10, MP 11, MP 12, and MP 31), radial probes are traversed. However, in this work only the data collected at the Euler radius are used, e.g. to determine the modal cut-off conditions as discussed in Sec. 4.3. Therefore, the radial aerodynamic characteristics of the turbine configuration in the different measurement planes are not specifically addressed here. A detailed description and interpretation on the aerodynamics of the considered 80 % axial-gap configuration at design-point operation is given by Henke et al. (2016).

In the inlet duct of the turbine in Sec A, the section of main interest as the validation is carried out with respect to this measurement plane, aerodynamic instrumentation is mounted next to the microphone ring in upstream direction. Using a permanently installed probe, total temperature and total pressure are captured near the center of the duct. The probe is not traversed, thus information on the flow field is gathered at one radial and circumferential position only. For operation at design point, Henke et al. (2016) showed that the flow field in MP 00 is fully developed and circumferentially uniform, as can be expected due to the long undisturbed inlet duct to the test rig. The boundary layer at the shroud and at the hub covers approx. 10% and 15% of the height of the flow path, respectively. The radial variation within the core flow is negligible. It can be convincingly assumed that these flow conditions also reflect the flow field upstream of MP 00, namely in the cylindrical duct in front of the turbine stage in Sec A. This assumption is confirmed by the results of radial probe traverses carried out in the inlet duct by Bartelt (2015). For the investigated two-stage turbine configuration in his work and a mass flow rate of $\dot{m} = 6.4 \text{ kg/s}$ and a rotational speed of $N = 6400 \text{ min}^{-1}$ the flow field is indeed characterized by a homogeneous distribution of the total pressure and only small variations in the total temperature in radial direction. In summary, data collection at one radial position is sufficient here. Furthermore, a uniform homogeneous flow profile, as required by the used flow model introduced in Sec. 2.3 can be satisfactorily assumed.

4.1.3 Instrumentation and Data Acquisition

Aerodynamic instrumentation and data acquisition

The inlet and outlet conditions of the turbine stage are monitored with built-in rake-type probes. Total temperature and total pressure Kiel-head probes are installed on the leading edge of each one of the six struts in measurement plane MP 00 at different radial

positions. At the turbine exit (MP 32), six circumferentially equally distributed rakes of combined Kiel-head and three-hole probes are used to capture the radial flow field characteristics. These two measurement planes are used to evaluate the boundary conditions of the aerodynamic measurement volume and to determine the global parameters of the test rig such as the total pressure ratio.

To characterize the three-dimensional flow field of the turbine configuration, probes are radially traversed in between the blade rows, as well as upstream and downstream of the 1.5-stage configuration (MP 10 to MP 31). For the measurements, steady five-hole pneumatic probes with a head diameter of 2.5 mm or 5.0 mm are used. Each of these probes is additionally equipped with a thermocouple to capture the total temperature of the flow field. The probes are calibrated in the high-speed calibration channel of the TFD for different yaw angles and pitch angles in the Mach number range from $M = 0.1$ to $M = 0.9$. With the combined information of the measurement data and calibration data, the static and total values of the aerodynamic quantities as well as three components of the flow velocity vector can be calculated iteratively. For further description of the calibration method and the calculation of the flow vector's components see Evers (1985), Herbst et al. (2011), and Aschenbruck and Seume (2015). Further information on the aerodynamic measurement techniques employed can be found in Henke et al. (2016).

The probe used in Sec A is a one-hole pneumatic probe equipped with a high-precision PT100 temperature sensor to acquire the flow's temperature. The probe is installed near the center of the inlet duct with the head aligned with the duct axis. Thus, the total values of the temperature and pressure can be measured.

For the aforementioned steady measurements, the pressure data is sampled using a differential pressure transducer of the type PSI 9816 mounted in the respective 98RK-1 rack. The pressure range is set corresponding to the sensor location along the turbine. The thermocouples of Type K of the probes and rakes are connected to an analogue input controller by Invensys/Eurotherm (2500MF-A) in combination with a TruRac Reference Unit Model 847 for reference. The temperature in Sec A is digitized using a PXIe-4357 module by National Instruments.

Acoustic instrumentation and data acquisition

To capture the unsteady pressure fluctuations of the sound field in the defined measurement planes, high-precision pressure sensors by G.R.A.S. are used. These sensors of the type G.R.A.S. 46BD are pressure standard microphone sets consisting of a microphone cartridge and a preamplifier. The chosen set combines the 1/4" pre-polarized condenser microphone G.R.A.S. 40BD-S9 with rear-venting and the CCP (constant current powered) high-temperature preamplifier G.R.A.S. 26CB-HT. According to the manufacturer's specification, this microphone set allows measurements from 38 dBA to sound pressure levels of 168 dB for frequencies up to 70 kHz, which by far exceeds the intended operating range. The turbine is driven by air and the inlet pressure and temperature are low in comparison with the conditions found in real engines; still, the sensors are placed in an environment demanding special properties for long-term high performance.

4.1 Measurement Setup

By request the microphones were subjected to an artificial aging process, which enables their application in conditions up to temperatures of 140 °C. The microphones are state-of-the-art at the TFD, and their application in the turbine test rig is well proven (cf. Bartelt (2015) and Laguna (2016)).

Each microphone set is calibrated at the factory as a unit. The sensitivity given in mV/Pa is measured at 250 Hz with a pistophone, and the frequency response curve is recorded by the electrostatic actuator method. Regarding frequency response, it can be safely assumed that the values have not significantly changed since the initial factory calibration. However, sensitivity may change with time and additionally depends on the measurement equipment employed such as cable length, cable material, measurement cards, etc. Taking this into account, the microphone sets are calibrated internally at the TFD at 1000 Hz using a certified sound calibrator (Brüel and Kjaer, Type 4231). To ensure highly reliable measurements, special care is taken that the measurement equipment used for the calibration is identical with the equipment used for the campaign. The calibrator has an accuracy of ± 0.2 dB with an unsteadiness of the emitted sound pressure level within ± 0.02 dB, where both values state the expanded uncertainty with a coverage factor of 2. The sets are characterized by low noise and a very flat frequency response throughout the entire frequency range. In the frequency range of interest, the average response deviation with respect to the internal calibration carried out at 1000 Hz is less than ± 0.07 dB. The accuracy of the acoustic pressure measurements is found to be sufficient.

In turbomachines, high-quality microphone measurements have to be performed under challenging conditions. Besides the thermodynamic restrictions mentioned above, other factors have to be considered. In the TFD turbine, the sensors are mounted flush with the inner casing wall in a way that the microphones are oriented parallel to the axial flow direction. The diaphragms are therefore not directly exposed to the flow as the flow radial component of the velocity is negligible. However, risk of damage to the sensitive surface by small particles in the flow is still present, and thus has to be considered. This holds especially true for the microphones placed in the diffuser. Contrary to the homogeneous axial flow at low Mach numbers in the inlet, the flow in Sec B has a strong circumferential component which drives the flow's particles outward to the casing wall. After the assembly and the alignment of the test rig, accessibility of the sensors in the diffuser is limited, and replacement in case of a failure is not possible. Considering this, symmetric protection grids are used for the microphones placed in Sec B. The use of protection grids is quite common for free-field as well as in-flow measurements. Besides facing the risk of damage during operation, material damage during assembly is avoided. While common, possible impacts of protection grids on the accuracy of in-flow measurements have to be considered as increased flow-induced noise and frequency-dependent resonances, or peaks may occur (cf. Hamid and Horne (1997) or Allen et al. (2002)). Positive effects due the spatial separation between the turbulent flow in the boundary layer and the microphones' diaphragms, however, are also discussed by e.g. Jaeger et al. (2000). Hurfar and Seume (2015) recently confirmed the results presented

by Shin et al. (2007), showing that above a Mach number dependent frequency-band, the noise level measured is indeed higher for microphones with a protection grid than for sensors without a grid. The author expanded these findings for flow velocities of $M_x > 0.5$. Below this frequency band, the sensors with a protection grid detect fewer pressure oscillations. This could be explained by the aforementioned spatial separation having an effect similar to recessing wall-mounted microphones. Beside the stated dependency on the Mach number, the authors suggested a dependency on the Reynolds number. Resonances or distinct peaks were not detected in the considered frequency range from 300 Hz to 25 kHz. Since Hurfar and Seume (2015) used the same sensors as employed in the LPT for their study, distorting influences of the protection grids on the results of the acoustic measurements are not to be expected. Moreover, statistical post-processing techniques are carried out to reduce the influence of noise (cf. Sec. 5.2). Nevertheless, as mentioned at the beginning of this section, the use of a protection grid is omitted for the microphones employed in Sec A.

The acoustic data acquisition system is optimized for unsteady pressure measurements and is also well proven at the TFD. The core of the PXI Modular System by National Instrument are three PXIe-4496/4497 modules mounted in a PXIe-1062Q chassis. Each module accepts 16 analogue inputs. This configuration allows highly accurate and simultaneous data sampling of the 40 microphone signals. The maximum sampling rate possible with this setup is 200 kHz. However, due to limitations of the memory capacity, data are sampled at a frequency of $f_S = 2^{16}$ Hz. A detailed overview and further specification of the NI PXI data acquisition system are provided by Laguna (2016).

For all measurements, the acoustic data are recorded for one second, which might be considered short. However, analysis has shown that this measurement time in combination with the statistical post-processing method applied, results in data with modal amplitudes of sufficient small confidence intervals to permit conclusive results.

4.2 Synthetic Sound Field Excitation

4.2.1 Sound generator design and excitation method

Experimental investigations of the propagation of modal sound fields often concentrate on acoustic modes produced by rotor-stator interaction, and thus on modes oscillating at the blade-passing frequency or its harmonics. Hurfar et al. (2016) pointed out that non-rotor synchronous acoustic modes are also found in the turbomachinery components of a jet engine and may significantly contribute to the internally measured or radiated sound field. The authors summarized the following possible sources:

- (1) rotor-stator interaction in multiple-shaft engines and modern geared turbofans
- (2) low-frequency pressure patterns generated by the combustion chambers, and
- (3) acoustic resonances e.g. as reported by Hellmich and Seume (2008).

4.2 Synthetic Sound Field Excitation

To investigate acoustic modes of arbitrary frequency as well as of arbitrary mode order, rather than be restricted to rotor-synchronous modes, an acoustic excitation system has been used for the acoustic measurements considered in this work. Installed in the inlet of the LPT, (modal) acoustic sources, as listed above, can be modeled.

In open literature, these excitation systems are often referred to as *sound generators* or *mode generators*. The sound generator applied here has been specifically designed for turbomachinery applications (cf. Bartelt et al. (2013)) and has been successfully applied by Bartelt (2015) for acoustic measurements in the turbine test rig. Figure 4.1 and Fig. 4.2 show that, the sound generator consists of one ring of sixteen acoustic excitation units equidistantly mounted on the outer wall of a circular duct segment in the circumferential direction. Each one of the 16 excitation units consists of one 2" mid-range compression driver by BMS (Type 4591) supplied with an 8 Ohm audio amplifier (RAM Audio RX600), a loading unit in front of the speaker's membrane, a guiding tube, and an acoustic horn for an improved impedance matching between the guiding tube and the opening to the duct. The compression drivers employed are characterized by a maximum sound pressure level of 136 dB, and a flat frequency response in the frequency range of interest. The loudspeakers can be operated in the frequency range between 200 Hz to 9 kHz. However, below 400 Hz the sound pressure levels achieved are very low. This frequency therefore marks the lower boundary of acoustic excitation. The design process of the excitation units has been supported by numerical methods focusing on achievable sound pressure levels and directivity patterns of the excited sound field. Detailed information on the design are provided by Bartelt et al. (2013).

For the synthetic excitation of modal sound fields, a harmonic signal with a specific frequency, phase, and amplitude is assigned to each unit. The generation of the signals is controlled by two field-programmable gate array chips (FPGA). A trigger impulse is sent to both FPGAs at the same time. The respective wires are of identical length for simultaneous signals. The control system is carefully designed to ensure only the smallest deviations from the assigned amplitudes and phases. Hurfar et al. (2016) show that phase shifts between the generated signals and relative deviation in the amplitudes are indeed minor.

One major requirement of sound generators for turbomachinery applications is the excitation of sound fields with a high signal-to-noise ratio as stressed by Bartelt et al. (2013). The amplitude of the signal can be positively influenced by the design of the sound generator (such as the design of the excitation units, the choice of the loudspeakers, and by the number of excitation units provided, of course). Furthermore, the signal-to-noise ratio depends on the excitation method chosen. The latter aims at a dominant excitation of specific modal sound field patterns to achieve high modal sound pressure levels in general and specifically in comparison to unintentionally excited modes. Bartelt et al. (2013) verified the possibility of synthetically generating acoustic modes by exciting the sound field near the respective cut-off frequencies. The assigned amplitudes and phases were the same for each excitation unit. To control the excitation in terms of the direction

of the modal rotation, Bartelt (2015) proposes the use of four units with an assigned phase difference of 90° relative to each other. Here, a different excitation method is applied. The approach chosen, allows control of both mode order and spinning direction, not only at the cut-off frequency but also over a wide frequency range. For this purpose, a specific phase is assigned to each loudspeaker. According to Eq. (3.4)

$$p_{(m,n)}^{\pm x}(r, x, \theta, t) = \operatorname{Re} \left\{ A_{(m,n)}^{\pm x} \cdot e^{i(\omega t - k_x^{\pm x} x - m\theta + \phi^0)} \cdot g(r) \right\}$$

for $m \in \mathbb{Z}$ and $n \in \mathbb{N}$,

the (complex) circumferential pressure distribution for a spinning mode of circumferential order m is determined by the expression $e^{-im\theta}$. Thus, for the excitation of a specific mode, the specific phase to be assigned to each excitation unit can be calculated based on the circumferential position θ . To reflect the spinning nature of the mode, the assigned amplitudes of the signals have to be kept identical. Application of this excitation method allows the excitation of specific modes, which are dominant not only at their cut-off-frequency but over a wide frequency range as also shown by Mumcu et al. (2016) and Hurfar et al. (2016).

Besides rotating modes, circumferential standing modes can be intentionally excited as well. Contrary to the case of a spinning mode, here identical phases are assigned to each loudspeaker signal whereas the amplitudes vary. Considering a superposition of two modes with the same amplitude A_m spinning in opposite direction ($\epsilon = 1$), it then follows from Eq. (3.13) that the amplitude A at the position θ can be obtained by

$$A(\theta) = A_m(e^{-im\theta} + e^{+im\theta}) = \frac{A_m}{2} (\cos(m\theta)). \quad (4.2)$$

With the excitation methods described above, control of the circumferential mode order is possible. Control of both the circumferential mode order as well as the radial mode order can be achieved by using multiple-ring excitation systems. Such a setup has been tested first by Smith et al. (1996) for active noise control systems and has been subsequently applied by e.g. Enghardt et al. (2002). Recently, Mumcu et al. (2016) and Hurfar et al. (2016) developed a two-ring sound generator for investigations of modal sound propagation properties.

Here, however, the specific excitation is restricted to the circumferential mode order due to the one-ring design of the sound generator.

4.2.2 Preliminary investigations in an aeroacoustic wind tunnel

Prior to the application in the turbine, the synthetic mode excitation is tested in the Aeroacoustic Wind Tunnel (AWT) of the TFD to validate the chosen excitation method and to verify the functionality of the control system in general. In contrast to the turbine, simple geometric conditions are found in this test rig. In fact, the AWT has been specifically designed to validate numerical simulations and analytical models (cf. Bartelt et al. (2012)). For the test measurements, the sound generator is installed in the inlet

4.2 Synthetic Sound Field Excitation

of the circular test-section of the AWT. The setup of the test rig is identical with the setup described by Bartelt et al. (2013) and Bartelt (2015). The test measurements are carried out without flow in order to minimize flow-induced background noise. An illustration of the AWT test rig, as well as information on the relevant parameters for the signal post-processing are given in the appendix in Sec. A.6. The signal post-processing method itself is described in the next chapter.

For the measurements, ten microphones are equidistantly employed at one axial position in the duct segment of the sound generator. The number of sensors allows the decomposition of modes up to the order $|m = 4|$. To avoid aliasing effects, the sound field excitation is carried out well below the cut-off frequency of the mode (5,0) of about $f_{(5,0),\text{cut}} \approx 1425$ Hz. Beginning at $f_{\text{exc}} = 400$ Hz, the frequency is steadily increased in intervals of 5 Hz up to $f_{\text{exc}} = 1200$ Hz. Within this frequency range, six modes are found to be cut-on. The respective cut-off frequencies are summarized in Tab. 4.1.

The results of the specific excitation of the acoustic modes of circumferential order $m = 1$ and $m = 2$ are presented in Fig. 4.3 and Fig. 4.4, respectively. Both modes are later used to experimentally test the hypothesis that the axial angle of the group velocity vector can be used to establish similarity of modal sound propagation. In order to compare the achieved pressure amplitudes of the intended modes with the amplitudes of the unintentionally excited modes, the respective values of the modes up to the order $m = 4$ are given. For the different modes, different colors are used. Here and also below, the colors purple and orange are used to mark the mode of order $m = 1$ and $m = 2$, respectively. The excitation targets a spin of the sound field in (mathematical) negative direction. The solid and dotted lines of the same color represent modes of the same order but spinning in a mathematically negative and positive direction, respectively. The efficiency of the excitation is evaluated by analyzing the dominance and stability of the sound pressure level of the intended mode. In the diagrams, the modal pressure amplitude is depicted in dB over the excitation frequency. Note that the sound pressure levels achieved work by way of example. Among other things, the overall pressure level depends on the inlet voltage of the excitation units, which is set here lower than for the measurements in the LPT. Tests with varying input voltages (not given here) have

Table 4.1: Calculated cut-off frequencies f_{cut} for the test measurements in the AWT. The given frequencies are restricted to the modes which are cut-on in the given range of excited frequencies from $f_{\text{exc}} = 400$ Hz to $f_{\text{exc}} = 1200$ Hz.

	$m = 0$	$m = 1$	$m = 2$	$m = 3$	$m = 4$
$n = 0$	0 Hz	≈ 407 Hz	≈ 675 Hz	≈ 930 Hz	≈ 1177 Hz
$n = 1$	≈ 850 Hz	≈ 1175 Hz	n.a.	n.a.	n.a.

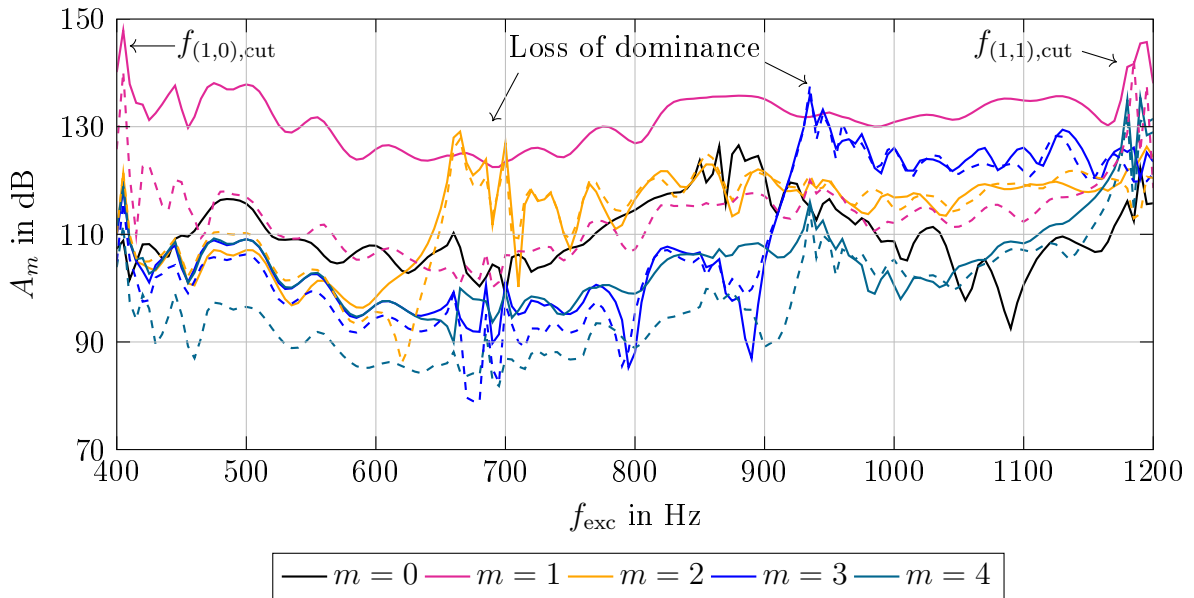


Figure 4.3: Synthetic sound field excitation of the mode $m = 1$ in the AWT. The solid and dashed lines represent a spin in (mathematical) positive and negative direction, respectively.

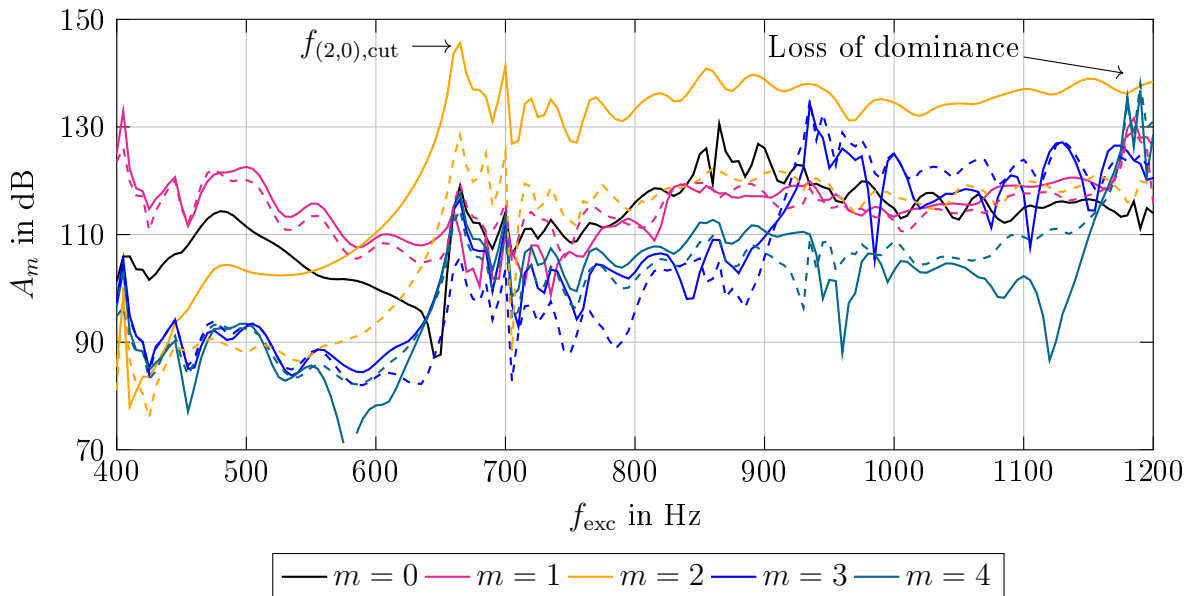


Figure 4.4: Synthetic sound field excitation of the mode $m = 2$ in the AWT. The solid and dashed lines represent a spin in (mathematical) positive and negative direction, respectively.

4.3 Cut-off Analysis

shown no other results than expected.

To begin with, both test cases show that within the frequency range considered, the intended mode is indeed, with few exceptions, dominant in the spinning direction as well as in the mode order. It is found that the dominance is in some instances lost around the cut-off frequencies of the other modes. At these frequencies, the amplitude of the respective modes partly exceeds the amplitude of the intended mode. The absolute amplitude of the excited mode, however, seems unaffected by the change in the cut-off condition of the other modes since an impact on the sound pressure level, such as a sharp decrease or increase of the amplitude, is not observed.

Generally, it can be observed that the amplitude of the intended mode is highest at its cut-off-condition. For the excitation of mode $m = 1$ peaks are found at $f_{(1,0),\text{cut}} \approx 407$ Hz and around $f_{(1,1),\text{cut}} \approx 1175$ Hz. In line with this observation, the maximum sound pressure level for the mode $m = 2$ is measured around $f_{(2,0),\text{cut}} \approx 675$ Hz.

In summary, the test measurements in the AWT confirm that the excitation methods chosen permit (dominant) excitation of sound fields of specific circumferential mode order, as well as control of the direction of spinning. Furthermore, the results show that at cut-off condition, distinct peaks in the amplitude of the respective modes are to be expected. Due to the extreme rise of the sound pressure level and the high pressure gradients detected, it is concluded that measurement data collected at cut-off conditions should not be used for the experimental validation.

4.3 Cut-off Analysis

Acoustic modes which are cut-on in the measurement planes, but cannot be resolved with the given microphone array, might impair measurement results. Therefore, a cut-off analysis is carried out to identify a frequency range for the experimental validation where an accurate resolution of the full sound field is possible. For this purpose, the modal cut-off frequencies and the radial as well as the circumferential mode order are determined for the operating points under consideration .

Generally, with respect to the given microphone arrays consisting of 20 sensors employed at one axial position, two limitations with respect to the resolvable mode order apply:

(1) $m \leq |9|$

Acoustic modes with a circumferential mode order exceeding the maximum resolvable mode order of $m = |9|$ will inevitably cause an inaccurate decomposition of the sound field as aliasing effects distort the spatial DFT (cf. Sec. 5.1.3). Acoustic modes of an order higher than $m = 9$ thus might impair measurement results and are therefore limiting the range of advisable excitation frequencies.

(2) $n = 0$ for $m \geq 1$

The sensor distribution does not support a radial decomposition of the sound field.

Hence, the amplitudes of modes with $n > 0$ will interfere with the amplitude of the respective mode with a radial order $n = 0$ as a distinction between the different radial mode orders is not possible. One exception is the mode of order $m = 0$: As the validation concentrates on modes with $m \geq 1$, radial components of the circumferential mode $m = 0$ are not limiting.

The first limitation specifies the maximum resolvable circumferential mode order m . The second limitation refers to the resolvable radial mode order n . These two limitations set the general boundaries for the excitation frequencies advisable to be used for the validation measurements. Besides being specifically excited, modes violating these limitations may also be unintentionally excited by the synthetic excitation (cf. Fig. 4.3 or Fig. 4.4) or might be naturally excited in the other sections of the LPT and traveling upstream to the acoustic measurement plane Sec A (cf. Fig 4.2). To get as complete a picture as possible and to accurately determine a suitable frequency range for experimental validation, the cut-off analysis is therefore carried out for all sections where major differences in the cut-off conditions are to be expected.

The cut-off analysis is based on the approximate geometric and flow model outlined in Sec. 3.1.1. For the inlet duct (Sec A) and the measurement plane directly upstream of the first stator (MP 10), the cut-off frequency is given by Eq. (3.10). In between the blade rows and downstream of the turbine stage, a strong circumferential flow component M_θ has to be considered. The cut-off frequency for these flow conditions is calculated according to

$$f_{(m,n)\text{cut}} = \frac{c}{2\pi} \left(\beta_{(m,n)}^{(\sigma)} \sqrt{1 - M_x^2} + M_\theta \frac{m}{R} \right), \quad (4.3)$$

which is derived from the axial wave number

$$k_x^{\pm x} = \frac{-M_x(k - M_\theta \frac{m}{R}) \pm \sqrt{(k - M_\theta \frac{m}{R})^2 - (1 - M_x^2) \left(\beta_{(m,n)}^{(\sigma)} \right)^2}}{(1 - M_x^2)}. \quad (4.4)$$

This formulation of the axial wave number is taken from Kousen (1996) and is based on the approximation of a solid body swirl (cf. Bartelt (2015)). When interpreting the results of the cut-off analysis, it has to be kept in mind that the analytical models only approximate the conditions in the LPT and therefore deviations between the cut-off frequencies measured and the calculated values are to be expected. The cut-off conditions in the measurement planes Sec A to MP 31 are calculated using the aerodynamic data collected near the center of the test section or at the Euler radius as explained in the previous section. In Sec B, only acoustic instrumentation is employed. Therefore, the results of the probe measurements in MP 31 are used for the analysis in the diffuser¹. Thus, deviations in the calculated cut-off conditions from real conditions are to be expected, particularly in this section.

¹The cut-off conditions in MP 31 and Sec A then differ due to the different geometry only.

4.3 Cut-off Analysis

The calculated cut-off frequencies are depicted in the diagrams in Fig. 4.5 and Fig. 4.6 for part-load operation and design-point operation, respectively. The frequencies are plotted on the abscissa and the circumferential mode order on the ordinate. The radial mode orders are represented by different markers. For example, modes with $n = 0$ are represented by circles and modes of order $n = 1$ by squares. The BPF and its harmonics are represented by the dashed vertical lines. The solid horizontal red lines show the boundaries of the spatial circumferential resolution. The ranges of suitable excitation frequencies ultimately identified are marked grey in the diagrams.

First, it can be observed that the cut-off frequencies in Sec A and in MP 10 are the same for both directions of spinning. In contrast, for $M_\theta > 0$, the cut-off frequencies of the modes rotating in the direction of the rotor are higher than for the counter-rotating modes (MP 11, MP 31, and Sec B). Vice versa, downstream of the rotor in the measurement plane MP 12 where $M_\theta < 0$ applies, the cut-off frequencies of the modes rotating in the direction opposite to the rotor are higher than the respective counter-rotating modes. These relations result in a characteristic horizontal symmetry of the cut-off frequencies with respect to the mode of order $m = 0$ for a purely axial flow, and in a characteristic asymmetry in the presence of a circumferential flow component, as also pointed out by Bartelt (2015). Excluding the inlet duct, modes with non-zero radial order are cut-on only well above or around 2 kHz for both operating points. In Sec A however, the circular duct without a hub favors the propagation of radial sound field components, and the respective cut-off frequencies are considerably lower than in the other sections. In fact, it is found that the cut-off frequency of the mode (1,1) in this section limits the range of the excitation frequency suitable for validation². The upper boundary is then set by $f_{(1,1)\text{cut}} \approx 1288$ Hz and $f_{(1,1)\text{cut}} \approx 1320$ Hz for part-load operation and design-point operation, respectively³.

In summary, the cut-off frequencies limiting an accurate resolution of the modal sound field in the LPT are determined based on an analytical study of the modal cut-off frequencies. Possible shifts of these calculated cut-off frequencies during test rig operation are to be expected since a flow model is used for the analysis which only approximates the real flow conditions in the LPT. Hence, a safety margin should be applied. The maximum excitation frequency for both operating points is therefore reduced to $f_{\text{exc}} = 1200$ Hz compared to the calculated values given above. As a consequence of this restriction on the maximum frequency of propagating modes, the synthetic sound field excitation for the validation measurements is restricted to modes of the circumferential order $m = |3|$.

²Note that the mode of order (0,1) does not limit the range of suitable excitation frequencies as described at the beginning of this section (second limitation).

³For completeness, it shall be added that for design-point operation, the acoustic modes of order $m = |6|$ produced by rotor-stator-interaction at the BPF are cut-on throughout all sections of the LPT. However, this is not relevant here, as the blade-passing-frequency is excluded by the suitable frequency range identified.

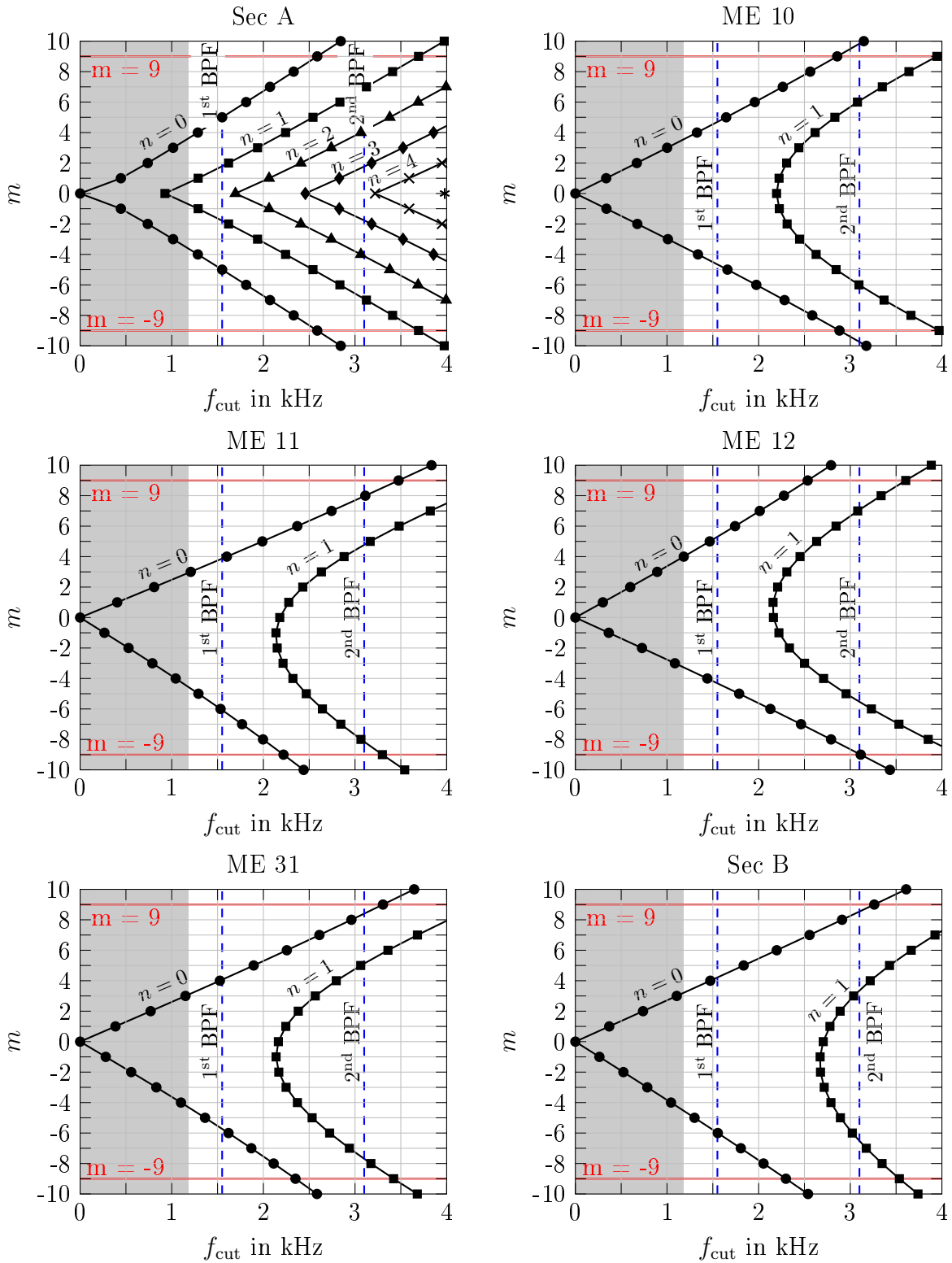


Figure 4.5: Cut-off conditions for different acoustic modes (m,n) in the measurement planes of the LPT for part-load operation. The areas marked grey give the range of suitable excitation frequencies for the validation measurements with respect to the resolvable modes.

4.3 Cut-off Analysis

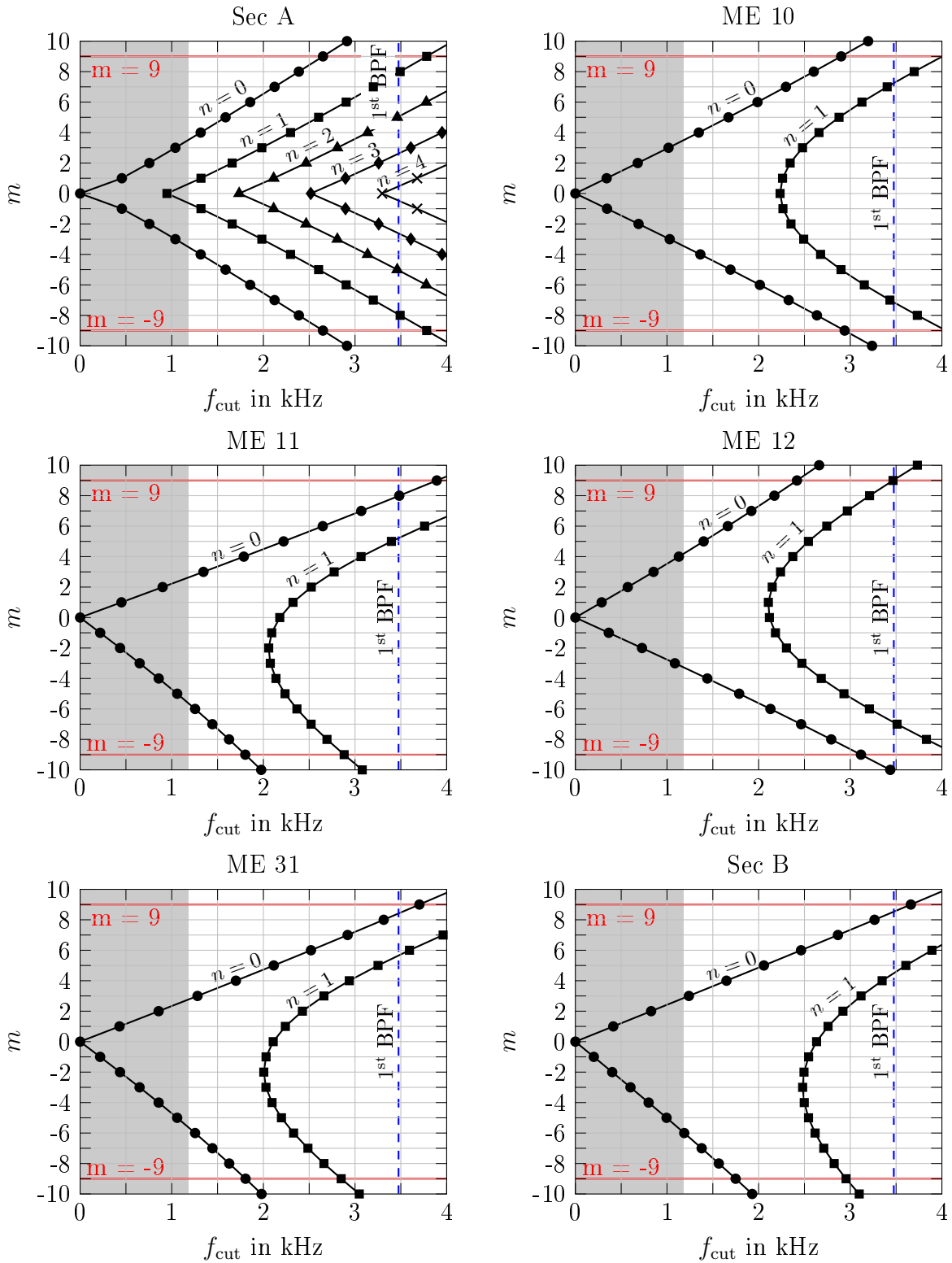


Figure 4.6: Cut-off conditions for different acoustic modes (m,n) in the measurement planes of the LPT for design-point operation. The areas marked grey give the range of suitable excitation frequencies for the validation measurements with respect to the resolvable modes.

5 Signal Processing Methods

In this work, the propagation properties of specific acoustic modes at discrete frequencies are examined. Hence, the analysis of the obtained measurement data is carried out in the frequency domain. This chapter addresses the method chosen to decompose the sound field in its modal components, and the statistical methods selected to evaluate the processed data.

In section 5.1, the modal decomposition method applied is presented and discussed. First a short introduction on different modal decomposition methods and the accompanying challenges in practical applications are given (cf. Sec. 5.1.1). Subsequently, the applied two-dimensional discrete Fourier Transform (2D-DFT) for modal decomposition is described in detail in Sec. 5.1.2. The mathematical description is based on the work of Oppenheim and Schaffer (2014), if not stated otherwise. Numerical approximation errors of the Fourier Transform inherently generated by the discretization of the collected signal are discussed in 5.1.3. The method applied is validated by means of numerically generated data sets (cf. Sec. 5.1.4).

In section 5.2 statistical methods to account for the impact of stochastic noise on the results of the measurements are discussed. The application of statistical measures necessitates a sample size exceeding one. For this purpose, the collected pressure data is segmented in individual intervals. The concept chosen for segmenting is described and the statistical measures employed are defined (cf. Sec. 5.2.1 and Sec. 5.2.2, respectively). In the third and last section of this chapter, in Sec. 5.3, undesired background noise of the measurements, mainly produced by the LPT itself, is analyzed and the impact on the results of the modal decompositions, and thus on the results of the validations, is discussed.

5.1 Spectral Analysis and Modal Decomposition

5.1.1 Decomposition methods

A modal sound field propagating in a circular duct is characterized by its circumferential and radial mode order, m and n , respectively. A sound field composed of several superposed modes (m,n) is then fully described by the modal amplitude, the modal initial phase and the axial as well as circumferential direction of propagation of each mode. To obtain these quantities, the sound pressure field has to be decomposed in its circumferential and radial components. The circumferential modal quantities can be determined by unsteady pressure sensors placed around the circumference of the specified test section. The radial decomposition of the sound field poses a greater challenge. For the determination of radial pressure distribution, the collected data are most commonly evaluated

by performing a so-called *Radial Mode Analysis* (RMA). This technique is based on an analytical or numerical solution of the linear set of equations according to Eq. (3.13), which describe in-duct sound propagation. Two setups for data collection for the RMA are state-of-the-art: (1) implementation of fixed or traversable radial microphone rakes in the respective duct section (as applied e.g. by Holste et al. (1997) and Enghardt et al. (2001) as two of the first ones), or (2) implementation of a specifically designed array of axially and circumferentially distributed sensors mounted flush with the casing wall as proposed by Enghardt et al. (1999) and applied for example by Tapken et al. (2009) and Enghardt et al. (2009). The first setup permits the direct measurement of radial pressure distribution. However, as pointed out by Enghardt et al. (1999), the application of radial rakes inherently alters the aerodynamic and acoustic field in the test section due to wake effects introduced by the probes. On the other hand, the second approach is based on a theoretical model of the propagating sound field and the achievable accuracy is therefore limited by the actual flow conditions in the machine respective the applied acoustic model. In the end, both methods have advantages and disadvantages and the application has to be decided on case by case. For the low pressure turbine test rig considered here, Laguna (2016) applied the RMA using microphones wall-flushed mounted on a circumferentially traversable measurement unit integrated in the annular flow path of the test rig.

Here, with the given measurement setup of only one circumferential microphone ring in Sec A and Sec B, the investigation concentrates on the analysis of the circumferential components of the propagating sound field¹. A differentiation between the modes traveling upstream and downstream is excluded by the setup. The sound pressure field is resolved in its spectral circumferential components by applying a *two-dimensional discrete Fourier Transform* to the collected data. This two-step spectral analysis involves a discrete Fourier Transform with respect to time and space, taking advantage of the time and space harmonic propagation of the acoustic modes. This procedure, which requires an equidistant circumferentially distribution of the sensors, is commonly also applied in the before mentioned radial decomposition.

Completeness demands that it should be mentioned that several approaches using cross-correlation methods to resolve the modal field exist. Sijtsma and Zillmann (2007) give an overview of correlation methods and compare the different techniques with respect to their performance in the presence of background noise for far-field and near-field measurements. Furthermore, Bartelt (2015) proposed a modal decomposition method, which is based on a spatial Fourier Transform of the bandpass-filtered sensor signals. Performing the Fourier Transform in the circumferential direction for each discrete time-step, Bartelt (2015) subsequently used the Hilbert Transform and the Single Value Decomposition to determine the modal spinning directions, the modal amplitudes, and the modal phases.

¹Note, if not stated otherwise, hereinafter the terms *modal decomposition*, *modal amplitudes*, and *modal phases* always refer to the evaluation of the circumferential modal components of the considered sound pressure field.

5.1.2 Two-dimensional discrete Fourier Transform

The Fourier Transform is a powerful and established mathematical tool to decompose an arbitrary periodic or aperiodic continuous signal into its (spectral) harmonic components. Handling measurement data, the signal is not continuous but discrete and finite in length. The corresponding Fourier Transform is referred to as the discrete Fourier Transform. Considering now a continuous and N -periodic signal $x = f(\eta)$ being sampled at regular intervals for a specific period of time, then $x_n := (x_0, x_1, \dots, x_{N-1})$ represents the respective sequence of N data points. Assuming the sequence is N -periodic ($x_n = x_{n+N}$), the corresponding DFT of the sequence x_n is generally written as

$$\underline{X}_k = \sum_{n=0}^{N-1} x_n e^{-i2\pi \frac{kn}{N}} \quad \text{for } k = 0, 1, 2, \dots, N-1. \quad (5.1)$$

The transformation according to Eq. (5.1) is referred to as the *forward* DFT, whereas

$$x_n = \frac{1}{N} \sum_{k=0}^{N-1} \underline{X}_k e^{i2\pi \frac{kn}{N}} \quad \text{for } n = 0, 1, 2, \dots, N-1 \quad (5.2)$$

gives the *inverse* DFT (cf. Oppenheim and Schaffer (2014)).

The output (sequence) \underline{X}_k , the forward DFT, represents the complex-valued, evenly spaced spectrum of the sequence x_n . In accordance with the input sequence, the DFT itself is finite and of the length N . The integer k corresponds to the k^{th} -spectral component. The (normalized) angular DFT frequencies are defined over an interval of the length 2π with an equal spacing of $2\pi/N$. In most cases, the signal x is a function of time or space and \underline{X}_k gives the frequencies in $\text{s}^{-1} = \text{Hz}$ or m^{-1} , respectively. The underline ($\underline{\cdot}$) indicates the complex nature of the output sequence. With $\underline{X}_k = X_k e^{i\angle X_k}$, the magnitude and phase are given for each spectral component.

In the inlet and the diffuser of the LPT, the unsteady (sound) pressure p' is measured simultaneously by J microphones equally distributed around the circumference of the test rig's casing. The data is thereby collected with the sampling frequency f_s . Thus, the pressure signal detected by each microphone is sampled at regular intervals of time and space resulting in J discrete-time signals $p'_{n,j}$ for each measurement plane. The integer j specifies both the considered microphone and the respective circumferential position of the equidistantly-spaced sensors. The integer n denotes the discretized measurement time respective time step. Hence, the discrete signal $p'_{n,j}$ is a two-dimensional sequence of time and space. To determine the properties of the propagating sound field, two discrete Fourier Transforms are subsequently performed with respect to these variables. At first, a temporal DFT and afterwards a spatial DFT is performed. Both Fourier Transforms are consecutively described below. An overview on the different steps of the modal decomposition method applied here is given in Fig. 5.1. In the illustration the input and output sequences of the Fourier Transforms are expressed as matrices.

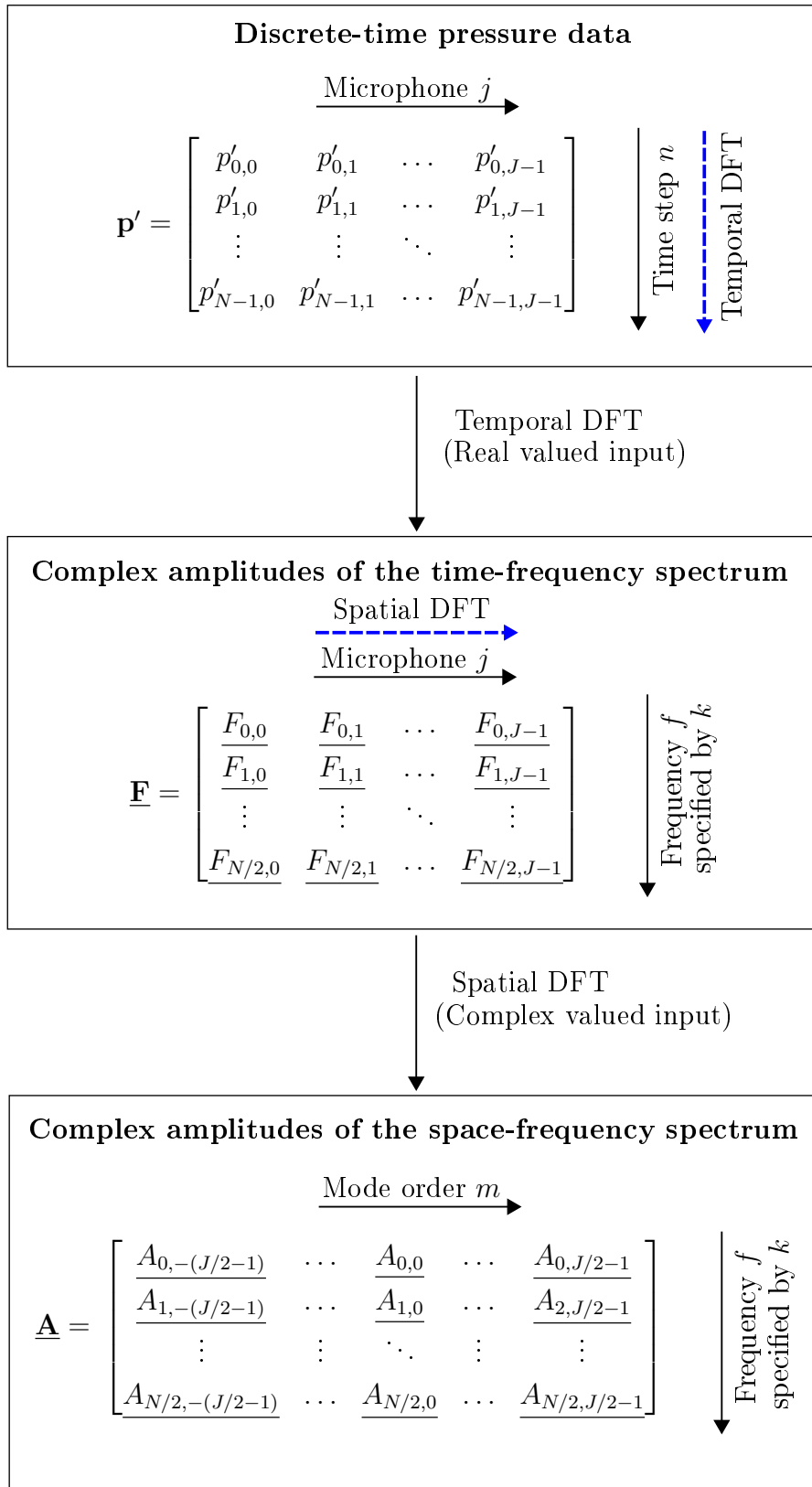


Figure 5.1: Concept of the 2D-DFT modal decomposition method for J equally-spaced circumferential measurement positions / microphones and N data points / time steps.

5.1 Spectral Analysis and Modal Decomposition

Temporal DFT

First, the temporal DFT $\underline{F}_{k,j}$ of the pressure data sampled by each microphone j is determined. Applying Eq. (5.1) to the discrete-time signal $p'_{n,j}$ of length N , where N is assumed to be an even number², the DFT

$$\underline{F}_{k,j} = \sum_{n=0}^{N-1} p'_{n,j} e^{-i2\pi f_k^* n} \quad \text{for } k = 0, \pm 1, \pm 2, \dots, \pm N/2 - 1, -N/2 \quad (5.3)$$

provides the complex temporal-frequency spectra of the sampled real-valued pressure data p' . The DFT $\underline{F}_{k,j}$ thus represents the complex-valued amplitude in the time frequency domain. This procedure is illustrated in the first half of Fig. 5.1. In Eq. (5.3) the parameter f_k^* denotes the discrete *time-domain frequency* of the spectral component k given by the relation

$$f_k^* = \frac{k}{N}. \quad (5.4)$$

The frequency is normalized by the number of data points N . The continuous-time frequency f_k and the discrete frequency f_k^* are related by

$$f_k = f_k^* f_s, \quad (5.5)$$

where f_s is the sampling frequency in data points per second (cf. Oppenheim and Schaffer (2014)). The continuous data are sampled over a finite period of time T , where T corresponds to the time of measurement. Thus, f_k can be interpreted as the k^{th} -harmonic of the fundamental frequency $1/T$ with a frequency resolution of

$$\Delta f = \frac{1}{T}. \quad (5.6)$$

With $|N/2|$ being the maximum value for k , the highest resolvable continuous-time frequency equals half the sampling frequency and therefore just the frequency given by the Nyquist-Shannon sampling theorem. According to Oppenheim and Schaffer (2014), this frequency is commonly referred to as the *Nyquist frequency*.

In Eq. (5.3), the integer k is chosen to take on positive as well as negative values. This is contrary to the general formulation according to Eq. (5.1), where the integer k is limited to real values. As a result of the definition of k in Eq. (5.3), the frequencies f_k^* and f_k are positive-valued as well as negative-valued. As far as the mathematical side is concerned, changing the definition of k is valid as it does not alter the result of the transformation. As mentioned before, the normalized angular frequencies range over an (arbitrary) interval of the length 2π . With the input sequence being periodic (or assumed to be periodic), the DFT is also periodic ($\underline{X}_k = \underline{X}_{k+N}$), and the analysis of the interval $[0, 2\pi[$ therefore yields the same result as analyzing the interval $[-\pi, +\pi[$ (cf. Oppenheim and Schaffer (2014)). Based on this observation, a second important property of the Fourier Transform becomes relevant for the current application, namely the symmetry

²In case of an odd number of N , k runs from zero to $\pm(N-1)/2$.

property of the DFT. For a real-valued input sequence, the DFT is conjugate-symmetric and $\underline{X}_{N-k} = \underline{X}_k^*$ holds true, where $(\cdot)^*$ denotes the complex conjugation. Thus, the frequency spectrum is paired and the temporal DFT for $[0, \pi]$ also specifies the interval $[-\pi, 0]$ (cf. Oppenheim and Schaffer (2014)).

The discrete time-signal $p'_{n,j}$ is real-valued. Hence, for the temporal DFT $\underline{F}_{k,j}$ of the pressure data $p'_{n,j}$, non-redundant information are therefore only obtained for half of the spectrum. Considering this symmetry, the integer k in Eq. (5.3) is reduced to $k = 0, 1, 2, \dots, N/2 - 1, N/2$ for the subsequent processing. This results in $N/2 + 1$ complex amplitudes of the time-frequency spectra $\underline{F}_{k,j}$, which are determined for each microphone j (cf. second matrix of Fig. 5.1).

Spatial DFT

So far, for each circumferential position $j = 0, 1, \dots, J-1$, the unsteady pressure data has been analyzed with respect to the spectral components in the time-frequency domain. To obtain information on the modal quantities of the pressure field (mode order, modal amplitudes, and modal phases), the complex temporal DFT $\underline{F}_{k,j}$ are used as the input sequence for a spatial Fourier Transform:

$$\underline{A}_{k,m} = \sum_{j=0}^{J-1} \underline{F}_{k,j} e^{-ik_m^* j} \quad \text{for } m = 0, \pm 1, \pm 2, \dots, \pm J/2 - 1, -J/2 \quad (5.7)$$

with

$$k_m^* = m \frac{2\pi}{J}. \quad (5.8)$$

The DFT $\underline{A}_{k,m}$ gives the spatial frequency spectrum, where the integer k specifies the frequency \underline{f}_k^* . The integer m is defined here - with respect to the given microphone arrays - according to an even number of inputs J . The latter thereby denotes the implemented number of sensors. The normalized discrete *spatial frequency* k_m^* in the exponent of Eq. (5.7) is then equivalent to the (normalized) circumferential wave number of the searched for circumferential mode order. Interpreting $J/(2\pi R)$ as the spatial sampling frequency in measurement positions per meter, the continuous circumferential wave number is given by

$$k_m = \frac{k_m^* J}{2\pi R}, \quad (5.9)$$

where R is the radius of the circumferential microphone array, here equivalent to the outer duct radius of the respective test section (turbine inlet or diffuser). Inserting Eq. (5.8) in Eq. (5.9) yields

$$k_m = m \frac{2\pi}{J} \frac{J}{2\pi R} = \frac{m}{R}. \quad (5.10)$$

Comparing the equation above with the familiar relation between the circumferential modal wave number and the mode order according to Eq. (3.12), it becomes apparent that the integer m of the output sequence of the spatial DFT corresponds to the circumferential mode order and k_m indeed to the circumferential modal wave number k_θ as stated before.

5.1 Spectral Analysis and Modal Decomposition

The input sequence $\underline{F}_{k,j}$ to the spatial Fourier Transform is complex-valued, and thus the spectrum of the spatial DFT $A_{k,m}$ is no longer paired as is the case for the temporal DFT. As a result, the symmetry-property does not hold and the spectrum contains only non-redundant information (cf. lower part of Fig. 5.1). Analogous to the integer k , the integer m is chosen to take positive and negative values. Thus, not only the mode order but also the spinning direction are given directly. One half of the spectrum represents the acoustic modes spinning against the direction of the circumferential sensor placement, the other half represents the modes spinning in the direction of the sensor placement.³ Eventually, the amplitude A_m and the phase φ_m for each modal component of the pressure field can be obtained from the complex spatial DFT $\underline{A}_{k,m}$ at every (temporal) frequency f_k^* .

The highest mode order which can be resolved, the *Nyquist mode*, depends on the number of microphones J instrumented in the test section. Both, the circumferential microphone array in the inlet and the array in the diffuser of the LPT consist of 20 microphones each. Thus, the maximum mode order resolvable is $m = \pm 9$ which corresponds to $J/2 - 1$. Accordingly $J - 1$ complex amplitudes of the spatial frequency spectra are determined (cf. third matrix in Fig. 5.1)⁴.

Note: During the measurement campaign, two sensors in the diffuser were found to be defective. Because of restricted access to this section of the test rig, exchanging the microphones was not possible. Furthermore, at two positions in Sec A, located next to the welding seam of the circular duct, the sound pressure measurements are altered by this geometric feature. The incorrect time measurement data may falsify the results of the 2D-DFT modal decomposition method, and therefore need to be corrected. This is done by interpolating the respective data in the time-frequency domain using the data collected at the non-affected sensor positions in the respective measurement plane. The interpolation is thus carried out subsequent to the first step of the 2D-DFT.

5.1.3 Approximation errors

The input signal to the temporal as well as the spatial Fourier Transform is discrete and finite in length. Consequently, the same holds true for the sets of the respective DFT-frequencies, which are finite and limited to plus/minus the Nyquist frequency/mode. Thus, the DFT only approximates the sampled continuous signal. Commonly known, the main types of errors which occur due to the discretization are *aliasing* and *spectral leakage*. To what extent these errors are accounted for in the implemented algorithm used for the modal decomposition, is discussed below.

³The proper assignment of the mode order to the respective circumferential spinning direction depends on the chronological order of the input sequence.

⁴If the number of inputs is odd, the (temporal or spatial) frequency vector is symmetric relative to zero. Thus, a corresponding negative frequency exists for every positive frequency and vice versa. In case of real-valued inputs, this property is trivial as one half of the spectrum is redundant, anyway. However, in case of complex-valued inputs, an even number of inputs, as is the case here, results in a non-symmetric frequency vector, and the highest frequency possible to resolve for both signs is reduced by one compared with the absolute value of the overall highest resolvable frequency.

Aliasing

The effect of *aliasing* occurs if frequencies in the continuous-time signal that are higher than the Nyquist frequency exist. These non-resolvable frequencies will then alter the lower frequencies in the spectrum in amplitude and phase. Generally, to minimize the effect of aliasing, the temporal-sampling frequency should be at least twice the highest frequency in the signal. As the synthetic sound field generation is carried out at low frequencies to avoid modes with a radial order of $n > 0$ propagating in the measurement section (cf. Sec. 4.3), the highest frequencies with significant amplitudes can be expected at the BPF or multiples of the BPF. The chosen sampling frequency of $f_S = 2^{16}$ Hz is about 18 times the blade-passing-frequency at design-point operation, and thus adequately high to avoid distortions in the time-frequency domain.

Aliasing may also occur in the space-frequency domain and alter the amplitudes and phases of the determined modes. Analogous to the time domain, the effect can be minimized by sampling at spatial intervals smaller than half the (circumferential) wavelength of the mode of highest circumferential order that is able to propagate in the test section. In other words, with the given measurement setup of 20 sensors distributed around the circumference, the existence of circumferential modes of an order higher than $m = |9|$ in the test section will distort the spatial DFT. Based on an analytical approach, a cut-off analysis has been carried out for the different operating points confirming the absence of naturally excited modes of higher order than the given Nyquist mode at the frequencies regarded. Furthermore, the order of the intentionally excited modes is limited to $m = |4|$ so that distortion effects in the spatial DFT are not to be expected. The results of this cut-off analysis are presented in Sec. 4.3.

Spectral leakage

In practical applications, signals are often sampled over a non-integer number of periods. This is unavoidable, for example, if several frequencies exist in the signal that are not multiples of one another, if the frequencies and thus the periodicities in the signal are unknown, and if the signal contains stochastic components. Sampling at non-integer numbers of the harmonic period generally might lead to that

- (1) continuous-frequency components in the signal are not represented by a respective DFT-frequency.
- (2) a discontinuity between the first and the last data point of the input sequence arises.

Both consequences result in *spectral leakage*. If there are frequencies in the original signal that do not match a DFT-frequency as outlined in (1), components of the non-represented frequencies spread over (or leak into) adjacent frequencies, resulting in a smeared spectrum. This effect cannot be completely avoided and has to be taken into account when analyzing frequencies which are in the immediate vicinity of dominant non-DFT frequencies.

The discontinuity in the input sequence addressed in (2) leads to high frequencies in the DFT-spectrum that were originally not present in the continuous signal. Furthermore,

5.1 Spectral Analysis and Modal Decomposition

these frequencies might induce aliasing if they exceed the Nyquist frequency, or induce spectral leakage if they do not match the DFT-frequencies. To mitigate the effect of these artificial frequencies, the *Hanning-function* given by

$$w_n = 0.5 \left(1 - \cos \left(2\pi \frac{n}{N-1} \right) \right) \quad \text{for } n = 0, 2, 3, \dots, N-1 \quad (5.11)$$

is used here as a window function with the objective of smoothing the discontinuity in the sequence (cf. Oppenheim and Schaffer (2014)). The function is applied to the discrete-time signal $p'_{n,j}$ prior to the computation of the temporal DFT.

Due to the periodic pressure pattern of modal sound fields, a circumferential periodic pressure distribution at the deliberately excited frequencies is assumed. Therefore, applying a window function to the input sequence $\underline{F}_{k,j}$ of the spatial Fourier Transform is not necessary.

In summary, the impact of aliasing on the temporal as well as spatial DFT can be assumed to be negligible due to the high sampling frequency in the time domain and sufficient spatial distribution of sensors, respectively. Spectral leakage is avoided by applying a window function. In conclusion, high quality data may be expected.

5.1.4 Validation of the 2D-DFT

The previously described two-dimensional DFT modal decomposition method is validated using numerically generated data sets. Using Eq. (3.4), which describes sound propagation in a hard-walled duct, the time-pressure data of different specific modal sound fields are calculated at 20 equally-spaced circumferential positions in accordance with the measurement setup in the LPT ($J = 20$). The data sets are generated at a time step of $\Delta t = 1/2^{16}$ s, thus reflecting the sampling frequency of the measurements of $f_S = 2^{16}$ Hz. The radius R in Eq. (3.4) is set equal to the respective circular inlet duct of $R = 0.248$ m. No flow is assumed ($M_x = M_\theta = 0$). The data sets generated are analyzed in the time-frequency and space-frequency domain, and the quantities determined are compared with the results of a theoretical analysis and with the exact solutions given by Eq. (3.4).

Three different test cases are considered:

- (1) a mode of order one spinning in clockwise direction ($m = +1$) with the modal amplitude A_1 and modal phase φ_1 ,
- (2) a corresponding mode spinning in counter-clockwise direction ($m = -1$) with the modal amplitude A_2 and modal phase φ_2 , and
- (3) a circumferential standing mode composed of both modes according to (1) and (2) with a modal amplitude relation of $\epsilon = \frac{A_1}{A_2} = 1$ as defined in Sec. 3.1.1.

For all test cases, the radial mode order is set to zero ($n = 0$). To study the accuracy of the determination of the modal phases, different phase shifts $\Delta\varphi$ with respect to the

phase calculated for test case (1) are considered. The modal amplitude of each mode is set to match

$$A_1 = A_2 = J_m(u_{(m,n)}). \quad (5.12)$$

The expected amplitude of the spatial DFT $A_{k,m}$ is thus given by Eq. (5.12) for all test cases. For the test cases $m = \pm 1$, Eq. (5.12) yields $A_{k,(1)} = A_{k,(-1)} = F_{k,j} = 0.5819$.

In the polar graphs on the left side of Fig. 5.2, the vectors of the calculated temporal DFT $F_{k=k_{\text{exc}},j}$ are depicted in the complex plane. In line with the given number of circumferential positions, 20 vectors are shown. The gradual change in color of the vectors allows a visual identification of the different direction of spinning between test case (1) and test case (2). The vectors of the spatial DFT $A_{k=k_{\text{exc}},m=m_{\text{exc}}}$ are displayed in the polar graphs in the middle of the figure. As mentioned previously, the modal phase of the spinning mode considered in test case (1) serves as reference for the other test cases. The respective vector (marked in grey) is therefore also depicted in the spatial polar graphs of test case (2) and (3). The analysis is completed by the absolute amplitude and phase characteristic of the temporal DFT shown in the diagrams on the right side of the figure. In these diagrams, the modal amplitudes and the modal phases for each vector of the temporal DFT are given. The sensors are equally distributed in circumferential direction. In the diagrams, the correct sequence with respect to the spatial position is considered, which is indicated by the connection of the points. The diagrams thus show the characteristic of the quantities considered in circumferential direction. In order to stress the periodicity of the circumferential mode propagation, the last sensor (here $j = 20$) corresponds to the first sensor (here $j = 0$).

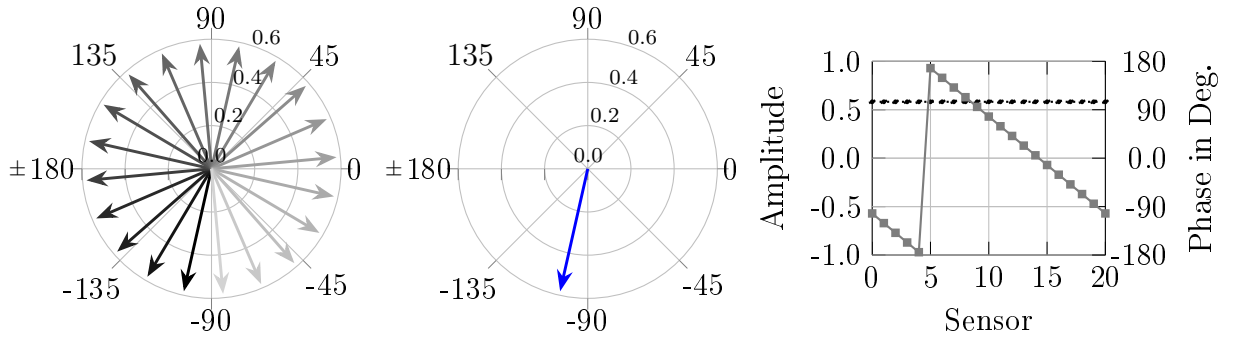
First a theoretical investigation of the expected results is carried out in order to verify the results of the 2D-DFT for the test cases depicted in Fig. 5.2. For the phase and amplitude characteristic of a pure spinning mode ($\epsilon = 0$) in the time domain, the following relations can be derived:

- (1) The temporal phase difference between two signals detected at adjacent circumferential positions has to follow $\frac{2\pi}{mJ}$, with J denoting the considered number of equally distributed measurement positions. The sign of the phase difference thereby determines the direction of spinning.
- (2) Due to the rotation of the sound field, the temporal amplitude is identical between all signals and for all positions and corresponds to the modal amplitude. Hence, in case of a spinning mode, Eq. (5.12) also gives the maximum temporal amplitude ($F_{k,j} = A_{k,m}$) at any arbitrary circumferential position.

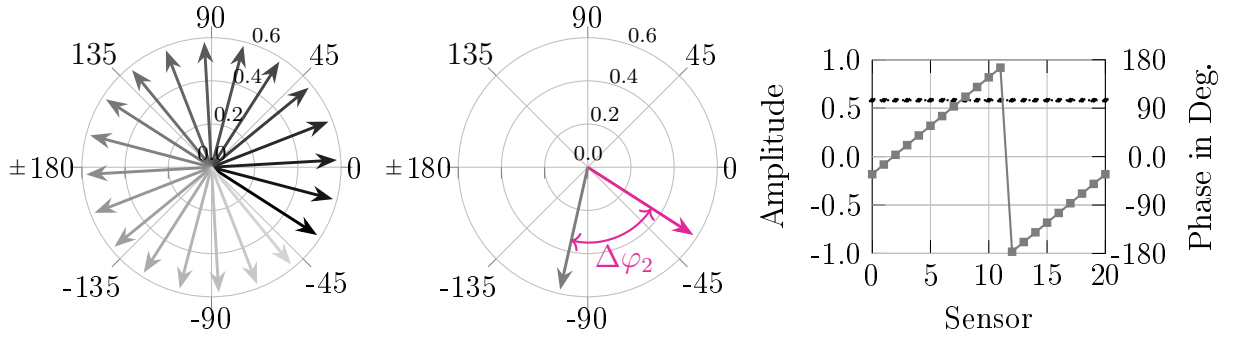
The respective quantities for a standing modal sound field can be studied in the form of two superposed sinusoidal waves of the same frequency and amplitude, propagating in opposite directions. As is well known, the latter results in a standing wave. The maximum temporal amplitude is no longer independent of the position, but a function of space, and the phase difference between two arbitrary positions is either zero or $\pm 180^\circ$.

5.1 Spectral Analysis and Modal Decomposition

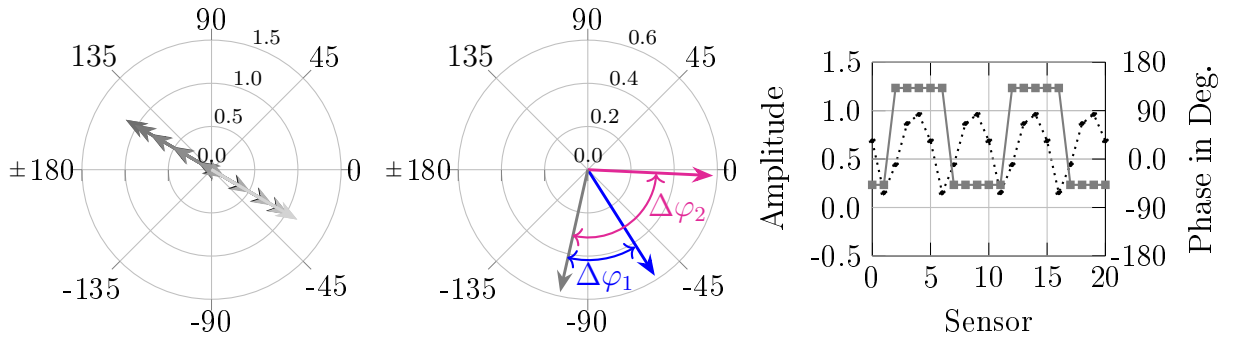
(1) Spinning mode of order $m = 1$ ($A_1 = 0.58, A_2 = 0, \Delta\varphi_1 = 0, \epsilon = 0$):



(2) Counter-spinning mode of order $m = -1$ ($A_1 = 0, A_2 = 0.58, \Delta\varphi_2 = 70^\circ, \epsilon = 0$):



(3) Standing mode of order $m = |1|$ ($A_1 = A_2 = 0.58, \Delta\varphi_1 = 45^\circ, \Delta\varphi_2 = 100^\circ, \epsilon = 1$):



Sensor in circumferential direction

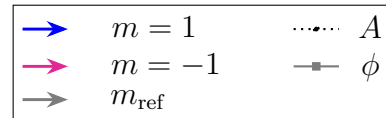


Figure 5.2: Validation of the 2D-DFT using numerically generated test cases considering the mode $m = |1|$ and 20 sensors equally distributed in circumferential direction. Left: Complex vectors of the temporal DFT $F_{k,j}$. Center: Complex vector(s) of the spatial DFT $A_{k,m}$. Right: Temporal amplitude and phase characteristic.

Figure 5.2 shows that, both the clockwise-spinning mode and the counter-clockwise spinning mode are characterized by an even distribution of the vectors of the temporal DFT. The phase difference between two adjacent circumferential positions is constant and equals 18° , thus following the relation $\frac{2\pi}{mJ}$. For the mode with the order $m = 1$, the phase gradient is negative, describing a clockwise rotation of the sound field. Correspondingly, the sound field of the second test case ($m = -1$) is characterized by a positive phase gradient that identifies the counter-clockwise direction of spinning. For both test cases, the vectors of the temporal DFT are all of identical length. Thus, the temporal amplitude is the same for every position. Furthermore, the temporal amplitude matches the calculated spatial amplitude as stated above. Comparing the amplitudes with the exact solution given by Eq. (5.12), it is found that the amplitudes are determined correctly up to the fourth decimal place by the modal decomposition method. The small variations are due to the time step chosen and the considered number of circumferential positions, as these define the spatial resolution. In addition, the assumed phase shift of $\Delta\varphi_2 = 70^\circ$ between the modes considered in test case (1) and (2) is found to be accurately reproduced.

According to the theoretical consideration of standing modes carried out beforehand, the vectors of the temporal DFTs calculated for test case (3) vary in length; correspondingly, the amplitude varies relative to the circumferential position. The phase difference between two positions is either zero or $\pm 180^\circ$ as claimed. Furthermore, the modal amplitudes match the calculated results according to Eq. (5.12), and the modal phase differences match the preset values of $\Delta\varphi_1 = 45^\circ$ and $\Delta\varphi_2 = 100^\circ$.

Thus, for all three test cases, analysis of the temporal and spatial DFTs yields the expected results. Similar investigations for the mode of order $m = |2|$ are given in the appendix in Sec. A.7 for confirmation. The analysis here concentrates on the validation of the method for the special case of a pure spinning acoustic mode with $\epsilon = 0$, and for the case of a pure circumferential standing mode with $\epsilon = 1$. Validation of the algorithm has also been systematically performed for sound fields composed of multiple modes of different order. For this purpose, the number of superposed modes, the modal amplitudes, and the modal phases have been varied. The respective values determined from the spatial DFT were always found to match the exact solution highly precisely.

In conclusion, the 2D-DFT reliably evaluates the modal quantities and is therefore found suitable for signal processing in this work.

5.2 Statistical Analysis

5.2.1 Overlapped-segmented DFT

In the first step of post-processing, prior to the calculation of the DFTs, each sampled pressure signal is divided into data segments (time intervals) of equal length as illustrated in Fig. 5.3. This procedure of segmenting in the time domain is carried out in order to

5.2 Statistical Analysis

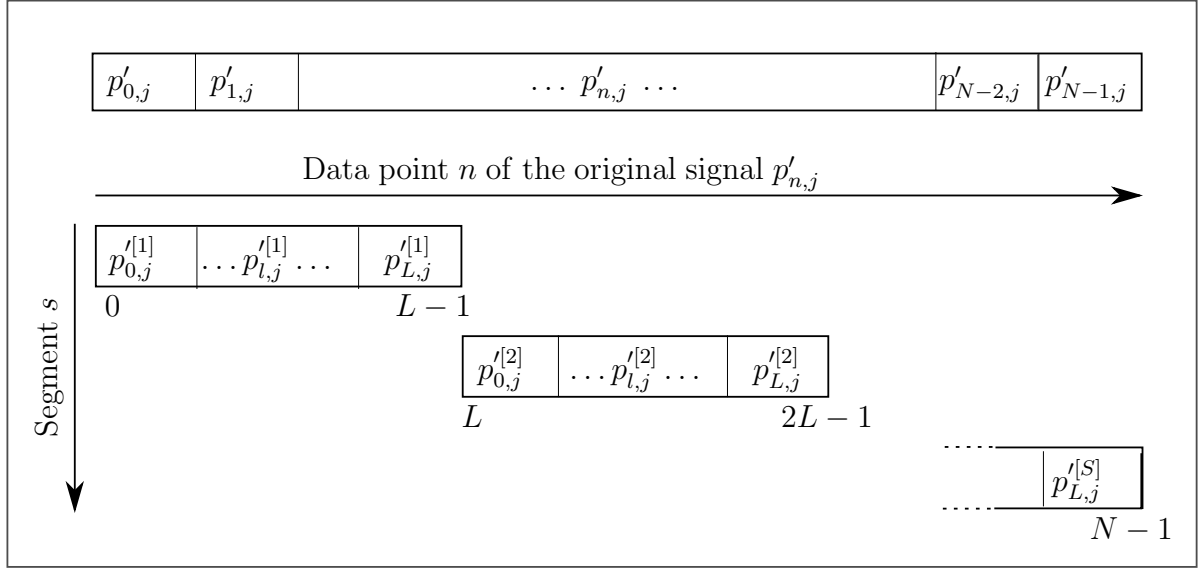


Figure 5.3: Concept of segmenting of the discrete-time signal $p'_{n,j}$ of length N sampled at the circumferential position j .

statistically evaluate the calculated modal quantities⁵. The following description of the overlapped-segmented DFT carried out here is based on the work of Oppenheim and Schaffer (2014)

Different concepts for segmenting exist. In the simplest form, the original sequence of length N is divided into S segments as shown in Fig. 5.3. With L denoting the length of each segment, then $S = N/L$ gives the number of segments obtained. In this case, each data point is uniquely assigned to one segment, and there is no overlap between segments. Alternatively, segments can be allowed to overlap in such a way that the same data points are assigned to two adjacent segments. The reason for this is as follows: As explained in Sec. 5.1.2, a Hanning-window is applied to the time data sequence prior to the calculation of the DFT. According to Eq. (5.11) the Hanning-window tapers off the amplitudes of the collected data to zero towards each end of the data sequence. Now, as the window is applied to each segment, a large part of the data would not be used if the segments do not overlap as also pointed out by Oppenheim and Schaffer (2014). Overlapping thus helps maximizing the information extracted from the data sequence. The concept of overlapping is carried out here as illustrated in Fig. 5.4.

The original pressure sequence $p'_{n,j}$ collected by the microphone j is divided into S segments according to

$$p'_{l,j}^{[s]} = p'_{(s-1)L+l,j} \quad \text{for } l = 0, 1, 2, \dots, L-1 \text{ and } s = 1, 2, \dots, S, \quad (5.13)$$

where the integer s , written as a superscript $(.)^{[s]}$, denotes the respective segment. The equation above gives a general description where the parameter R denotes the number

⁵Literature on this topic can be found under the search terms *Time-dependent Fourier Transform* or *Short-time Fourier Transform*.

of data points between the starting points of two adjacent segments. For the parameter R , the length L of each segment, and the length N of the original data sequence, generally the condition $R \leq L \leq N$ holds. In this work specifically, the segments are set to overlap by one half of their length, here, $R = L/2$, as suggested by Oppenheim and Schaffer (2014). In this case, all data points are assigned to two segments, so that no information is lost by windowing⁶.

The drawback of segmenting is a drop in frequency resolution, which inevitably goes along with spectral leakage (cf. Sec. 5.1.3). As a consequence, the choice of the segment length L becomes a trade-off between the achievable frequency resolution $\Delta f^{[s]}$ and the number of segments S available for statistical processing.

In this work, the length of each segment is set to $L = 6552$, which corresponds to a measurement time of approximating 0.1 seconds with respect to the the sampling frequency $f_S = 2^{16}$ Hz specified. Thus, the frequency resolution takes on the value of $\Delta f^{[s]} = f_S/L = 10.0024$ Hz, and only approximates an integer value. The modal sound fields are excited at integer frequencies. Thus, the (temporal) DFT frequencies of the

⁶Excluding the first data points in the interval $[0, R]$ and the last data points in the interval $[N - R, N]$ of the original sequence.

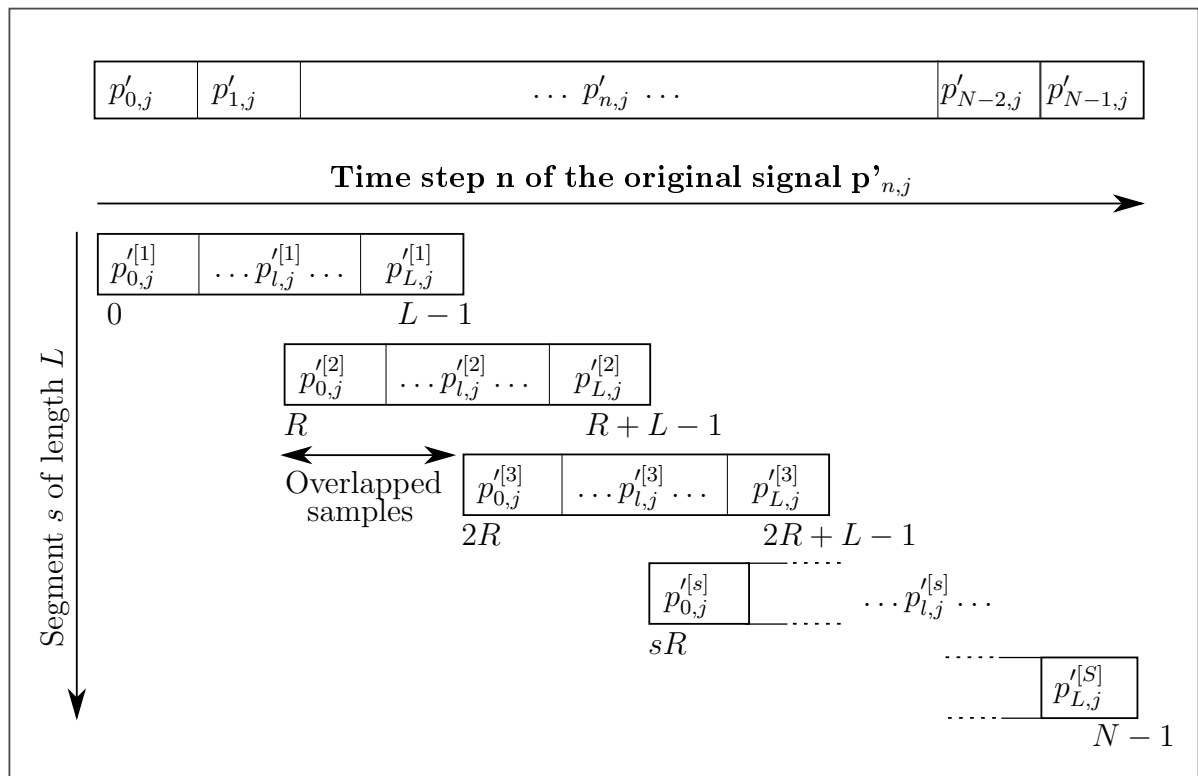


Figure 5.4: Concept of overlapping segmenting of the discrete-time signal $p'_{n,j}$ of length N sampled at the circumferential position j .

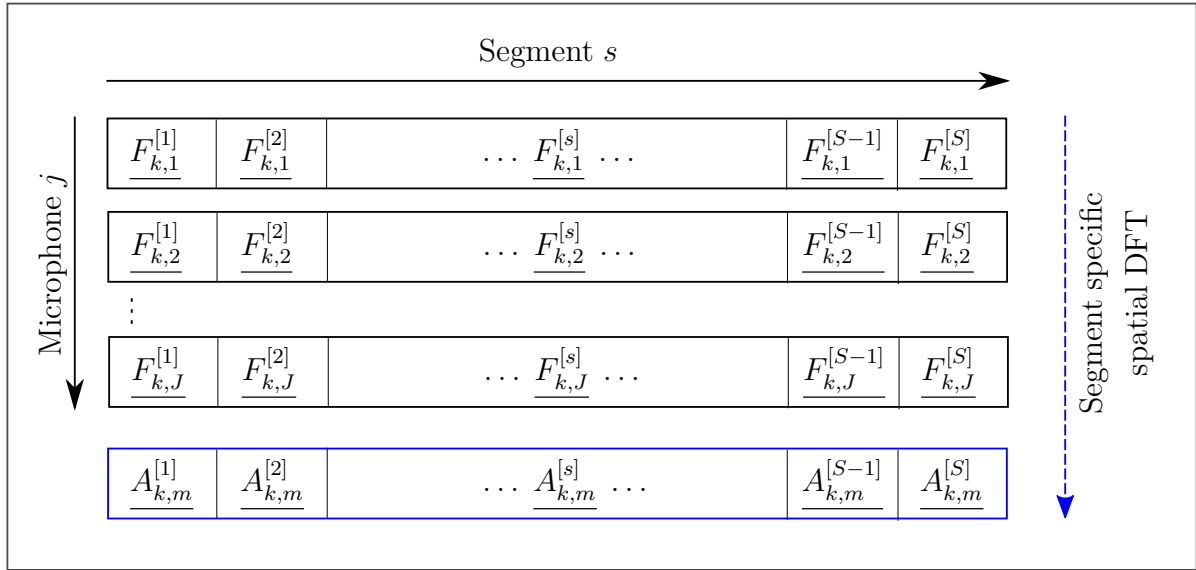


Figure 5.5: Concept of segment-specific application of the 2D-DFT modal decomposition method.

segmented data sequences do not match exactly the excitation frequencies investigated. Even though the difference between the two frequencies is minor, and the impact on the spectrum is expected to be small, each segmented data sequence is augmented with values of zero so that the DFT length of each segment is artificially increased to $N = 2^{16}$ data points according to

$$p'_{l,j} = \begin{cases} p'_{(s-1)R+l,j} & \text{for } l = 0, 1, 2, \dots, L-1 \\ 0 & \text{for } l = L, \dots, N-1. \end{cases} \quad (5.14)$$

By these means, spacing between two DFT frequencies is altered to $\Delta f = f_s/N = 1$ Hz, and the DFT frequencies are thereby shifted to integer values. Thus, the excitation frequencies are accurately represented in the spectrum. This procedure is commonly known as *zero-padding* and described as an example by Oppenheim and Schaffer (2014). The Nyquist frequency is not influenced by the segmenting and remains at $f_{\text{Nyquist}} = 0.5 \cdot 10^{16}$ Hz = 32,768 Hz.

With the chosen number of data points per segment, each data sequence is divided into S segments. The modal decomposition method as described in Sec. 5.1.2 is then carried out for each one of the segments (cf. Fig. 5.5). For this purpose, the temporal DFT $F_{k,j}^{[s]}$ is calculated for each segment separately. Subsequently, the spatial DFT $A_{m,k}^{[s]}$ is determined for each time interval using the results of the temporal DFT of the respective segments. Eventually S -values of the spectral quantities are available for statistical analysis. The statistical measures applied are described in the section below.

5.2.2 Statistical measures

In this work, *average*, *standard deviation*, and *relative standard deviation* (RSD) are the three statistical measures used to evaluate the results of the measurements. The application of statistical methods is essential since stochastic effects such as electrical noise from the instrumentation and most importantly, random noise produced by the turbine itself, interfere with the measurement of the intentionally excited signal. The size of the sample available for statistical analysis corresponds to the number of segments S into which the original data sequence is divided into. The data sets of the segments are understood to be independent of one another, insofar as information on the spectral phases and amplitudes of noise in one segment give no indication of the respective quantities in another segment.

The mean of the investigated quantities is estimated by averaging over the number of segments (sample size) according to

$$\bar{q} = \frac{\sum_{s=1}^S q^{[s]}}{S}, \quad (5.15)$$

where $q^{[s]}$ denotes the value of the quantity q determined for the segment s . The variation of the quantity is assessed using standard deviation σ given by

$$\sigma_q = \left(\frac{1}{S-1} \sum_{s=1}^S (q^{[s]} - \bar{q})^2 \right)^{1/2}. \quad (5.16)$$

As the average \bar{q} is not known, but rather estimated according to Eq. (5.15), the standard deviation itself is only an estimate of the standard deviation of the sample. Assuming that the distribution of the quantity investigated follows a standard normal distribution, the confidence interval for the unknown mean for a confidence level of 95% is given according to

$$\text{CI}_{95\%} = \bar{q} \pm 1.96 \frac{\sigma_q}{\sqrt{S}}, \quad (5.17)$$

where 1.96 is the critical value for the confidence level chosen.

Average and standard deviation are convenient statistical measures to quantify the spread of q in the unit of the quantity. They do not, however, permit a relative evaluation in terms of the extent of dispersion. For this, the *relative standard deviation* (RSD) is used. The RSD gives the standard deviation in relation to average

$$\text{RSD}_q = \frac{\sigma_q}{\bar{q}}, \quad (5.18)$$

and is thus a dimensionless measure of variation.

Hereinafter in the plots displaying the aerodynamic and acoustic measurement data for validation, the solid lines represent average, and the error bars indicate the 95% confidence interval according to Eq. (5.17), thus assuming a Gaussian distribution of

5.3 Background Noise

the respective quantity (cf. Chap. 6). For the aerodynamic data, the error bars describe the measurement uncertainty with respect to calibration, to instrumentation (sensor accuracy) as well as with respect to stochastic fluctuations. The error bars for the aeroacoustic pressure amplitude A_m represent the stochastic fluctuations, which are mainly due to stochastic background noise from the turbine. The possible impact of noise is investigated in Sec. 5.3.

Furthermore, in order to quantify linear dependence between two quantities x and y with sample size N , Pearson correlation coefficient is used. With the covariance

$$\text{Cov}(X, Y) = \left(\frac{1}{N-1} \sum_{i=1}^N (x_i - \bar{x})(y_i - \bar{y}) \right), \quad (5.19)$$

the correlation coefficient is given by

$$r = \frac{\sum_{i=1}^N (x_i - \bar{x})(y_i - \bar{y})}{\sqrt{\sum_{i=1}^N (x_i - \bar{x})^2 (y_i - \bar{y})^2}}. \quad (5.20)$$

The value of the coefficient ranges from $r = -1$ to $r = 1$, where a value of one indicates a total linear correlation and a value of zero indicates an absence of a linear dependence between the two quantities. Generally, one can state the greater the absolute value, the stronger the correlation between the quantities. In addition, Pearson correlation coefficient also gives the direction of the correlation. A value of $r > 0$ thereby represents a positive relationship, and vice versa a value of $r < 0$ a negative relationship.

5.3 Background Noise

The term *noise* or *background noise* refers here to any stochastic and non-stochastic frequency components in the frequency spectra which are not associated to the synthetic sound field excitation. This includes mainly noise inherently produced by the LPT test rig itself (including the acoustic modes produced by rotor-stator interaction), flow-induced noise additionally introduced by instrumentation like probes and sensors, and noise from electrical devices used for signal collection. The latter all superpose the intentionally excited spectral components, and thus might alter the amplitudes measured for the mode investigated.

In this work, similarity of modal sound propagation is evaluated by considering variations in the modal sound pressure amplitude determined between different measurements. For conclusive results of the experimental validation, it is mandatory that the variation between two samples (amplitudes), if detected, is statistically significant. Variations are considered to be statistically significant if the respective confidence intervals of the samples do not overlap. Now, stochastic noise, superposing the intentionally excited signal, results in a spread of the quantity considered. According to Eq. (5.17), the size of the confidence interval is proportional to the standard deviation of the quantity, on

the one hand, and inversely proportional to the square root of the inverse of the sample size, on the other hand. The sample size can easily be modified, but is still restricted by memory capacities and available measurement time. On the contrary, the standard deviation can hardly be influenced as it is governed by noise inherently produced by the LPT itself. For a low standard deviation, measurement data with low stochastic noise are therefore required. In contrast to stochastic noise, non-stochastic noise components which superpose the excited signal result in a time-constant increase or decrease of the value of the amplitude affected⁷. Depending on the spatial characteristic, this might eventually alter modal amplitude characteristics. This alteration cannot be expressed by statistical measures, and therefore non-stochastic components should be identified prior to measurements, if possible.

Based on these considerations, the (noise) frequency spectrum of the turbine is characterized in the paragraphs below with respect to dominant (high amplitude) stochastic and non-stochastic components for both operating points investigated. The objective is to identify frequency (ranges) where the amplitudes of the modes excited might be altered by stochastic or non-stochastic components which are not related to the sound field excitation.

For this purpose, the temporal frequency spectrum of the LPT is determined for every microphone position in both measurement planes, Sec A and Sec B, for measurements without synthetic sound field excitation⁸. The resulting circumferential spectra are visualized as colored shaded surface plots for part-load and design-point operation in the upper part of Fig. 5.6 and Fig. 5.7, respectively. The frequency, ranging from 400 Hz to 4000 Hz, and the circumferential position of the microphones, ranging from 0° to 360°, are displayed on the abscissa and ordinate, respectively⁹. For better visualization, the last circumferential position thereby corresponds to the first position. The frequency resolution is $\Delta f = 10$ Hz (x-axis). In circumferential direction (y-axis), the spatial resolution is 18°, corresponding to the number of microphones installed. The amplitudes of the frequency spectra are normalized with the maximum amplitude determined for both measurement planes. In all diagrams, the values are represented by colors ranging from blue (zero) to red (one). A summary of the parameters used for the signal post-processing is given in Tab 5.1. The Nyquist mode is not listed here, as the spatial noise spectra are not analyzed.

In the surface plots at the bottom of Fig. 5.6 and Fig. 5.7, the values of the relative standard deviation calculated according to Eq. (5.18) are shown as a measure of variation of the spectral amplitudes. Low values of the RSD (colored blue) indicate a small deviation of the spectral amplitude from the mean, while high values (colored

⁷This might also hold true for noise components at frequencies close to the frequency investigated, if spectral leakage as described in Sec. 5.1.3 occurs.

⁸The experimental validation is carried out with respect to acoustic data collected in measurement plane Sec A. Nevertheless, the results of the noise analysis are also shown for Sec B in order to compare and verify findings identified for Sec A.

⁹The maximum excitation frequency is set to $f_{exc} = 1200$ Hz as a result of the cut-off analysis. However, in order to capture the BPF for design-point operation, a larger frequency range up to 4000 Hz is considered here for noise analysis.

5.3 Background Noise

Table 5.1: Analysis of the (noise) frequency spectra of the LPT test rig. 2D-DFT processing parameters and properties.

Parameter	Value
Measurement time T	1 s
(Temporal) sampling frequency f_s	65536 Hz
Nyquist frequency f_{Nyquist}	32768 Hz
Number of microphones J per array	20
Number of segments S	19
Segment length L	6552
Overlap R	$L/2$
Frequency resolution $\Delta f^{[s]}$	≈ 10 Hz

red) indicate a large spread. A value of zero or close to zero implies the particular case of nearly no variation of the amplitude, and thus characterizes non-stochastic spectral components.

Comparison of the spectral temporal amplitudes and the RSD shows that the frequency spectra have similar characteristics for both operating points. First, it can be observed that the amplitude level in Sec A is considerably lower than in Sec B, which especially holds true for the frequency range up to approx. 700 Hz for part-load operation and up to approx. 1000 Hz for design-point operation. The respective regions in the diagrams are marked (A). Increased low-frequency hydrodynamic pressure fluctuations downstream of the turbine stage and increased flow-induced noise can most likely be assumed to be responsible for this. Analysis of the respective values of the calculated RSD depicted in the surface plots at the bottom of each figure shows that the spectral components in the lower frequency range are stochastic, as expected.

The first harmonic of BPF can be clearly identified for both operating points in both measurement planes, the respective regions are marked (B). In addition, for part-load operation, the second harmonic of BPF lies within the displayed frequency range as well (C). In all cases, the amplitude of BPF is always higher in Sec B than in Sec A. Low values of the RSD, which indicate non-stochastic components, are mainly found in these frequency ranges. Assuming constant rotor speed and thus constant rotor-stator-interaction, non-stochastic components are to be expected.

For part-load operation, three frequency ranges with uncharacteristic peaks in the spectral amplitude are found in Sec A at lower frequencies. These peaks occur in a narrow frequency range around 500 Hz (D), 770 Hz (E), and around 950 Hz and 1010 Hz (F). The values of the RSD identify the amplitude peaks at 770 Hz to be related to stochastic noise components, and the peaks around 500 Hz, 950 Hz, and 1010 Hz related to non-stochastic noise components. Remarkably, the peaks at 500 Hz and 770 Hz are

characterized by a very even distribution around the circumference, whereas the peaks in region (F) are dependent on the circumferential position. Bartelt (2015) also detected an uncharacteristic peak in the frequency spectra for the circular duct segment of the sound generator around 750 Hz, however, at a slightly higher mass flow rate of ≈ 5 kg/s in comparison to ≈ 4.1 kg/s for the measurements here. The peak did not appear in the pre-tests in the AWT, therefore the author excluded duct-specific, flow-induced resonance effects. Furthermore, the peak was found to be independent of the rotor speed so that Bartelt (2015) concluded that flow separations at the pressure probes installed in the duct are the causes. Probes of similar dimensions are also used in the measurements for this work. Thus, the same explanation probably holds true for the spectral component with low RSD at 950 Hz and 1010 Hz (F). An explanation for the uncharacteristically high non-stochastic and stochastic noise amplitudes in region (D) and (E), respectively, cannot be given here. For design-point operation the latter can also be observed.

By resuming the observations above and relating them to the experimental validations, the following three conclusions can be drawn with respect to the measurement plane Sec A focused on:

- (1) Stochastic variations of the temporal and spectral amplitudes determined can be expected to be small for both operating points since the spectral noise amplitudes and the RDS are low.
- (2) Non-stochastic components around 500 Hz, 950 Hz, and 1010 Hz might alter the amplitudes, and thus the modal response function determined for the excited sound fields in these frequency ranges for part-load operation.
- (3) Impact from non-stochastic components are not to be expected for design-point operation.
- (4) In section 4.3, the excitation frequency range suitable for the validation measurements has been limited up to the maximum frequencies of around 1200 Hz. Therefore, interferences with BPF and its harmonics are excluded.

For the sake of completeness, it shall be noted that for Sec B the situation is slightly different. Non-stochastic components beside the one observed at the BPF are not observed. However, in contrast to Sec A, a large spread of the temporal and modal amplitudes can be anticipated at low frequencies for both operating points due to the combination of high amplitudes and high values of the RSD.

5.3 Background Noise

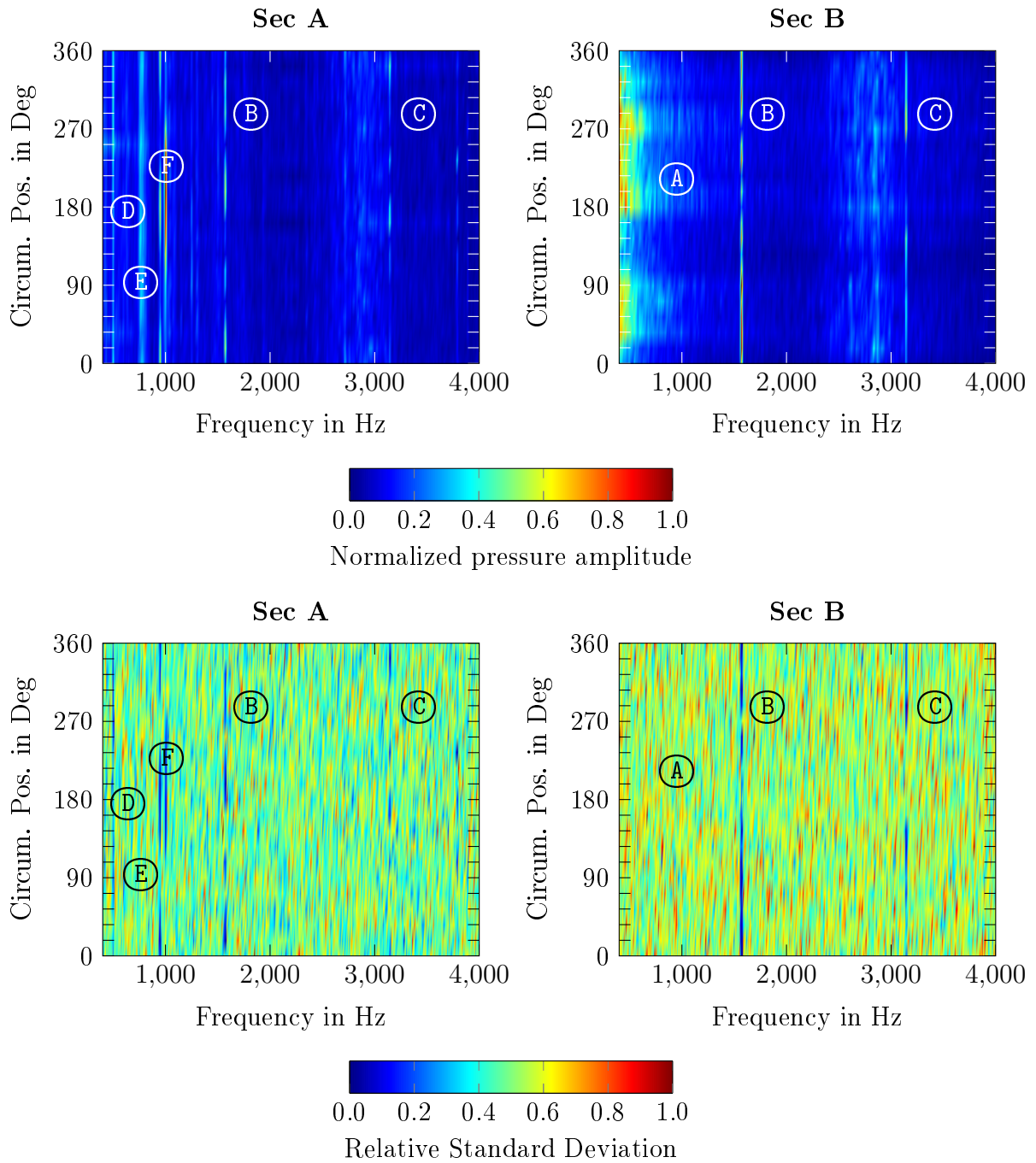


Figure 5.6: Noise analysis of the LPT test rig for part-load operation in Sec A and Sec B. Top: Frequency spectrum. Bottom: Relative standard deviation of the spectral amplitudes (RSD).

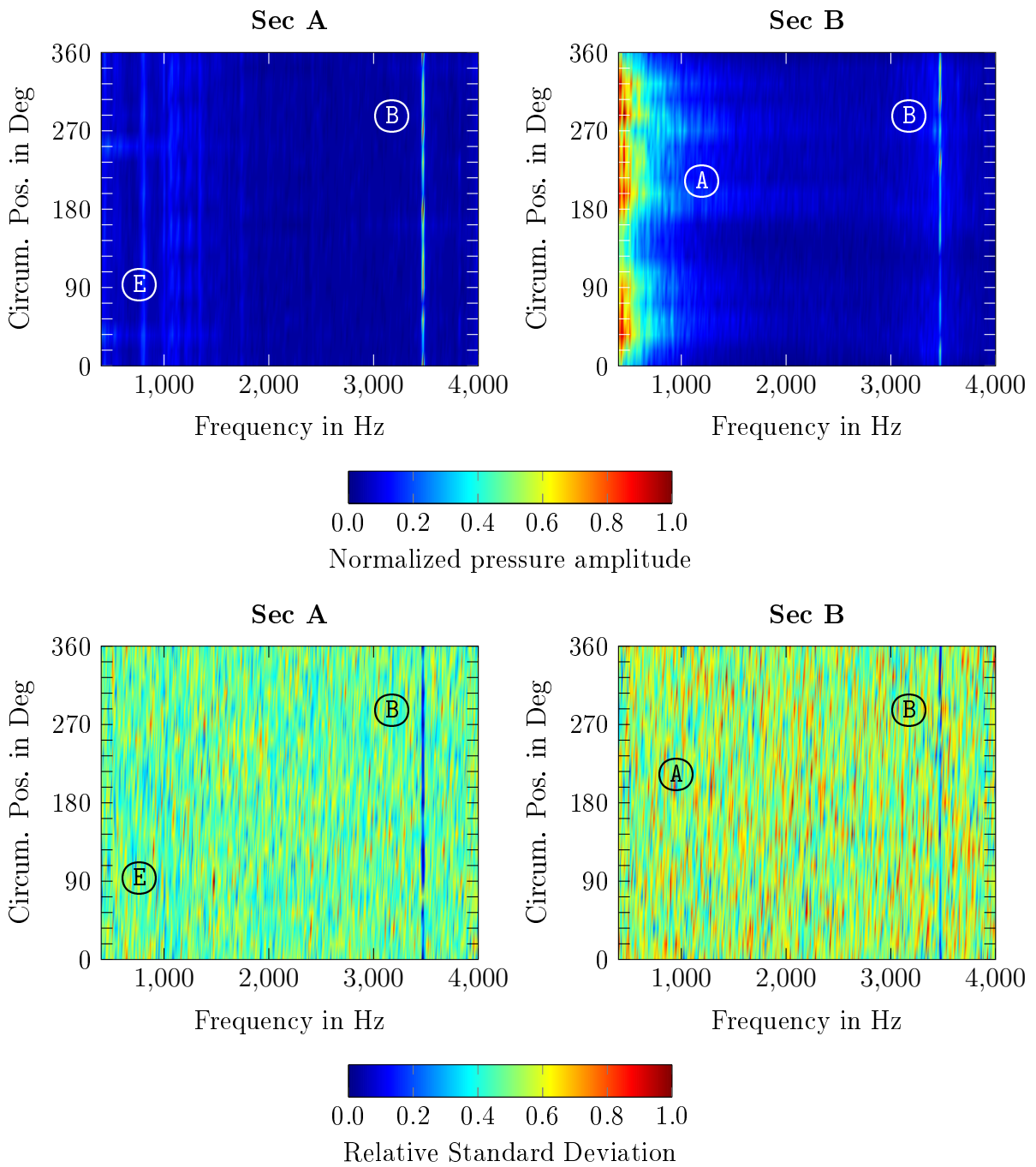


Figure 5.7: Noise analysis of the LPT test rig for design-point operation in Sec A and Sec B. Top: Frequency spectrum. Bottom: Relative standard deviation of the spectral amplitudes (RSD).

6 Experimental validation

In this chapter, the results of the experimental validation of the suitability of the modal group velocity angle relative to the duct axis for establishing (partial) similarity conditions for modal sound propagation in ducts are presented. The validation is carried out for the conditions in the cylindrical intake duct of the LPT. Similarity is evaluated with regard to the modal response function of the measurement section determined for the synthetically excited sound fields. The data sets used to test the hypothesis of this work have been obtained from acoustic measurements where aeroacoustic similarity has not been considered in advance. Thus, the hypothesis is tested using the results of a post-hoc scaling.

In section 6.1 of this chapter, the measurements conducted are specified and the chosen test cases are introduced. The consequences of non-compliance with similarity of modal sound propagation are illustrated. Observations are explained by means of the similarity relation and the similarity map, respectively. Subsequently, in Sec. 6.2, the procedure of post-hoc scaling is described. The results of the post-hoc scaling with respect to the achievement of similarity are discussed in Sec. 6.3 and the limits of this approach are addressed in Sec. 6.4. The chapter closes with a summary of the findings in Sec. 6.5 .

6.1 Non-compliance with Similarity

The experimental data used here are obtained from acoustic measurements taken on the turbine test rig of the TFD using the 1.5-stage low-pressure turbine configuration and the measurement setup as described in Chap. 4. Specific acoustic modes were excited in the inlet of the LPT by means of the sound generator and the excitation method presented in Sec. 4.2. Selected data collected in measurement section Sec A (cf. Fig. 4.2) are used for validation. To verify and confirm generality of the findings, validation is carried out at two operating points, namely at part-load operation and design-point operation. The respective operating parameters, rotational speed and mass flow rate are given in Tab. 6.1.

Table 6.1: Mean aerodynamic operating parameters for part-load operation and design-point operation.

	Rotational speed N in 1/min	Mass flow rate \dot{m} in kg/s
Part-load	3100	4.135
Design-point	6950	7.94

Table 6.2: 2D-DFT processing parameters and properties. The Nyquist mode m_{Nyquist} refers to the highest mode resolvable with respect to both directions of spinning. The frequency resolution $\Delta f^{[s]}$ is valid for the segmented data sequences.

Parameter	Value
Measurement time T	3 s
(Temporal) sampling frequency f_S	65.536 Hz
Number of microphones J per array	20
Nyquist frequency f_{Nyquist}	32.768 Hz
Nyquist mode m_{Nyquist}	9
Number of segments S	59
Segment length L	6.552
Overlap R	$L/2$
Frequency resolution $\Delta f^{[s]}$	≈ 10 Hz

For each of the two test cases, a specific mode is synthetically excited in a defined frequency range which covers 21 frequencies in steps of one Hertz. The modes and the exact frequency ranges considered for the validation are chosen with respect to a stable excitation of the mode on the one hand and low stochastic background noise on the other hand (cf. Sec. 5.3). The sound field is resolved for each excitation frequency in its modal components, applying the 2D-DFT modal decomposition method presented in detail in Sec. 5.1 to the collected measurement data. For statistical evaluation, the original data sequence is subdivided into data segments prior to the modal decomposition as described in Sec. 5.2. In Tab. 6.2, the most important properties of the signal post-processing are summarized. In addition to the listed parameters regarding the acoustic measurements, the following parameters for the aerodynamic measurements were used:

- (1) Aerodynamic measurement time: $T = 40$ s
- (2) Aerodynamic sampling frequency: $f_S = 5$ Hz.

To analyze the impact of changing boundary conditions, the measurements are repeated 30 times extending over several hours. Thus, 30 data sets with identical excitation are available in total for analysis and validation. With regard to future works on possible effects of clocking on acoustic transmission, the clocking position of the second stator has been evenly varied over the 30 measurements, while the clocking position of the first stator vane carrier has been kept constant. With respect to the investigation carried out for this work, the assumption holds that clocking of the second stator carrier has no impact on the results of validation (cf. discussion in Sec. 6.4). The following procedure was applied to sound field excitation and data collection: For each of the 30 data sets collected, the acoustic mode considered was excited over the frequency range specified

6.1 Non-compliance with Similarity

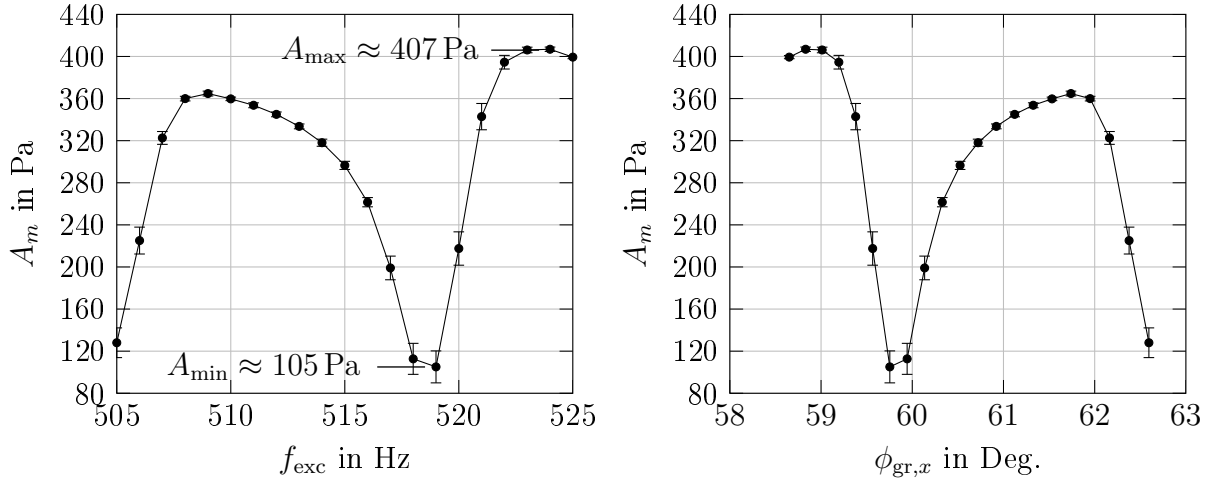


Figure 6.1: Acoustic characterization of the measurement section Sec A. Left: Measured modal response subject to the excitation frequency. Right: Measured modal response function to the calculated axial angle of the group velocity vector. [Test case 1 | part-load operation | $m = -1$ | Data set No. 1]

in frequency steps of $\Delta f_{exc} = 1$ Hz. The acoustic pressure data were collected according to the settings listed in Tab. 6.2. Steady aerodynamic data are collected in parallel with the acoustic measurements. In summary, 30 data sets consisting of 21 excited frequencies each as well as the corresponding aerodynamic data sets are available for validation.

Similarity is evaluated here on the basis of the modal response function measured in the LPT. In the following, the measured modal amplitudes (also referred to as the *modal responses*) are either described by

$$A_m = \mathbf{A}(f_{exc}), \quad (6.1)$$

or by the following description

$$A_m = \mathbf{A}(\phi_{gr,x}). \quad (6.2)$$

In the first description, \mathbf{A} is the *modal frequency-response function*, and thus corresponds to the spatial DFT $\underline{A}_{k,m}$ for a specified mode m . However, in this work the description according to Eq. (6.2) is also used. Then \mathbf{A} denotes the response function subject to the axial angle of the group velocity vector.

6.1.1 Test case 1: Part-load operation

The test case evaluated in this section considers the mode of order $m = -1$ synthetically excited at part-load operation. The respective mode was excited in the frequency range from $f_{exc} = 505$ Hz to $f_{exc} = 525$ Hz in steps of one Hertz. First, the modal response function is depicted to characterize the acoustic behavior of modes that travel in the

measurement section considered. Subsequently, selected aerodynamic and aeracoustic data are presented and dependencies between the different quantities are discussed. A correlation analysis is carried out to determine the statistical dependency between the observed variations in the modal response and the three considered similarity parameters.

Modal frequency-response function

In the diagram on the left side of Fig. 6.1, the modal response function according to the description in Eq. (6.1) is displayed for the excited frequencies for data set No. 1. Over the small range of excited frequencies, the function shows an uneven distribution with pronounced local extrema. A maximum is located around a frequency of $f_{\text{exc}} = 509$ Hz with a steep gradient towards lower frequencies. A second maximum, also with steep gradient towards lower frequencies, can be identified around $f_{\text{exc}} = 523$ Hz. A further extremum in the form of a distinct local minimum can be identified at $f_{\text{exc}} = 519$ Hz. Again, steep gradients relative to the amplitudes measured can be observed. Here, the amplitude increases about $\Delta A_m \approx 300$ Pa within four Hertz from $f_{\text{exc}} = 519$ Hz to $f_{\text{exc}} = 523$ Hz. Overall, the measurement data themselves are nearly constant over the sample size with negligible stochastic fluctuations. On the right side of the figure, the modal response function is given subject to the analytically calculated angles of the group velocity vector relative to the duct axis (cf. description according to Eq. (6.2)). Due to the inverse relation between the frequency and the angle, the two profiles are reversed. At the operating point regarded and for the frequency range considered, the group velocity angle varies between $\phi_{\text{gr},x} = 58.65^\circ$ and $\phi_{\text{gr},x} = 62.59^\circ$ for the mode $m = -1$, thus well below cut-off.

For the following analysis, the modal response function of data set No. 1 as shown in the diagrams in Fig. 6.1 is used as reference for evaluating similarity.

Variations in the aerodynamic conditions in Sec A

In Fig. 6.2 selected aerodynamic and aeroacoustic quantities are depicted for all 30 data sets collected. Here, as well as in the diagrams below, the abscissa is the data set number. The data sets are presented in the correct sequence with respect to the time of measurement, which is indicated by the connection of the points. The error bars in all diagrams indicate the 95% confidence interval. The statistical methods employed are described in detail in Sec. 5.2.2.

In the diagrams in Fig. 6.2, ambient temperature, total flow temperature, total flow pressure, reduced mass flow rate as well as both similarity parameter, Mach number and Helmholtz number are depicted. The total temperature and pressure values are used for the calculation of the mass flow rate and are obtained from measurements with a pressure probe steadily located in the center of the inlet duct as described in Sec. 4.1.3. The first diagram on the top left side shows the ambient temperature collected outside the test hall. Over the period of measurement, the temperature steadily changed with a maximum temperature difference of $\Delta T_{\text{amb}} \approx 2.3$ K. In accordance with the ambient temperature, the conditions in the measurement plane Sec A changed as the turbine test rig is operated in an open-circuit mode.

6.1 Non-compliance with Similarity

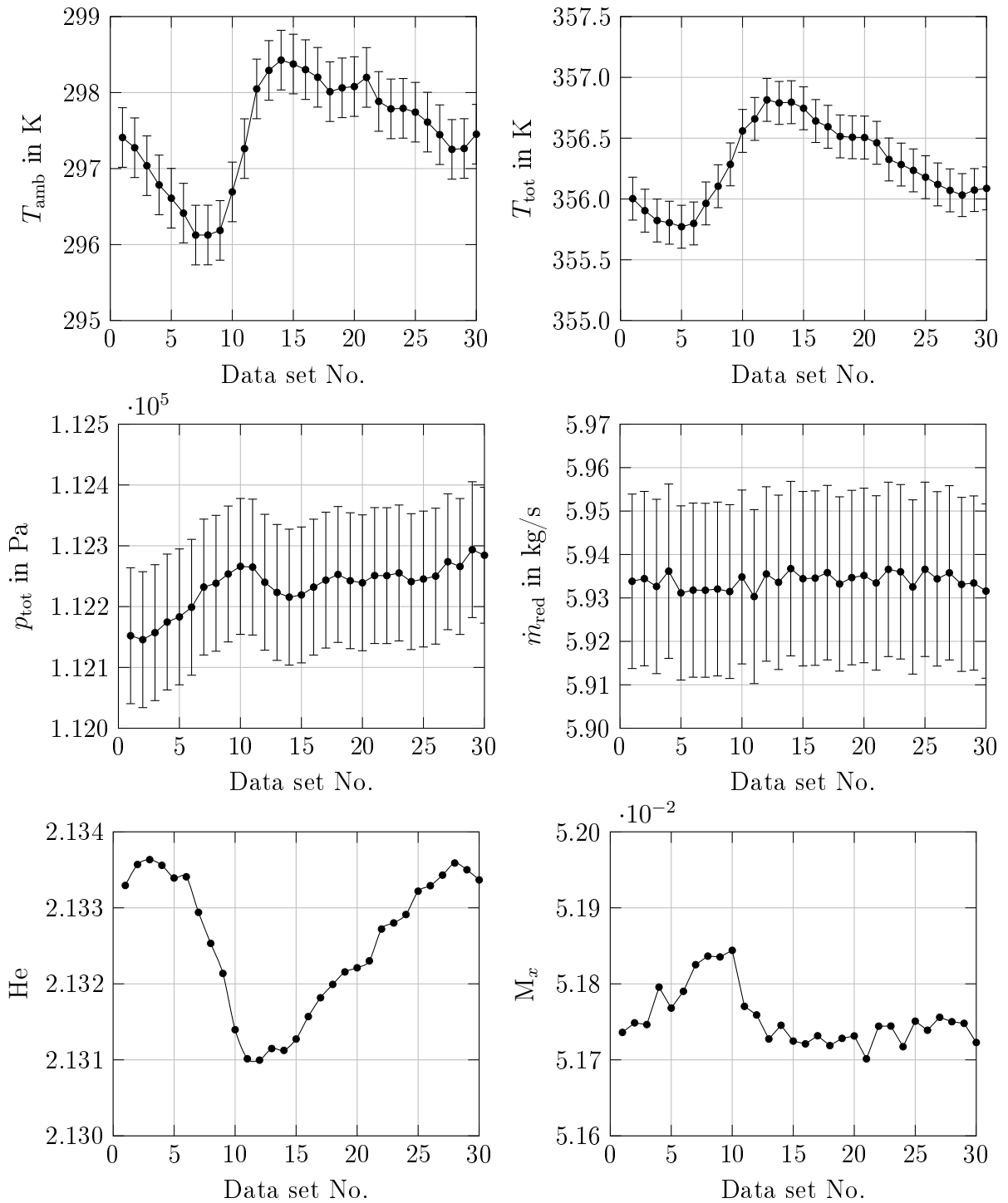


Figure 6.2: Variations in the aerodynamic data and in the similarity parameters for measurement Sec A. Top left: Ambient temperature. Top right: Total flow temperature. Center left: Total flow pressure. Center right: Reduced mass flow rate. Bottom left: Helmholtz number. Bottom right: Mach number. [Test case 1 | part-load operation | $m = -1$ | $f_{\text{exc}} = 520$ Hz]

The impact of the variation in ambient temperature becomes most apparent in the total flow temperature, where a similar temperature distribution with a maximum temperature difference of $\Delta T_{\text{tot}} \approx 1.0$ K can be observed. The impact on the total pressure is less pronounced since the operating conditions of the turbine test rig are constantly adapted to compensate for the changes in the inlet conditions as described in Sec. 4.1.1. The same applies for the reduced mass flow rate which characterizes the operating point¹.

The distribution of the Helmholtz number follows the characteristics of the distribution of the total flow temperature as implied by the relation

$$\text{He} = \frac{2\pi f R}{\sqrt{\kappa R_s T^0}},$$

which is introduced in Eq. (2.24)². Contrary to the Helmholtz number, a clear relationship between the flow temperature and the axial Mach number is not observed, which is due to the constant adaptation of the test rig's operating point.

Correlation Analysis

In the diagrams in Fig. 6.3, the modal response detected for $m = -1$, the group velocity angle, and the correlation between these two quantities are plotted for the different measurements. The quantities depend on the excitation frequency and are given here by way of example for the frequency $f_{\text{exc}} = 520$ Hz. The group velocity angle is calculated from the averaged value of the similarity parameters Helmholtz number and Mach number (see also Fig. 6.4).

The modal response for the frequency regarded shows large variations across the data sets, and thus over time. A variation of up to $\Delta A_m \approx 115$ Pa between the maximum and the minimum detected amplitude can be identified. This corresponds to a relative difference of approx. 43%. Following the hypothesis of this work, the assumption is that these variations in the modal frequency response are due to changes in the modal propagation properties, namely due to changes in the angle of the group velocity vector of the propagating sound field. The latter is depicted in the diagram on the top right of the figure showing clear variations over the time of measurement with a maximum variation of $\Delta\phi_{\text{gr},x} \approx 0.12^\circ$. The biggest absolute changes with respect to reference data set No. 1, can be observed for the measurements of data set No. 8 to data set No. 24. An inverse dependency between the variation in the angle and the variation in the modal response can be observed visually. This dependency is confirmed by a correlation analysis which shows a very strong relationship between the two parameters. A Pearson correlation coefficient of $r = -0.9422$ is determined indicating an approximately complete linear dependency. In this case, the coefficient is negative. Hence, an increase in the modal response is related to a decrease in the angle considered. Here, it should be emphasized that the direction of correlation is not analytically given but determined by the acoustic characteristic of the measurement section.

¹Note that the group velocity angle and the similarity parameters are calculated from the averaged values of the respective aerodynamic quantities.

²Here κ denotes the ratio of specific heats, R_s the gas constant, and T^0 the steady-state temperature.

6.1 Non-compliance with Similarity

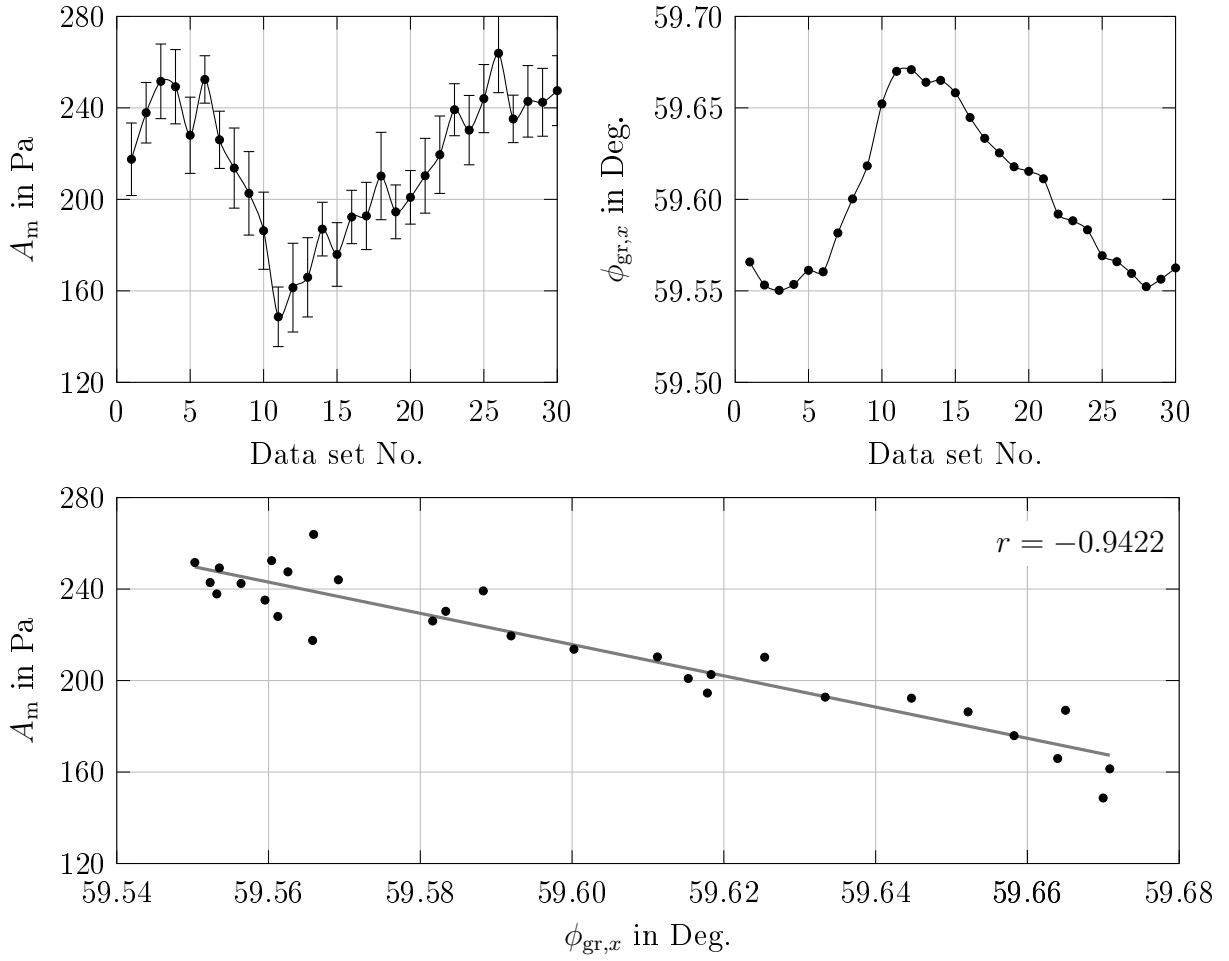


Figure 6.3: Correlation Analysis for test case 1. Top left: Variations in the modal response. Top right: Variations in the angle of the group velocity vector. Bottom: Correlation of the modal response with the angle of the group velocity vector.

[Test case 1 | part-load operation | $m = -1$ | $f_{exc} = 520$ Hz]

Plausibility check of the similarity relation

From the similarity relation derived, it follows that the variation in the axial angle of the group velocity vector observed in Fig. 6.3 is related to the variation in the similarity parameters, Mach number and Helmholtz number. The latter are depicted in Fig. 6.2. According to the similarity relation between the group velocity angle and the similarity parameters in Eq. (3.38), a decrease in either the Helmholtz number or the Mach number leads to an increase in the angle under consideration, and vice versa. Visually, it can be observed that the profile of the angle corresponds to the characteristic of the variations in the Helmholtz number, whereas the characteristic of the Mach number is not clearly reflected. Referring to the modal similarity map in Sec. 3.4, it is observed that for the frequency range and operating point investigated, small variations in the

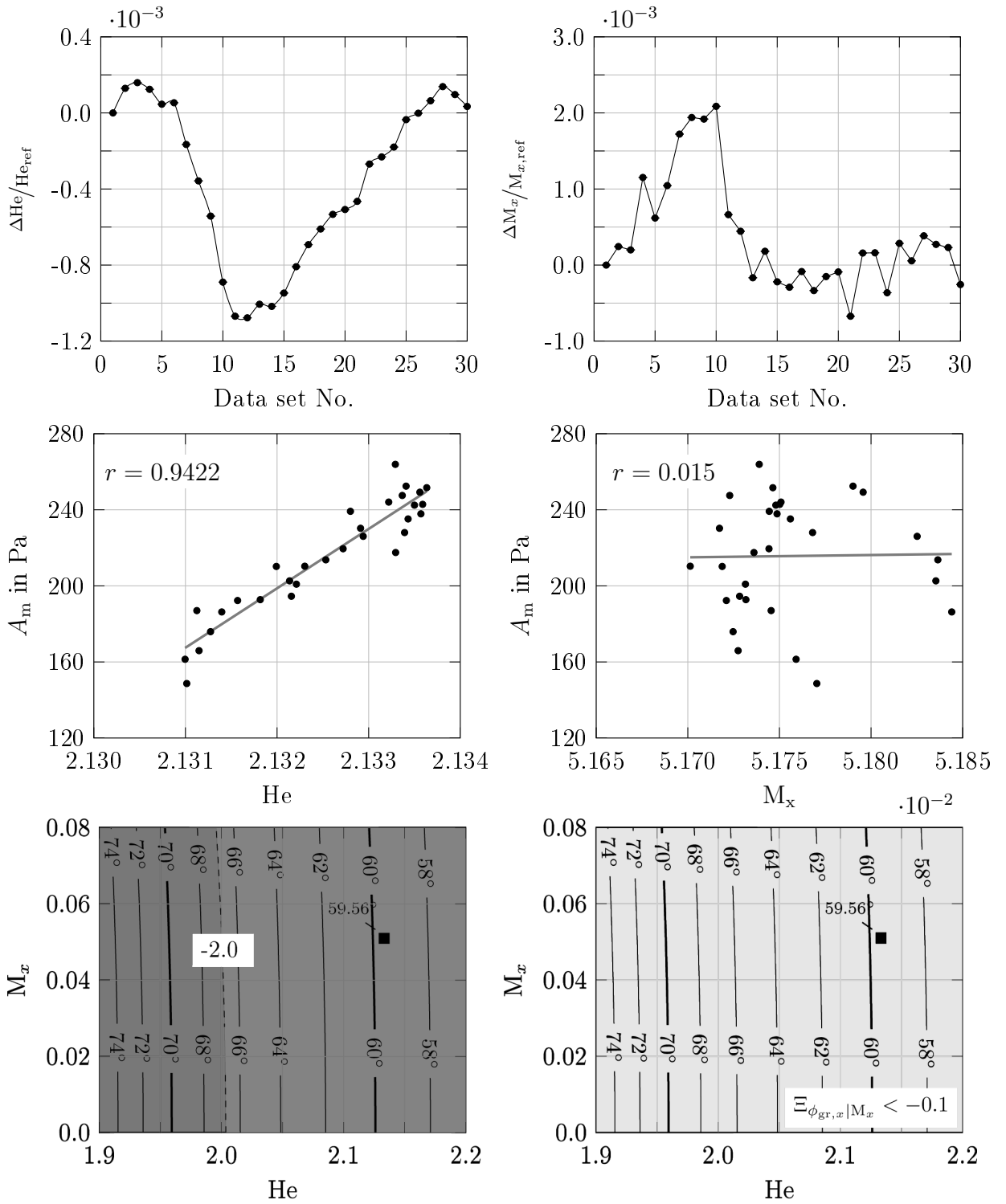


Figure 6.4: Relation between linear dependencies and the similarity relation. Top left: Relative change of the Helmholtz number. Top right: Relative change of the Mach number. Center left: Correlation of the modal response with the Helmholtz number. Center right: Correlation of the modal response with the axial Mach number. Bottom left: Extract of the similarity map ($\Xi_{\phi_{gr,x}|He}$). Bottom right: Extract of the similarity map ($\Xi_{\phi_{gr,x}|M_x}$). The square marks the operating point.

[Test case 1 | part-load operation | $m = -1$ | $f_{exc} = 520$ Hz]

6.1 Non-compliance with Similarity

Mach number have nearly no impact on the angle whereas variations of the same order in the Helmholtz number lead to considerable changes in the quantity considered. Extracts of the relevant region of the similarity maps are given at the bottom of Fig. 6.4. For the operating point considered, sensitivity of the angle with respect to the Helmholtz number is $-2.0 < \Xi_{\phi_{\text{gr},x}|\text{He}} < -1.0$, whereas sensitivity with respect to the Mach number is below $\Xi_{\phi_{\text{gr},x}|\text{M}_x} < -0.1$ ³ In other words, sensitivity with respect to the Helmholtz number is approx. eight times higher than with respect to the Mach number. This explains why in this case, the profile of the angle of the group velocity vector follows the characteristic of the Helmholtz number and not of the Mach number, although the changes in both parameters are of the same order (cf. relative change of the two parameters with respect to reference data set No. 1 depicted in the diagrams at the top of Fig. 6.4). With respect to the variations in the modal response, it can be concluded that for test case 1 these are predominantly caused by variations in the Helmholtz number. This statement is supported by the correlation depicted in the diagrams in the center of Fig. 6.4. It is found that the variation in the amplitude also correlate strongly with the variation in the Helmholtz number with exactly the same correlation coefficient of $|r| = 0.9422$. The reversed direction of the coefficient for the Helmholtz number results from the inverse relation between the axial angle of the group velocity vector and the Helmholtz number pointed out before. On the same time, dependency on the Mach number is negligible ($r = 0.015$).

In fact, it is found that for all excited frequencies, the absolute correlation coefficient for the angle of the group velocity vector exactly matches the respective coefficient for the Helmholtz number. This observation is independent of the value of the correlation coefficient for the Mach number and supports the validity of the calculated sensitivities and thus the similarity relation. In the appendix in Sec. A.8, the correlation coefficients are analyzed for all excitation frequencies.

Relation between flow temperature and angle of the group velocity vector

According to the diagram in Fig. 6.2 and Fig. 6.3, the axial angle of the group velocity vector and the flow temperature are positively related. This observation is supported by analysing the similarity relation. The flow temperature enters Eq. (3.38) given by

$$\cos(\phi_{\text{gr},x}) = \sqrt{1 - \left(\frac{\text{He}^2}{(u_{(m,n)}^{(\sigma)})^2} + \text{M}_x^2 \right)^{-1}},$$

via the Helmholtz number as well as the Mach number. For the Helmholtz number, the relation is inverse. With respect to Mach number, a general statement is more difficult as the flow temperature impacts flow velocity on the one hand, and speed of sound on the other hand. Anyhow, with the determined sensitivities for the angle of the group velocity vector for the operating point considered, it follows here, that an increase in the

³The sensitivity is calculated here with respect to $f_{\text{exc}} = 520$ Hz. For lower frequencies, with an angle $\phi_{\text{gr},x} > 62^\circ$ an even higher sensitivity of $\Xi_{\phi_{\text{gr},x}|\text{He}} < -0.9$ holds.

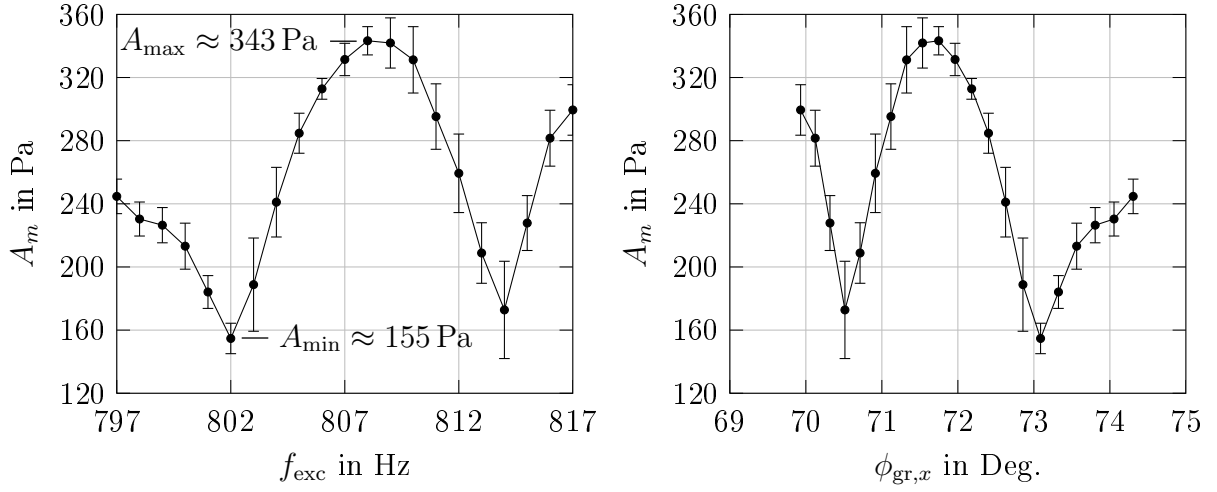


Figure 6.5: Acoustic characterization of the measurement section Sec A. Left: Measured modal response subject to the excitation frequency. Right: Measured modal response subject to the calculated axial angle of the group velocity vector. [Test case 2 | design-point operation | $m = 2$ | Data set No. 1]

temperature will lead to an increase in the angle due to the much more higher sensitivity with respect to the Helmholtz number than with respect to the Mach number.

6.1.2 Test case 2: Design-point operation

For the second test case, measurement data collected for design-point operation are investigated. Here, the mode of order $m = 2$ was synthetically excited in steps of one Hertz in a frequency range from $f_{exc} = 797$ Hz to $f_{exc} = 817$ Hz. The excitation was repeated 30 times. Thus, in line with the first test case, 30 data sets with 21 excited frequencies each are investigated.

Modal frequency-response function

The modal response functions for test case 2 are depicted in Fig. 6.5. The response functions for the mode $m = 2$ are characterized by two local minima and one local maximum. The values of the pressure amplitude measured lie between $A_{min} \approx 155$ Pa and $A_{max} \approx 343$ Pa. The minima are quite distinct and are located at the frequencies $f_{exc} = 802$ Hz and $f_{exc} = 814$ Hz. The maximum between the two minima is not as distinct, but has a broad peak with the highest pressure amplitude around $f_{exc} = 808$ Hz. The calculated angle of the group velocity vector equals $\phi_{gr,x} = 74.30^\circ$ and $\phi_{gr,x} = 69.93^\circ$ for the lowest frequency and for the highest frequency, respectively. Thus, the angles are higher than for the mode considered in test case 1, but still below cut-off condition.

Variations in the aerodynamic conditions in Sec A

In line with the analysis of test case 1, the variations of the aerodynamic quantities and

6.1 Non-compliance with Similarity

both similarity parameters, Helmholtz number and Mach number, are depicted in Fig. 6.6. Again, a test case is chosen in which a steady change in the ambient temperature, and thus in the flow temperature can be observed. In this case, the ambient temperature constantly rises over the period of the measurement, except for a slow decline at the end of the measurement. The total temperature of the flow in the inlet duct follows the temporal change of the ambient temperature and rises about $\Delta T_{\text{tot}} \approx 0.95$ K between the measurement of data set No. 1 and data set No. 29. An impact on the total pressure cannot be identified as the mass flow rate is adapted to the changing boundary conditions. Following the previous observations and explanations for the relation between the flow temperature and the Helmholtz number, the latter constantly decreases over the time of measurements except for an increase observed for the last data sets. The axial Mach number is not as clearly correlated as the Helmholtz number with the changes in the aerodynamic boundary conditions. However, a decline in the Mach number can be identified over the time of measurement.

Correlation Analysis

In Fig. 6.7, the modal response, the angle of the group velocity vector and the correlation between both are shown for an excitation frequency of $f_{\text{exc}} = 813$ Hz. The distribution of the modal response plotted in the diagram on the top left again shows significant discrepancies in the amplitudes between the different measurements. Here, a maximum absolute difference of $\Delta A_m \approx 59$ Pa is detected between data set No. 1 and data set No. 28 ($A_m = 208.84$ Pa and $A_m = 267.87$ Pa). This corresponds to a relative difference of approx. 22%. Variations of the same characteristics are observed for the angle considered. In total, the angle varies most $\Delta \phi_{\text{gr},x} \approx 0.17^\circ$ between data set No. 1 of an angle of $\phi_{\text{gr},x} = 70.713^\circ$ and data set No. 25 of an angle of $\phi_{\text{gr},x} = 70.883^\circ$. In this case, an increase in the modal response is correlated with an increase in the angle. Correlation analysis confirms the linear dependency as well as the direction of relation with a Pearson correlation coefficient of $r = 0.9584$.

Plausibility check of the similarity relation

The extracts of the relevant region of the similarity maps given at the bottom of Fig. 6.8 show again that sensitivity with respect to the Mach number is negligible with $\Xi_{\phi_{\text{gr},x}|M_x} < -0.1$ for the frequency range and operating point investigated for test case 2, whereas variations of the same order in the Helmholtz number lead to considerable changes in the axial angle of the group velocity vector with $\Xi_{\phi_{\text{gr},x}|He} < -2.0$. Also in line with test case 1, relative changes of the same order can be observed for the Helmholtz number and the Mach number as depicted in the diagrams at the top of the figure. In contrast to part-load operation, however, the variation of the parameters has the same direction. Thus, the variations in the modal response correlates with both the Helmholtz number and the Mach number, respectively (cf. diagrams in the center of Fig. 6.8). However, in line with test case 1, the coefficient of the correlation with the Helmholtz number matches nearly exactly the coefficient of the correlation with axial angle of the group velocity vector. Taking the calculated sensitivities into account, it can be again concluded again that in this case the variation in the modal response is

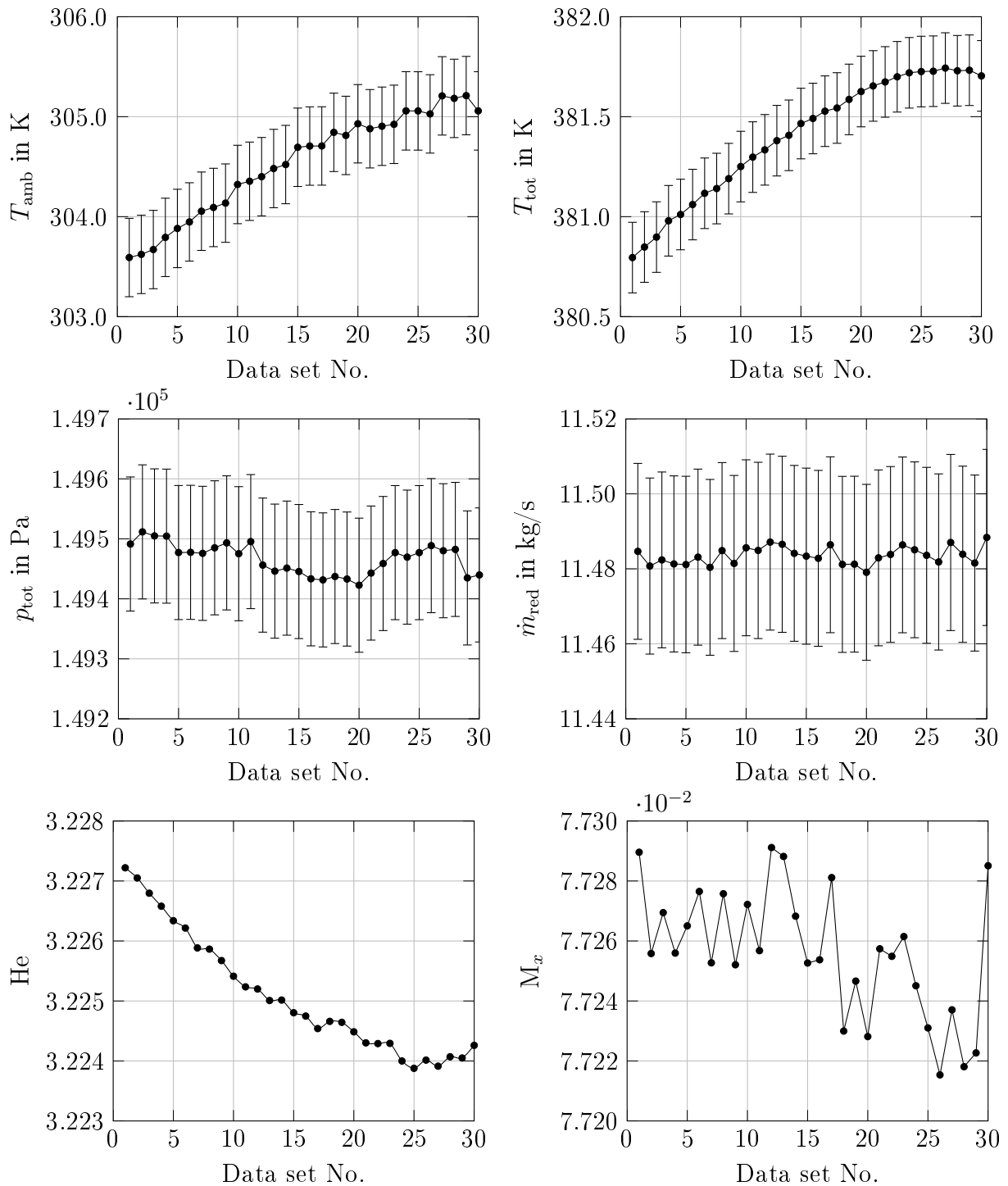


Figure 6.6: Variations in the aerodynamic data and in the similarity parameters for measurement Sec A. Top left: Ambient temperature. Top right: Total flow temperature. Center left: Total flow pressure. Center right: Reduced mass flow rate. Bottom left: Helmholtz number. Bottom right: Mach number.
 [Test case 2 | design-point operation | $m = 2$ | $f_{\text{exc}} = 813$ Hz]

6.1 Non-compliance with Similarity

caused by the variation in the Helmholtz number.

6.1.3 Findings

The major findings of this section for both test cases are as follows:

- (1) For an identical synthetic excitation of a specific acoustic mode, partial substantial variations in the modal frequency response are detected between different measurements.
- (2) Over the period of measurements, variations in the angle of the group velocity vector as well as variations in both similarity parameters, the Mach number and the Helmholtz number, are observed. These are related to changes in the aerodynamic conditions; here changes in the flow temperature, in particular.
- (3) The variation in the modal response correlate strongly with the variation in the angle of the group velocity vector for both test cases.
- (4) For both test cases, it is found that the variation in the modal response also strongly correlate with the variation in the Helmholtz number, where the absolute value of Pearson's correlation coefficient matches nearly exactly the respective value for correlation with the variations in the axial angle of the group velocity vector. Linear correlation with the Mach number, is however negligible (test case 1) or only moderately (test case 2). This is in so far interesting, as the relative change of the values of the Helmholtz number and Mach number are of the same order.
- (5) Finding (4), can be explained by considering the similarity maps respective similarity relation. It is found that for both test cases the angle of the group velocity vector is significantly more sensitive to changes in the Helmholtz number than to changes in the Mach number.
- (6) Based on (4) and (5), it can be concluded that for the operating points considered, the impact of changes in the Mach number on the compliance of similarity is negligible. Furthermore, the derived similarity relation and respective sensitivities provide explanations for the physical relationship between the non-compliance of similarity and Helmholtz number and Mach number.

Regarding the acoustic quantities, the excitation frequencies of $f_{\text{exc}} = 520$ Hz and $f_{\text{exc}} = 813$ Hz are analyzed here by the way of example, for test case 1 and test case 2 respectively. The findings are confirmed for the other excitation frequencies (cf. Sec. A.9 and Sec. A.10 in the appendix). Variation in the modal frequency response can be observed for all excitation frequencies. The order of the variation in terms of the relative or absolute difference of the modal response relative to reference, however, varies for different data set in accordance with the modal response function depicted in Fig. 6.1 and Fig. 6.5. Results of the correlation analysis for all excitation frequencies are summarized in the appendix in Sec. A.8.

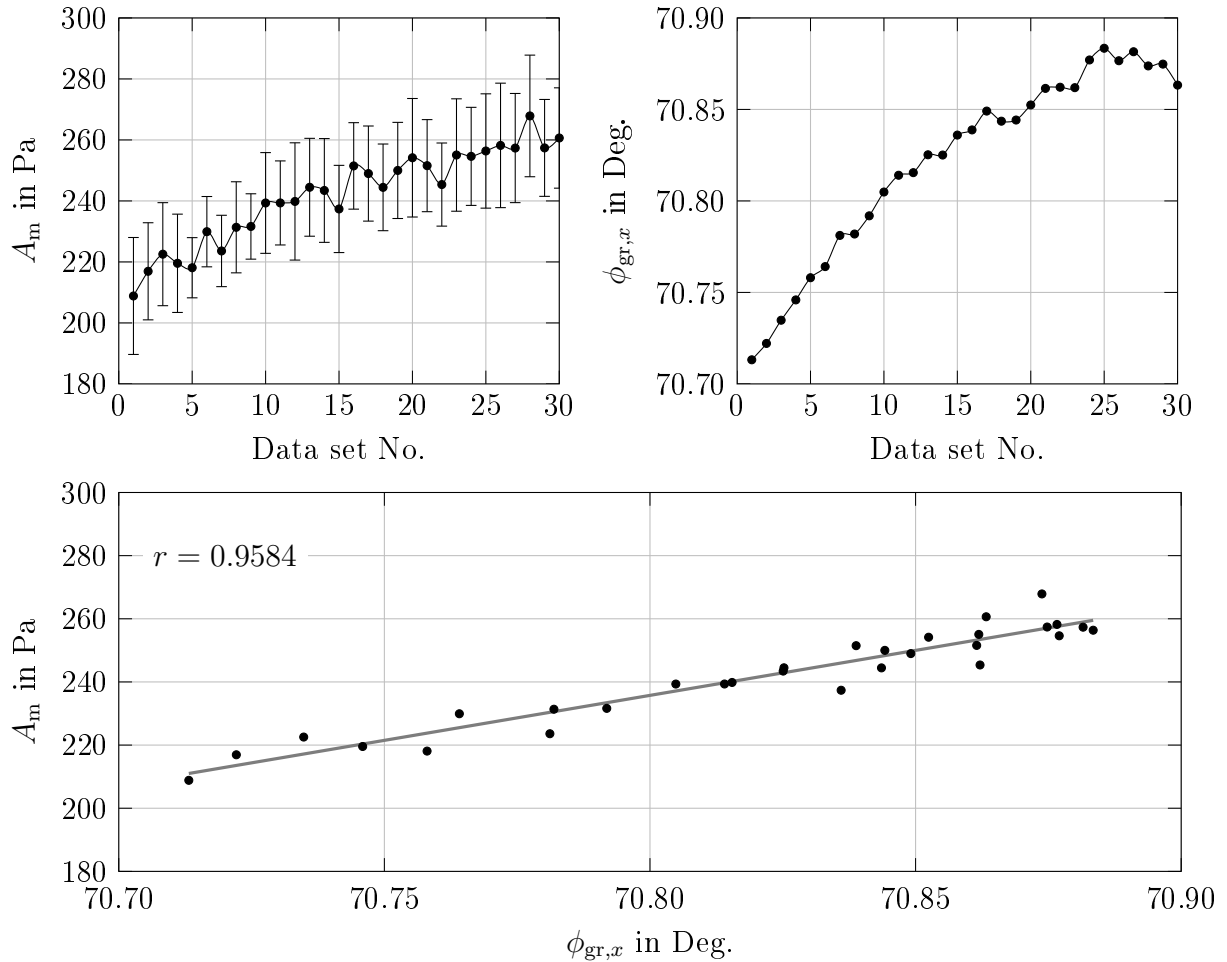


Figure 6.7: Correlation analysis for test case 2. Top left: Variations in the modal response. Top right: Variations in the angle of the group velocity vector. Bottom: Correlation of the modal response with the angle of the group velocity vector.

[Test case 2 | design-point operation | $m = 2$ | $f_{exc} = 813$ Hz]

6.1 Non-compliance with Similarity

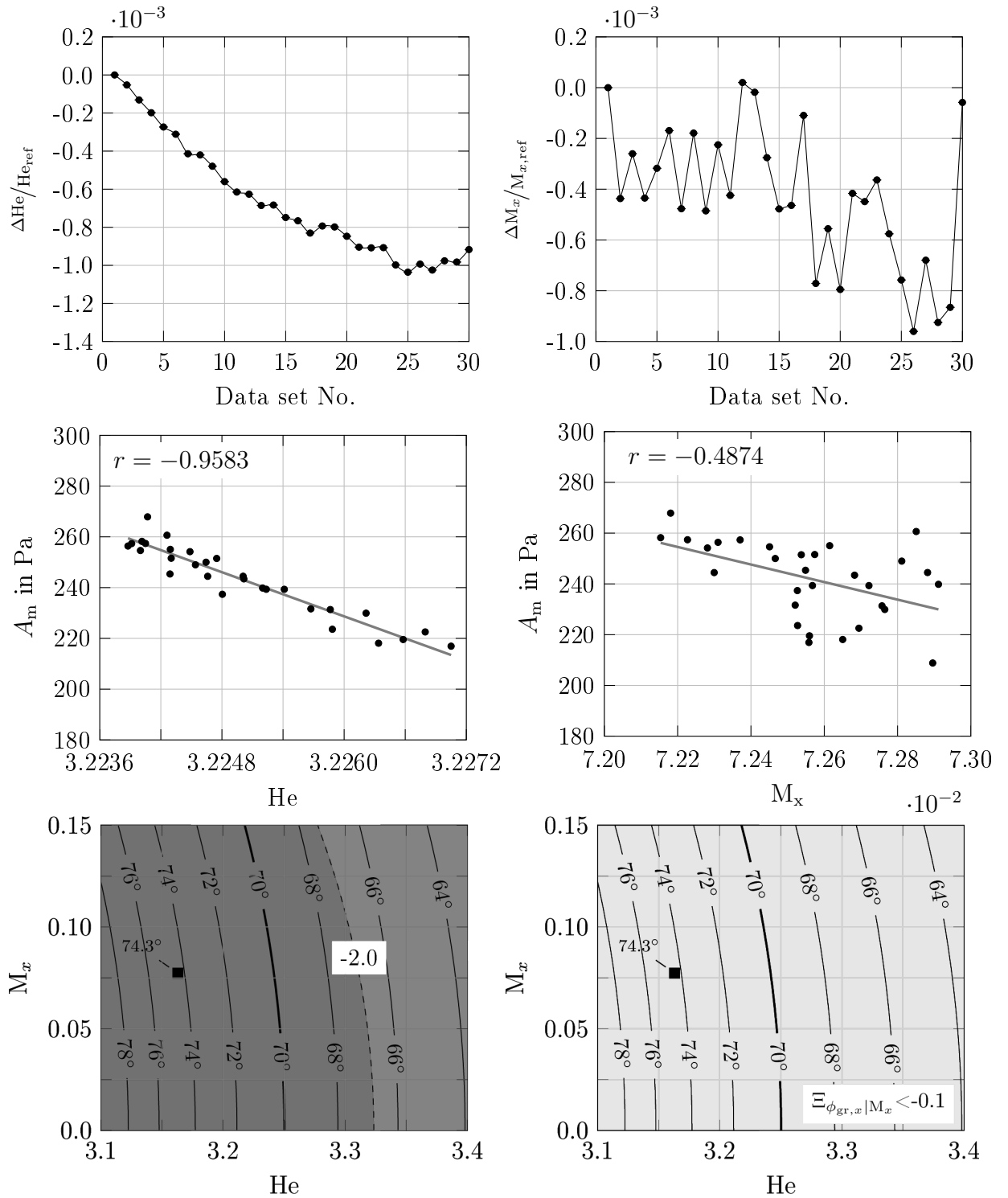


Figure 6.8: Relation between linear dependencies and the similarity relation. Top left: Relative change of the Helmholtz number. Top right: Relative change of the Mach number. Center left: Correlation of the modal response with the Helmholtz number. Center right: Correlation of the modal response with the axial Mach number. Bottom left: Extract of the similarity map ($\Xi_{\phi_{gr,x}|He}$). Bottom right: Extract of the similarity map ($\Xi_{\phi_{gr,x}|M_x}$). The square marks the operating point.

6.2 Procedure of Post-hoc Scaling

For the test cases, similarity conditions for sound propagation are not satisfied since equality of the similarity parameters, the Mach number and the Helmholtz number, is not achieved between the individual measurements. Non-compliance with similarity becomes readily apparent in the substantial differences in the modal responses measured in the inlet duct of the LPT for the different measurements.

As outlined in Sec. 2.3, complete similarity of sound field propagation can only be achieved if the exact values of both parameters are met. For this, full control of the parameters is necessary. Practically, the Helmholtz number can be controlled comparatively easily by adapting the excitation frequency of the synthetic sound field generation. While the Helmholtz number can thus be fully controlled, control of the Mach number is limited. For an open circuit test rig, especially, at least small variations in the Mach number are nearly always to be expected, as is the case here.

The hypothesis of this work implies that even though the Mach number and / or the Helmholtz number are not equal, partial similarity in terms of the propagation properties for one specific mode can still be achieved if the axial angle of the group velocity vector is kept equal between the measurements.

Similarity of modal sound propagation has not been considered in particular in advance of the current measurements. Therefore, the validation of the angle of the group velocity vector relative to the duct axis as a possible parameter for partial similarity has to be carried out by means of a post-hoc scaling approach. For this purpose, the data sets already collected are post-processed with the objective to identify measurements for which similarity holds. Similarity is evaluated here on the basis of the modal response function. If the determined pressure amplitudes of the reconstructed modal sound fields are equal for the same axial angle of the group velocity vector $\phi_{\text{gr},x}$, the latter thus presents a suitable parameter for establishing partial similarity with respect to modal sound propagation.

With the *reduced frequency* defined in Eq. (3.42), given by

$$(f_{\text{red}})^2 = \frac{c^2 [M_x^2 (\cos(\phi_{\text{gr},x}^*)^2 - 1) + 1] u_{mn}^2}{(2\pi R)^2 (1 - \cos(\phi_{\text{gr},x}^*)^2)}$$

the exact frequency can be determined which will, according to the hypothesis, establish modal propagation similarity between the 30 measurements for each of the two test cases presented in the previous section. In other words, the reduced frequency is the excitation frequency which yields the reference angle $\phi_{\text{gr},x}^*$ even though Mach number and / or Helmholtz number changed with respect to reference. The post-hoc scaling approach developed here is based on this frequency and can be described for a reference set of similarity parameters M_x^* and He^* by the following relation

6.2 Procedure of Post-hoc Scaling

$$\phi_{gr,x}^* = \Psi_{\phi}(M_x^*, He^*, m) = \Psi_{\phi}(M_x, He_{red}, m),$$

where the reduced Helmholtz number depends on the reduced frequency (cf. Sec. 3.3).

The process of the post-hoc scaling carried out for each data set is schematically illustrated in Fig. 6.9. The general procedure involves the following main steps:

- (1) Stipulation of reference conditions and calculation of the reference angle $\phi_{gr,x}^*$.
- (2) Determination of the reduced frequency by using the aerodynamic data collected at the time of the acoustic measurements.
- (3) Reconstruction of the modal response function \mathbf{A} by determining the pressure amplitudes A_m at the reduced frequency for each data set.

First, a reference condition has to be defined. The second activity involves the calculation of the reduced frequency with respect to reference condition. The modal pressure amplitude at the reduced frequency is then determined post-hoc based on the modal frequency-response function measured for the data set considered. As the reduced frequency has not been explicitly considered for sound field excitation, the set of excited frequencies does not necessarily include the reduced frequency calculated. Post-hoc scaling is thus restricted by the excited frequency range. If the reduced frequency is not within the frequency range specified, but smaller than the lowest frequency excited ($f_{red} < f_{exc,min}$), or larger than the highest frequency excited ($f_{red} > f_{exc,max}$), post-hoc scaling cannot be performed. In this case, the modal response measured for the lowest or highest excitation frequency is used, respectively. If the reduced frequency lies within the frequency range, but does not exactly match one of the excitation frequencies, linear interpolation is used to reconstruct the modal pressure response. The acoustic modes have been excited in uniform frequency steps of one Hertz in the frequency range specified. Hence, a finite but large set of frequencies is available for post-hoc scaling. If the reduced frequency lies within the frequency range, the modal pressure amplitude is interpolated to that frequency using the values of the adjacent frequencies. The described process is repeated for all frequencies or angles of the group velocity vector, respectively, under consideration.

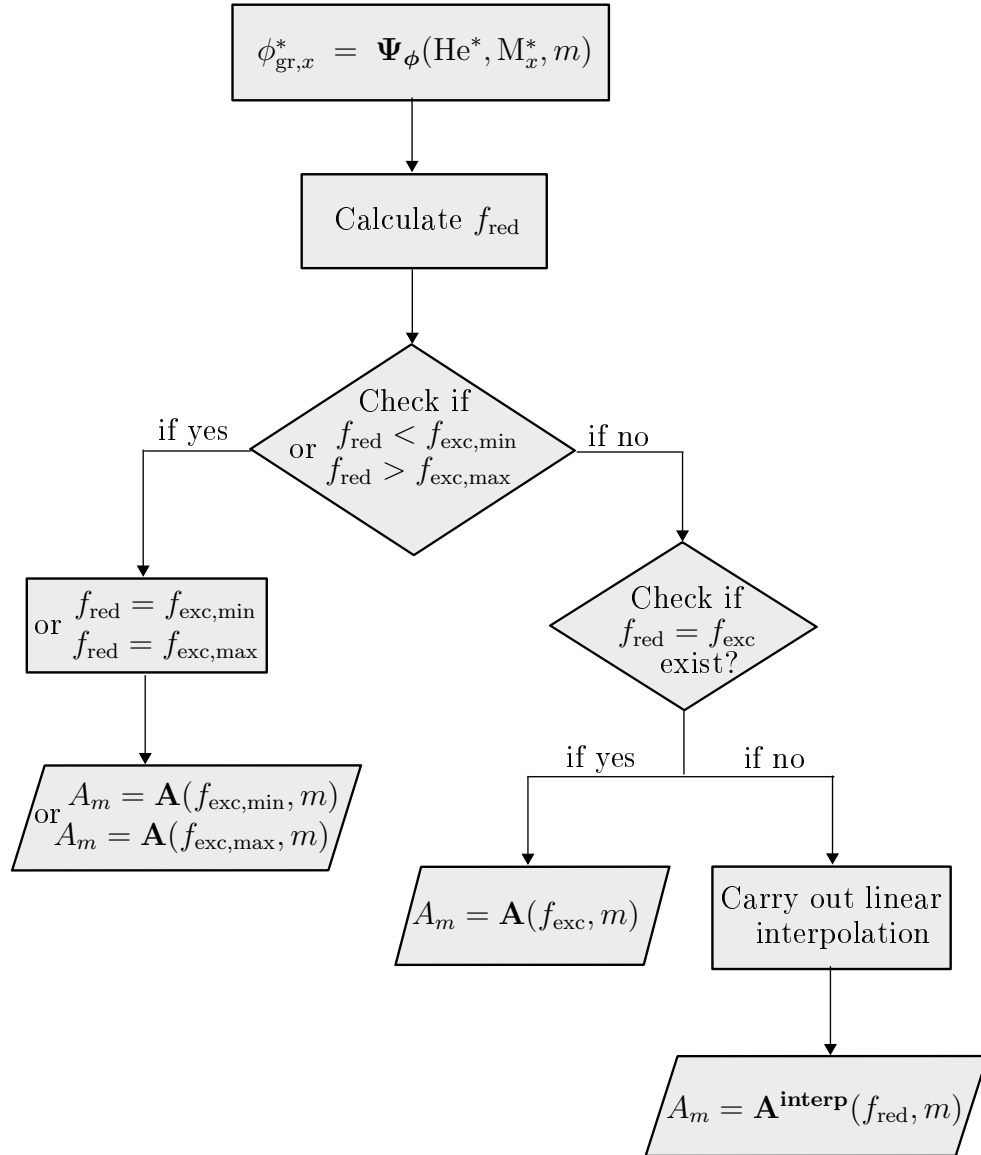


Figure 6.9: Schematic illustration of the process of applied post-hoc scaling for approximation of modal sound propagation similarity.

6.3 Discussion of the Results

In this section, the results of the post-hoc scaling performed are presented and analyzed with respect to the achievement of modal similarity. The results of post-hoc scaling are shown for test case 1 at part-load operation and for test case 2 at design-point operation in Fig. 6.10 and Fig. 6.12, respectively. For both test cases the conditions during the measurement of data set No. 1 are taken as reference, thus $\text{He}^* = \text{He}^{[1]}$, $\text{M}_x^* = \text{M}_x^{[1]}$, and $\phi_{\text{gr},x}^* = \phi_{\text{gr},x}^{[1]}$. The results of post-hoc scaling are evaluated with respect to the modal frequency-response function as displayed in the left diagram of Fig. 6.1 and Fig. 6.5. The corresponding modal group velocity angles depicted in the right diagram of the respective figures therefore represent the reference angle $\phi_{\text{gr},x}^*$ for the frequency considered.

In the diagrams on top of Fig. 6.10 and Fig. 6.12, the modal response functions of the different data sets are displayed as colored shaded surface plots. This form of presentation has the advantage that the variations in the pressure amplitudes between the measurements are very well displayed visually. The surface plot on the left side shows the values of the pressure amplitude measured for the original sound field, whereas in the plot on the right side, the determined amplitudes of the reconstructed sound field are shown⁴. In both diagrams the abscissa is the data set number. The ordinate, however, differs between the two plots. In the surface plot showing the original modal response, the excitation frequencies are displayed on the ordinate. For the post-hoc version, the angle of the group velocity vector is used to define the range on the ordinate. The pressure amplitudes in the two diagrams at the top of the figure are normalized with the maximum value of the respective response function. Low values are thereby indicated by the color blue and high values by the color red, where the maximum value is one due to normalization. The color legend is the same for the original values and for the post-hoc values. Please note the different ranges of values for test case 1 and test case 2. For the part-load operation displayed in Fig. 6.10, the normalized pressure amplitude is evaluated in the range from approx. 0.17 to a value of 1. For design-point operation, the values range from approx. 0.44 to 1.

The hypothesis of this work is tested by evaluating similarity of modal sound propagation in terms of variations in the measured modal response. To quantify the differences and the improvements due to post-hoc scaling, the relative change between two responses is determined. For the original sound field, the relative change between the modal response for a specific excitation frequency f_{exc} with respect to the modal response measured for that frequency at reference condition is calculated. For analysis of the results of post-hoc scaling, the relative change is calculated with respect to the modal response determined for the respective reference angle $\phi_{\text{gr},x}^*$; thus the angle determined for data set No. 1 for the respective frequency. The absolute values of the relative change are shown in the surface plots at the bottom of Fig. 6.10 and Fig. 6.12. Low values of the relative difference are indicated by the color blue and high values by the color red. Please note again the different range of values for test case 1 and test case 2.

⁴Here, the term *original* refers to the sound field actually measured in comparison to the reconstructed field from post-hoc scaling.

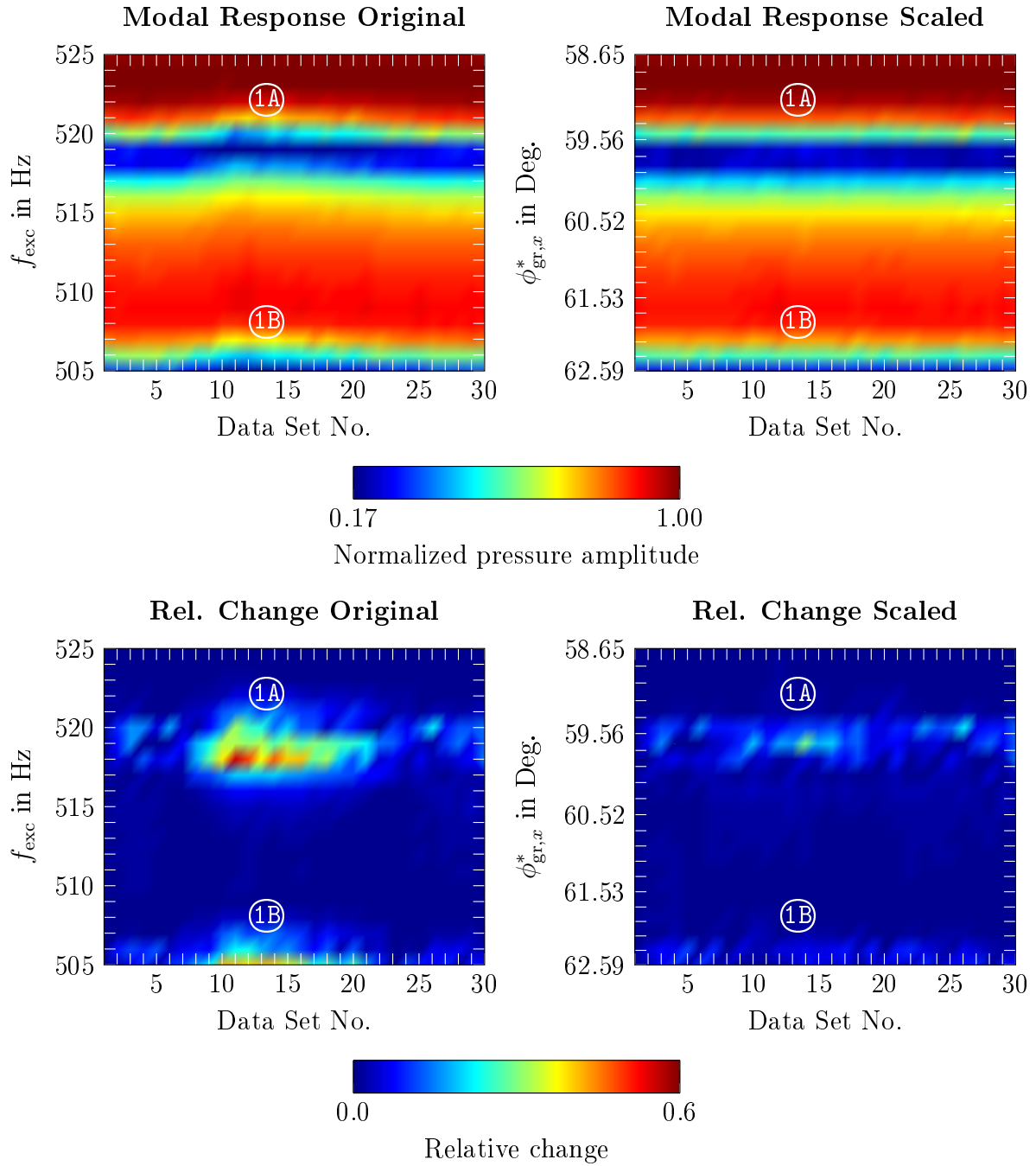


Figure 6.10: Surface plots of results of post-hoc scaling. Top: Normalized modal amplitudes before and after post-hoc scaling. Bottom: Absolute relative difference of the modal amplitudes relative to reference before and after post-hoc scaling.

[Test case 1 | part-load operation | $m = -1$]

6.3 Discussion of the Results

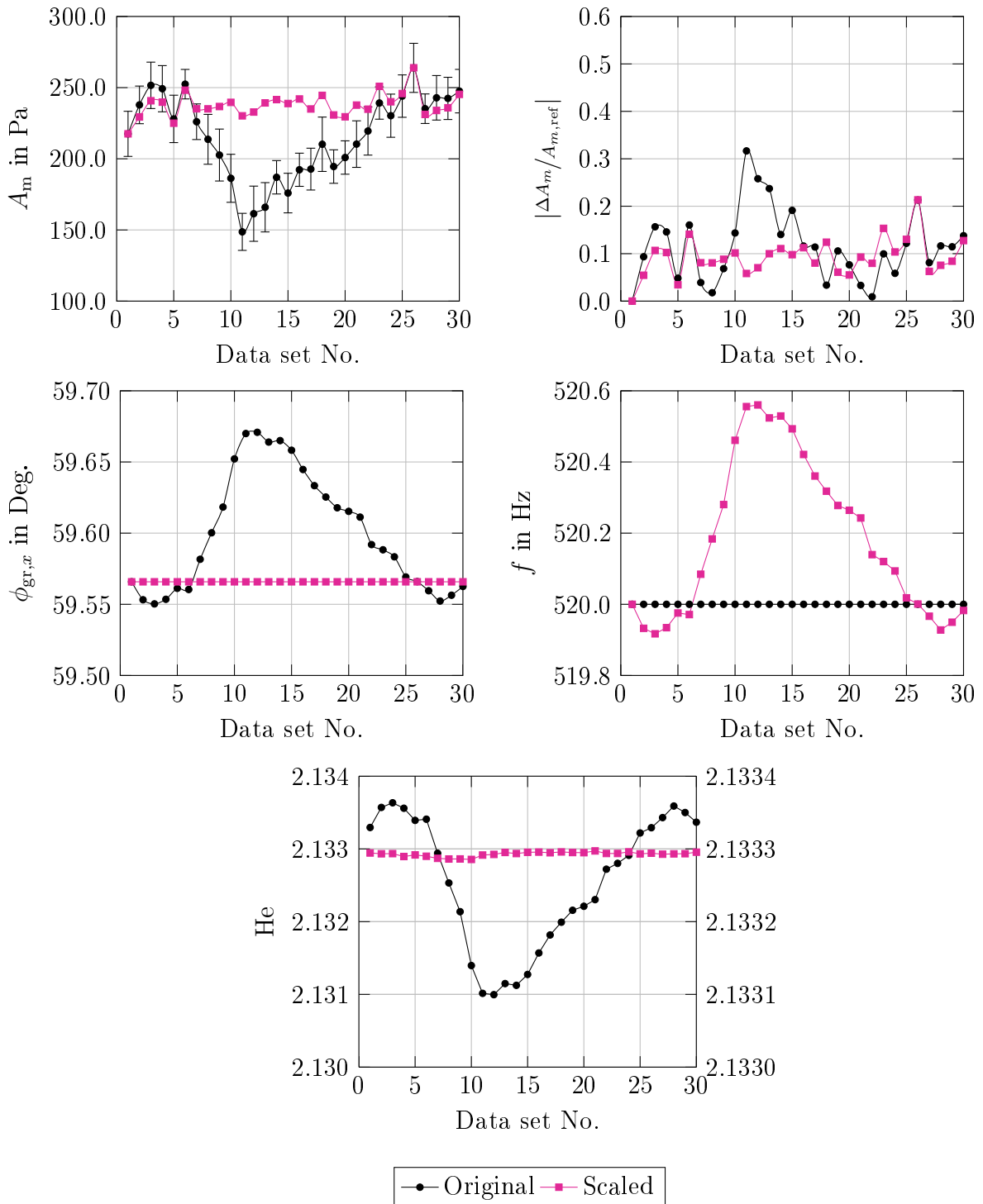


Figure 6.11: Results of post-hoc scaling. Top left: Modal amplitude. Top right: Relative change of the modal amplitude with respect to reference data set No.1. Center left: Group velocity angle. Center right: Excitation frequency and calculated reduced frequency. Bottom: Helmholtz number (the lines and markers colored in black and magenta refer to the left and the right ordinate, respectively).

[Test case 1 | part-load operation | $m = -1$ | $f_{exc} = 520$ Hz]

For the part-load operation displayed in Fig. 6.10, the relative change is evaluated in the range from zero to a value of 0.6. For design-point operation, the relative change ranges from zero to 0.35. The surface plots are analyzed for both test cases in detail below. and test case 2. For the part-load operation displayed in Fig. 6.10, the relative change is evaluated in the range from zero to a value of 0.6. For design-point operation, the relative change ranges from zero to 0.35. The surface plots are analyzed for both test cases in detail below.

6.3.1 Test case 1: Results of post-hoc scaling

Analysis of the surface plots

The color-shaded visualisation of the modal frequency response in the left diagram of Fig. 6.10 shows that the general characteristic of the response function is comparable for all data sets. In the surface plots, high pressure gradients are reflected by large shade differences in the direction of the ordinate. Regions of only slowly changing color characterize a gentle decrease or increase in the pressure amplitude. The distinct local extrema as already described in Sec. 6.1.1 when analyzing the modal response function of the reference data set No. 1, can also be identified from the surface plots in this manner.

Although the general characteristic of the modal response function is similar for all data sets, two regions with significant discrepancies in the modal pressure amplitude with respect to reference data set No. 1 can be identified. These regions are restricted in their spatial distribution with respect to the data sets on the one hand and with respect to the range of frequencies on the other hand. With respect to the colored visualization, a kind of blur-type effect can be observed, as the contours of the color shades are no longer unambiguously identifiable. The direction of the streaks are towards higher frequencies. For the sake of conciseness, these regions are highlighted by a number-letter combination in a circle. The first region marked (1A) stretches approximately from data set No. 10 to set No. 20 and from $f_{\text{exc}} = 517 \text{ Hz}$ to $f_{\text{exc}} = 522 \text{ Hz}$. The second region marked (1B), also stretches approximately from data set No. 10 to set No. 20. The concerned frequencies range from approximately $f_{\text{exc}} = 505 \text{ Hz}$ to $f_{\text{exc}} = 507 \text{ Hz}$. Comparison with the modal frequency-response function depicted in Fig. 6.1, shows that these frequencies are within an area where large gradients of the pressure amplitude occur. Furthermore, according to the analysis of the variations in the angle of the group velocity vector (cf. Fig. 6.3), it is found that the variations detected here are highest for the same data sets for which the highest variation in the angle considered are detected. Comparison with the calculated relative changes displayed in the diagram at the bottom left shows that the highest differences in the modal response with respect to reference are indeed detectable in the areas (1A) and (1B) described above. The maximum value of a relative change of 0.549 refers to a frequency of $f_{\text{exc}} = 518 \text{ Hz}$ for data set No. 11 in the region (1A). The second highest value of 0.416 is located in the region (1B) and is detected for $f_{\text{exc}} = 505 \text{ Hz}$ and data set No. 10. For the other measurements, similarity is approximately achieved as can be seen from the very low relative changes visualized by the blue coloring. The still existing difference, might be attributed to different causes which are discussed below in

6.3 Discussion of the Results

Sec. 6.4 of this chapter. This section is concerned with the limits of post-hoc scaling with respect to the given measurement data and measurement setup.

The surface plot on the right side of Fig. 6.10 show the pressure amplitudes after post-hoc scaling. A significant decline of the variations in the modal pressure amplitudes in the previously identified areas can be observed. This is confirmed by the calculated relative changes. Here, the maximum value of the regions (1A) and (1B) declines from 0.5493 (at $f_{\text{exc}} = 518$ Hz for set No. 11) to 0.284 (at $f_{\text{exc}} = 519$ Hz for set No. 14), and from 0.416 (at $f_{\text{exc}} = 505$ Hz for set No. 10) to 0.105 (at $f_{\text{exc}} = 506$ Hz for set No. 5). Overall, the surface plots are smoothed out as the differences in the modal responses are reduced due to post-hoc scaling.

It can be summarized that most significant variations in the modal response occur in areas of high pressure gradients. This observation is focused on in more detail in the subsequent section (cf. Sec. 6.3.3). Furthermore, post-hoc scaling with respect to the axial angle of the group velocity vector results in considerable improvements in modal similarity. This supports the hypothesis of this work.

Results for $f_{\text{exc}} = 520$ Hz

The diagrams in Fig. A.22 show the results of post-hoc scaling by way of example for the previously analyzed excitation frequency of $f_{\text{exc}} = 520$ Hz. The respective values for the other frequencies are depicted in the diagram in the appendix in Sec. A.9. The black lines with the circle markers present the original values also depicted in the diagrams in Fig. 6.3. The purple lines with the square markers present the quantities resulting from post-hoc scaling. The distribution of the modal response and the relative change in the diagram on the top left side and right side, respectively, show in detail the major improvement in modal similarity as a result of post-hoc scaling. In the diagram at the center left the values of the axial angle of the group velocity vector are shown. Both, the angles of the measured sound field as well as the angles calculated with respect to the reduced frequency, are depicted. In the diagram at the center right, the excitation frequencies and the calculated reduced frequencies are depicted for each data set. The latter is the frequency with which the acoustic mode should be excited to establish similarity relative to the reference. The respective Helmholtz numbers are displayed in the diagram at the bottom. For better clarity, two ordinates are used in these diagrams where the left ordinate serves as a measure for the original values and the left ordinate for the scaled values.

The angle of the group velocity vector calculated after post-hoc scaling has exactly the same value for each data set, which confirms the accurate calculation of the reduced frequency. In contrast to the axial Mach number, the Helmholtz number is directly affected by the establishment of partial similarity. In the previous section, it has been shown, that the variations in the group velocity angle are predominantly caused by variations in the Helmholtz number. Therefore, the reduced Helmholtz number is nearly constant after post-hoc scaling for all data sets. Minor variations still exist, however. The reduced frequency of data set No. 1 corresponds to the excitation frequencies as

this data set is taken as reference. Generally, the reduced frequency approximates the excitation frequency if the group velocity angle approximates the reference angle $\phi_{\text{gr},x}^*$. Finally, it should be emphasized that even though the absolute difference between the excitation frequency and the reduced frequency is in an order smaller than one Hertz for all data sets⁵, the impact on the modal response is profound and highly impairs the comparability of the measurements. The reason for this lies in the high pressure gradients characterizing the modal response function of the mode considered.

6.3.2 Test case 2: Results of post-hoc scaling

Analysis of the surface plots

The surface plots for test case 2 are shown in Fig. 6.12. Here, two regions with a distinct color blurring in the direction of higher frequencies can be identified for the original measurement data. The regions are marked (2A) and (2B). The corresponding excitation frequencies are $f_{\text{exc}} = 802$ Hz and $f_{\text{exc}} = 814$ Hz. At these frequencies, the local extrema of the modal frequency-response function are located (cf. Fig. 6.1). For test case 2, the regions are not restricted to specific measurements as for test case 1, but stretch from reference data set No. 1 to the last data set. Thereby, the blurring slowly increases in intensity and, correspondingly the relative change with respect to reference condition illustrated in the diagram on the bottom increases. This correlates with the slowly rising flow temperature and the resulting change in the similarity parameters as explained in Sec. 6.3.1. The maximum values for the relative change are determined for data set No. 28 and No. 30 with a maximum value of 0.336 and 0.311, respectively. For frequencies where the pressure gradient is comparatively low, the modal response again shows little variation across the different data sets, e.g. around a frequency of $f_{\text{exc}} = 807$ Hz. Overall, it can be observed, that the absolute values for the relative changes between the modal responses are lower than for test case 1, where a maximum relative deviation of 0.549 is determined. This can be explained by the smaller pressure gradients detected for the modal frequency-response function of test case 2 in comparison to test case 1.

The results of post-hoc scaling are visualized in the surface plots on the right side of Fig. 6.12. Blurring is still apparent but reduced. Analysis of the relative change of the modal response displayed in the plot at the bottom right shows that similarity of modal propagation is approximated. The maximum deviations in the two characteristic regions decrease from 0.336 to 0.191 (at $f_{\text{exc}} = 802$ Hz for set No. 28 and at $f_{\text{exc}} = 802$ Hz for set No. 28, respectively), and from 0.311 to 0.189 (at $f_{\text{exc}} = 814$ Hz for set No. 30 and at $f_{\text{exc}} = 814$ Hz for set No. 26, respectively), respectively. Furthermore, the spatial spread of high deviations is now limited to two narrow bands around the angles $\phi_{\text{gr},x} = 73.08^\circ$ and $\phi_{\text{gr},x} = 70.51^\circ$. These angles correspond to the frequencies $f_{\text{exc}} = 802$ Hz and $f_{\text{exc}} = 814$ Hz for reference condition (data set No. 1).

⁵In fact, the maximum difference is $\Delta f = 0.56$ Hz for data set No. 12.

6.3 Discussion of the Results

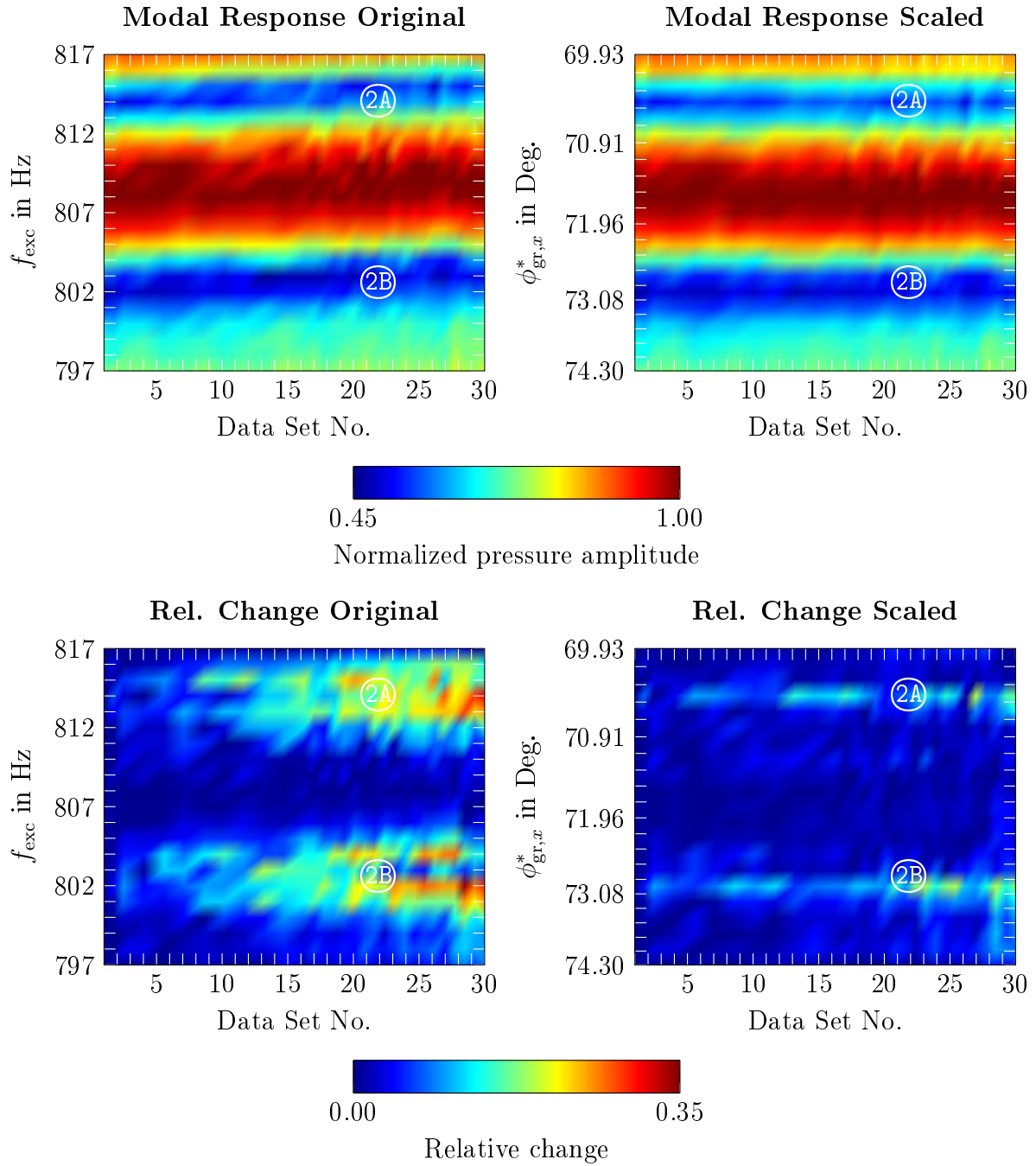


Figure 6.12: Surface plots of results of post-hoc scaling. Top: Normalized modal amplitudes before and after post-hoc scaling. Bottom: Absolute relative difference of the modal amplitudes relative to the reference before and after post-hoc scaling.

[Test case 2 | design-point operation | $m = 2$]

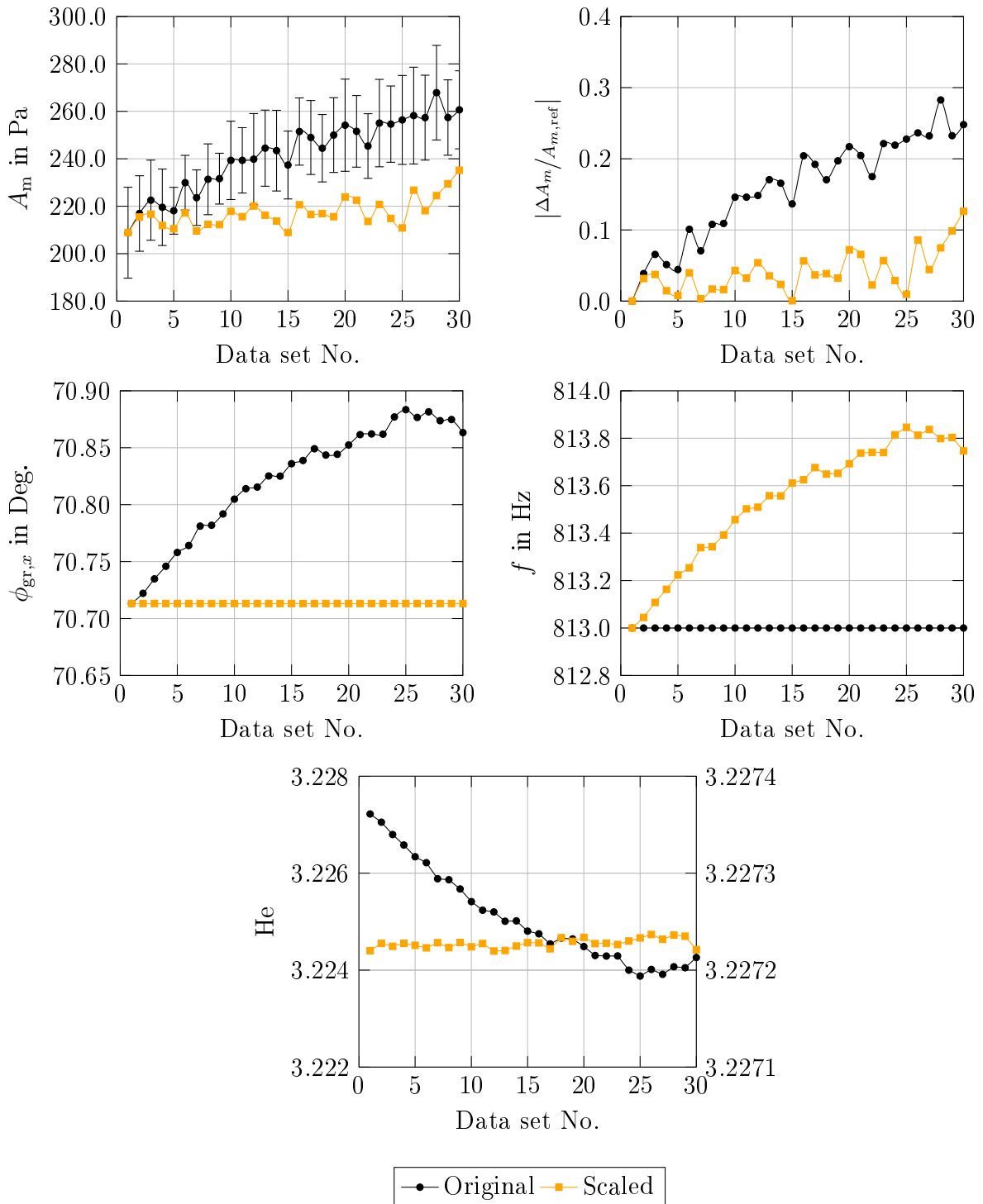


Figure 6.13: Results of post-hoc scaling. Top left: Modal amplitude. Top right: Relative change of the modal amplitude with respect to reference data set No.1. Center left: Group velocity angle. Center right: Excitation frequency and calculated reduced frequency. Bottom: Helmholtz number (the lines and markers colored in black and orange refer to the left and the right ordinate, respectively).

[Test Case 2 | design-point operation | $m = 2$ | $f_{exc} = 813$ Hz]

6.3 Discussion of the Results

Results for $f_{\text{exc}} = 813 \text{ Hz}$

In Fig. A.44, the results of post-hoc scaling for the previous analyzed frequency of $f_{\text{exc}} = 813 \text{ Hz}$ are shown. The respective values for the other frequencies are depicted in the diagram in the appendix in Sec. A.9. For the major part, the same observations as for test case 1 can be made: The angle of the group velocity vector calculated with respect to the determined reduced frequency is the same for each data set, confirming the calculation procedure of the post-hoc scaling. The scaled Helmholtz number is again nearly constant with only small variations due to strong correlation of the latter with the group velocity angle. The difference between the excitation frequency and the frequency with which the sound field should have been excited in order to satisfy modal similarity under the changed aerodynamic conditions is again marginal with less than one Hertz. The scaled values for the modal responses show fewer variations. For the major part of the data sets (up to No. 25), the amplitudes fluctuate quite constantly around the same value. Only for the last measurements, modal similarity is still impaired.

In summary, the analysis of the surface plots in Fig. 6.12 shows that regions with pronounced blurring, and thus with high relative changes in the amplitudes measured, correspond to regions of high pressure gradients of the modal response function. Comparison of the relative changes of the modal response for the original data and the scaled data as well as analysis of the individual responses for a chosen frequency shows that even though similarity is not met for all data sets and frequencies, it can be noted that the post-hoc scaling results in significant improvements in the modal similarity evaluated with regard to the modal responses. Both findings are in line with the findings of the analysis of test case 1.

6.3.3 Alteration of the modal response function

In this section, the modal response functions for two chosen data sets are compared in detail with the response functions of reference data set No.1 for test case 1 and test case 2. The objective is to provide physical explanations to the observed variations in the modal response and the observed dependence of the magnitude of variation on the pressure gradient. For this, the modal response functions are analyzed as a function of the excitation frequency $A_m = \mathbf{A}(f_{\text{exc}})$ (cf. Sec. 6.1) first, and further also relative to the angle of the group velocity vector, $A_m = \mathbf{A}(\phi_{gr,x})$.

Test Case 1

In figure 6.14, the modal response functions determined for data set No. 5 and No. 11 of test case 1 are represented by the magenta-colored lines and markers. The response function for reference data set No. 1 is depicted in addition and represented by the lines and markers colored in black. In the diagrams at the top of the figure, the modal responses for data set No. 1 and data set No. 5 are shown for comparison. For both forms of displays of the response function, the modal pressure amplitudes match nearly exactly for all data points. This confirms the previous finding that similarity of modal propagation is adequately satisfied for the first data sets, thus $\text{He}^{[5]} \approx \text{He}^*$,

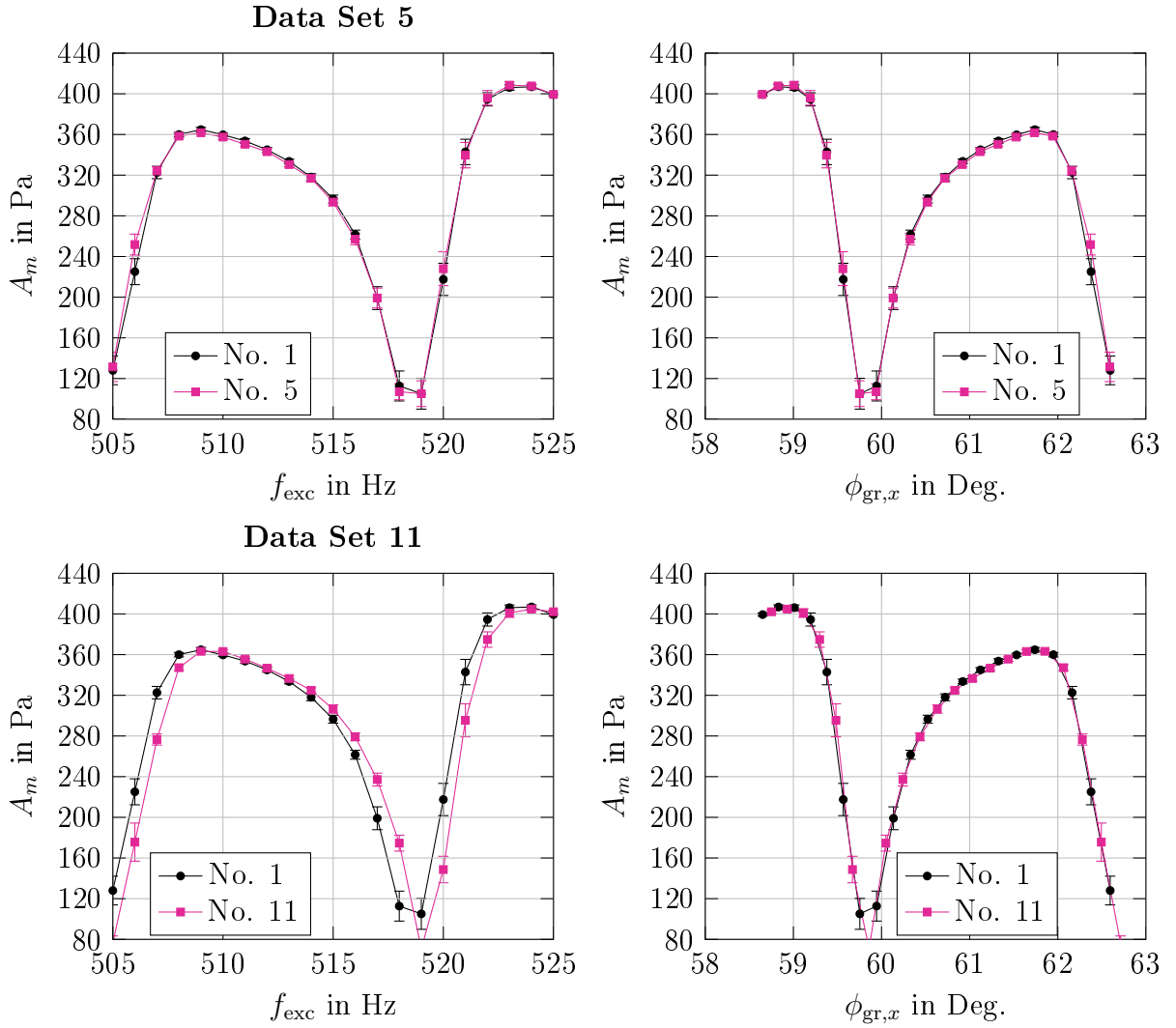


Figure 6.14: Alteration of the modal response function. Top: Modal frequency-response function relative to the excitation frequency and relative to the angle of the group velocity vector for data Set No. 5. Bottom: Modal frequency-response function relative to the excitation frequency and relative to the angle of the group velocity vector for data Set No. 11.

[Test case 1 | part-load operation | $m = -1$ | different data sets]

$M_x^{[5]} \approx M_x^*$, and $\phi_{gr,x}^{[5]} \approx \phi_{gr,x}^*$ holds. Accordingly, the modal response functions depicted as a function of the group velocity angle in the diagrams on the right side of the figure, lie nearly perfectly above one another. For the second example chosen, the situation is substantially different. The modal frequency-response functions for data set No. 1 and set No. 11 do not match and clearly deviate from each other. As outlined before, the flow temperature measured for data set No. 11 and as a result the angle of the group velocity vector differs from the reference value, and thus similarity conditions are not

6.3 Discussion of the Results

met ($\text{He}^{[11]} \neq \text{He}^*$, $M_x^{[11]} \neq M_x^*$, and $\phi_{\text{gr},x}^{[11]} \neq \phi_{\text{gr},x}^*$). Analyzing the divergence of the individual modal responses of data set No. 11 with respect to the reference function, it becomes evident that the individual points are shifted along the abscissa in the direction of higher frequencies. Taking the frequency $f_{\text{exc}} = 520$ Hz as an example, it is found that in order to excite the same modal response as for data set No. 1, the sound field has to propagate with a higher frequency. In fact, the exact value is known from the analysis of post-hoc scaling results and is $f_{\text{red}} = 520.55$ Hz (cf. calculated reduced frequencies in the diagram on the top right of Fig. A.22). This example shows that the differences detected in the modal amplitudes at the same frequency can be explained by a shift of the modal frequency-response function. Although the shift is only minor, it noticeably alters the modal response and results in high relative deviations of the modal pressure amplitude with respect to reference. Visually, this results in the formerly identified blur-type effect in the surface plots. In the diagrams on the right side of Fig. 6.14, the modal response functions are depicted as a function of the group velocity angle. Again the response functions lie nearly perfectly above one another. However, while the markers overlap for the pair of data set No. 1 and set No. 5, the markers of data set No. 11 are displaced with respect to reference for the pair of data set No. 1 and data set No. 11. The latter is the result of non-compliance with similarity and the cause for the variation in the measured pressure amplitudes. The angles for data set No. 11 are higher than the angles for data set No. 1 at the same frequency. This results from the positive correlation of flow temperature and group velocity angle given here. Furthermore it provides explanation why the modal responses with respect to the excitation frequency are shifted towards higher frequencies, as the left diagrams reveal⁶.

For the sake of clarity regarding the observation that high deviations in the amplitude are not detected across the complete frequency range but mainly for frequencies located in areas with a high pressure gradient, a second example shall be considered. For this purpose, the modal response at the excitation frequency of $f_{\text{exc}} = 509$ Hz is investigated. From the results of post-hoc scaling it is known that in order to achieve partial similarity, the sound field of data set No. 11 should be excited at $f_{\text{red}} = 509.54$ Hz. However, as the modal frequency-response function is comparatively even at the specified frequency, it is found that nearly the same modal pressure amplitude is detected when exciting the sound field with the original frequency of $f_{\text{exc}} = 509$ Hz. The shift in the response function therefore does not result in a change in the amplitude in this case. Accordingly, no blurring in the area of this frequency can be detected in the surface plots (cf. Fig. 6.10). Thus, although similarity conditions are not met here, the same amplitude is excited, simply because the modal response is not sensitive to changes in the frequency range investigated. In the diagrams on the right side of Fig. 6.14, the modal response functions are depicted as a function of the group velocity angle. Again the response functions lie nearly perfectly above one another. However, while the markers overlap for the pair of data set No. 1 and set No. 5, the markers of data set No. 11 are displaced to data set No. 1. The latter is the result of non-compliance with similarity and the cause for the variation in the measured pressure amplitudes. The angles for

⁶Note that the flow temperature measured for data set No. 11 is increased compared to data set No. 1 (cf. Fig. 6.2).

data set No. 11 are higher than the angles for data set No. 1 at the same frequency. This results from the positive correlation of flow temperature and group velocity angle given here. This also provides explanation why the modal responses with respect to the excitation frequency are shifted towards higher frequencies, as the left diagrams reveal.⁷

Test Case 2

For test case 2, corresponding observations can be made. For the measurements at design-point operation, similarity is not met for any of the data sets. Hence, the modal response function relative to the excitation frequency deviates from reference in all data set. In figure 6.15, the response functions of data set No. 15 (top) and data set No. 28 (bottom) are depicted together with the reference function. During the measurements for test case 2, the flow temperature constantly increased (cf. Fig. 6.6). With respect to the modal frequency responses, the change in temperature again causes a shift of the individual points towards higher frequencies as the angle of the group velocity vector increases. The variations in the modal response for the example of $f_{\text{exc}} = 813$ Hz, as previously analyzed in Fig. A.44, can be explained, thereby. A higher amplitude is measured for $f_{\text{exc}} = 813$ Hz than for data set No. 1 for both data sets. Considering the change in flow temperature for the respective data set, the sound field should theoretically have been excited with $f_{\text{red}} = 813.611$ Hz and $f_{\text{red}} = 813.798$ Hz for data set No. 15 and No. 28, respectively, in order to achieve partial similarity and excite the same modal response.

If the modal response is displayed relative to the group velocity angle, the two response functions approximate each other. For the pair of data set No. 1 and No. 15, the two functions match very well inasmuch as the confidence intervals overlap along the profile of the function. For data set No. 1 and No. 28 showed in the diagram at the bottom of the figure, the modal response functions only partly lie on top of each other. For higher angles, even though the confidence intervals still overlap, the mean pressure amplitudes are discernibly higher than the reference amplitudes. This effect seems to be frequency-dependent on the one hand, and, considering the surface plots, also dependent on the data set number (thus, on the time of measurement), on the other hand. A possible explanation of these phenomena can be reflection at turning points when the mode propagates throughout the turbine as discussed in Sec. 6.4.

Theoretical analysis

Up to this point, the shifts in the modal responses have not been further quantified. From the non-linear relation between the angle of the group velocity vector and the frequency of the propagating acoustic mode according to Eq. (3.38), where the frequency enters via the Helmholtz number, it follows that the magnitude of the shift is frequency dependent. Thus, the alteration of the response function might be explained by shifts in the individual modal responses, but in total the function is compressed or stretched compared to reference. This characteristic of alteration is not discernible in the functions displayed because of the merely marginal shifts.

⁷Note that the flow temperature measured for data set No. 11 is increased compared to data set No. 1 (cf. Fig. 6.2).

6.3 Discussion of the Results

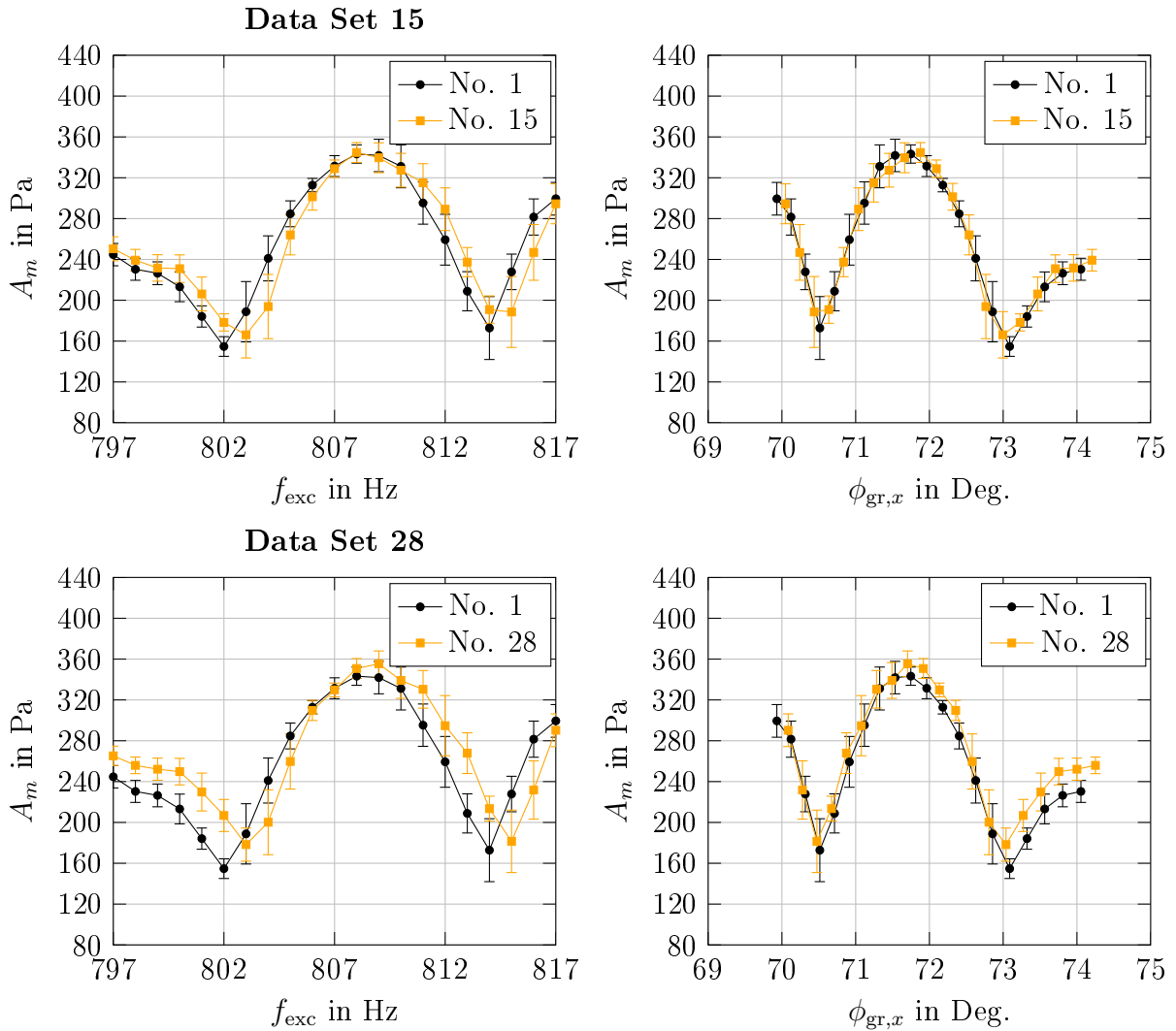


Figure 6.15: Alteration of the modal response function. Top: Modal frequency-response function relative to the excitation frequency and relative to the angle of the group velocity vector for data Set No. 15. Bottom: Modal frequency-response function relative to the excitation frequency and relative to the angle of the group velocity vector for data Set No. 28.

[Test case 2 | design-point operation | $m = 2$ | different data sets]

Based on this observation, two general cases of non-compliance with similarity with varying consequences can be identified, which are schematically shown in Fig. 6.16. The two cases differ in the characteristic of the modal response function. In the diagrams at the top of the figure, two modal response functions dependent on the excitation frequency are displayed for an arbitrary point in time $t = 1$. At this point in time, the modal response $A_m^{[1]}$ is detected at the frequency $f^{[1]}$. In the diagrams at the bottom, the

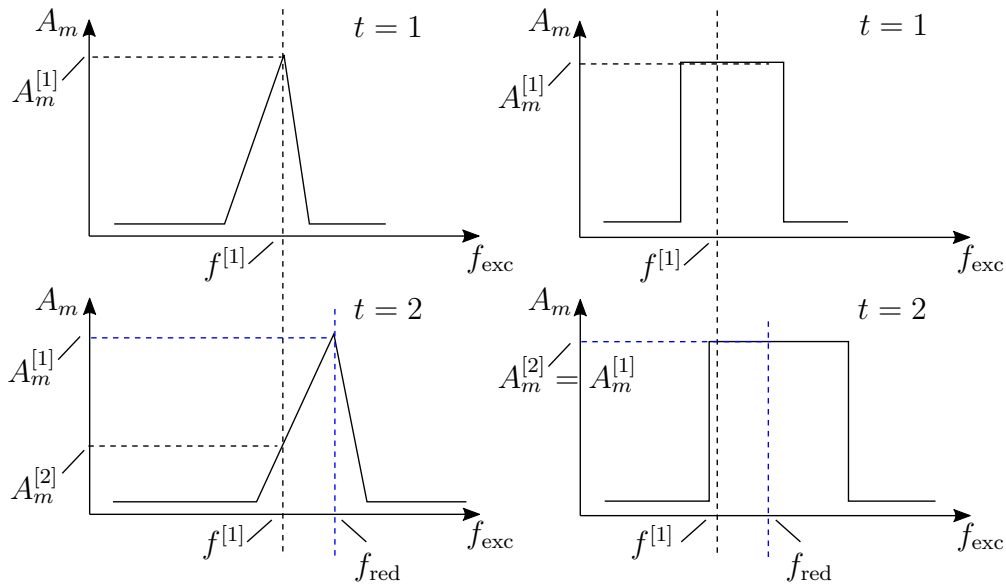


Figure 6.16: Schematic illustration of the impact of varying similarity conditions on the modal response function. Left: Modal response function with a pronounced peak. Right: Modal response function with a flat plateau.

same modal response functions are given under the assumption of changed aerodynamic conditions at an arbitrary point in time $t = 2$. For $t = 2$ both the amplitudes for $f^{[1]}$ and for f_{red} are marked, showing the impact of the changed conditions on the amplitudes measured.

The first case (left) reflects a situation where a narrowband effect with high pressure gradients towards lower and higher frequencies is investigated. As a result of the (assumed) variation of the similarity parameters, the function is stretched at $t = 2$ compared to $t = 1$ and the amplitude $A_m^{[2]}$ detected at $f^{[1]}$ is considerably lower than the amplitude $A_m^{[1]}$. In the extreme case, the considered effect would no longer be in the particular frequency range. The second case considers a modal response with a characteristic flat plateau over a certain frequency range. Again the illustration considers a stretching of the response function. However, in this case, the same modal response is measured at $t = 2$ and $t = 1$ even though the modal frequency response is altered. This is illustrated in the diagrams on the right side of the figure.

6.3.4 Findings

Based on the results of post-hoc scaling and the analysis of the alteration of the modal response function, it can be stated that

- (1) varying similarity conditions result in an axial compression or stretching of the modal frequency-response function, which is the cause for the observed variations in the measured amplitudes with respect to reference, and thus non-compliance of

6.4 Limits of post-hoc scaling

similarity.

- (2) the alteration of the response function can be revised by displaying the pressure amplitudes as a function of the group velocity angle, which supports that the latter is a suitable parameter for establishing partial similarity with respect to modal sound propagation.
- (3) post-hoc scaling by means of a reduced frequency derived from the similarity relation results in significant improvements in the modal similarity evaluated.
- (4) the level of impact of non-compliance with similarity differs from one case to another depending on the pressure gradient of the function in the considered area.

6.4 Limits of post-hoc scaling

The results of the post-hoc scaling with respect to the angle of the group velocity vector have shown significant improvements in the establishment of partial modal similarity between the different measurements. Nevertheless, for some frequencies and data sets, deviations between the determined (scaled) amplitudes and the reference amplitude still exist. Possible reasons for these deviations are discussed below.

Stability of sound field excitation

For sound field excitation, loudspeakers with a flat frequency response and a stable sound pressure level are chosen (cf. Sec. 4.2). Nevertheless, small differences between the amplitudes of two frequencies at the same power supply exist. Furthermore, long-term monitoring of the loudspeakers shows that the frequency response is irreversibly altered and that the sound pressure level becomes more irregular with long use of the speakers in demanding conditions of high temperature and pressure like in the LPT. Regular tests of the sound level of each loudspeaker between the measurement for the data sets used for the validation, however, have shown no significant variations. Thus, if existent, fluctuations in the modal pressure amplitude due to variations in the performance of the sound generator are to be considered negligible here.

Temporal offset between aerodynamic and acoustic measurements

Aerodynamic data are collected only once for each data set and the averaged values are then used to calculate the similarity parameter. As the aerodynamic measurement time is set to 40 s and the measurement time for one data set is about 4.5 minute, a time difference between the acoustic and aerodynamic measurements inherently exists. Furthermore, the collection of the aerodynamic and acoustic data was not necessarily performed simultaneously or with the same time difference as the two data collection systems are not coupled. Thus, a varying temporal offset between the measurements of the acoustic data and the aerodynamic data exists, which is not considered in post-hoc scaling. Analysis of the shift in the modal response shows that even very small variations in the aerodynamic boundary conditions result in high differences in the pressure

amplitudes, especially for regions with a high pressure gradient. As the varying boundary conditions within this temporal offset are not considered and with the knowledge gathered in this work, it can be concluded that this non-consideration impairs the result of post-hoc scaling and might explain the variations in the scaled modal responses still existing.

Limitations of the linear interpolation

In both test cases, it has been observed that the relative deviations between the modal frequency responses are highest for areas with a high pressure gradient. Post-hoc scaling is limited here by the given sample for the linear interpolation. With respect to the hypothesis tested in this work, this means that the variations in modal response after post-hoc scaling in the area of high pressure gradients do not (necessarily) indicate that the angle of the group velocity vector is unsuitable for establishing similarity. The variations might be simply due to the fact that the spacing of samples is too large. Furthermore, post-hoc scaling is also limited by the frequency range regarded. If the calculated reduced frequency is outside the considered range, the minimum or maximum frequency is used, respectively (cf. process of post-hoc scaling as shown in Fig 6.9 in Sec. 6.2).

Impact of clocking

With respect to the investigation carried out for this work, the assumption is made that clocking of the second stator carrier has no impact on the aerodynamic as well as the aeroacoustic conditions in the inlet duct of the LPT due to the large distance between the second stator located between measurement planes MP 31 and MP 32 and the microphone array in Sec A. In doing so, it is especially assumed that possible altered reflection characteristics of the turbine stage due to different relative positions of the first and second stator row have no significant impact on the modal amplitude measurements in Sec A. Generally, it can be expected, of course, that modal reflections superimpose the excited sound field in the inlet duct of the LPT. Among others things, reflections at the hub, the struts, and at the stator and rotor blades might influence the sound field characteristic. In how far, the clocking has an impact on these acoustic reflections and eventually alter the modal sound pressure amplitudes upstream of the LPT cannot be conclusively answered here. However, provided that a possible impact of clocking is periodic to the relation of stator to rotors blades, it can be stated that within the analysis of the variation of the modal responses between the different data sets before and after the post-hoc scaling, no impact of clocking is observed. If existent and non-periodic, the impact is of an order of magnitude smaller than the amplitude differences determined for the original data sets. In summary, the impact of non-consideration of altered reflections due to clocking effects cannot be definitively answered within this work and should therefore be addressed in future works.

Reflections due to turning points

Reflections due to changing cut-off conditions in the direction of the modal propagation might be also causal for the variation in the modal response in Sec A over the time of

6.4 Limits of post-hoc scaling

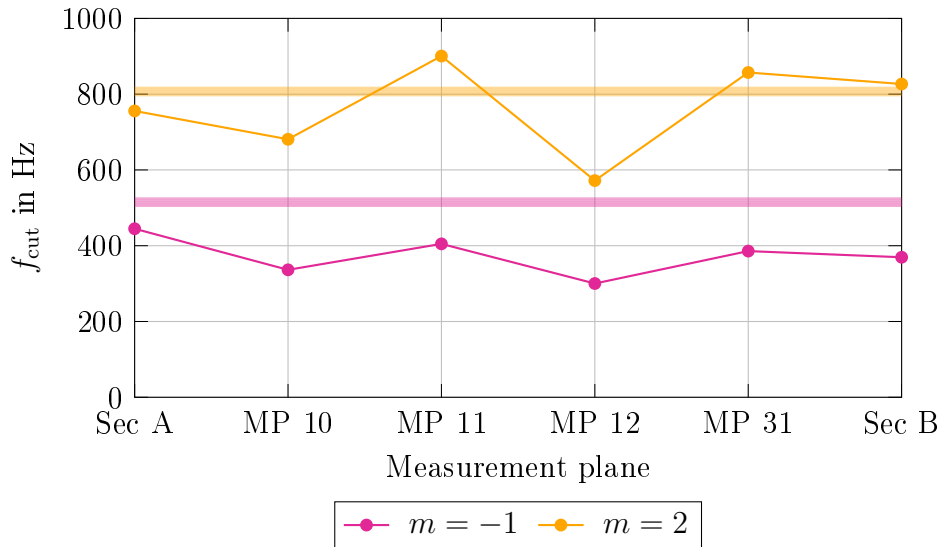


Figure 6.17: Change of the cut-off condition throughout the LPT. The line colored in magenta and the line colored in orange give the cut-off frequencies for part-load operation and design-point operation, respectively. The marked areas show the range of excited frequencies.

measurement. These reflections might at least explain part of the variations detected for test case 2 before and after post-hoc scaling. Due to different flow conditions and changes in the geometry, acoustic modes excited in the inlet duct might experience changing cut-off conditions when propagating downstream throughout the LPT. For hard-walled ducts with an axial mean flow (and a slowly varying cross section), analytical and numerical solutions show that the affected mode is reflected at these so-called *turning points* with a phase shift of $\pi/2$ as discussed intensively by Rienstra (1999) and Rienstra (2003) among others. Applied to real conditions in the LPT, reflections at turning points in the turbine might affect the pressure amplitude of the respective mode in the measurement plane of interest.

In Fig. 6.17, the calculated cut-off frequencies for the acoustic modes considered for the different aerodynamic measurement planes are depicted. The values are taken from the detailed cut-off analysis described in Sec. 4.3. The lines represent the results for part-load operation and design-point operation, respectively. The areas marked purple and orange show the range of excited frequencies for the two test cases. First, it can be observed that for the measurement planes upstream of the first stator (Sec A and MP 10), both modes are well cut-on with respect to the respective operating point and excitation frequencies⁸. Furthermore, for the counter-spinning mode $m = -1$, the cut-off frequencies are below the considered frequency range throughout the whole turbine. For test case 2 and the respective mode $m = 2$ however, the cut-off frequencies deter-

⁸In fact, the calculated angles of the group velocity vector in Sec A are well below $\phi_{\text{gr},x,(\text{cut})} = 90^\circ$.

mined for plane MP 11 upstream the first stator lie above the excited frequency range ($f_{\text{cut}} > f_{\text{exc}}$). In addition, for design-point operation this also holds for MP 31 and Sec B. Taking small shifts in the calculated cut-off frequency due to changing aerodynamic boundary conditions into account, it can be reasonably assumed that acoustic modes that propagate with a frequency close to or matching the cut-off frequency experience reflections in these sections. As a result, the sound field in the inlet duct might be affected by the modal reflections.

6.5 Summary of the Experimental Validation

Two test cases for the validation of the work's hypothesis are investigated. For both test cases variations in the modal pressure amplitudes of the propagating acoustic mode for identical synthetic sound field excitation can be detected for different measurements in time. During the period of the measurements, the boundary conditions of the open-cycle turbine test rig changed, so that similarity with respect to reference conditions was not accomplished. The similarity parameters Helmholtz number and Mach number are not equal between the measurements. It is found that variations in the pressure amplitudes of the modal response function correlate strongly with both, changes in the axial angle of the group velocity vector and changes in the Helmholtz number. Contrary, linear correlation with the Mach number is only moderately or even negligible. These findings can be explained by the similarity approach developed in this work. The similarity maps for the specific modes show that the axial angle of the group velocity vector is not sensitive to changes in the Mach number for the test cases investigated, but highly sensitive to changes in the Helmholtz number for the considered operating points.

In order to clarify the reasons for modal amplitude variations, the modal response functions dependent on the excitation frequency have been analyzed for the different data sets with respect to reference. It can be concluded that the changes in aerodynamic boundary conditions lead to a shift of the modal responses towards higher or lower frequencies. This shift causes the variations in the pressure amplitudes. With respect to the observed changes in flow temperature during the time of measurement, a shift towards higher frequencies can be observed for an increase of the latter and, conversely, a shift towards lower frequencies for a decrease in temperature. The direction of the shift is determined here by the relation between flow temperature and the group velocity angle of the propagating mode, which is positive for the operating point considered here. The individual shifts of the modal responses result overall in a compression or stretching of the modal frequency-response function with respect to reference. This alteration can be revised by using the modal response dependent on the angle of the group velocity vector instead of the excitation frequency. In other words, it can be concluded that the change in the group velocity angle due to changing aerodynamic conditions results in a shift in the frequency with respect to the modal response function.

Furthermore, it can be stated that the impact of non-compliance with similarity is most pronounced for regions of high pressure gradients in the modal response function in combination with significant changes in aerodynamic boundary conditions. This effect

6.5 Summary of the Experimental Validation

manifests itself clearly in the color-shaded surface plots (cf. Fig. 6.10 and Fig. 6.12), which show a blur-type effect of the colors for the areas ①A and ①B and ②A and ②B. It also highlights that even marginal variations in the similarity parameters, Helmholtz number and Mach number, might severely impair measurement results.

The hypothesis of this work is further tested quantitatively by a post-hoc scaling approach. For this purpose, the collected data are post-processed to reflect measurements where modal similarity has been considered. Based on a so-called reduced frequency, the modal response at the reference angle of the group velocity vector is interpolated to approximate similarity conditions post-hoc. The results of scaling, show significant improvements in the similarity. An analysis of possible faults and failures related to post-hoc scaling explains the still-existing deviations. In summary, the results of post-hoc scaling support the hypothesis that the axial angle of the group velocity vector is a suitable parameter for the establishment of modal sound propagation similarity.

7 Conclusions and Outlook

The triad of Mach number, Helmholtz number, and hub-to-tip ratio establishes complete similarity of sound propagation in a circular duct carrying an ideal, inviscid, and uniform flow in the axial direction. Based on an analytical analysis and under consideration of the theory of similarity, the hypothesis is developed that for a given geometry, the modal axial angle of the group velocity vector can be used to establish partial similarity with respect to the propagation of one specific mode in cases where equality of the Mach number and / or Helmholtz number cannot be achieved.

A similarity relation between this angle and the aforementioned triad of similarity parameters is derived. Based on this relation it is found that for a given geometry and a specific acoustic mode, an infinite number of combinations of the Mach number and the Helmholtz number can be determined that yield the same axial angle of the group velocity vector. That means, any variation in the numerical value of one of the two parameters can be compensated by a respective adaptation of the other parameter in order to meet equality of the group velocity angle, and thus to establish partial similarity of modal sound propagation between two measurements. For this, full control of either the Mach number or the Helmholtz number is mandatory.

Based on the similarity relation, a similarity map is developed, which allows easy identification of areas of different sensitivity of the group velocity angle towards changes in the Mach number and Helmholtz. It is found that sensitivity with respect to both similarity parameters is highest when the respective mode approximates cut-off condition. Furthermore, sensitivity with respect to the Mach number and sensitivity with respect to the Helmholtz number can differ considerably for the same operating point. This qualitative statement holds up irrespective of the mode and hub-to-tip ratio under consideration.

The hypothesis developed is tested using aerodynamic and acoustic data from validation measurements carried out in the LPT test rig. For two operating points, similarity conditions of modal sound field propagation in the inlet duct upstream of the first stage are evaluated by analyzing the modal response function excited by the specified acoustic modes for different measurements. It is found that for measurements where equality of the similarity parameters, Mach number and Helmholtz number, is not achieved, partially substantial variations in the modal pressure amplitudes measured are detected with respect to reference. These variations in the pressure amplitudes can be explained by shifts in the modal responses due to changes in the group velocity angle. Furthermore, these variations are identified to have a strong linear correlation with changes in the Helmholtz number, but only a moderate or negligible with the Mach number. The similarity relation developed implies that the axial angle of the group velocity vector is

almost insensitive to changes in the Mach number for the operating points considered. The observation described can thus be explained by means of the similarity relation and the similarity map derived which supports the validity of the hypothesis developed.

The suitability of the axial angle of the group velocity vector for establishing partial similarity is further quantified by means of a post-hoc scaling approach. For this purpose, the collected acoustic data are post-processed in order to reflect measurements for which partial similarity conditions are met. It is shown that the variations in the modal response can be significantly reduced in magnitude if equality of the group velocity angle is achieved. Based on the findings of the experimental measurements, it can be concluded that the axial angle of the group velocity vector is a suitable parameter for establishing partial similarity of modal sound propagation for the geometry and flow conditions under consideration here. In other words, partial similarity with respect to the propagation of one specific mode is achieved between two measurements if equality of the axial angle of the group velocity vector is met.

In order to experimentally establish similarity conditions of modal sound propagation, a so-called reduced frequency is introduced in this work, which, similar to the reduced mass flow rate or the reduced rotor speed, serves as an operating parameter for controlling the Helmholtz number and thus similarity conditions in test rigs equipped with a sound generator. If equality of the Mach number and / or Helmholtz number is not met, partial similarity can be achieved if the reduced frequency is determined with respect to equality of the axial angle of the group velocity vector. If equality of the Mach number is met, complete similarity can be achieved if the reduced frequency is determined with respect to equality of the Helmholtz number.

The investigations for this work demonstrate that even minor changes in the similarity conditions might result in significant changes in the modal sound propagation properties, which manifests in substantial variations in the measured pressure amplitudes. Eventually, the latter can severely impair research results if not considered properly. This work highlights the necessity to consider acoustic similarity for modal sound propagation investigation in general and in the design of the measurement setup in particular. In a first step, the similarity map can be used to assess the impact of changes in the similarity parameters, the Mach number and Helmholtz number on the modal propagation properties for any acoustic effect that is governed by the axial angle of the group velocity vector.

Future efforts regarding the establishment of modal similarity for research measurements should concentrate on further development of the similarity relation or similarity map, respectively, presented in this work. Similarity conditions are determined here with respect to the aerodynamic conditions in the inlet duct of the LPT test rig. For this purpose, an ideal, inviscid, and uniform one-dimensional flow is assumed. Furthermore, a plane wave approach is used here to analytically describe modal propagation. In a next step, it can be investigated how far the results of this work apply to velocity profiles with a circumferential and / or a radial flow component in order to reflect the conditions in between and after the rotor and stator vanes. In addition, the plane-wave approach used here can be further extended to consider three-dimensional modal propagation

characteristics by using the equations developed within the investigation on the radial dependency of the group velocity vector. Furthermore, it is recommended to extend the study to include similarity conditions for modes propagating with a higher radial order. Eventually, if the flow conditions are too complex to be accurately approximated by analytical models (like, for example, if viscosity effects as shear layers or thermal conductions are no longer negligible, but have to be considered to accurately reflect propagation of acoustic modes in the respective turbomachine), empirical studies have to be carried out to support the analytically derived relations for partial and complete similarity.

In addition to the measurements carried out here, further measurements are recommended, which should aim at extending the validation to operating points, where the axial angle of the group velocity vector is not only sensitive to changes in the Helmholtz number, but also sensitive to changes in the Mach number.

Lastly, the similarity approach presented here has the potential to be enhanced with the objective to allow transfer of research results on acoustic propagation phenomena governed by the axial angle of the group velocity vector from one test rig to another, or from the test rig to the full-scale machine. For this purpose, a similarity map as presented here can serve as a basis to determine similar operating conditions with respect to the propagation of sound. However, for significant variations in the Mach number in comparison to reference, investigations on similarity with respect to the sound pressure level should be carried out in order to enhance the similarity approach by considering possible amplitude modulations caused by major variations in the aerodynamic conditions.

Based on the results of this work, it is recommended to further develop the operational concept of the LPT test rig. An application of a sound generator for synthetic sound field generation presumed, it is recommended to implement an on-time calculation of the reduced frequency in the control and monitoring system of the test rig, which takes the actual aerodynamic conditions into consideration in order to establish similarity of modal sound propagation from the start of measurements.

Bibliography

- Allen, C. S.; Blake, W. K.; Dougherty, R. P.; Lynch, D.; Soderman, P. T.; Underbrink, J. R.; and Mueller, T. J. (Ed.) (2002): *Aeroacoustic Measurements. Experimental Fluid Mechanics*. Springer Berlin Heidelberg, Berlin, Heidelberg and s.l. ISBN 9783642075148. doi:10.1007/978-3-662-05058-3.
- Angerer, J. R.; McCurdy, D. A.; and Erickson, R. A. (1991): Development of an annoyance model based upon elementary auditory sensations for steady-state aircraft interior noise containing tonal components, Vol. 104147 of NASA technical memorandum. National Aeronautics and Space Administration, Langley Research Center.
- Aschenbruck, J.; and Seume, J. R. (2015): Experimentally Verified Study of Regeneration-Induced Forced Response in Axial Turbines. In: *Journal of Turbomachinery*, Vol. 137(3): p. 031006. doi:10.1115/1.4028350.
- Bartelt, M. (2015): Ein Beitrag zum Ausbreitungsverhalten modaler Schallfelder in Niederdruckturbinen. Phd thesis, Gottfried Willhelm Leibniz Universität Hannover, Hanover, Germany.
- Bartelt, M.; Laguna, J. D.; and Seume, J. R. (2013): Synthetic Sound Source Generation for Acoustical Measurements in Turbomachines. In: ASME (Ed.) *Proceedings of ASME Turbo Expo*, pp. GT2013-95045. doi:10.1115/GT2013-95045.
- Bartelt, M.; Meinzer, C. E.; Laguna, J. D.; and Seume, J. R. (2012): Design Methodology and Experimental Validation of an Aeroacoustic Test Rig for Turbomachinery Applications. In: *Proceedings of 13th International Symposium on Unsteady Aerodynamics, Aeroacoustics and Aeroelasticity of Turbomachines 2012 (ISUAAAT 13)*.
- Berckmans, D.; Janssens, K.; Van der Auweraer, H.; Sas, P.; and Desmet, W. (2008): Model-based synthesis of aircraft noise to quantify human perception of sound quality and annoyance. In: *Journal of Sound and Vibration*, Vol. 311(3-5): pp. 1175-1195. ISSN 0022460X. doi:10.1016/j.jsv.2007.10.018.
- Biester, M. H.-O. (2016): Ausmischverluste und instationärer Arbeitsumsatz in Turbinen. Phd thesis, Gottfried Willhelm Leibniz Universität Hannover, Hanover, Germany.
- Biester, M. H.-O.; Guendogdu, Y.; and Seume, J. R. (2013a): Clocking Effects on Surface-Pressure Fluctuations for Variable Axial-Gaps. In: *Proceedings of the 21st*

- AIAA Computational Fluid Dynamics Conference. American Institute of Aeronautics and Astronautics, Fluid Dynamics and Co-located Conferences. doi:10.2514/6.2013-2955.
- Biester, M. H.-O.; Mueller, L.; Seume, J. R.; and Guendogdu, Y. (2011): Time-Resolved Numerical Investigation of the Interaction of Labyrinth Seal Leakage and Main-Flow in a 1.5-Stage LP Turbine. In: ASME (Ed.) Proceedings of ASME 2011 Turbo Expo: Turbine Technical Conference and Exposition. ASME, pp. GT2011-45883. ISBN 978-0-7918-5467-9. doi:10.1115/GT2011-45883.
- Biester, M. H.-O.; Wiegmann, F.; Guendogdu, Y.; and Seume, J. R. (2013b): Time-Resolved Numerical Study of Axial Gap Effects on Labyrinth-Seal Leakage and Secondary Flow in a LP Turbine. In: ASME (Ed.) Proceedings of ASME Turbo Expo 2013: Turbomachinery Technical Conference & Exposition. ASME, pp. GT2013-95628. doi:10.1115/GT2013-95628.
- Binner, M. (2011): Experimentelle Untersuchung von Teil- und Schwachlastzuständen in Hochdruckdampfturbinen. Phd thesis, Institute of Turbomachinery and Fluid Dynamics, Leibniz Universität Hannover, Hanover, Germany.
- Binner, M.; and Seume, J. R. (2014): Flow Patterns in High Pressure Steam Turbines During Low-Load Operation. In: Journal of Turbomachinery, Vol. 136(6): p. 061010. doi:10.1115/1.4025162.
- Braeunling, W. J. (2015): Flugzeugtriebwerke. Springer Berlin Heidelberg, Berlin, Heidelberg. ISBN 978-3-642-34538-8. doi:10.1007/978-3-642-34539-5.
- Bridgman, P. W. (1922): Dimensional Analysis. Yale Univ. Press, New Haven.
- Buckingham, E. (1914): On Physically Similar Systems; Illustrations of the Use of Dimensional Equations. In: Physical Review, Vol. 4(4): pp. 345-376. doi:10.1103/PhysRev.4.345.
- Buckingham, E. (1915): The Principle of Similitude. In: Nature, Vol. 96: p. 396. ISSN 0028-0836. doi:10.1038/096396d0.
- Chapman, C. J. (1994): Sound radiation from a cylindrical duct. Part 1. Ray structure of the duct modes and of the external field. In: Journal of Fluid Mechanics, Vol. 281: pp. 293-311. ISSN 00221120. doi:10.1017/S0022112094003113.
- Dick, E. (2015): Fundamentals of Turbomachines, Vol. 109 of Fluid mechanics and its applications. Springer, Dordrecht. ISBN 978-94-017-9626-2.
- Enghardt, L.; Moreau, A.; Tapken, U.; and Kennepohl, F. (2009): Radial Mode Decomposition in the Outlet of a LP Turbine - Estimation of the Relative Importance of Broadband Noise. In: 15th AIAA/CEAS Aeroacoustics Conference (30th AIAA Aeroacoustics Conference). American Institute of Aeronautics and Astronautics. doi:10.2514/6.2009-3286.

Bibliography

- Enghardt, L.; Tapken, U.; Neise, W.; Kennepohl, F.; and Heinig, K. (2001): Turbine blade/vane interaction noise - Acoustic mode analysis using in-duct sensor rakes. In: 7th AIAA/CEAS Aeroacoustics Conference and Exhibit. American Institute of Aeronautics and Astronautics, Reston, Virginia. doi:10.2514/6.2001-2153.
- Enghardt, L.; Tapken, U.; Neise, W.; Schimming, P.; Maier, R.; and Zillmann, J. (2002): Active control of fan noise from high-bypass ratio aeroengines: Experimental results. In: *The Aeronautical Journal* (1968), Vol. 106(1063): pp. 501–506. ISSN 0001-9240. doi:10.1017/S0001924000092356.
- Enghardt, L.; Zhang, Y.; and Neise, W. (1999): Experimental verification of a radial mode analysis technique using wall-flush mounted sensors. In: *The Journal of the Acoustical Society of America*, Vol. 105(2): p. 1186. ISSN 0001-4966. doi:10.1121/1.425598.
- Evers, H. B. (1985): Strömungsformen im Ventilationsbetrieb einer ein- und mehrstufig beschaufelten Modellturbine. Phd thesis, Institute of Turbomachinery and Fluid Dynamics, Leibniz Universität Hannover, Hanover, Germany.
- Farassat, F.; and Myers, M. K. (1996): A Study on Wave Propagation in a Duct and Mode Radiation. In: AIAA/CEAS, Aeroacoustic Conference, 2nd. American Institute of Aeronautics and Astronautics, Reston, Virginia.
- Farassat, F.; and Myers, M. K. (1997): A Graphical Approach to Wave Propagation in a Rigid Duct. In: *Journal of Sound and Vibration*, Vol. 200(5): pp. 729–735. ISSN 0022460X. doi:10.1006/jsvi.1996.0691.
- Goldstein, M. E. (1976): *Aeroacoustics*. McGraw-Hill, New York.
- Grimm, D. W.; and Hurst, C. J. (1979): A geometric acoustics approach to the study of sound propagation in ducts containing sheared flows. In: *The Journal of the Acoustical Society of America*, Vol. 66(6): pp. 1867–1875. ISSN 0001-4966. doi:10.1121/1.383619.
- Hamid, H.; and Horne, C. (1997): An experimental study of the response of a condenser microphone installed in a flat plate. In: 35th Aerospace Sciences Meeting and Exhibit. American Institute of Aeronautics and Astronautics, Reston, Virginia. doi:10.2514/6.1997-491.
- Hauptmann, T.; Aschenbruck, J.; and Seume, J. R. (2017): Forced Response Excitation due to Stagger Angle Variation in a Multi-Stage Axial Turbine. In: *International Journal of Gas Turbine, Propulsion and Power Systems*, Vol. 9(3).
- Hellman, R. P. (1982): Loudness, annoyance, and noisiness produced by single-tone-noise complexes. In: *The Journal of the Acoustical Society of America*, Vol. 72(1): pp. 62–73. ISSN 0001-4966. doi:10.1121/1.388025.

- Hellman, R. P. (1984): Growth rate of loudness, annoyance, and noisiness as a function of tone location within the noise spectrum. In: *The Journal of the Acoustical Society of America*, Vol. 75(1): pp. 209–218. ISSN 0001-4966. doi:10.1121/1.390397.
- Hellman, R. P. (1985): Perceived magnitude of two-tone-noise complexes: Loudness, annoyance, and noisiness. In: *The Journal of the Acoustical Society of America*, Vol. 77(4): pp. 1497–1504. ISSN 0001-4966. doi:10.1121/1.392044.
- Hellmich, B.; and Seume, J. R. (2008): Causes of Acoustic Resonance in a High-Speed Axial Compressor. In: *Journal of Turbomachinery*, Vol. 130(3): pp. 031003–1 – 031003–9. doi:10.1115/1.2775487.
- Henke, M.; Biester, M. H.-O.; Guendogdu, Y.; Lippl, F.; Mass, E.; and Seume, J. R. (2012): Numerical assisted Design of a Variable Rotating Vane Carrier Device for Turbine Test Rigs with Split Housing Structures using a Segmented Half-Ring Bearing Concept. In: *Proceedings of the 53rd AIAA/ASME/ASCE/AHS/ASC Structures, Structural Dynamics, and Materials Conference*. AIAA 2012-1660.
- Henke, M.; Wein, L.; Kluge, T.; Biester, M. H.-O.; Guendogdu, Y.; and Seume, J. R. (2016): Experimental and Numerical Verification of the Core-Flow in a new Low-Pressure Turbine. In: *ASME (Ed.) Proceedings of ASME Turbo Expo 2016: Turbomachinery Technical Conference & Exposition*. pp. GT2016–57101.
- Herbst, F.; Bluemel, S.; Fakiolas, E.; and Seume, J. R. (2011): Numerical Investigation of the Interaction between Probe, Flow, and Blading in an Axial-Turbine. In: *Proceedings of the International Gas Turbine Congress*. pp. IGTC2011–0194.
- Holste, F.; Neise; and W. (1997): Noise Source Identification in a Propfan Model by Means of Acoustical Near Field Measurements. In: *Journal of Sound and Vibration*, Vol. 203(4): pp. 641–665. ISSN 0022460X. doi:10.1006/jsvi.1996.0890.
- Hurfar, C. M.; Bartelt, M.; and Seume, J. R. (2015): A Scaling Method For Modal Sound Propagation In Annular Ducts. In: *ASME (Ed.) Proceedings of ASME Turbo Expo 2015: Turbomachinery Technical Conference & Exposition*. pp. GT2015–42839.
- Hurfar, C. M.; Keller, C.; Mumcu, A.; and Seume, J. R. (2016): An Acoustic Excitation System For The Generation Of Turbomachinery Specific Sound Fields - Part II: Experimental Verification. In: *ASME (Ed.) Proceedings of ASME Turbo Expo 2016: Turbomachinery Technical Conference & Exposition*. pp. GT2016–56969.
- Hurfar, C. M.; and Seume, J. R. (2015): Untersuchung des Einflusses von Schutzgittern für Mikrofone in einem Hochgeschwindigkeits-Windkanal. In: *41. Jahrestagung für Akustik – DAGA 2015*.
- J. Aschenbruck; T. Hauptmann; and J. Seume (2015): Influence of a Multi-Hole Pressure Probes on the Flow-Field in Axial-Turbines. In: *Proceedings of the 11th European Conference on Turbomachinery Fluid Dynamics & Thermodynamics*.

Bibliography

- Jaeger, S.; Horne, W.; and Allen, C. (2000): Effect of surface treatment on array microphone self-noise. In: 6th Aeroacoustics Conference and Exhibit. American Institute of Aeronautics and Astronautics, Reston, Virginia. doi:10.2514/6.2000-1937.
- Kaji, S.; and Okazaki, T. (1970): Propagation of sound waves through a blade row: I. Analysis based on the semi-actuator disk theory. In: *Journal of Sound and Vibration*, Vol. 11(3): pp. 339–353. ISSN 0022460X. doi:10.1016/S0022-460X(70)80038-4.
- Kaltenbach, M.; Maschke, C.; Heß, F.; Niemann, H.; and Führ, M. (2016): Health Impairments, Annoyance and Learning Disorders Caused by Aircraft Noise-Synopsis of the State of Current Noise Research. In: *International Journal of Environmental Protection*, pp. 15–46. ISSN 22266437. doi:10.5963/IJEP0601003.
- Kline, S. J. (1986): *Similitude and Approximation Theory*. Springer Berlin Heidelberg, Berlin, Heidelberg. ISBN 9783642648946. doi:10.1007/978-3-642-61638-9.
- Kousen, K. (1996): Pressure modes in ducted flows with swirl. In: AIAA/CEAS, Aeroacoustic Conference, 2nd. American Institute of Aeronautics and Astronautics, Reston, Virginia. doi:10.2514/6.1996-1679.
- Laguna, J. D. (2016): On the sensitivity of the radial mode analysis (RMA) for the experimental evaluation of sound propagation in a low-pressure turbine. Phd thesis, Institute of Turbomachinery and Fluid Dynamics, Leibniz Universität Hannover, Hanover, Germany.
- Landau, L. D.; and Lifshitz, E. M. (1959): *Fluid Mechanics: Volume 6*. Elsevier Reference Monographs, s.l., first Edition. ISBN 0080291422.
- Landström, U.; Åkerlund, E.; Kjellberg, A.; and Tesarz, M. (1995): Exposure levels, tonal components, and noise annoyance in working environments. In: *Environment International*, Vol. 21(3): pp. 265–275. ISSN 01604120. doi:10.1016/0160-4120(95)00017-F.
- Lighthill, M. J. (1965): Group velocity. In: *IMA Journal of Applied Mathematics*, Vol. 1(1): pp. 1–28. ISSN 0272-4960.
- Lighthill, M. J.; and Whitham, G. B. (1955): On Kinematic Waves. I. Flood Movement in Long Rivers. In: *Proceedings of the Royal Society A: Mathematical, Physical and Engineering Sciences*, Vol. 229(1178): pp. 281–316. ISSN 1364-5021. doi:10.1098/rspa.1955.0088.
- Lord Rayleigh (1915): The Principle of Similitude. In: *Nature*, Vol. 95(2368): pp. 66–68. ISSN 0028-0836. doi:10.1038/095066c0.
- Meinzer, C. E.; Bittner, S. L.; Schmitt, S.; Kielb, R. E.; and Seume, J. R. (2015): Design of a Single Stage Turbine for the Quantification of Aerodynamic Damping. In: ASME (Ed.) *Proceedings of ASME Turbo Expo 2015: Turbomachinery Technical Conference & Exposition*. pp. GT2015–42641.

- Mumcu, A.; Keller, C.; Hurfar, C. M.; and Seume, J. R. (2016): An Acoustic Excitation System For The Generation Of Turbomachinery Specific Sound Fields - Part I: Design And Methodology. In: ASME (Ed.) Proceedings of ASME Turbo Expo 2016: Turbomachinery Technical Conference & Exposition. pp. GT2016-56020.
- Murphy, G. (1950): Similitude in engineering. Ronald Press Comp, New York.
- Oppenheim, A. V.; and Schaffer, R. W. (2014): Discrete-Time Signal Processing. Pearson Education Limited, Harlow (Essex), Great Britain, 3rd Edition. ISBN 1-292-02572-7.
- Prandtl, L. (1910): Eine Beziehung zwischen Wärmeaustausch und Strömungswiderstand der Flüssigkeiten. In: Phys. Z, Vol. 11: pp. 1072–1078.
- Reynolds, O. (1883): An Experimental Investigation of the Circumstances Which Determine Whether the Motion of Water Shall Be Direct or Sinuous, and of the Law of Resistance in Parallel Channels. In: Philosophical Transactions of the Royal Society of London, Vol. 174: pp. 935–982. ISSN 02610523.
- Riabouchinsky, D. (1915): The Principle of Similitude. In: Nature, Vol. 95(2387): p. 591. ISSN 0028-0836. doi:10.1038/095591c0.
- Rice, E. J. (1979): Modal propagation angles in ducts with soft walls and their connection with suppressor performance. In: AIAA 5th Aeroacoustics Conference, Vol. 76. doi:10.2514/6.1979-624.
- Rice, E. J.; Heidmann, M. F.; and Sofrin, T. G. (1979): Modal propagation angles in a cylindrical duct with flow and their relation to sound radiation. In: Paper No. AIAA-79-0183, 17th Aerospace Sciences Meeting, Vol. 25. doi:10.2514/6.1979-183.
- Rienstra, S. W. (1999): Sound transmission in slowly varying circular and annular lined ducts with flow. In: Journal of Fluid Mechanics, Vol. 380: pp. 279–296. ISSN 00221120. doi:10.1017/S0022112098003607.
- Rienstra, S. W. (2003): Sound propagation in slowly varying lined flow ducts of arbitrary cross-section. In: Journal of Fluid Mechanics, Vol. 495: pp. 157–173. ISSN 00221120. doi:10.1017/S0022112003006050.
- Rienstra, S. W.; and Hirschberg, A. (2017): An Introduction to Acoustics. PhD Thesis, Eindhoven University of Technology, Eindhoven, Netherlands.
- Schlichting, H. (2016): Boundary-Layer Theory. Springer Berlin Heidelberg, Berlin, Heidelberg, 9. Edition. ISBN 9783662529171.
- Shin, H.-C.; Graham, W.; Sijtsma, P.; Andreou, C.; and Faszer, A. C. (2007): Implementation of a Phased Microphone Array in a Closed-Section Wind Tunnel. In: AIAA Journal, Vol. 45(12): pp. 2897–2909. ISSN 0001-1452. doi:10.2514/1.30378.

Bibliography

- Sijtsma, P.; and Zillmann, J. (2007): In-Duct and Far-Field Mode Detection Techniques. In: 13th AIAA/CEAS Aeroacoustics Conference (28th AIAA Aeroacoustics Conference). American Institute of Aeronautics and Astronautics, Aeroacoustics Conferences. doi:10.2514/6.2007-3439.
- Smith, J.; Burdisso, R.; and Fuller, C. (1996): Experiments on the active control of inlet noise from a turbofan jet engine using multiple circumferential control arrays. In: AIAA/CEAS, Aeroacoustic Conference, 2nd. American Institute of Aeronautics and Astronautics, Reston, Virginia. doi:10.2514/6.1996-1792.
- Spurk, J. H. (1992): Dimensionsanalyse in der Strömungslehre. Springer Berlin Heidelberg, Berlin, Heidelberg and s.l. ISBN 9783662015810. doi:10.1007/978-3-662-01581-0.
- Strouhal, V. (1878): Ueber eine besondere Art der Tonerregung. In: Annalen der Physik und Chemie, Vol. 241(10): pp. 216–251. ISSN 00033804. doi:10.1002/andp.18782411005.
- Tapken, U.; Raitor, T.; and Enghardt, L. (2009): Tonal Noise Radiation from an UHBR Fan - Optimized In-Duct Radial Mode Analysis. In: 15th AIAA/CEAS Aeroacoustics Conference (30th AIAA Aeroacoustics Conference). American Institute of Aeronautics and Astronautics. doi:10.2514/6.2009-3288.
- Traupel, W. (2001): Thermische Turbomaschinen: Thermodynamisch-strömungstechnische Berechnung. Klassiker der Technik. Springer, Berlin and Heidelberg, forth Edition. ISBN 978-3-642-62102-4. doi:10.1007/978-3-642-17469-8.
- Tyler, J. M.; and Sofrin, T. G. (1962): Axial Flow Compressor Noise Studies. SAE International, Warrendale, PA. doi:10.4271/620532.
- White, F. M. (2011): Fluid mechanics. McGraw-Hill, New York, NY, 7. Edition. ISBN 978-0-07-352934-9.
- White, K. (2018): Subjective and physiological responses to aircraft noise. Phd thesis, Vrije Universiteit Amsterdam, Amsterdam, The Netherlands.
- White, K.; Bronkhorst, A. W.; and Meeter, M. (2017): Annoyance by transportation noise: The effects of source identity and tonal components. In: The Journal of the Acoustical Society of America, Vol. 141(5): pp. 3137–3144. ISSN 0001-4966. doi: 10.1121/1.4982921.
- Whitham, G. B. (1960): A note on group velocity. In: Journal of Fluid Mechanics, Vol. 9(03): p. 347. ISSN 00221120. doi:10.1017/S0022112060001158.
- WHO (1999): Guidelines for community noise. World Health Organization, Geneva, Switzerland. ISBN 9789971887704.
- WHO Regional Office for Europe (2009): Night noise guidelines for Europe. World Health Organization Regional Office for Europe, Copenhagen, Denmark. ISBN 9789289041737.

WHO Regional Office for Europe (2011): Burden of Disease from Environmental Noise: Quantification of Healthy Life Years Lost in Europe. World Health Organization, Geneva, Switzerland. ISBN 9789289002295.

WHO Regional Office for Europe (2018): Environmental noise guidelines for the European Region. World Health Organization, Regional Office for Europe, Copenhagen, Denmark. ISBN 9789289053563.

A Appendix

A.1 Derivation of the Dispersion Relation

The dispersion relation

$$(k^0 - M_x k_x)^2 = (k_x)^2 + (\beta_{(m,n)})^2 \quad (\text{A.1})$$

presented in Sec. 3.1.2 can be either deduced by inserting the modal solution of Eq. (3.4) in the wave equation Eq. (3.3) as suggested by Rice et al. (1979), or by rearranging the equation of the axial wave number (Eq. (3.8)) as proposed by Farassat and Myers (1996) and Farassat and Myers (1997). The latter approach is tracked step-by-step as follows.

Taking the axial wave number for modal sound propagation in an unidirectional flow as given in Eq. (3.8)

$$k_x = \frac{-k^0 M_x \pm \sqrt{(k^0)^2 - (1 - M_x^2)(\beta_{(m,n)})^2}}{(1 - M_x^2)} \quad (\text{A.2})$$

and multiplying the equation with the denominator $(1 - M_x^2)$ and adding the term $(k^0 M_x)$ on both sides of the equation yields

$$k_x(1 - M_x^2) + k^0 M_x = \pm \sqrt{(k^0)^2 - (1 - M_x^2)(\beta_{(m,n)})^2}. \quad (\text{A.3})$$

Subsequently, squaring both sides of the equation, expanding the square, and rearranging gives

$$k_x^2(1 - M_x^2)^2 + 2k_x(1 - M_x^2)k^0 M_x = (k^0)^2(1 - M_x^2) - (1 - M_x^2)(\beta_{(m,n)})^2. \quad (\text{A.4})$$

Now, multiplying the equation with $(1 - M_x^2)^{-1}$ so that

$$k_x^2(1 - M_x^2) + 2k_x k^0 M_x = (k^0)^2 - (\beta_{(m,n)})^2. \quad (\text{A.5})$$

Subsequently, inserting the relation

$$k_x^2(1 - M_x^2) = k_x^2 - k_x^2 M_x^2, \quad (\text{A.6})$$

in Eq. (A.5) and rearranging gives

$$(k_x)^2 + (\beta_{(m,n)})^2 = (k^0)^2 - 2k_x k^0 M_x + k_x^2 M_x^2. \quad (\text{A.7})$$

The equation above can be finally written as

$$(k_x)^2 + (\beta_{(m,n)})^2 = \left((k^0)^2 - M_x k_x \right)^2, \quad (\text{A.8})$$

which corresponds to the dispersion relation given in Eq. (A.1).

A.2 Radial Dependency of the Group Velocity Vector

The angle of the group velocity vector relative to the duct axis $\phi_{\text{gr},x}$ on which this work focuses on, can be determined from the vector's magnitude c_{gr} and the axial component $c_{\text{gr},x}$ using trigonometric relations (cf. Eq. (3.22))

$$\cos(\phi_{\text{gr},x}) = \frac{c_{\text{gr},x}}{c_{\text{gr}}}. \quad (\text{A.9})$$

The magnitude and the axial component themselves can be derived with a geometrical approach as proposed by Rice et al. (1979). This approach approximates the modal phase fronts locally by plane waves and application yields the relations already introduced according to Eq. (3.20)

$$c_{\text{gr}} = c\sqrt{1 + 2M_x \cos(\phi_x) + M_x^2} \quad (\text{A.10})$$

and to Eq. (3.21)

$$c_{\text{gr},x} = c(\cos(\phi_x) + M_x). \quad (\text{A.11})$$

The axial propagation angle ϕ_x is thereby defined in Eq. (3.17)

$$\cos(\phi_x) = \frac{k_x}{\sqrt{(k_x)^2 + \left(\frac{u_{(m,n)}^{(\sigma)}}{R}\right)^2}} \quad (\text{A.12})$$

with

$$k_x^{\pm x} = \frac{-k^0 M_x \pm \sqrt{(k^0)^2 - (1 - M_x^2) \left(\frac{u_{(m,n)}^{(\sigma)}}{R}\right)^2}}{(1 - M_x^2)} \quad \text{and} \quad k^0 = \frac{\omega}{c}. \quad (\text{A.13})$$

The axial wave number given above is also defined in Eq. (3.8) in Sec. 3.4.

Inserting the relation for the propagation angle in Eq. (A.12) in Eq.(A.10) and Eq.(A.11) shows that the group velocity vector depends on the frequency, the speed of sound, the axial Mach number, the outer duct radius, the hub-to-tip ratio, and the mode orders. A dependency on the spatial coordinate, i.e. the axial or radial position, is not observed. Now, given that a three-dimensional problem is considered, it can easily be assumed or even concluded that the derived relations for the group velocity vector then represent the overall global (spatial) behaviour of the respective acoustic mode. However, Rice (1979) pointed out that the equations are valid near or at the outer duct radius: "*The approximate solutions are found to be sufficiently accurate near the cylindrical duct wall ... where most of the acoustic intensity usually exists.*" However, beyond this, the authors drew attention to a radial dependency of the quantities in pointing out that "*the exact solution using Henkel functions show ϕ_x to actually be a function of radius ...*", where the mentioned angle ϕ_x corresponds to the axial propagation angle used here. Consequently, this statement must hold true for the group velocity vector as well. Based on these findings, the following two non-trivial questions arise:

1. At which radial position are the relations derived for the group velocity vector (Eq. (3.20), Eq. (3.21), and Eq. (3.22)) valid?
2. How far do the conditions at the *to-be-determined* radial position represent the overall global modal propagation?

To answer these questions, a new enhanced geometric approach is developed, which is based on the consideration of the fully three-dimensional geometrical structure of the modal phase fronts. The proposed approach allows an investigation of the propagation properties at any arbitrary radial position of the duct considered. The objective is to validate the range of validity of the relations presented above, and to enhance the basic physical understanding of local modal propagation properties. For this purpose, the model problem outlined in Sec. 3.1 is assumed (hard-walled boundary conditions, annular shaped duct, uniform steady flow in axial direction). In line with the focus of this work, purely circumferential modes are considered ($n = 0$).

The three-dimensional geometry of the phase fronts of purely circumferential modes can be described by the class of surfaces called *helicoids*, as has already been pointed out by Rienstra and Hirschberg (2017). Helicoids can be parametrized in cartesian coordinates by the general equation

$$\mathbf{h} = \begin{bmatrix} r \cos(\theta) \\ r \sin(\theta) \\ p \theta \end{bmatrix}, \quad (\text{A.14})$$

where the radius r and the angle θ are the respective parameters. For a specific radius r , Eq. (A.14) then represents the parametrization of the curve known as a helix. The constant p determined by

$$p = \frac{m\lambda_x}{2\pi} = \frac{m}{k_x} \quad (\text{A.15})$$

denotes the pitch of the helicoid and can be obtained from the phase in Eq. (3.4) (cf. Rienstra and Hirschberg (2017)). As shown in Sec. 3.1, the group velocity vector can be geometrically constructed by adding the flow vector \mathbf{U} to the velocity vector of propagation \mathbf{c} as follows:

$$\mathbf{c}_{\text{gr}} = \mathbf{c} + \mathbf{U} = c(\mathbf{n} + \mathbf{M}_x). \quad (\text{A.16})$$

The velocity vector itself is determined by the unit space vector \mathbf{n} and the speed of sound c . The unit space vector is perpendicular to the phase fronts, thus to the helicoid. Now, the local unit space vector at any arbitrary position is given by the cross product of the helicoid's surface tangents divided by the magnitude of the respective cross product

$$\mathbf{n} = \frac{\frac{\partial \mathbf{h}}{\partial r} \times \frac{\partial \mathbf{h}}{\partial \theta}}{\left| \frac{\partial \mathbf{h}}{\partial r} \times \frac{\partial \mathbf{h}}{\partial \theta} \right|}. \quad (\text{A.17})$$

A.2 Radial Dependency of the Group Velocity Vector

Carrying out the mathematical operations yields

$$\mathbf{n} = \frac{1}{\sqrt{p^2 + r^2}} \begin{bmatrix} p \sin(\theta) \\ -p \cos(\theta) \\ r \end{bmatrix}. \quad (\text{A.18})$$

Thus, the unit space vector depends on the radial position r . Consequently, so does the propagation vector. With $\mathbf{c} = c\mathbf{n}$ the three-dimensional modal propagation vector is fully described

$$\mathbf{c}^* = \frac{c}{\sqrt{p^2 + r^2}} \begin{bmatrix} p \sin(\theta) \\ -p \cos(\theta) \\ r \end{bmatrix}. \quad (\text{A.19})$$

The group velocity vector is eventually obtained by

$$\mathbf{c}_{\text{gr}}^* = \mathbf{c}^* + c \begin{bmatrix} 0 \\ 0 \\ M_x \end{bmatrix} = \frac{c}{\sqrt{p^2 + r^2}} \begin{bmatrix} p \sin(\theta) \\ -p \cos(\theta) \\ r + M_x \sqrt{p^2 + r^2} \end{bmatrix}. \quad (\text{A.20})$$

The respective angles of the propagation vector and the group velocity vector relative to the duct axis are given by the dot product

$$\cos(\phi_x^*) = \frac{\mathbf{c}^* \cdot \mathbf{e}_x}{|\mathbf{c}^*| |\mathbf{e}_x|} = \frac{r}{\sqrt{p^2 + r^2}} \quad (\text{A.21})$$

and

$$\cos(\phi_{\text{gr},x}^*) = \frac{\mathbf{c}_{\text{gr}}^* \cdot \mathbf{e}_x}{|\mathbf{c}_{\text{gr}}^*| |\mathbf{e}_x|} = \frac{\cos(\phi_x^*) + M_x}{\sqrt{1 + 2M_x \cos(\phi_x^*) + M_x^2}}, \quad (\text{A.22})$$

respectively. For clear differentiation from the former non-radial dependent relations, the derived radial-dependent relations are marked by an asterisk (\cdot)*.

The three-dimensional geometrically approach presented here verifies that the propagation properties indeed depend on the radial position as stated by Rice et al. (1979). Furthermore, a relation is presented with Eq. (A.20) that allows the calculation of the modal group velocity vector at any radial (and circumferential) position.

To answer the first of the two initial questions - At which radial position are the relations according (Eq. (3.20), Eq. (3.21), and Eq. (3.22)) valid? - the equation for the propagation angle according to Eq. (A.21) is set equal to Eq. (3.17)

$$\begin{aligned} \cos(\phi_x^*) &= \cos(\phi_x) \\ \frac{r^*}{\sqrt{p^2 + (r^*)^2}} &= \frac{k_x}{\sqrt{(k_x)^2 + \left(\frac{u_{(m,n)}^{(\sigma)}}{R}\right)^2}}. \end{aligned} \quad (\text{A.23})$$

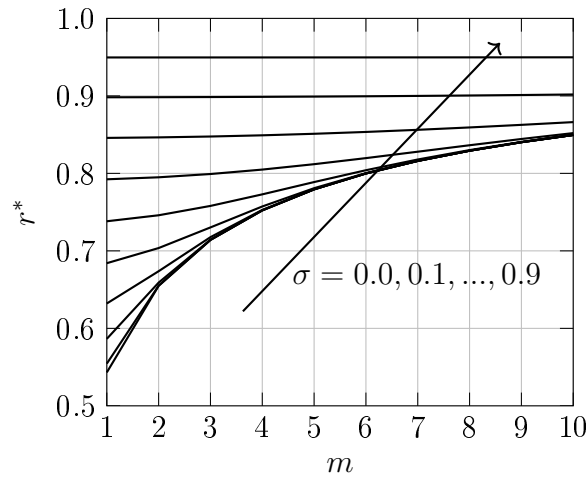


Figure A.1: Dependency of the radius r^* on the circumferential mode order m and the hub-to-tip ratio σ for $n = 0$.

Solving for the radius r^* and rearranging yields

$$r^* = \frac{m}{u_{(m,n)}^{(\sigma)}} R. \quad (\text{A.24})$$

Thus, Equation (3.20), Eq. (3.21), and Eq. (3.22) are valid for the radius r^* given by Eq. (A.24). This radius solely depends on the mode orders, the hub-to-tip ratio, and the outer duct radius.

Interestingly, Rice et al. (1979) assumed validity of the aforementioned equations near or at the duct wall. With the geometrical approach presented here, it can be explicitly shown that the equations are valid at the specific radius r^* . This radius can of course approximate the outer radius depending on the geometry and mode order but does not inherently have to do so. In Fig. A.1, the normalized radius is depicted over the circumferential mode order for different hub-to-tip ratios. The radial mode order is set to zero. It is found that the ratio $m/u_{(m,n)}^{(\sigma)}$ grows with increasing azimuthal mode order, on the one hand, and with increasing hub-to-tip ratio, on the other hand. Thus, the radius indeed approaches the outer duct radius for both variables.

Now the radius found is not unfamiliar. In fact, this radius corresponds to the radius referred to as the *caustic* or *caustic radius* in *ray theory*. This theory approximates wave propagation along straight or curved lines called rays and is applied in the field of *geometrical acoustics* (cf. Landau and Lifshitz (1959)). Considering the propagation of a ray through a cylindrical cross section with hard-walled boundary conditions, such as the model considered here, then a specific pattern of intersecting rays is formed due to reflections on the wall. The intersecting rays form an envelope, a so-called *caustic* as for example described by Grimm and Hurst (1979). The author analyzed sound propagation in a duct with a sheared flow by applying the approach of geometrical acoustic. The location of the caustic along the radius of the duct depends on the propagation angle

A.2 Radial Dependency of the Group Velocity Vector

of the rays in the respective (r, θ) -plane. Focusing on the modal propagation considered here, propagation in the (r, θ) -plane can then be approximated by $k_{r\theta}^2 \approx k_r^2 + k_\theta^2 = \beta_{(m,n)}^2$, cf. Rice et al. (1979). Inserting $r = r^*$ in $k_\theta = m/r$, it is found that the radial wave number is zero at the caustic radius

$$\begin{aligned} \left(\frac{u_{(m,n)}^{(\sigma)}}{R} \right)^2 &= k_r^2 + \left(\frac{m}{r^*} \right)^2 \\ \left(\frac{u_{(m,n)}^{(\sigma)}}{R} \right)^2 &= k_r^2 + \left(\frac{u_{(m,n)}^{(\sigma)}}{R} \right)^2 \\ &\Rightarrow k_r|_{r=r^*} = 0. \end{aligned} \tag{A.25}$$

This has also been observed by Chapman (1994). The author analyzed sound propagation and radiation based on a ray theory approach and worked out that the caustic radius gives the point, where the radial wave number turns from real ($r > r^*$) to imaginary ($r < r^*$). Thus, the three-dimensional modal propagation can be described in terms of a two-dimensional wave propagation locally at the caustic radius.

At this point, the second of the two initial questions - How far do the conditions at the *now-identified* caustic radius represent overall mode propagation? - remains unanswered and has to be discussed. This discussion, however, is not part of the work at hand.

Here, a new geometrical approach has been presented that allows a fully three-dimensional investigation of modal propagation properties, and thus represents a powerful tool not only to answer the question posed earlier, but to enhance knowledge of modal sound propagation in general. Furthermore, the approach can be used to extend approximate analytical sound propagation models since the three-dimensional propagation angle can be now exactly calculated for every radial position.

A.3 Derivation of the Similarity Relation for the Axial Angle of the Group Velocity Vector

In section 3.3 a relation between the axial angle of the group velocity vector and the triad, Mach number, Helmholtz number, and hub-to-tip ratio, is presented. For convenience of the reader of this work, a detailed step-by-step description of the deduction of this similarity relation is provided in this section.

Substituting the relation for the cut-off ratio

$$\xi = \frac{\text{He}}{u_{(m,n)} \sqrt{(1 - M_x^2)}} \quad (\text{A.26})$$

into Eq. (3.27)

$$\cos(\phi_{\text{gr},x}) = \sqrt{1 - M_x^2} \sqrt{\frac{1 - \frac{1}{\xi^2}}{1 - M_x^2 (1 - \frac{1}{\xi^2})}} \quad (\text{A.27})$$

taken from Rice et al. (1979), gives

$$\cos(\phi_{\text{gr},x}) = \sqrt{1 - M_x^2} \sqrt{\frac{1 - \frac{u_{(m,n)}^2 (1 - M_x^2)}{\text{He}^2}}{1 - M_x^2 \left[1 - \frac{u_{(m,n)}^2 (1 - M_x^2)}{\text{He}^2} \right]}}. \quad (\text{A.28})$$

By rearranging the Helmholtz number in the equation above, the relation

$$\cos(\phi_{\text{gr},x}) = \sqrt{1 - M_x^2} \sqrt{\frac{\frac{1}{\text{He}^2} [\text{He}^2 - u_{(m,n)}^2 (1 - M_x^2)]}{1 - \frac{M_x^2}{\text{He}^2} [\text{He}^2 - u_{(m,n)}^2 (1 - M_x^2)]}}. \quad (\text{A.29})$$

is determined. When expanding the fraction under the root with He^2 , the expression

$$\cos(\phi_{\text{gr},x}) = \sqrt{1 - M_x^2} \sqrt{\frac{\text{He}^2 - u_{(m,n)}^2 (1 - M_x^2)}{\text{He}^2 - M_x^2 [\text{He}^2 - u_{(m,n)}^2 (1 - M_x^2)]}} \quad (\text{A.30})$$

follows. Now, rearranging the denominator so that

$$\cos(\phi_{\text{gr},x}) = \sqrt{1 - M_x^2} \sqrt{\frac{\text{He}^2 - u_{(m,n)}^2 (1 - M_x^2)}{(1 - M_x^2)(\text{He}^2 + u_{(m,n)}^2 M_x^2)}} \quad (\text{A.31})$$

can be deduced, which is an equivalent form of the preceding equation (A.30). Then, combining then the expression $\sqrt{1 - M_x^2}$ with the main root of the equation and further rearranging yields

$$\cos(\phi_{\text{gr},x}) = \sqrt{\frac{\text{He}^2 - u_{(m,n)}^2 (1 - M_x^2)}{\text{He}^2 + u_{(m,n)}^2 M_x^2}}. \quad (\text{A.32})$$

A.3 Derivation of the Similarity Relation for the Axial Angle of the Group Velocity Vector

Finally, by expanding the parenthesis of the numerator of the fraction under the root, the relation

$$\cos(\phi_{\text{gr},x}) = \sqrt{\frac{\text{He}^2 + u_{(m,n)}^2 M_x^2 - u_{(m,n)}^2}{\text{He}^2 + u_{(m,n)}^2 M_x^2}}, \quad (\text{A.33})$$

is obtained, from which the final form

$$\cos(\phi_{\text{gr},x}) = \sqrt{1 - \left(\frac{1}{\frac{\text{He}^2}{u_{(m,n)}^2} + M_x^2} \right)} \quad (\text{A.34})$$

as presented in Sec. 3.3 can be deduced.

A.4 Similarity Map for Mode (2,0)

The similarity maps are shown here for the mode (2,0) for a hub-to-tip ratio of $\sigma = 0$. The illustrations are in line with the similarity maps of mode (1,0) as displayed in Fig. 3.4 and Fig. 3.4 in Sec. (3.4). The depicted contour lines for constant values of the axial angle of the group velocity vector $\phi_{gr,x}$ are calculated based on the similarity relation given in Eq. (3.37). The dashed lines in Fig. A.2 and Fig. A.2 represent sensitivity of the angle with respect to changes in the Mach number and Helmholtz number, respectively. Calculations of sensitivities are based on Eq. (3.49) and Eq. (3.50).

A.4 Similarity Map for Mode (2,0)

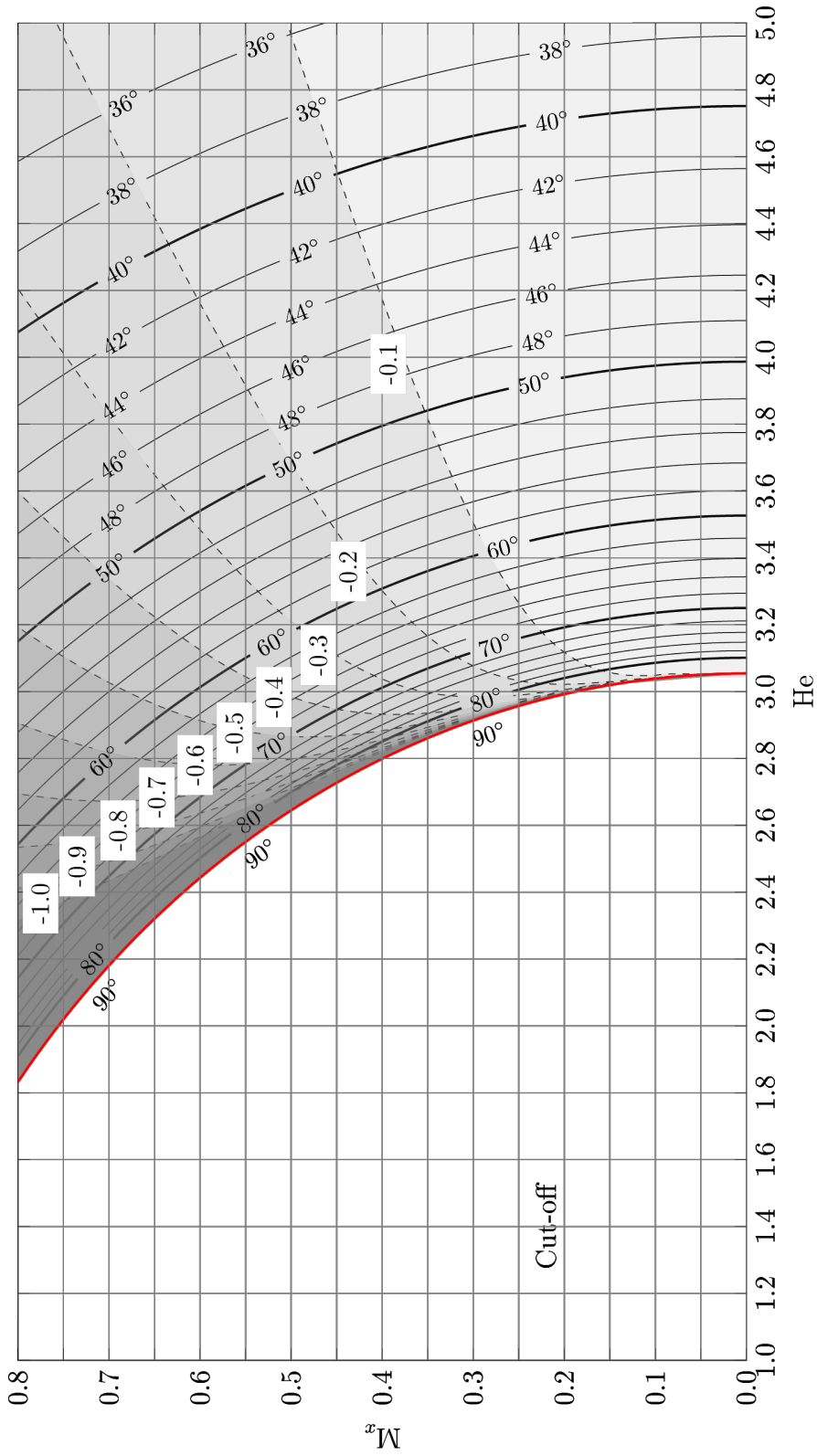


Figure A.2: Similarity map for modal sound propagation. The map is characteristic of the mode (2,0) and a hub-to-tip ratio of $\sigma = 0$. The solid lines represent constant values of the axial angle of the group velocity vector $\phi_{gr,x}$. The dashed lines represent the boundaries of selected values of sensitivity of $\phi_{gr,x}$ with respect to the Mach number $(\Xi_{\phi_{gr,x}|M_x})$.

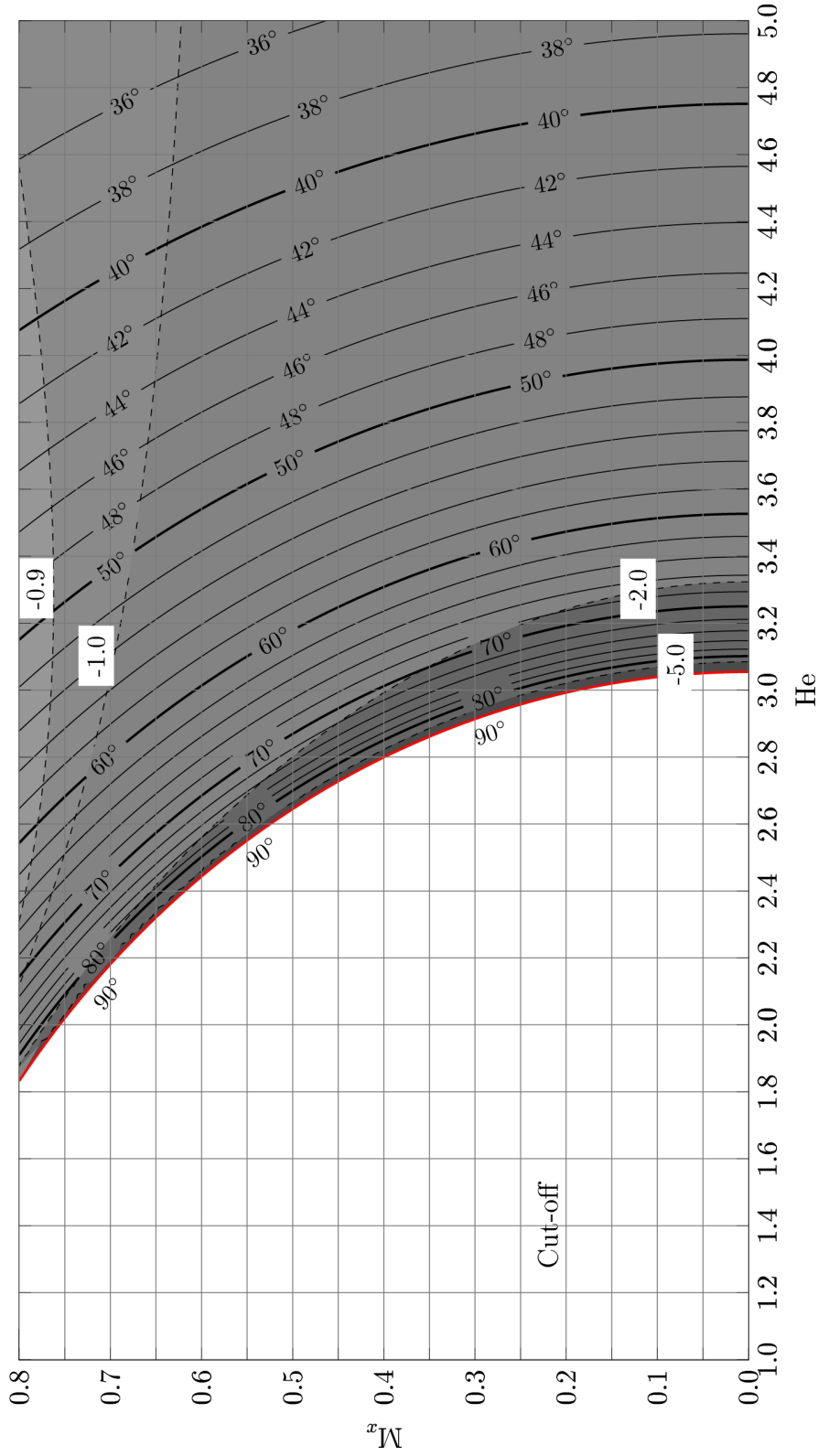


Figure A.3: Similarity map for modal sound propagation. The map is characteristic of the mode (2,0) and a hub-to-tip ratio of $\sigma = 0$. The solid lines represent constant values of the axial angle of the group velocity vector $\phi_{gr,x}$. The dashed lines represent the boundaries of sensitivity of $\phi_{gr,x}$ with respect to the Helmholtz number ($\Xi_{\phi_{gr,x}|\text{He}}$).

A.5 Aerodynamic Characteristics of the LPT

A.5.1 Design Parameter

Table A.1: Test conditions at design-point operation and blade characteristics as given by Biester et al. (2011).

Parameter	Value		
Rotor speed in RPM	7000		
Inlet pressure in kPa	156.7		
Inlet temperature in K	370		
Mass flow rate in kg/s	8.5		
Stage pressure ratio	1.43		
Net Power in kW	278		
	Stator 1	Rotor	Stator 2
Number of blades V and B	18	30	36
Blade height to axial chord length	2.15	2.15	2.15
Pitch to chord length	0.986	0.729	0.722
Stagger angle in Deg	39.08	51.21	67.98
Flow coefficient	—	0.59	—
Stage loading coefficient	1.95		—
Stage reaction	0.55		—
Reynolds number outlet ($Re \cdot 10^{-5}$)	7.54	6.48	4.17

A.6 Test Measurements in the AWT

Synthetic sound field excitation is a major methodical tool in this work. Therefore, test measurements of the applied excitation method are carried out in the test-section of the aeroacoustic wind tunnel (AWT) of the TFD. The setup of the test section is identical to the setup used for the measurements carried out previously by Bartelt et al. (2013) and Bartelt (2015). Figure A.4 gives an overview of the test rig. The sound generator is implemented in the inlet of the test section. Important components of the test rig are labelled. Detailed information on the design of the test-rig are given in Bartelt et al. (2012).

In Tab. A.2 the relevant parameters of the 2D-DFT modal decomposition method applied are summarized. The measurements are carried out without flow so that flow-induced noise has not to be considered. The data signal collected is therefore not segmented as described in Sec. 5.2.

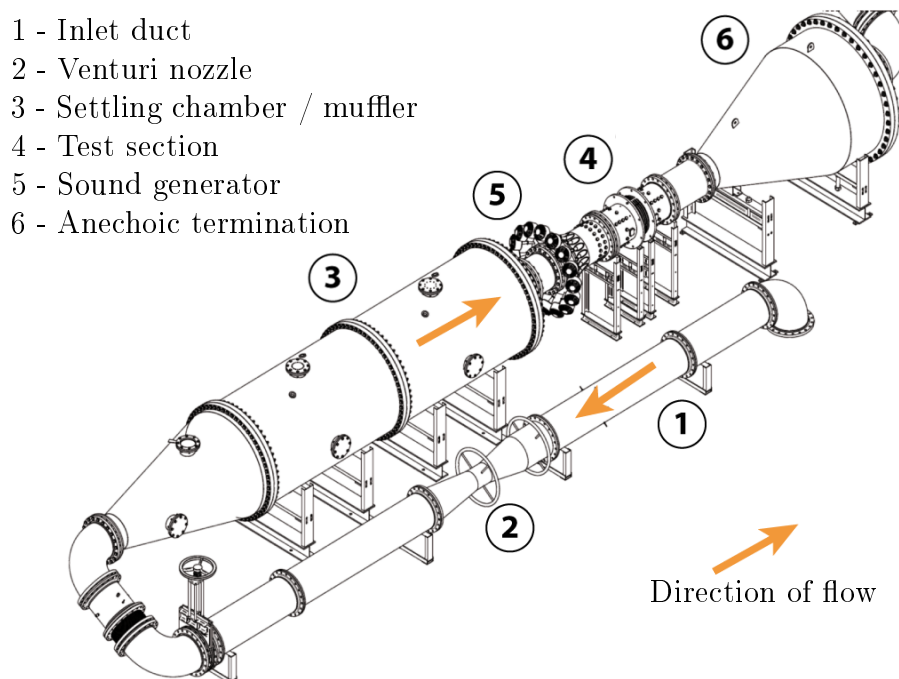


Figure A.4: Test measurements of the synthetic modal sound field excitation method. The figure is taken from Bartelt (2015).

A.6 Test Measurements in the AWT

Table A.2: Test measurements of the synthetic modal sound field excitation method: 2D-DFT processing parameters and properties. The Nyquist mode refers to the highest mode resolvable with respect to both directions of spinning.

Parameter	Value
Measurement time T	1 s
(Temporal) sampling frequency f_s	60.000 Hz
Nyquist frequency f_{Nyquist}	30.000 Hz
Number of microphones J per array	10
Nyquist mode m_{Nyquist}	4
Frequency resolution Δf	1 Hz

A.7 Validation of the 2D-DFT: Further test cases

Numerically generated data sets are used for the validation of the 2D-DFT modal decomposition method. In accordance with the test cases regarded in Sec. 5.1.4, the temporal DFT and spatial DFT are calculated for three test cases considering the mode $m = \pm 2$:

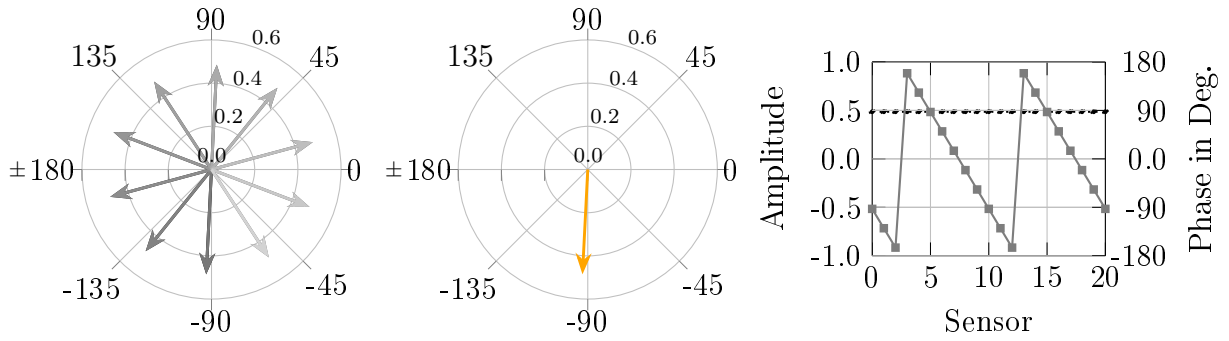
- (1) a mode of order one spinning in clockwise direction ($m = +2$) with the modal amplitude A_1 and modal phase φ_1 ,
- (2) a corresponding mode spinning in counter-clockwise direction ($m = -2$) with the modal amplitude A_2 and modal phase φ_2 , and
- (3) a circumferential standing mode composed of both modes according to (1) and (2) with a modal amplitude relation of $\epsilon = \frac{A_1}{A_2} = 1$ as defined in Sec. 3.1.1.

The parameters for the calculation are the same as used for the generation of the test cases in Sec. 5.1.4. According to Eq. (5.12) the modal amplitudes for $m = \pm 2$ are given by $F_{k,j} = A_{k,(2)} = A_{k,(-2)} = 0.4865$. For test case (1) and (2), $F_{k,j} = A_{k,m}$ holds. The graphs and diagrams for the test cases are depicted in Fig. A.5.

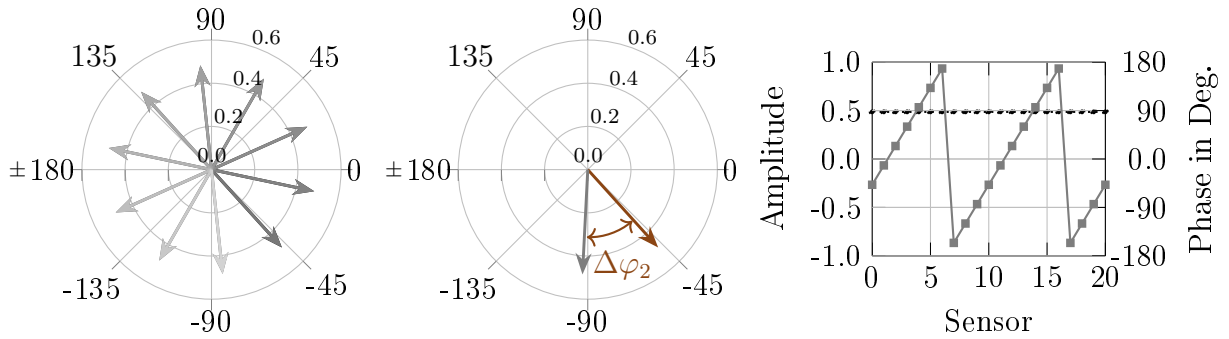
The amplitude and phase characteristics on the right side of Fig. A.5 show the expected results for all test cases. For the pure spinning modes, the temporal phase difference between two adjacent circumferential positions is $|36^\circ|$, whereas the sign of the phase difference depends on the direction of spinning. The latter is determined correctly. For the standing mode, the temporal phase difference between two arbitrary positions is $|0^\circ|$ or $|180^\circ|$. The calculated values for the temporal amplitudes (for case (1) and (2)) and the modal amplitudes (case (1) to (3)) match the expected values calculated according to Eq. (5.12) up to the fourth decimal place. Furthermore, the preset phase differences with respect to the modal phase calculated for test case (1) are calculated accurately. In summary, these additional test cases also confirm the applied modal decomposition method.

A.7 Validation of the 2D-DFT: Further test cases

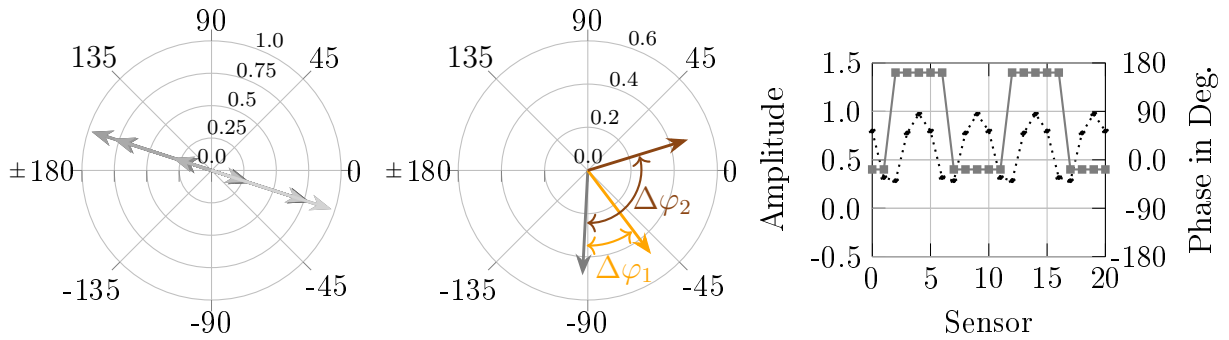
(1) Mode of order $m = 2$ ($A_1 = 0.48, A_2 = 0, \Delta\varphi_1 = 0, \epsilon = 0$):



(2) Counter-spinning mode of order $m = -2$ ($A_1 = 0, A_2 = 0.48, \Delta\varphi_2 = 45^\circ, \epsilon = 0$):



(3) Standing mode of order $m = |2|$ ($A_1 = A_2 = 0.48, \Delta\phi_1 = 40^\circ, \Delta\varphi_2 = 110^\circ, \epsilon = 1$):



Sensor in circumferential direction

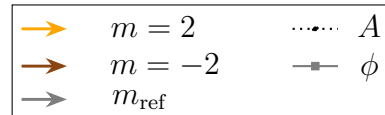


Figure A.5: Validation of the 2D-DFT using numerically generated test cases considering the mode $m = |2|$ and 20 sensors equally distributed in circumferential direction. Left: Complex vectors of the temporal DFT $F_{k,j}$. Center: Complex vector(s) of the spatial DFT $A_{m,k}$. Right: Temporal amplitude and phase characteristic.

A.8 Correlation Analysis

Pearson's correlation coefficient is calculated to determine the dependency between the variation in the modal response and the variation in the angle of the group velocity vector, the Helmholtz number, and the Mach number, respectively. In figure A.6 the calculated coefficients are given for all excitation frequencies for the respective mode excited. The diagrams on the left and right show the values for part-load operation and design-point operation, respectively. For both operating points, it is found that the absolute values of the correlation coefficient for the angle considered match exactly the respective absolute value of the Helmholtz number. This observation holds true independently of the correlation coefficient determined for the Mach number. Assuming the angle tested is a suitable parameter for establishing partial similarity, these two facts support the analysis based on the similarity maps, which shows that for the operating points considered, the Mach number has only a negligible impact on the angle of the group velocity vector and thus on similarity, whereas sensitivity of the latter is high with respect to the Helmholtz number.

For correlation with the axial angle of the group velocity vector and the Helmholtz number, in particular, the correlation coefficient is around or above a value of $r = 0.8$ indicating a very strong linear dependency. However, it can be observed that for a small number of excitation frequencies, the correlation coefficient with respect to all three parameters is smaller than $r = 0.5$ and even approximating the value of zero for some frequencies (in particular, for $f_{exc} = 509$ Hz and $f_{exc} = 524$ Hz for part-load

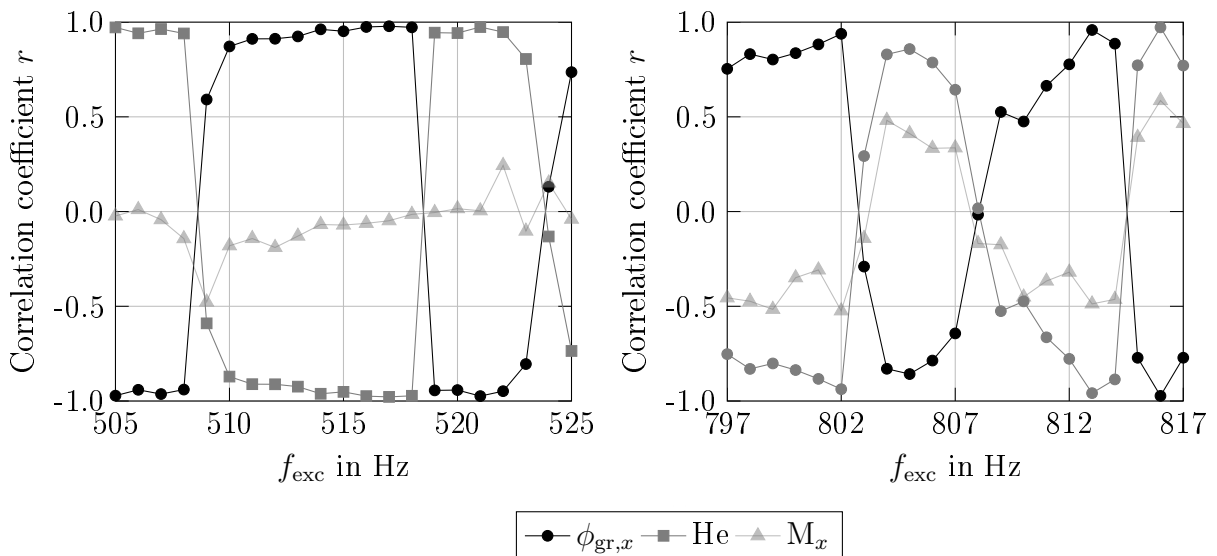


Figure A.6: Correlation analysis for all excitation frequencies. Left: Test case 1, part-load operation, and $m = -1$. Right: Test case 2, design-point operation, and $m = 2$.

A.8 Correlation Analysis

operation, and for $f_{\text{exc}} = 803 \text{ Hz}$ and $f_{\text{exc}} = 808 \text{ Hz}$ for design-point operation). These low values of the coefficient indicate that no linear dependency between the variations in the modal response and the variation in the similarity parameter exists. Comparison with the modal frequency response functions in Fig. 6.1 and Fig. 6.5 for part-load operation and design-point operation, respectively, shows that for these frequencies either high stochastic fluctuations occur, or that the response function around the respective frequency has a very even profile. In both cases, variations in the modal response cannot be unambiguously related to changing boundary conditions, and are therefore not conclusive enough to be considered for the test of the hypothesis of this work. The case of a very even profile and the impact on the alteration of the modal response function is also discussed in Sec. 6.3.3.

A.9 Results of Post-hoc Scaling for Test Case 1

In Fig. A.7 to Fig. A.27 the results of post-hoc scaling are depicted for each excitation frequency of test case 1. The black lines with circle markers, represent the data of the original measurement. The lines colored in magenta with the square marker, represent the data after post-hoc scaling. The diagrams at the top of the figures, show the modal response respective modal pressure amplitude and the calculated relative change with respect to reference data set No.1 according to

$$\left| \frac{A_m - A_{m,\text{ref}}}{A_{m,\text{ref}}} \right| = \left| \frac{\Delta A_m}{A_{m,\text{ref}}} \right|, \quad (\text{A.35})$$

where $A_{m,\text{ref}} = A_m^{[1]}$. For sake of brevity, the absolute values of the relative change is depicted. In the center on the left side of the figures, the original and the scaled angle of the group velocity vector is depicted. On the right side, the excitation frequency and the reduced frequency are given. The reduced frequency gives the frequency with which the acoustic mode has to propagate in the duct, in order to generate the same axial angle of the group velocity vector with respect to reference. At the bottom, the original Helmholtz number and the Helmholtz number after post-hoc scaling are depicted. For better clarity, two ordinates are used in these diagrams where the left ordinate serves as a measure for the original values and the left ordinate for the scaled values.

A.9 Results of Post-hoc Scaling for Test Case 1

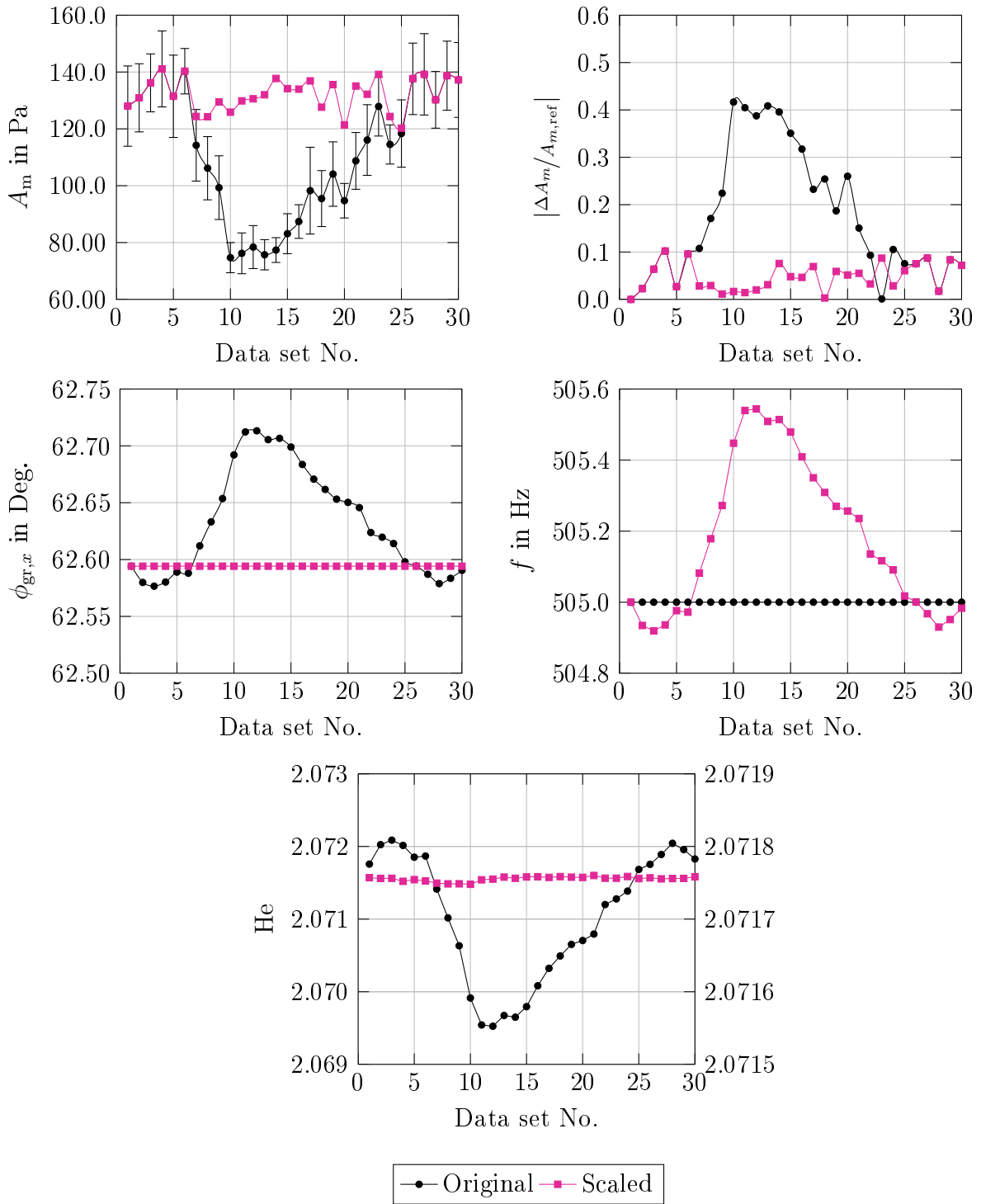


Figure A.7: Results of post-hoc scaling. Top left: Modal amplitude. Top right: Relative change of the modal amplitude with respect to reference data set No.1. Center left: Group velocity angle. Center right: Excitation frequency and calculated reduced frequency. Bottom: Helmholtz number (the lines and markers colored in black and magenta refer to the left and the right ordinate, respectively).

[Test case 1 | part-load operation | $m = -1$ | $f_{exc} = 505$ Hz]

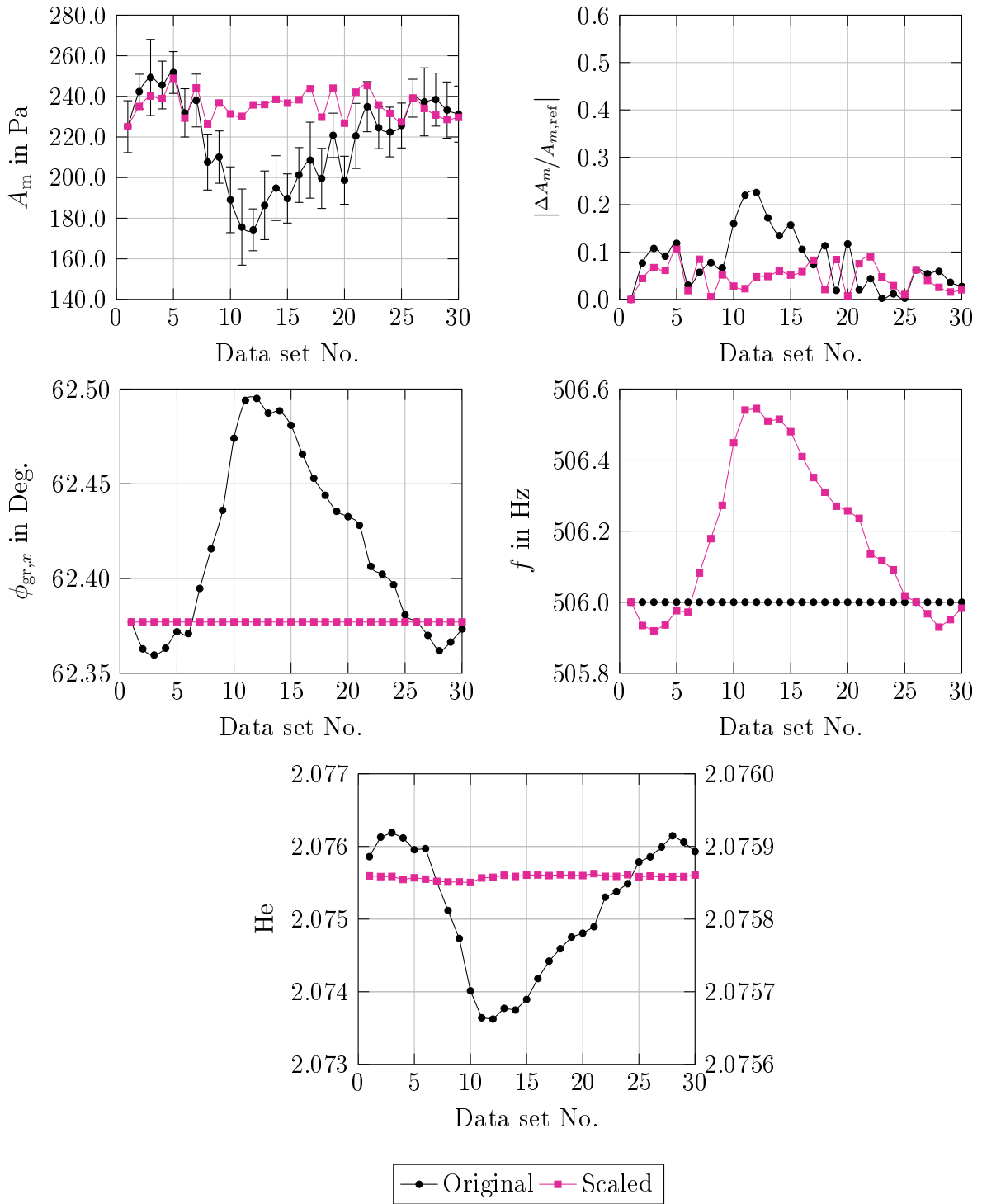


Figure A.8: Results of post-hoc scaling. Top left: Modal amplitude. Top right: Relative change of the modal amplitude with respect to reference data set No.1. Center left: Group velocity angle. Center right: Excitation frequency and calculated reduced frequency. Bottom: Helmholtz number (the lines and markers colored in black and magenta refer to the left and the right ordinate, respectively).

[Test case 1 | part-load operation | $m = -1$ | $f_{exc} = 506$ Hz]

A.9 Results of Post-hoc Scaling for Test Case 1

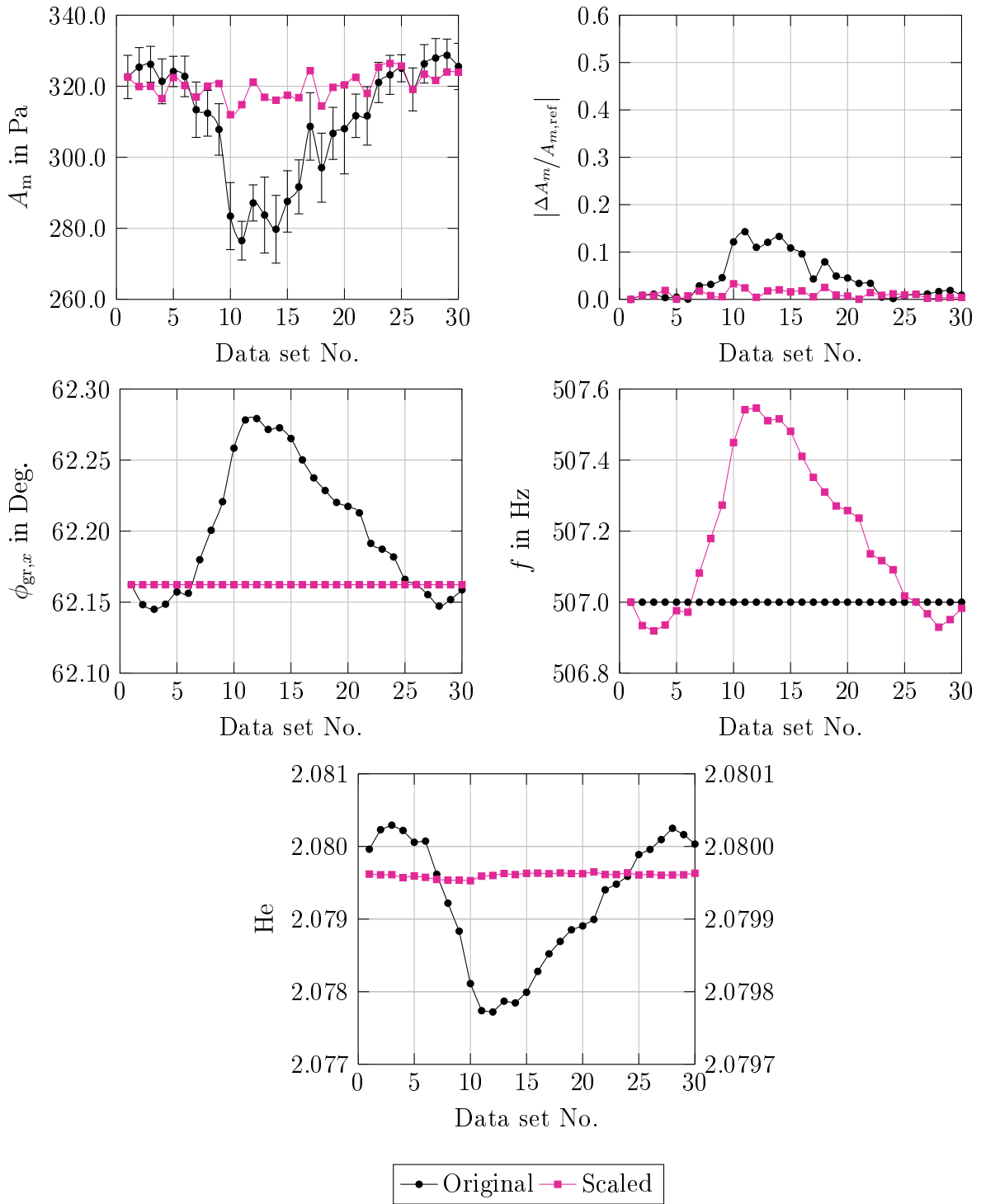


Figure A.9: Results of post-hoc scaling. Top left: Modal amplitude. Top right: Relative change of the modal amplitude with respect to reference data set No.1. Center left: Group velocity angle. Center right: Excitation frequency and calculated reduced frequency. Bottom: Helmholtz number (the lines and markers colored in black and magenta refer to the left and the right ordinate, respectively).

[Test case 1 | part-load operation | $m = -1$ | $f_{exc} = 507$ Hz]

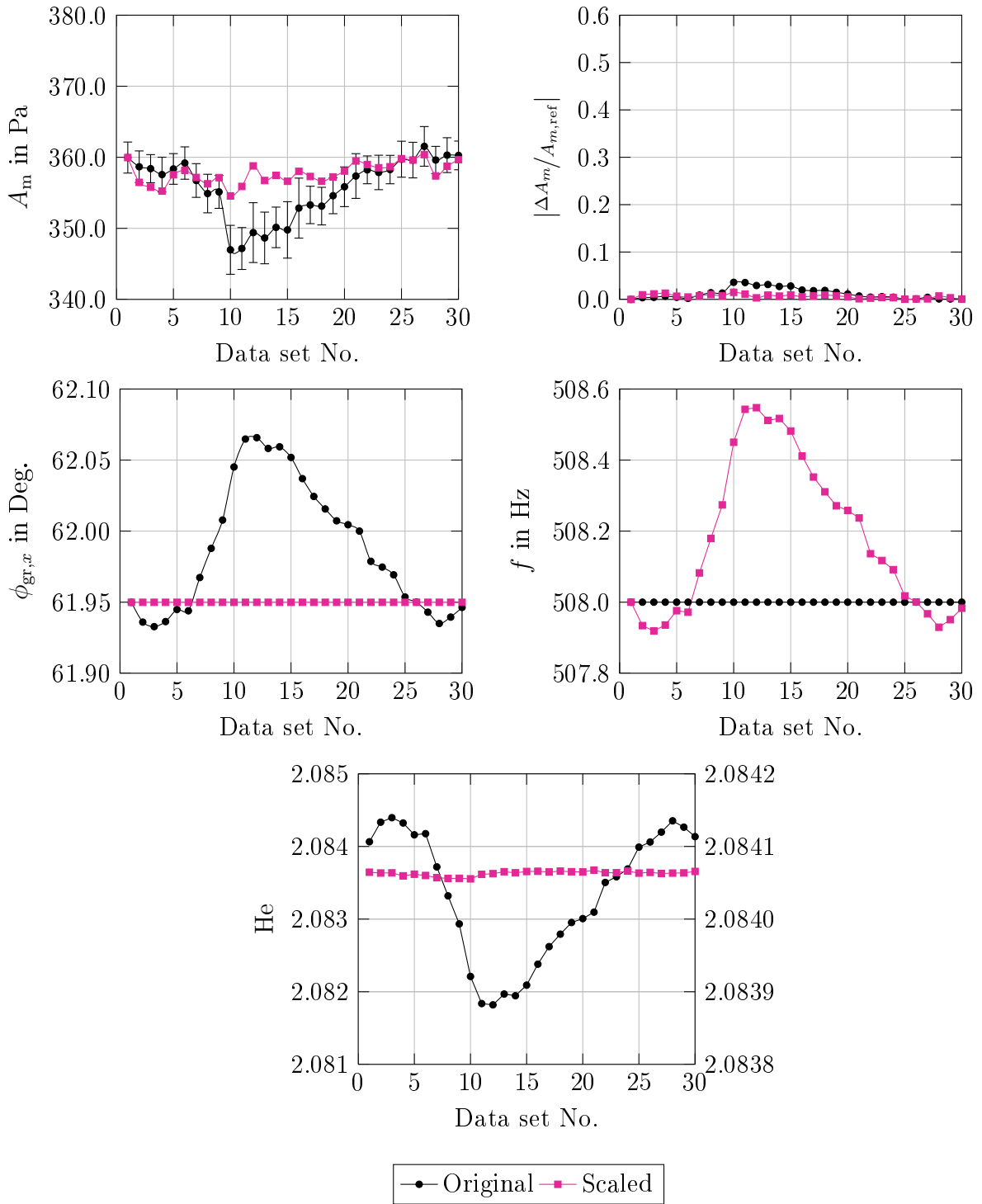


Figure A.10: Results of post-hoc scaling. Top left: Modal amplitude. Top right: Relative change of the modal amplitude with respect to reference data set No.1. Center left: Group velocity angle. Center right: Excitation frequency and calculated reduced frequency. Bottom: Helmholtz number (the lines and markers colored in black and magenta refer to the left and the right ordinate, respectively).

[Test case 1 | part-load operation | $m = -1$ | $f_{exc} = 508$ Hz]

A.9 Results of Post-hoc Scaling for Test Case 1

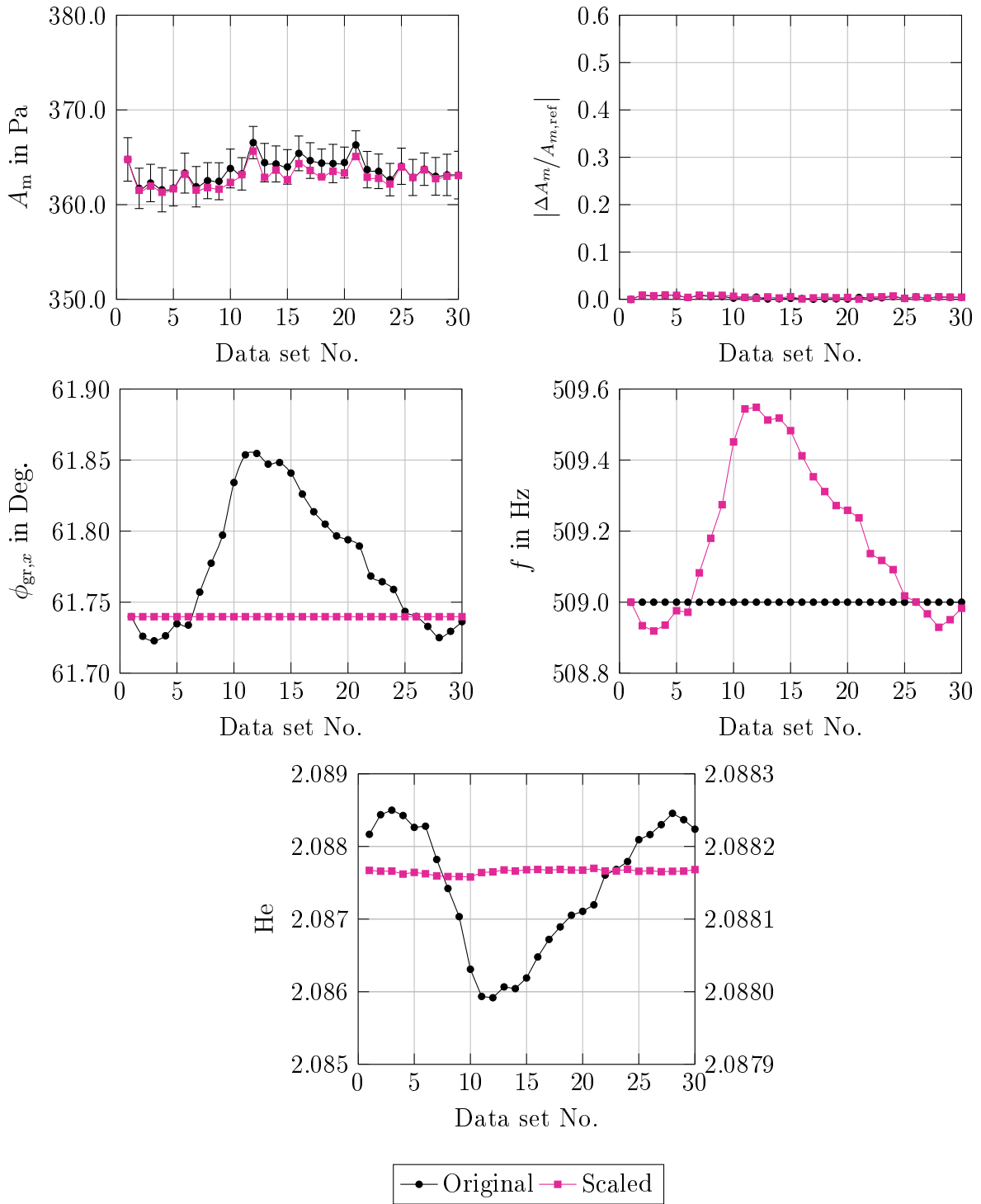


Figure A.11: Results of post-hoc scaling. Top left: Modal amplitude. Top right: Relative change of the modal amplitude with respect to reference data set No.1. Center left: Group velocity angle. Center right: Excitation frequency and calculated reduced frequency. Bottom: Helmholtz number (the lines and markers colored in black and magenta refer to the left and the right ordinate, respectively).

[Test case 1 | part-load operation | $m = -1$ | $f_{exc} = 509$ Hz]

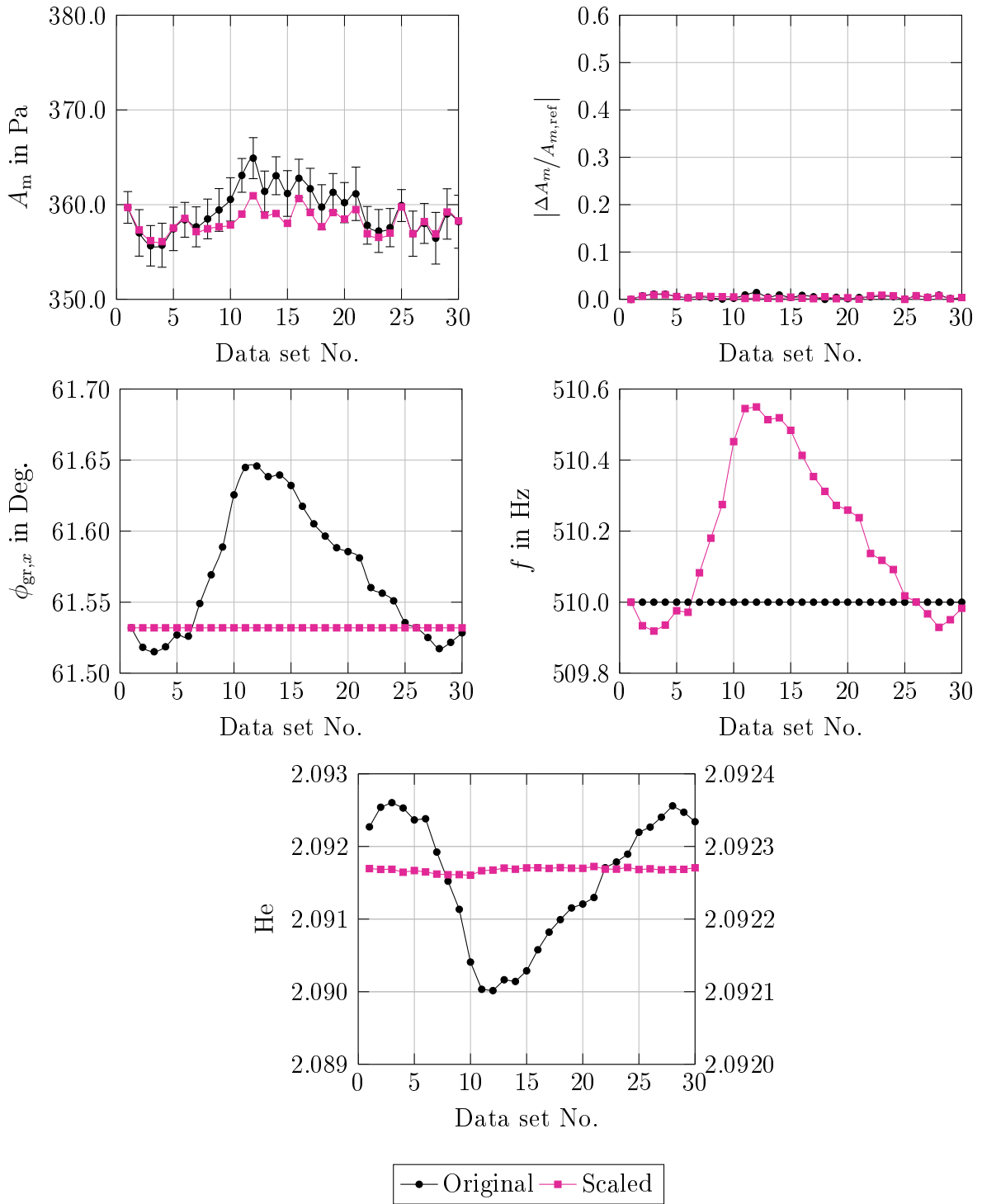


Figure A.12: Results of post-hoc scaling. Top left: Modal amplitude. Top right: Relative change of the modal amplitude with respect to reference data set No.1. Center left: Group velocity angle. Center right: Excitation frequency and calculated reduced frequency. Bottom: Helmholtz number (the lines and markers colored in black and magenta refer to the left and the right ordinate, respectively).

[Test case 1 | part-load operation | $m = -1$ | $f_{exc} = 510$ Hz]

A.9 Results of Post-hoc Scaling for Test Case 1

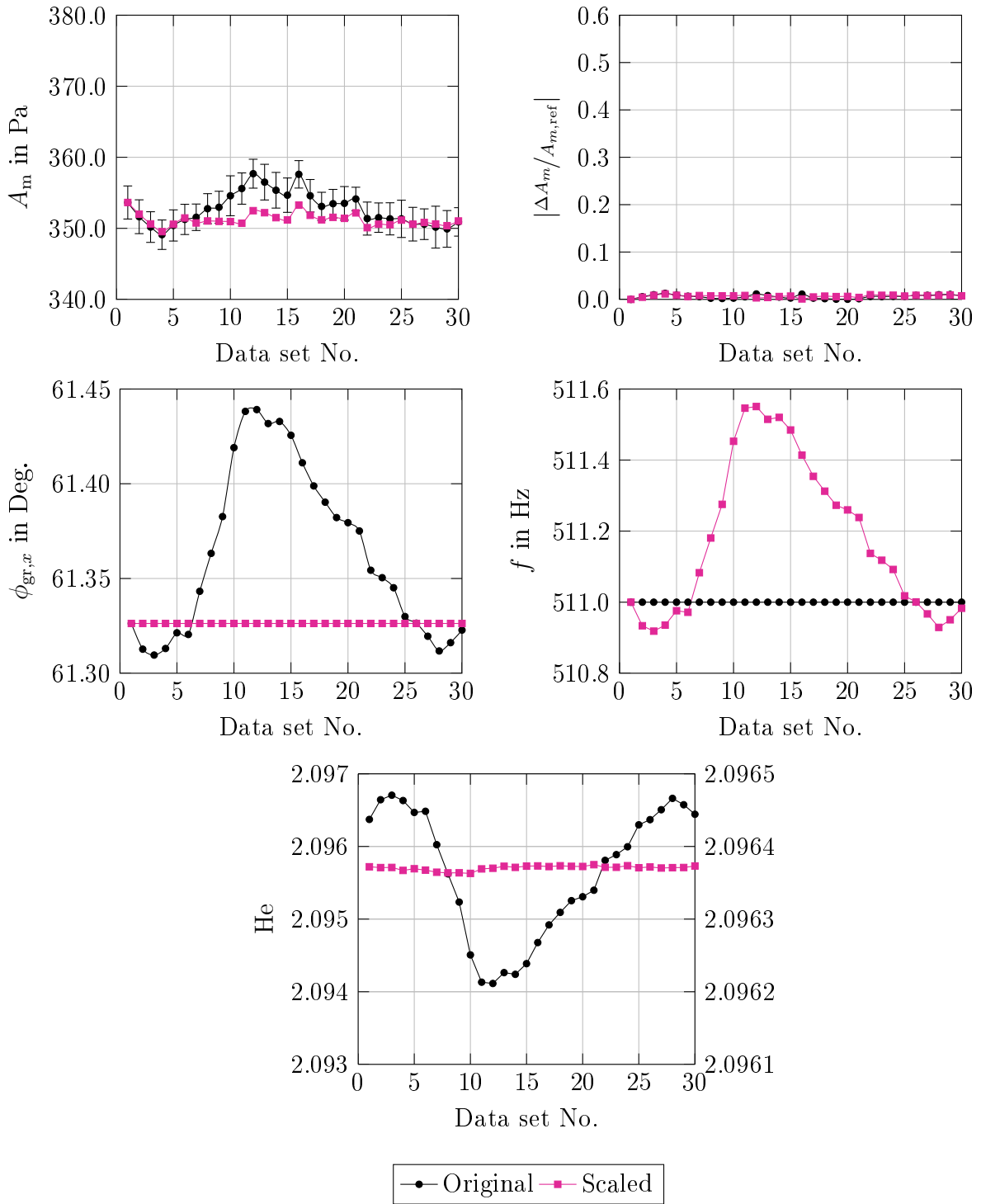


Figure A.13: Results of post-hoc scaling. Top left: Modal amplitude. Top right: Relative change of the modal amplitude with respect to reference data set No.1. Center left: Group velocity angle. Center right: Excitation frequency and calculated reduced frequency. Bottom: Helmholtz number (the lines and markers colored in black and magenta refer to the left and the right ordinate, respectively).

[Test case 1 | part-load operation | $m = -1$ | $f_{exc} = 511$ Hz]

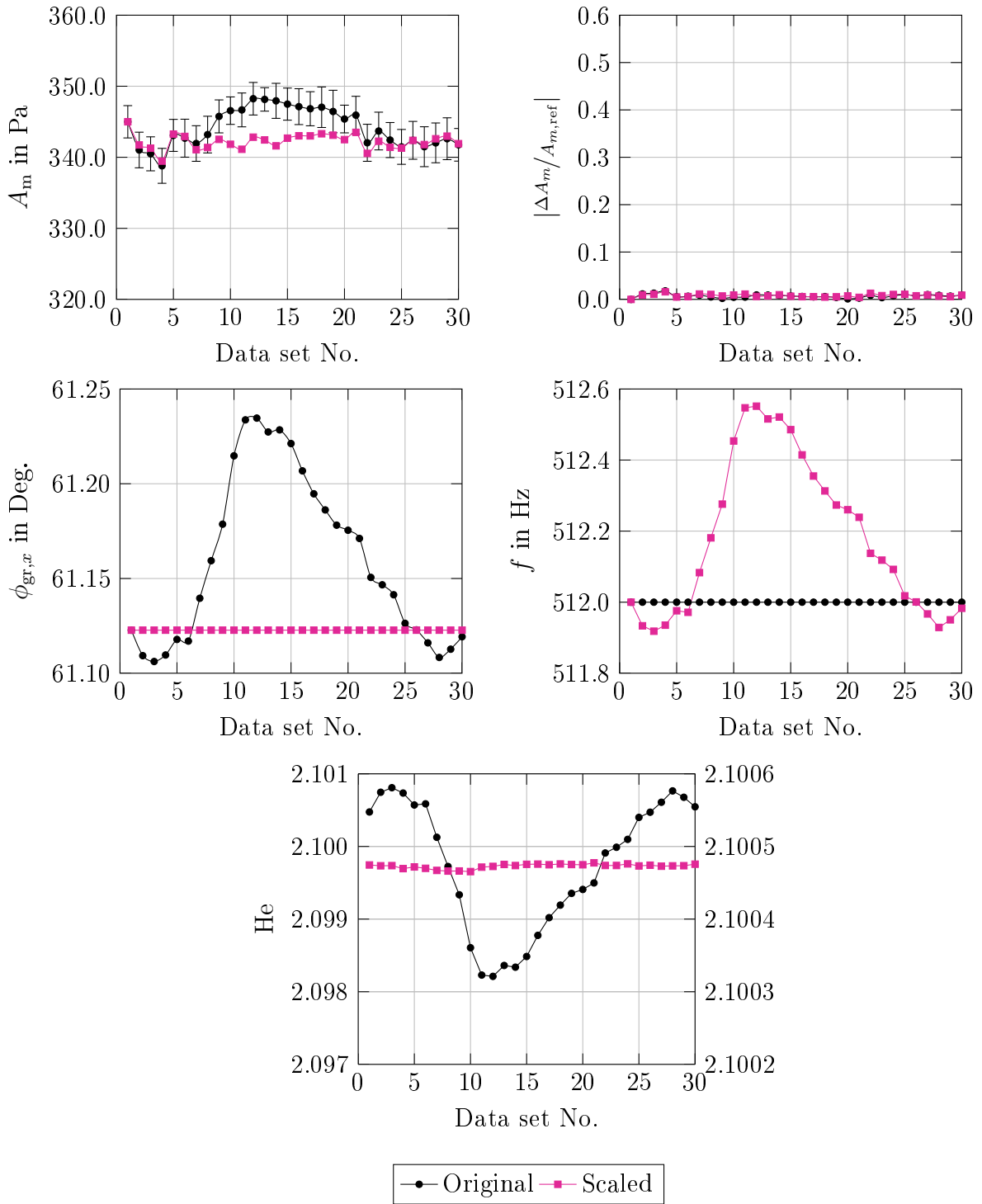


Figure A.14: Results of post-hoc scaling. Top left: Modal amplitude. Top right: Relative change of the modal amplitude with respect to reference data set No.1. Center left: Group velocity angle. Center right: Excitation frequency and calculated reduced frequency. Bottom: Helmholtz number (the lines and markers colored in black and magenta refer to the left and the right ordinate, respectively).

[Test case 1 | part-load operation | $m = -1$ | $f_{exc} = 512$ Hz]

A.9 Results of Post-hoc Scaling for Test Case 1

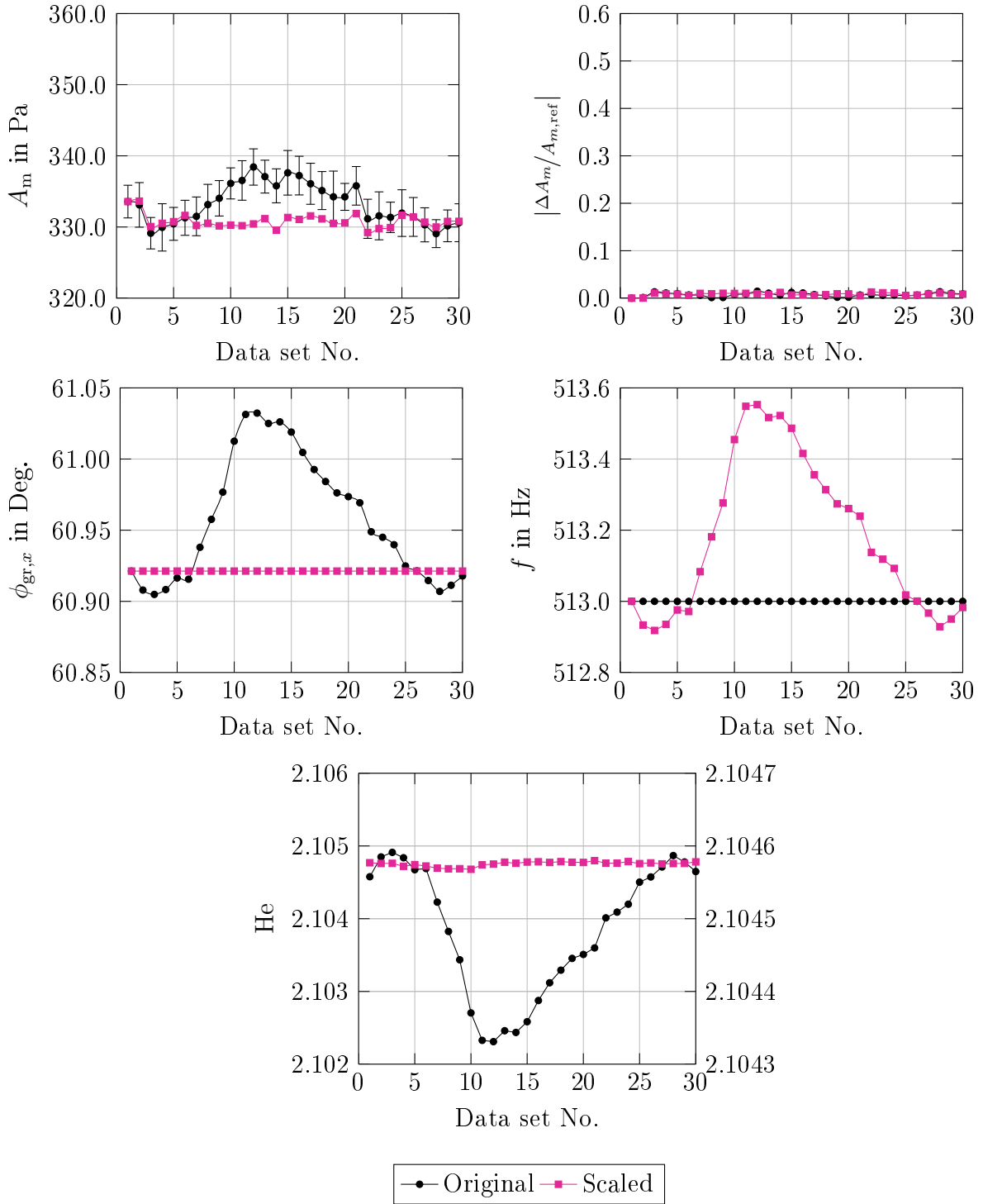


Figure A.15: Results of post-hoc scaling. Top left: Modal amplitude. Top right: Relative change of the modal amplitude with respect to reference data set No.1. Center left: Group velocity angle. Center right: Excitation frequency and calculated reduced frequency. Bottom: Helmholtz number (the lines and markers colored in black and magenta refer to the left and the right ordinate, respectively).

[Test case 1 | part-load operation | $m = -1$ | $f_{exc} = 513$ Hz]

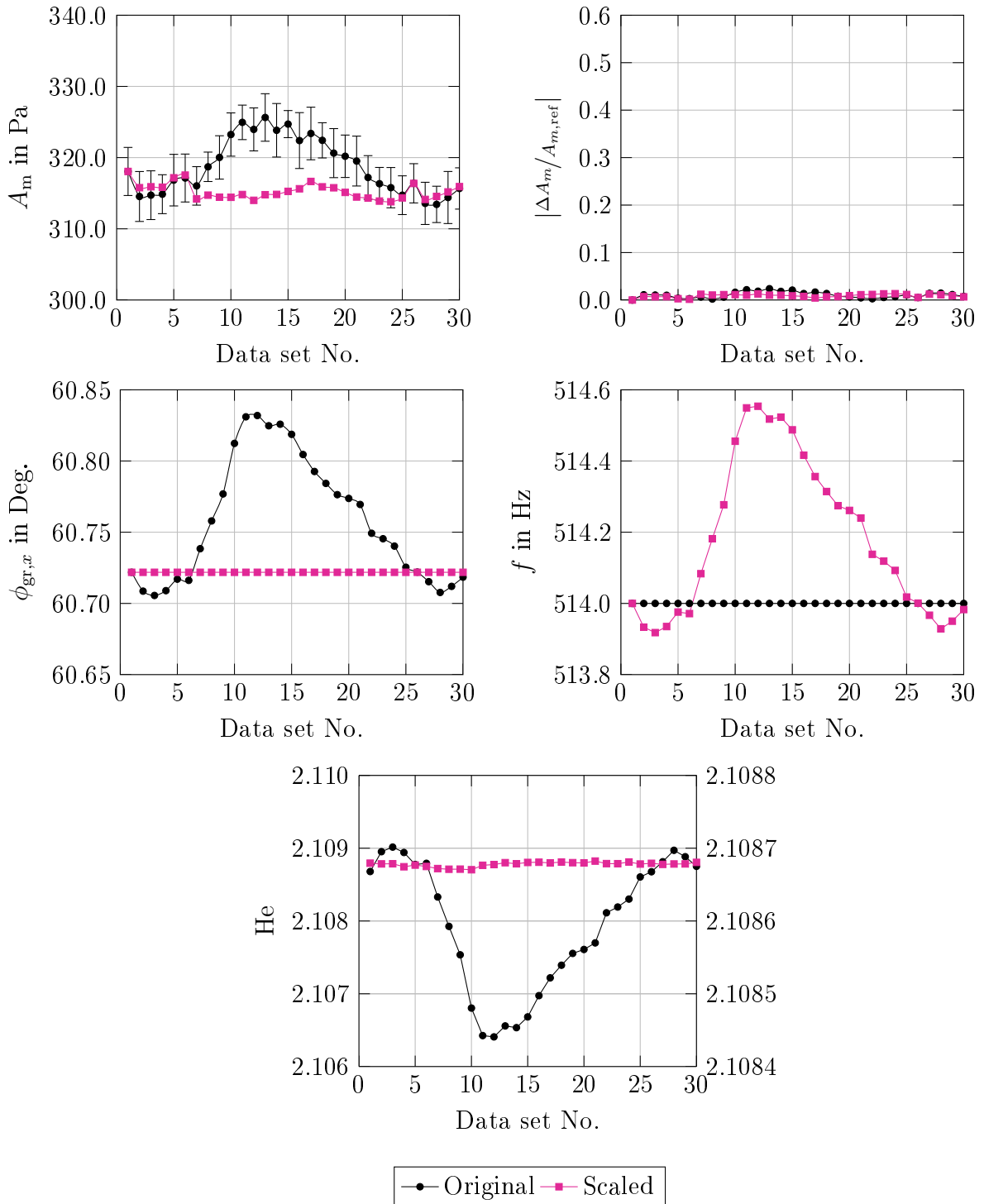


Figure A.16: Results of post-hoc scaling. Top left: Modal amplitude. Top right: Relative change of the modal amplitude with respect to reference data set No.1. Center left: Group velocity angle. Center right: Excitation frequency and calculated reduced frequency. Bottom: Helmholtz number (the lines and markers colored in black and magenta refer to the left and the right ordinate, respectively).

[Test case 1 | part-load operation | $m = -1$ | $f_{exc} = 514$ Hz]

A.9 Results of Post-hoc Scaling for Test Case 1

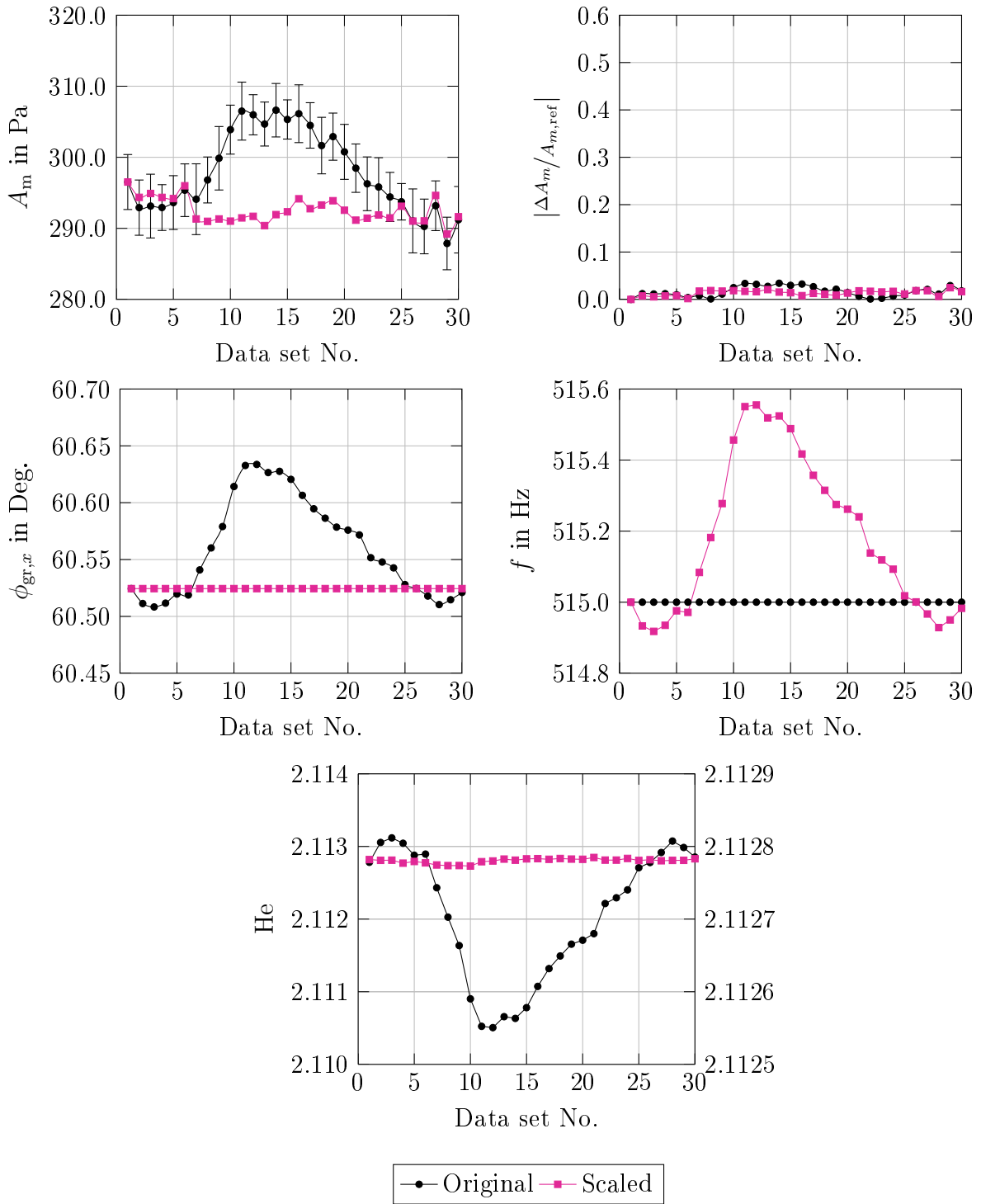


Figure A.17: Results of post-hoc scaling. Top left: Modal amplitude. Top right: Relative change of the modal amplitude with respect to reference data set No.1. Center left: Group velocity angle. Center right: Excitation frequency and calculated reduced frequency. Bottom: Helmholtz number (the lines and markers colored in black and magenta refer to the left and the right ordinate, respectively).

[Test case 1 | part-load operation | $m = -1$ | $f_{exc} = 515$ Hz]

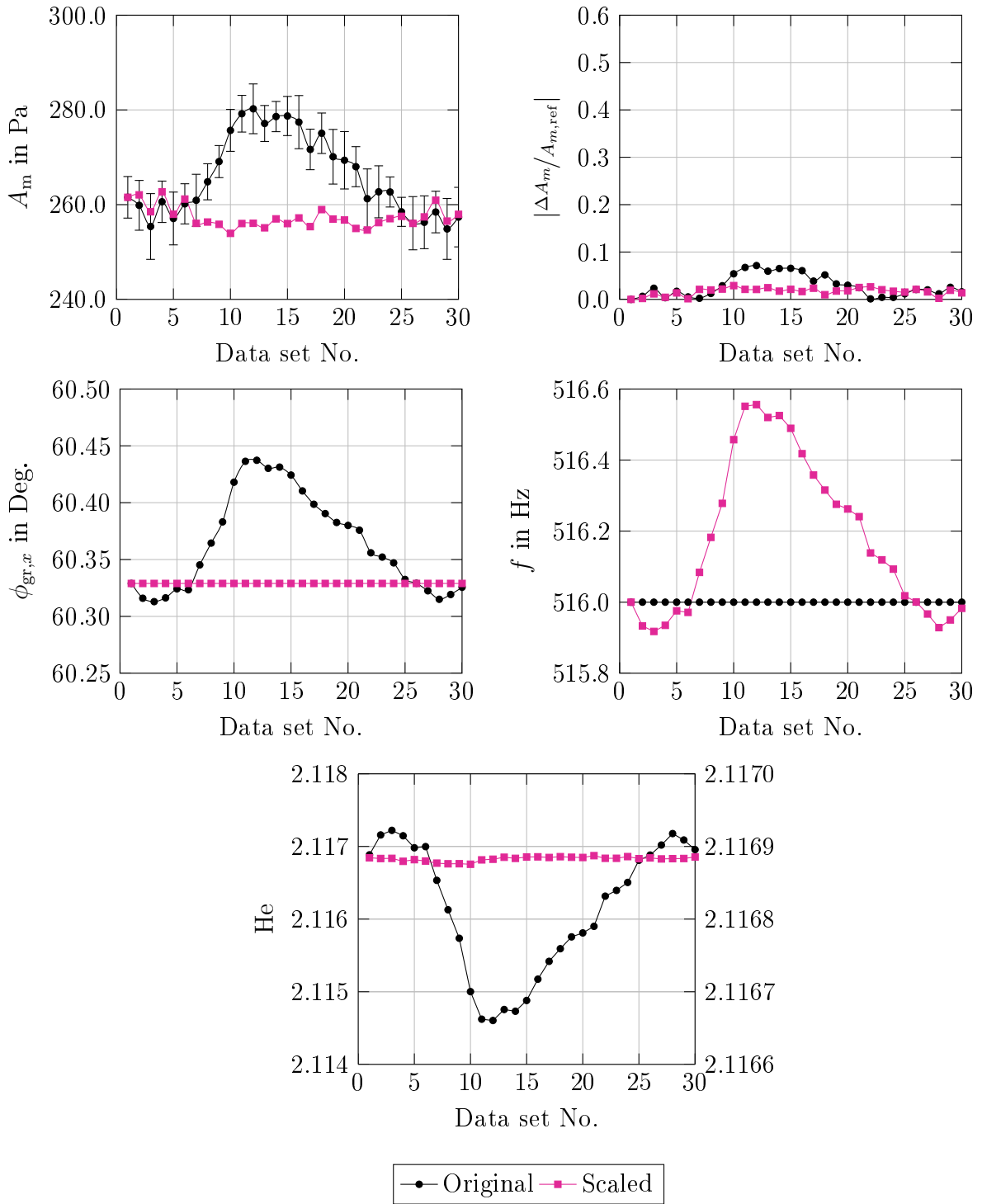


Figure A.18: Results of post-hoc scaling. Top left: Modal amplitude. Top right: Relative change of the modal amplitude with respect to reference data set No.1. Center left: Group velocity angle. Center right: Excitation frequency and calculated reduced frequency. Bottom: Helmholtz number (the lines and markers colored in black and magenta refer to the left and the right ordinate, respectively).

[Test case 1 | part-load operation | $m = -1$ | $f_{exc} = 516$ Hz]

A.9 Results of Post-hoc Scaling for Test Case 1

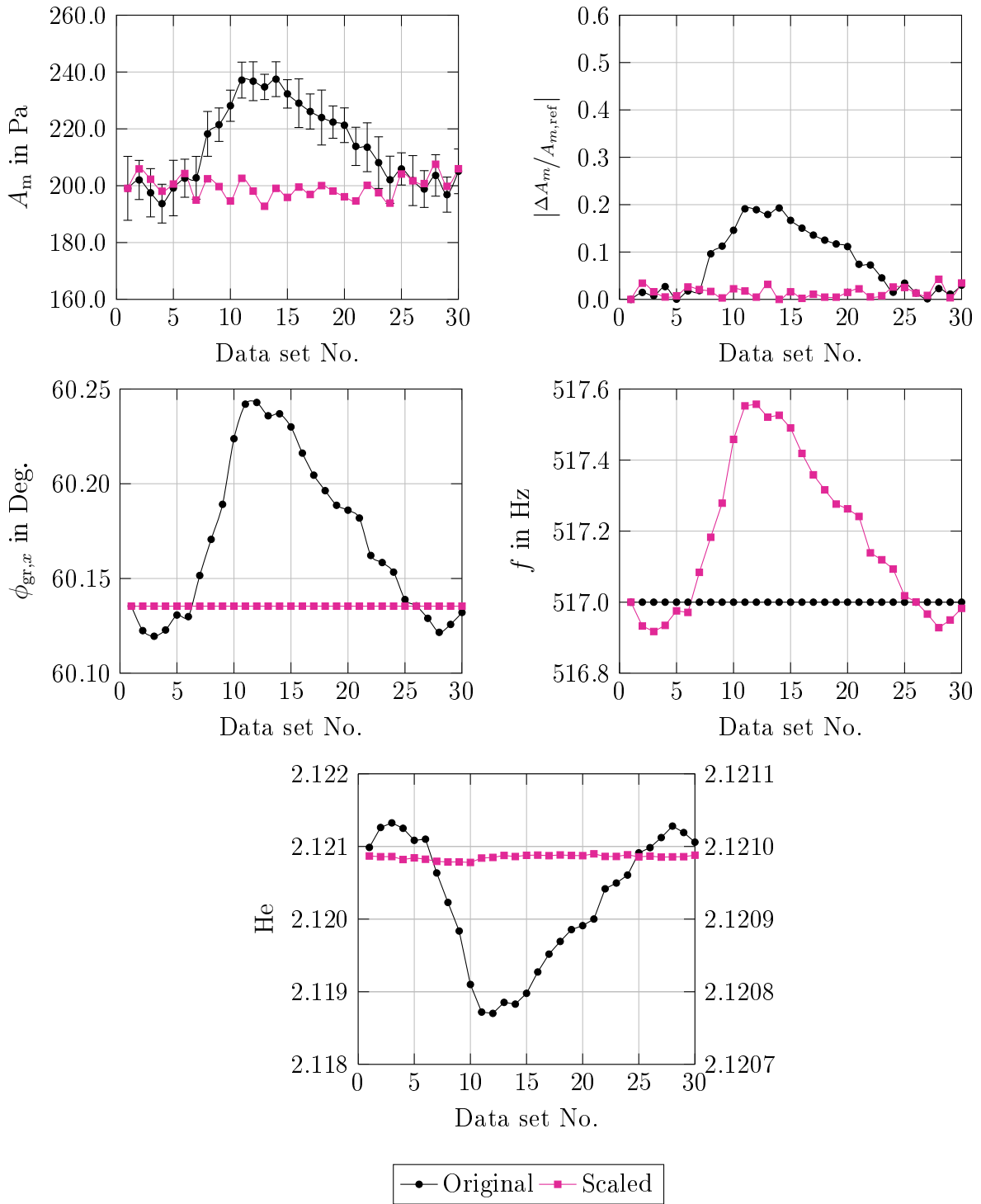


Figure A.19: Results of post-hoc scaling. Top left: Modal amplitude. Top right: Relative change of the modal amplitude with respect to reference data set No.1. Center left: Group velocity angle. Center right: Excitation frequency and calculated reduced frequency. Bottom: Helmholtz number (the lines and markers colored in black and magenta refer to the left and the right ordinate, respectively).

[Test case 1 | part-load operation | $m = -1$ | $f_{exc} = 517$ Hz]

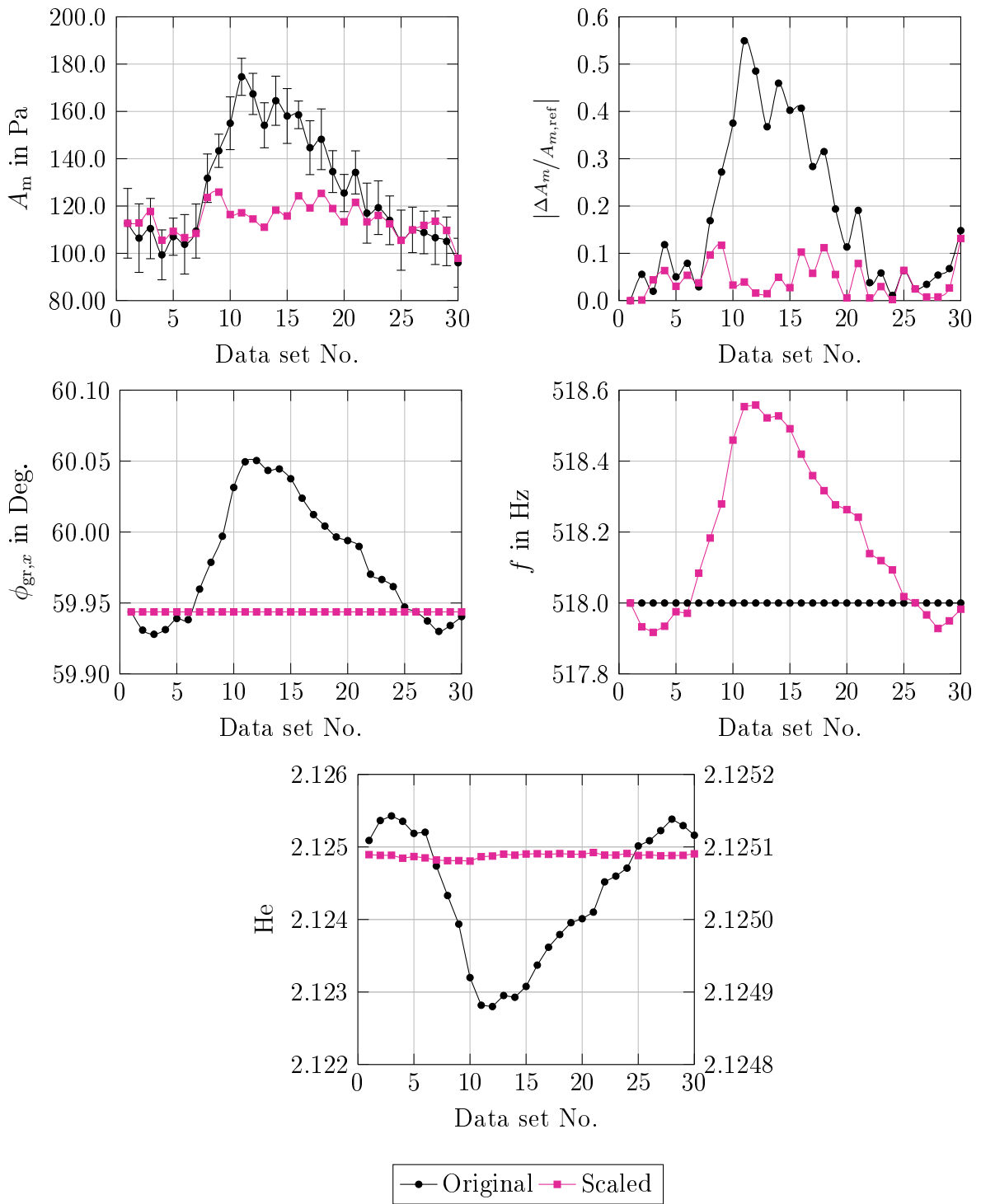


Figure A.20: Results of post-hoc scaling. Top left: Modal amplitude. Top right: Relative change of the modal amplitude with respect to reference data set No.1. Center left: Group velocity angle. Center right: Excitation frequency and calculated reduced frequency. Bottom: Helmholtz number (the lines and markers colored in black and magenta refer to the left and the right ordinate, respectively).

[Test case 1 | part-load operation | $m = -1$ | $f_{exc} = 518$ Hz]

A.9 Results of Post-hoc Scaling for Test Case 1

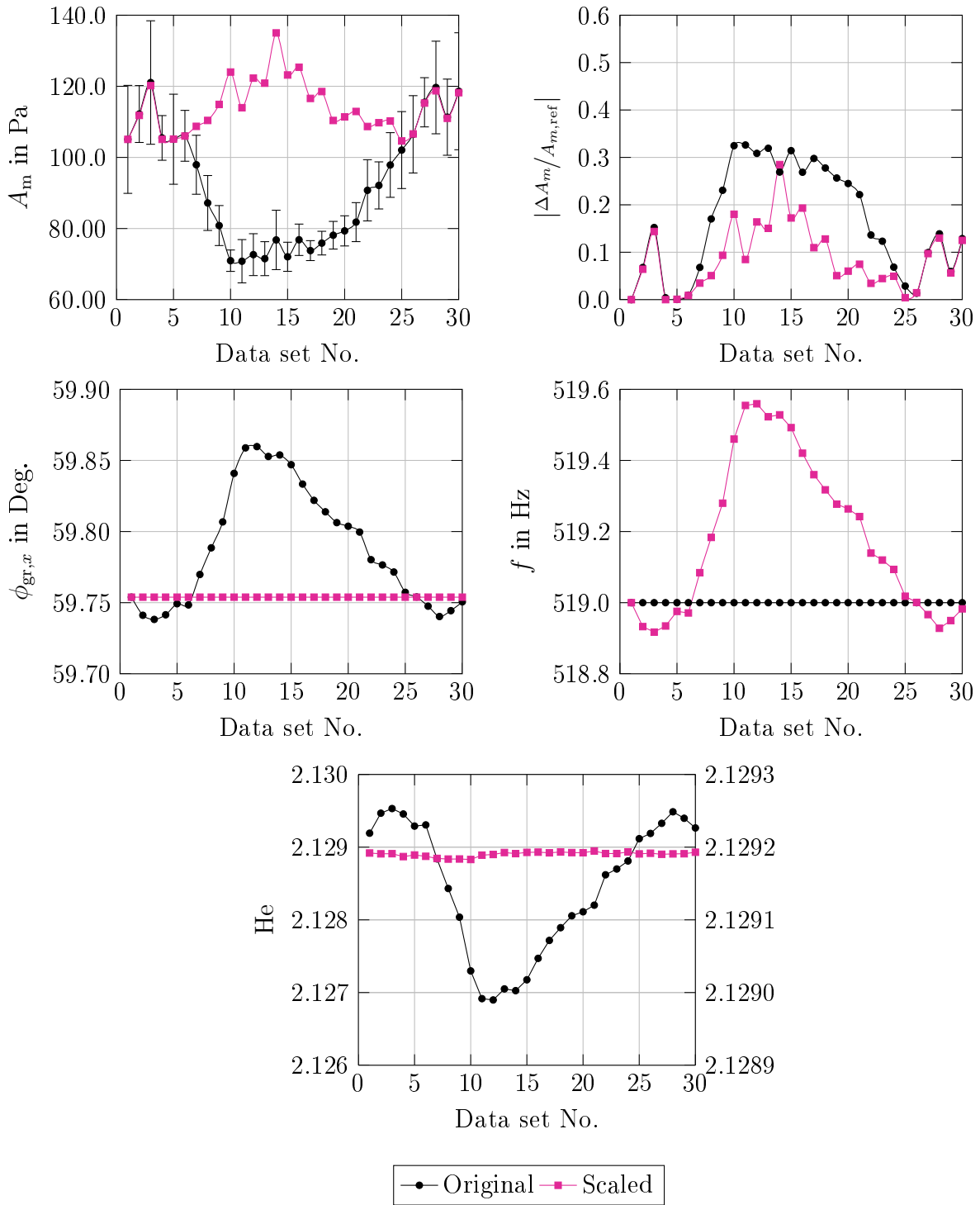


Figure A.21: Results of post-hoc scaling. Top left: Modal amplitude. Top right: Relative change of the modal amplitude with respect to reference data set No.1. Center left: Group velocity angle. Center right: Excitation frequency and calculated reduced frequency. Bottom: Helmholtz number (the lines and markers colored in black and magenta refer to the left and the right ordinate, respectively).

[Test case 1 | part-load operation | $m = -1$ | $f_{exc} = 519$ Hz]

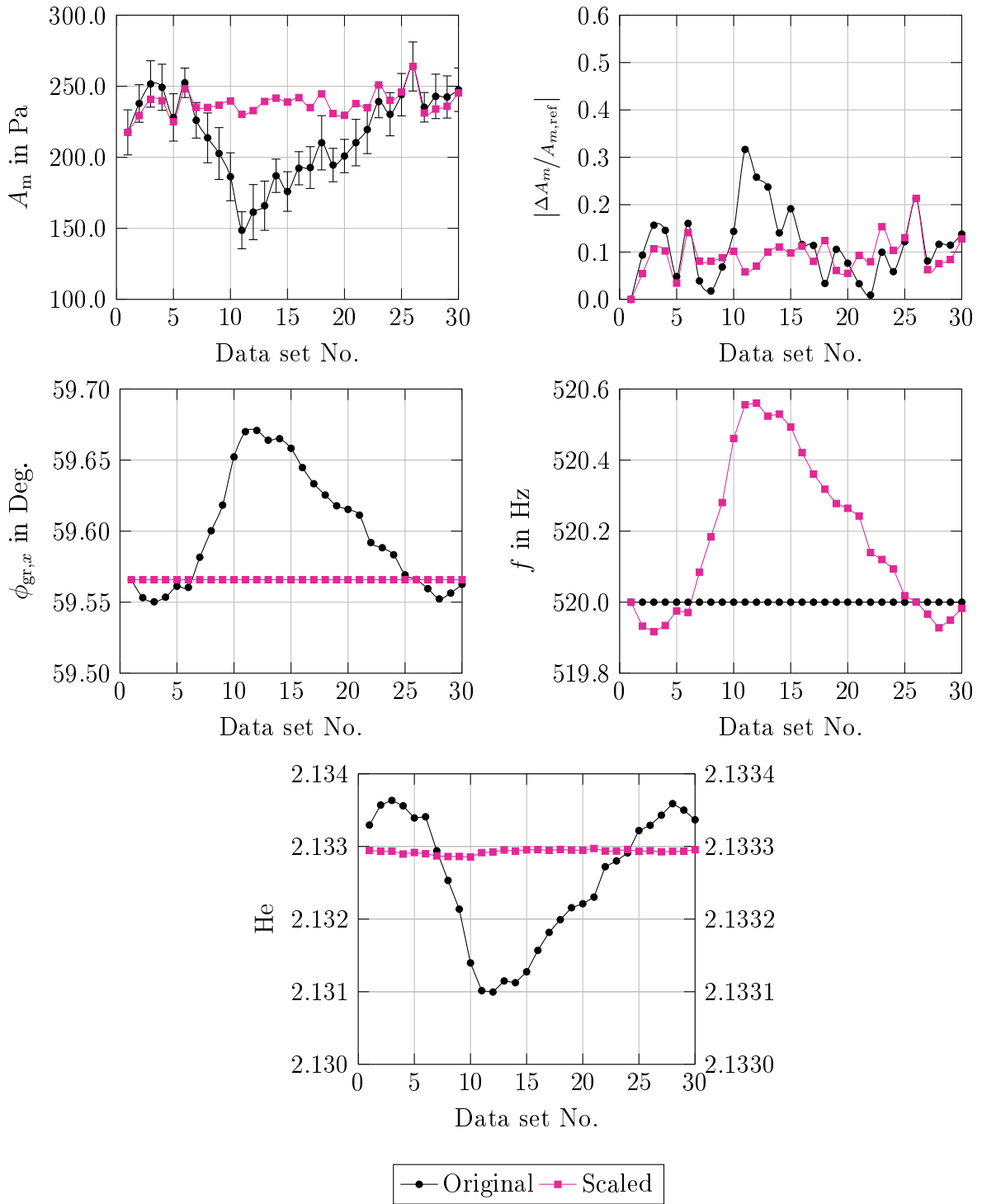


Figure A.22: Results of post-hoc scaling. Top left: Modal amplitude. Top right: Relative change of the modal amplitude with respect to reference data set No.1. Center left: Group velocity angle. Center right: Excitation frequency and calculated reduced frequency. Bottom: Helmholtz number (the lines and markers colored in black and magenta refer to the left and the right ordinate, respectively).

[Test case 1 | part-load operation | $m = -1$ | $f_{exc} = 520$ Hz]

A.9 Results of Post-hoc Scaling for Test Case 1

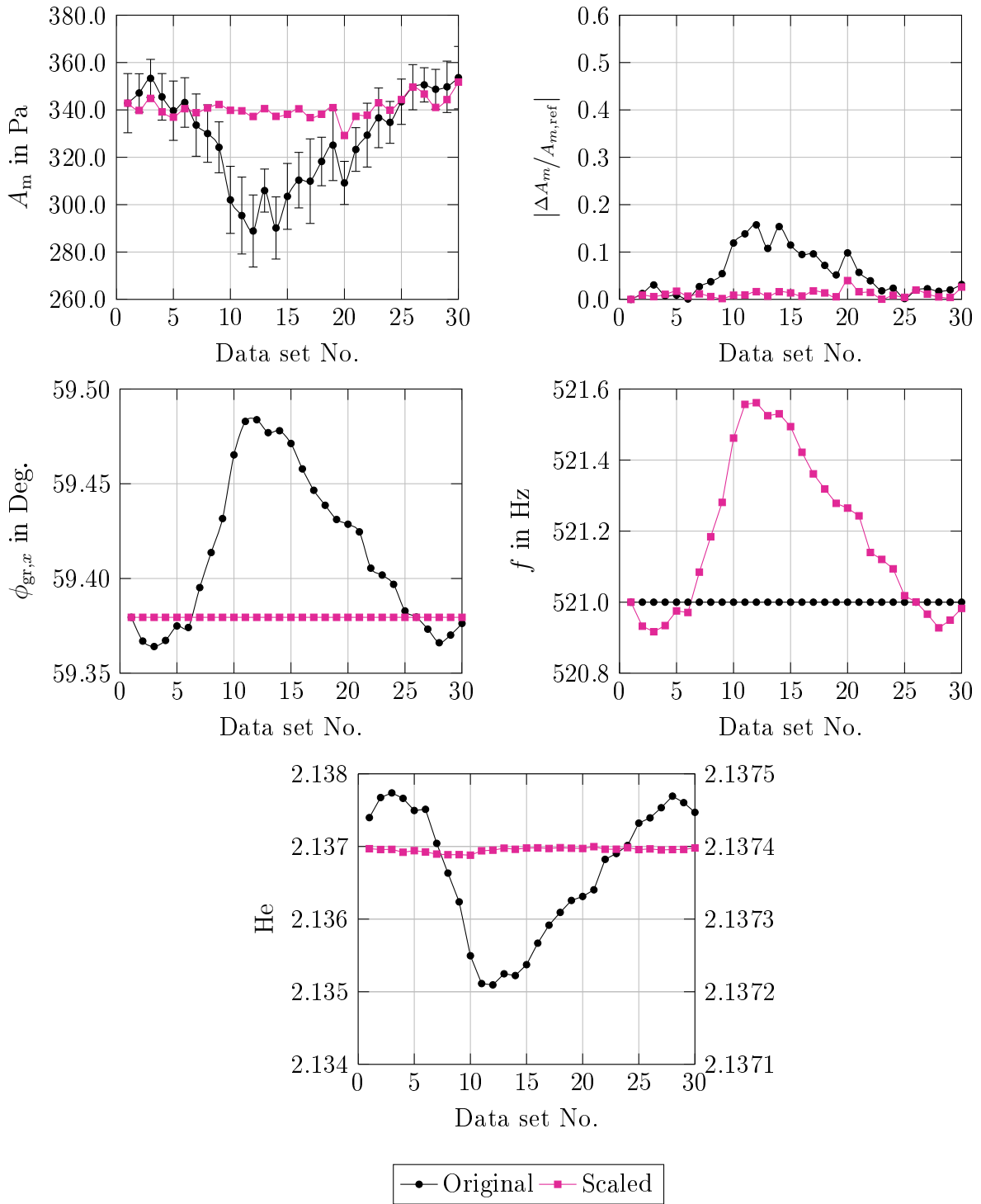


Figure A.23: Results of post-hoc scaling. Top left: Modal amplitude. Top right: Relative change of the modal amplitude with respect to reference data set No.1. Center left: Group velocity angle. Center right: Excitation frequency and calculated reduced frequency. Bottom: Helmholtz number (the lines and markers colored in black and magenta refer to the left and the right ordinate, respectively).

[Test case 1 | part-load operation | $m = -1$ | $f_{exc} = 521$ Hz]

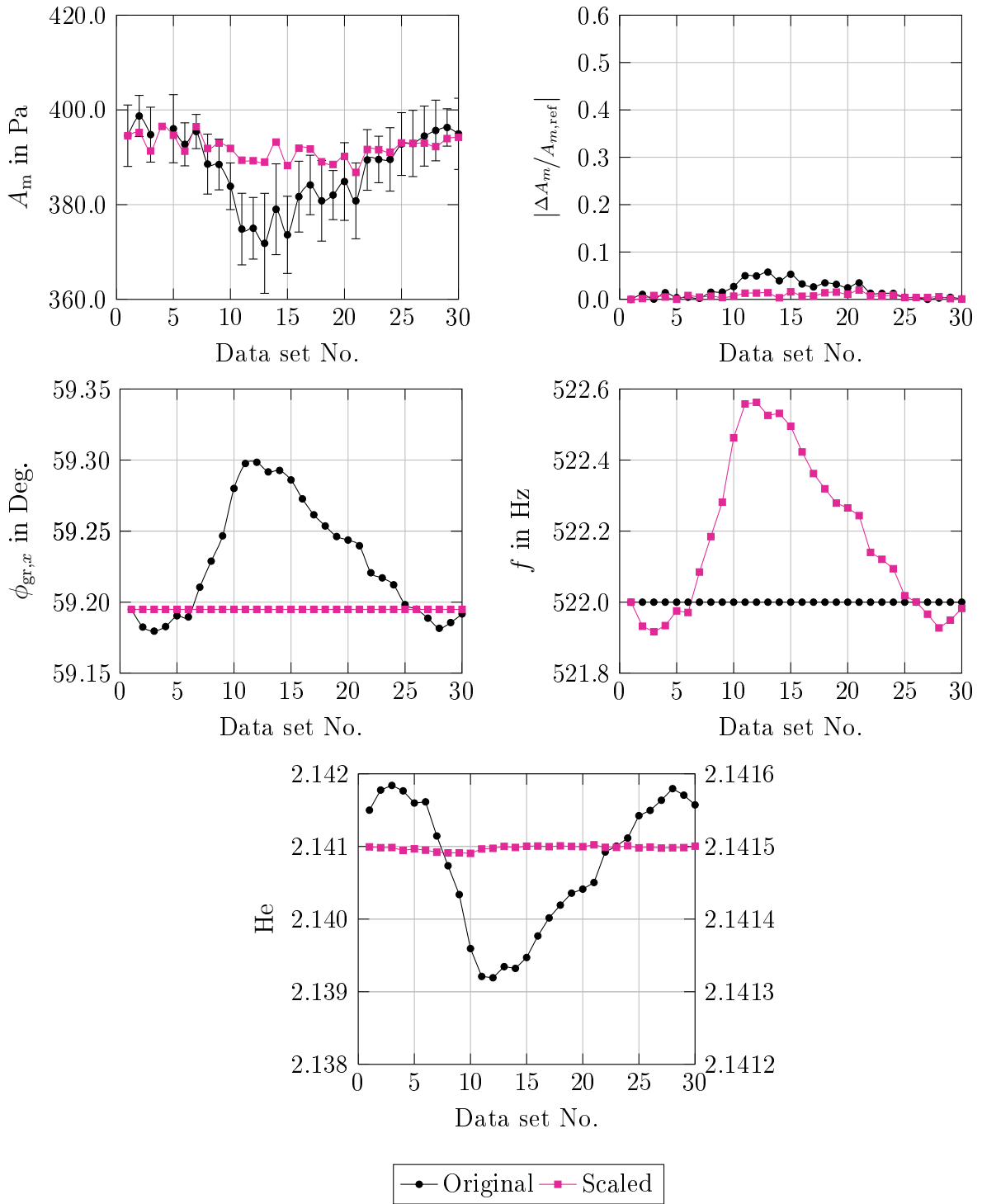


Figure A.24: Results of post-hoc scaling. Top left: Modal amplitude. Top right: Relative change of the modal amplitude with respect to reference data set No.1. Center left: Group velocity angle. Center right: Excitation frequency and calculated reduced frequency. Bottom: Helmholtz number (the lines and markers colored in black and magenta refer to the left and the right ordinate, respectively).

[Test case 1 | part-load operation | $m = -1$ | $f_{exc} = 522$ Hz]

A.9 Results of Post-hoc Scaling for Test Case 1

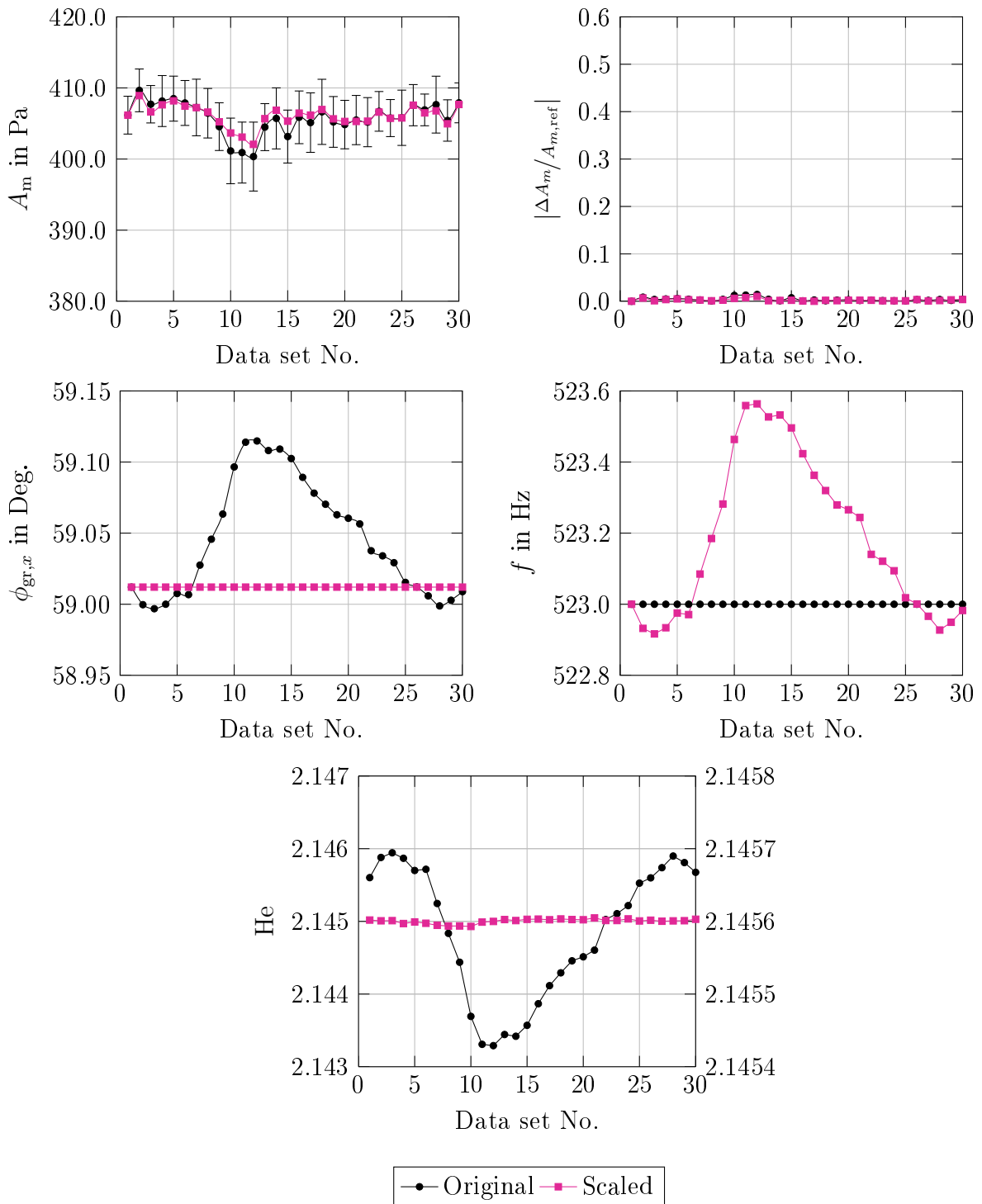


Figure A.25: Results of post-hoc scaling. Top left: Modal amplitude. Top right: Relative change of the modal amplitude with respect to reference data set No.1. Center left: Group velocity angle. Center right: Excitation frequency and calculated reduced frequency. Bottom: Helmholtz number (the lines and markers colored in black and magenta refer to the left and the right ordinate, respectively).

[Test case 1 | part-load operation | $m = -1$ | $f_{exc} = 523$ Hz]

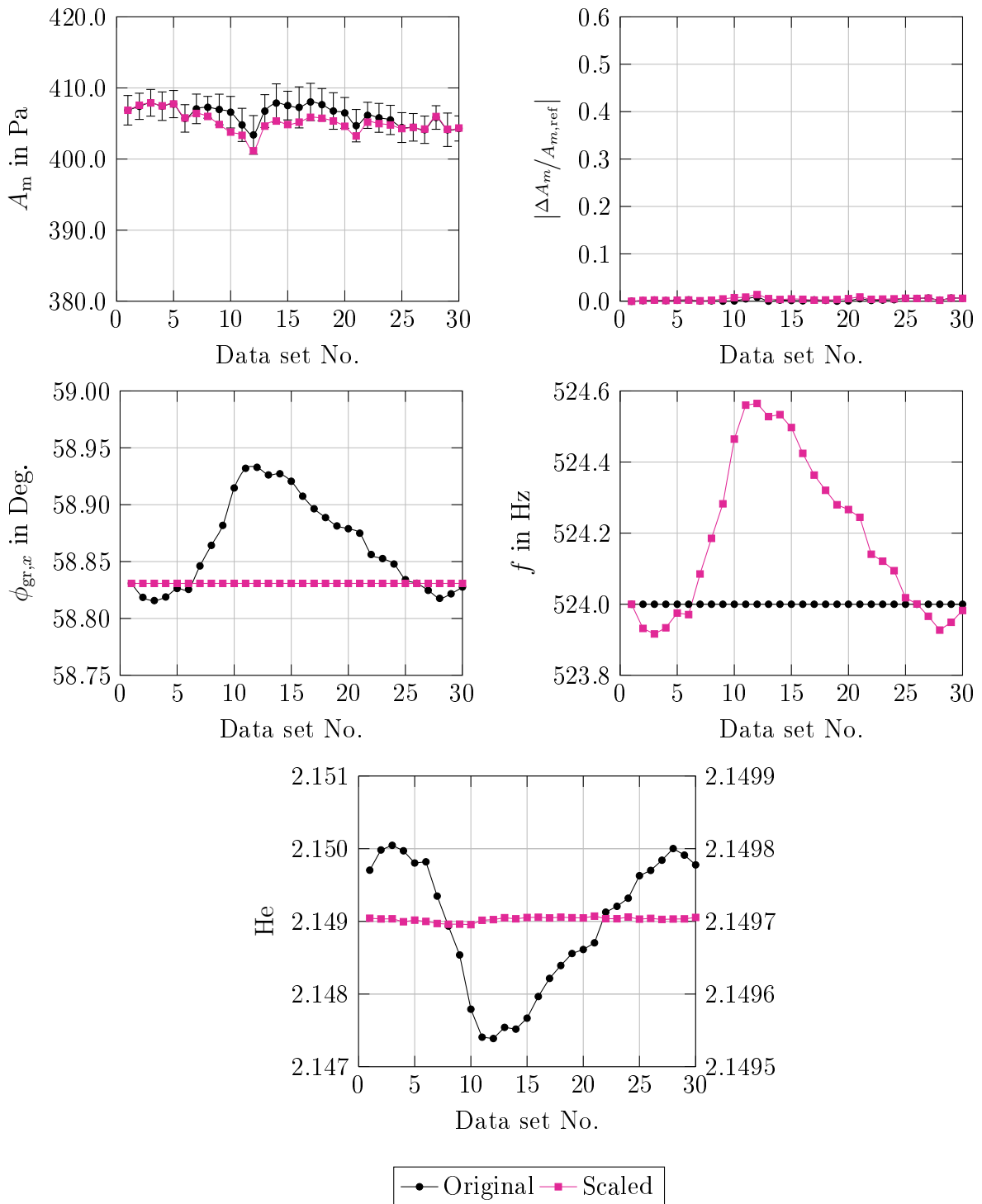


Figure A.26: Results of post-hoc scaling. Top left: Modal amplitude. Top right: Relative change of the modal amplitude with respect to reference data set No.1. Center left: Group velocity angle. Center right: Excitation frequency and calculated reduced frequency. Bottom: Helmholtz number (the lines and markers colored in black and magenta refer to the left and the right ordinate, respectively).

[Test case 1 | part-load operation | $m = -1$ | $f_{exc} = 524$ Hz]

A.9 Results of Post-hoc Scaling for Test Case 1

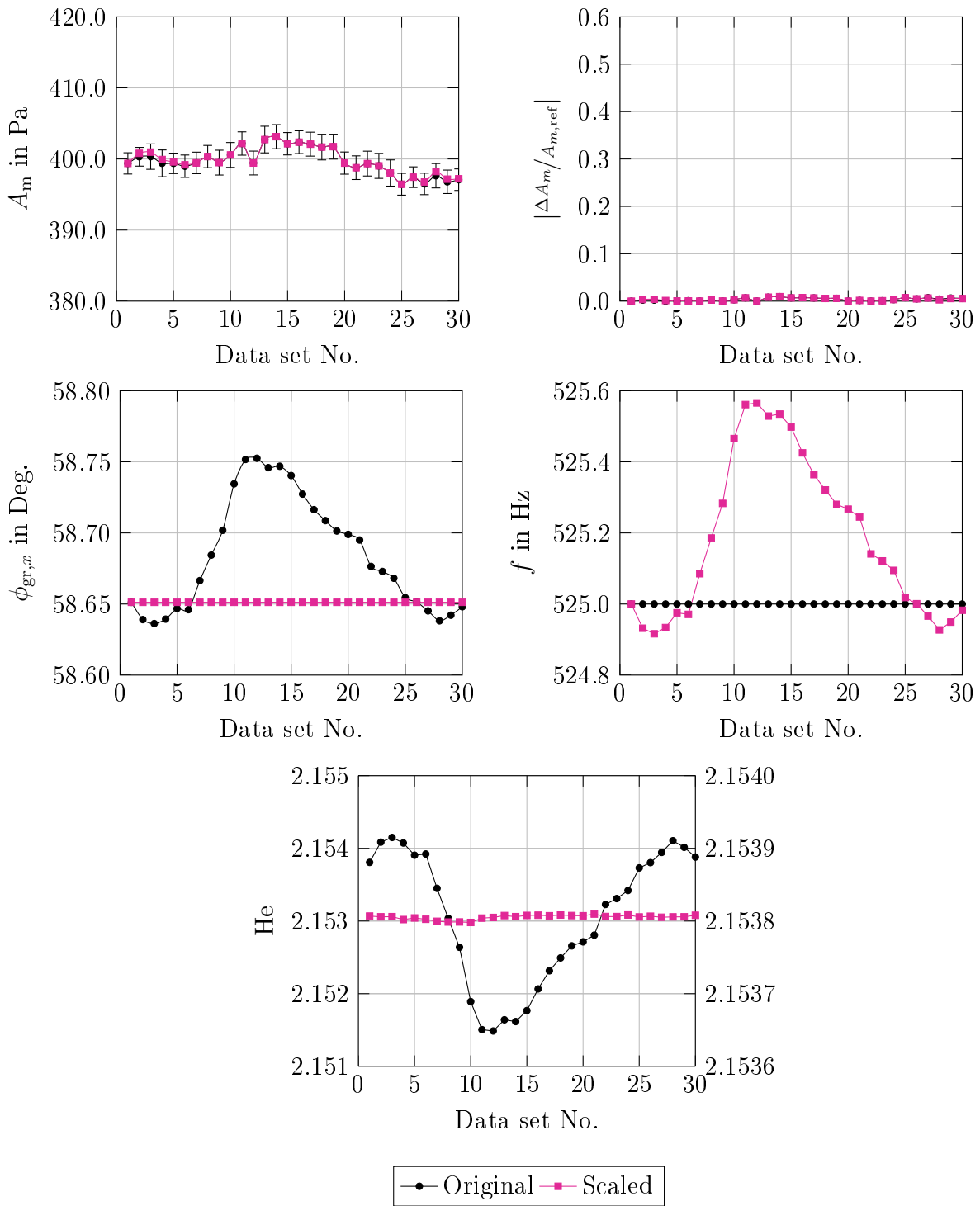


Figure A.27: Results of post-hoc scaling. Top left: Modal amplitude. Top right: Relative change of the modal amplitude with respect to reference data set No.1. Center left: Group velocity angle. Center right: Excitation frequency and calculated reduced frequency. Bottom: Helmholtz number (the lines and markers colored in black and magenta refer to the left and the right ordinate, respectively).

[Test case 1 | part-load operation | $m = -1$ | $f_{exc} = 525$ Hz]

A.10 Results of Post-hoc Scaling for Test Case 2

In Fig. A.28 to Fig. A.48 the results of post-hoc scaling are depicted for each excitation frequency of test case 2.

A.10 Results of Post-hoc Scaling for Test Case 2

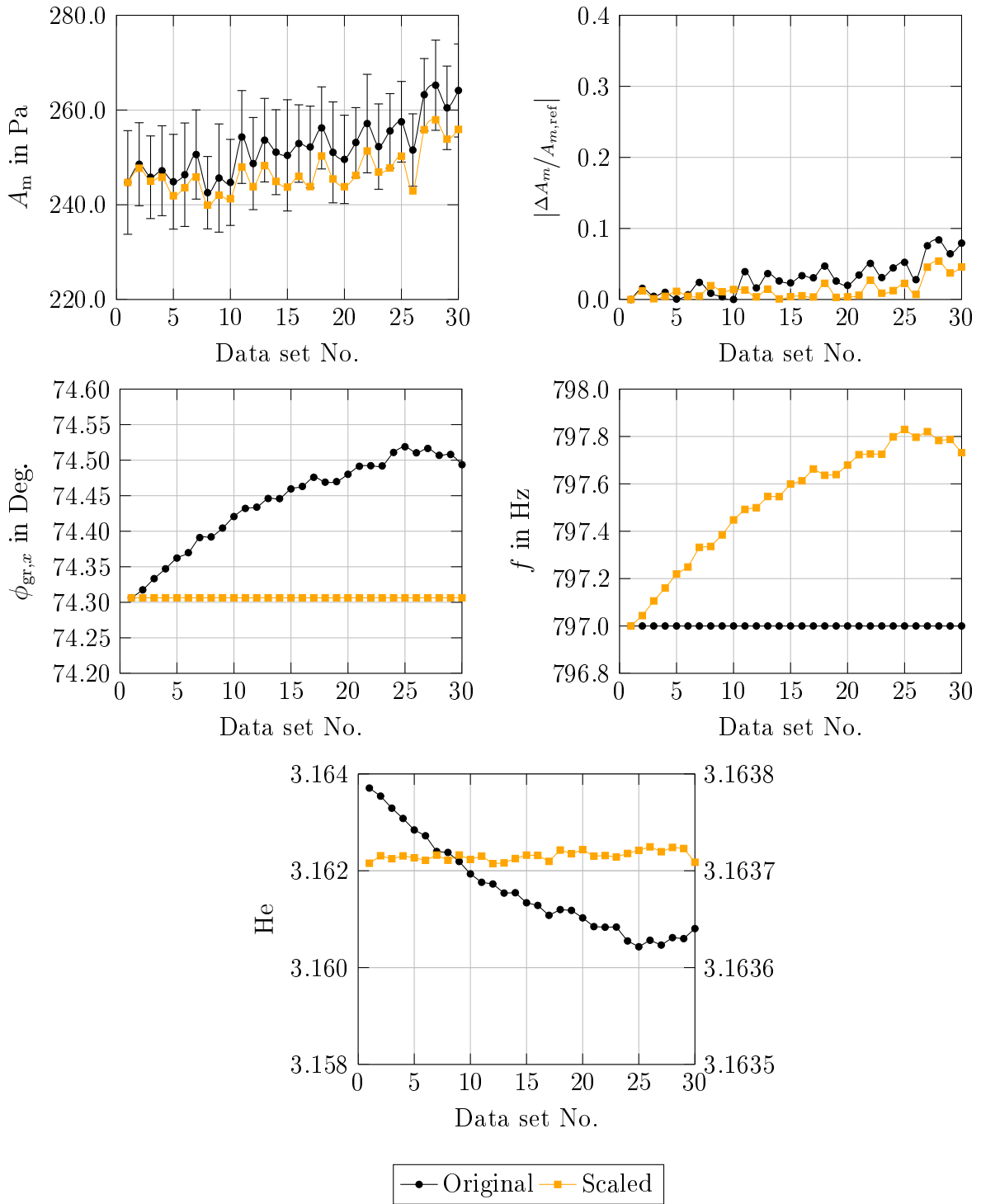


Figure A.28: Results of post-hoc scaling. Top left: Modal amplitude. Top right: Relative change of the modal amplitude with respect to reference data set No.1. Center left: Group velocity angle. Center right: Excitation frequency and calculated reduced frequency. Bottom: Helmholtz number (the lines and markers colored in black and orange refer to the left and the right ordinate, respectively).

[Test Case 2 | design-point operation | $m = 2$ | $f_{exc} = 797$ Hz]

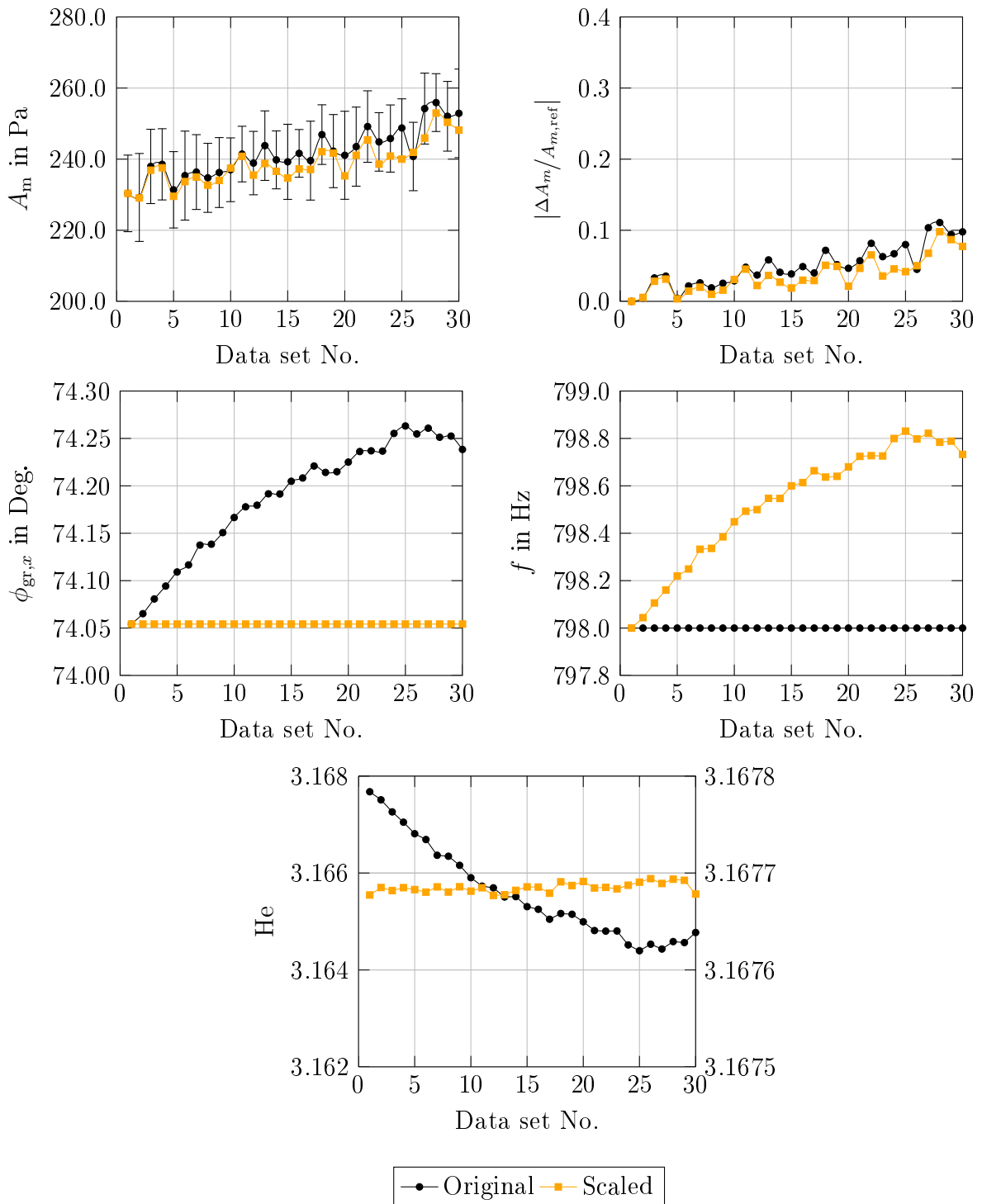


Figure A.29: Results of post-hoc scaling. Top left: Modal amplitude. Top right: Relative change of the modal amplitude with respect to reference data set No.1. Center left: Group velocity angle. Center right: Excitation frequency and calculated reduced frequency. Bottom: Helmholtz number (the lines and markers colored in black and orange refer to the left and the right ordinate, respectively).

[Test Case 2 | design-point operation | $m = 2$ | $f_{exc} = 798$ Hz]

A.10 Results of Post-hoc Scaling for Test Case 2

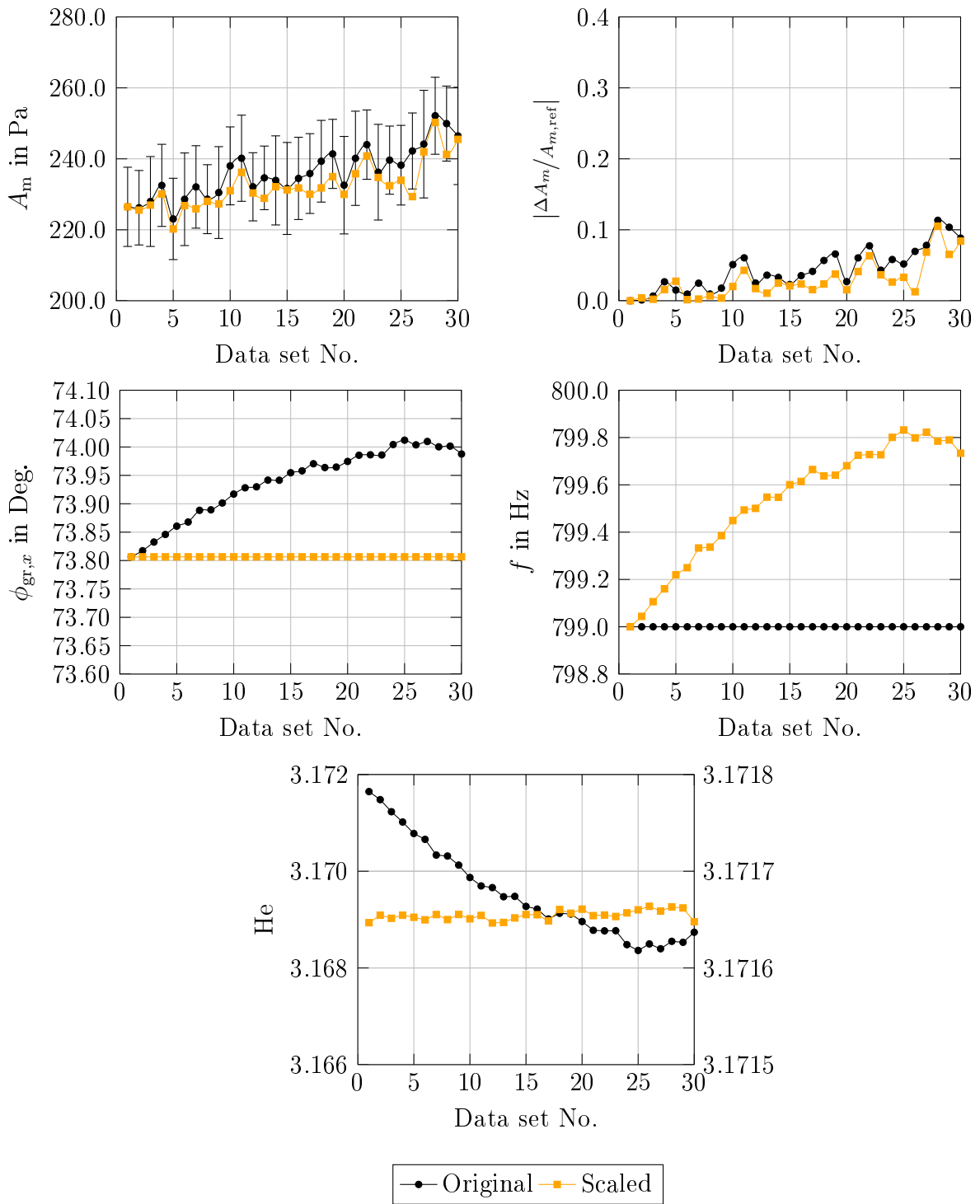


Figure A.30: Results of post-hoc scaling. Top left: Modal amplitude. Top right: Relative change of the modal amplitude with respect to reference data set No.1. Center left: Group velocity angle. Center right: Excitation frequency and calculated reduced frequency. Bottom: Helmholtz number (the lines and markers colored in black and orange refer to the left and the right ordinate, respectively).

[Test Case 2 | design-point operation | $m = 2$ | $f_{exc} = 799$ Hz]

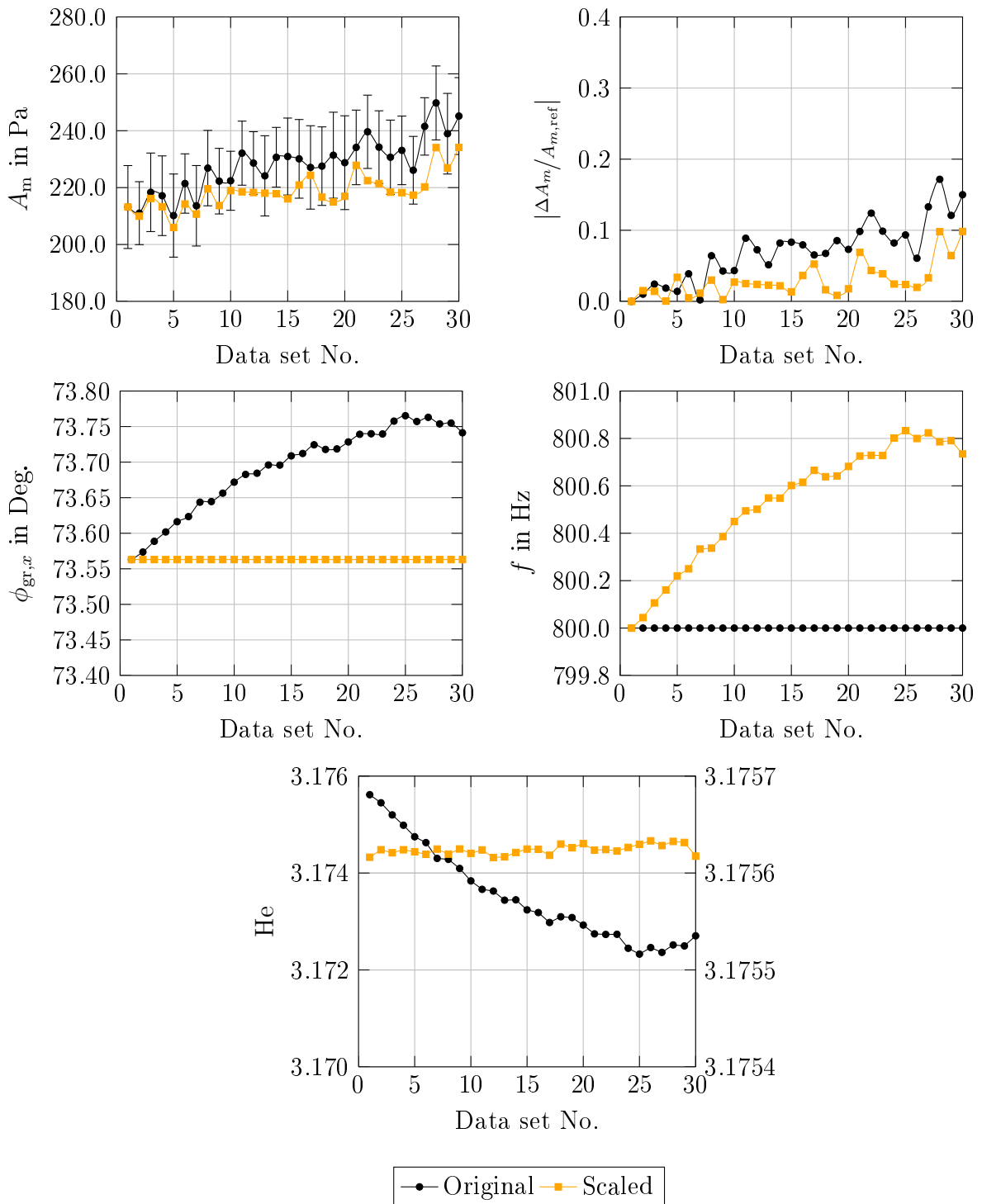


Figure A.31: Results of post-hoc scaling. Top left: Modal amplitude. Top right: Relative change of the modal amplitude with respect to reference data set No.1. Center left: Group velocity angle. Center right: Excitation frequency and calculated reduced frequency. Bottom: Helmholtz number (the lines and markers colored in black and orange refer to the left and the right ordinate, respectively).

[Test Case 2 | design-point operation | $m = 2$ | $f_{exc} = 800$ Hz]

A.10 Results of Post-hoc Scaling for Test Case 2

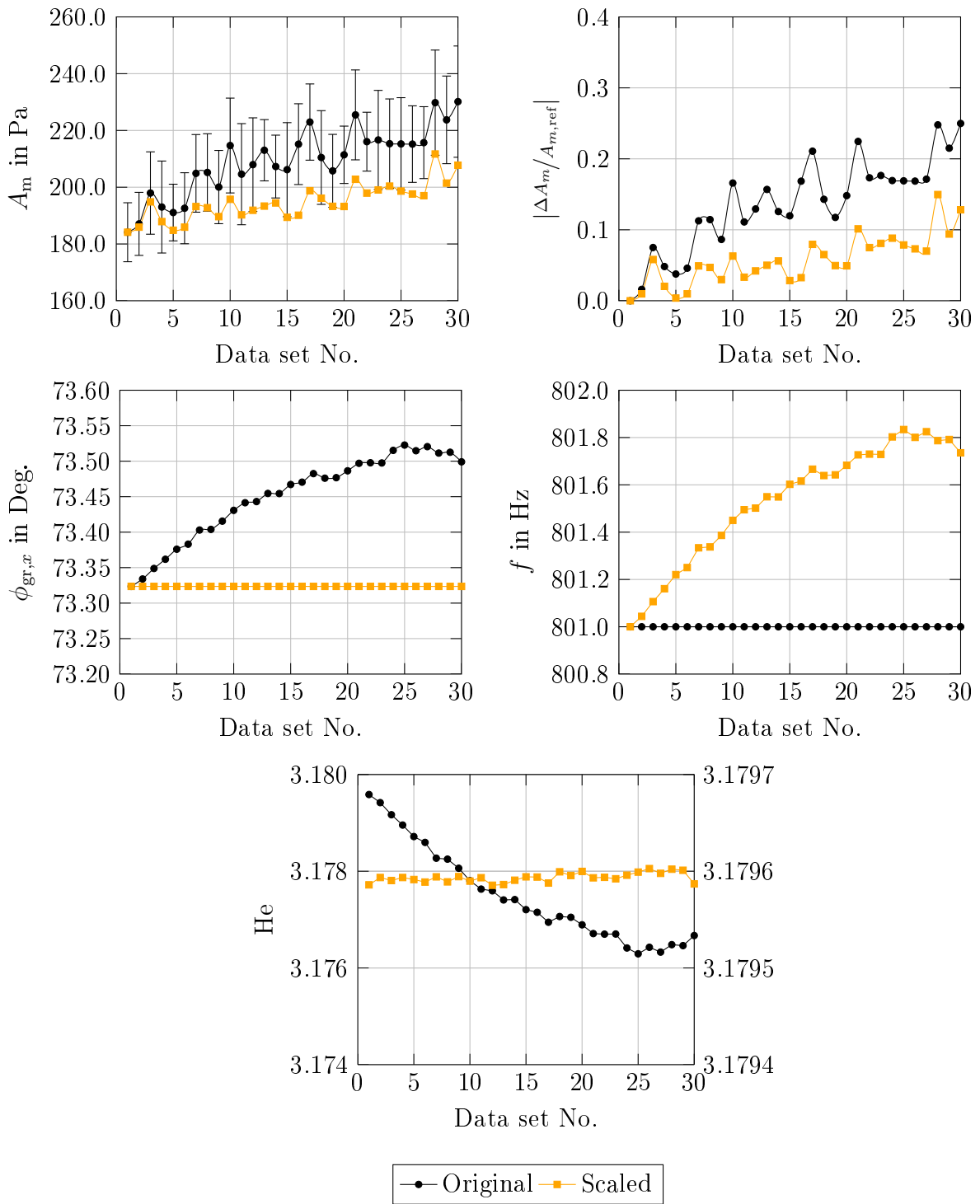


Figure A.32: Results of post-hoc scaling. Top left: Modal amplitude. Top right: Relative change of the modal amplitude with respect to reference data set No.1. Center left: Group velocity angle. Center right: Excitation frequency and calculated reduced frequency. Bottom: Helmholtz number (the lines and markers colored in black and orange refer to the left and the right ordinate, respectively).

[Test Case 2 | design-point operation | $m = 2$ | $f_{exc} = 801$ Hz]

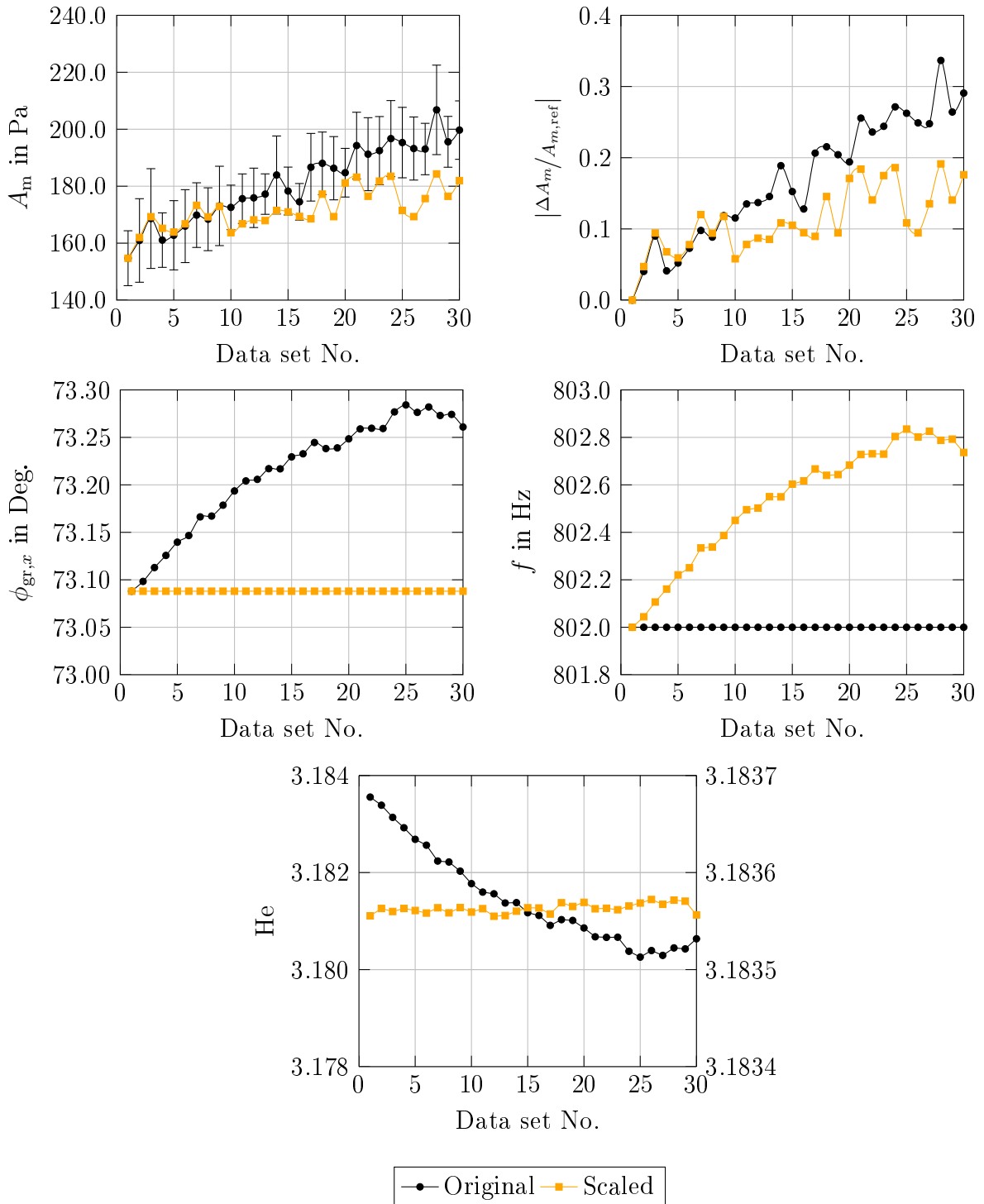


Figure A.33: Results of post-hoc scaling. Top left: Modal amplitude. Top right: Relative change of the modal amplitude with respect to reference data set No.1. Center left: Group velocity angle. Center right: Excitation frequency and calculated reduced frequency. Bottom: Helmholtz number (the lines and markers colored in black and orange refer to the left and the right ordinate, respectively).

[Test Case 2 | design-point operation | $m = 2$ | $f_{exc} = 802$ Hz]

A.10 Results of Post-hoc Scaling for Test Case 2

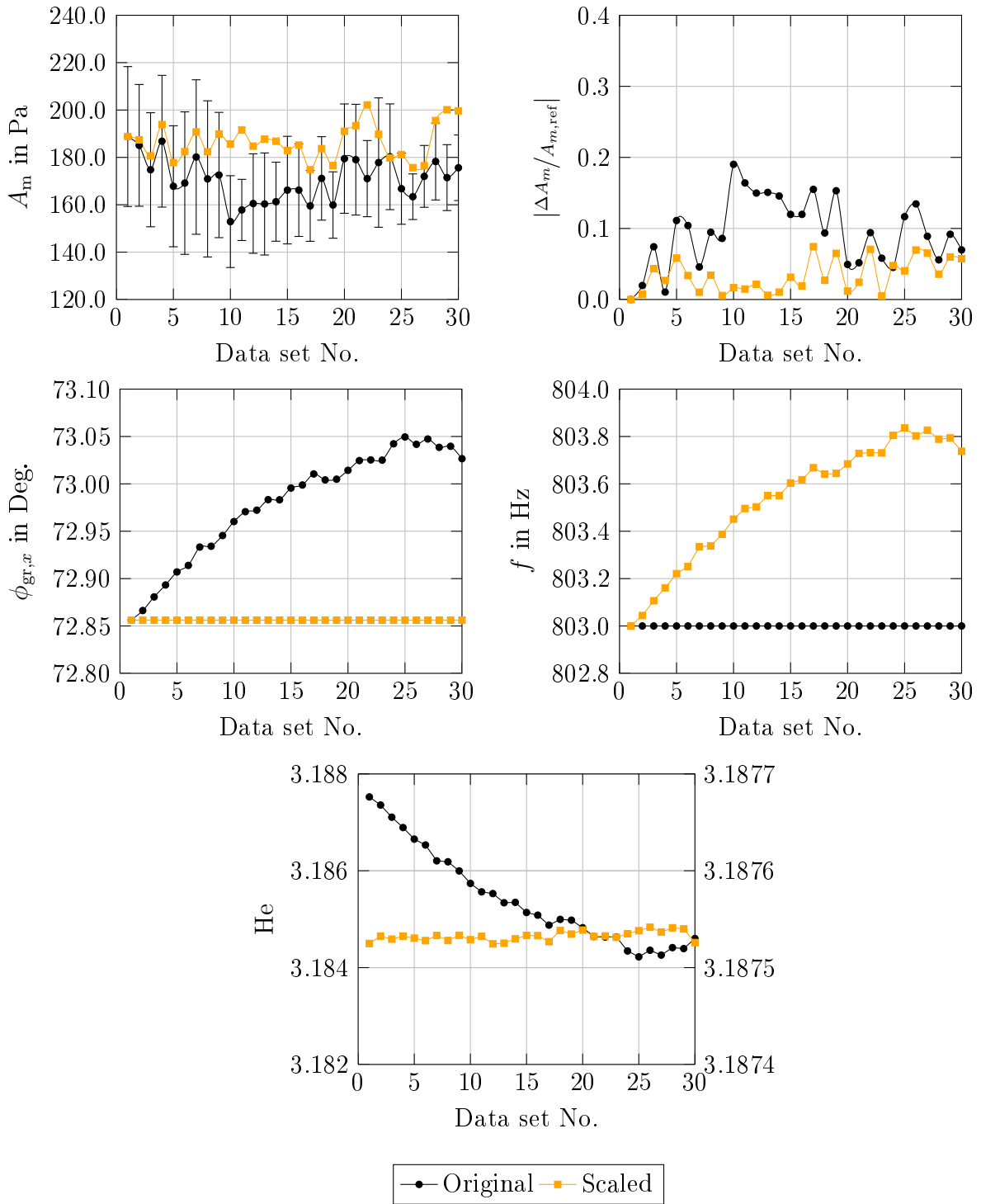


Figure A.34: Results of post-hoc scaling. Top left: Modal amplitude. Top right: Relative change of the modal amplitude with respect to reference data set No.1. Center left: Group velocity angle. Center right: Excitation frequency and calculated reduced frequency. Bottom: Helmholtz number (the lines and markers colored in black and orange refer to the left and the right ordinate, respectively).

[Test Case 2 | design-point operation | $m = 2$ | $f_{exc} = 803$ Hz]

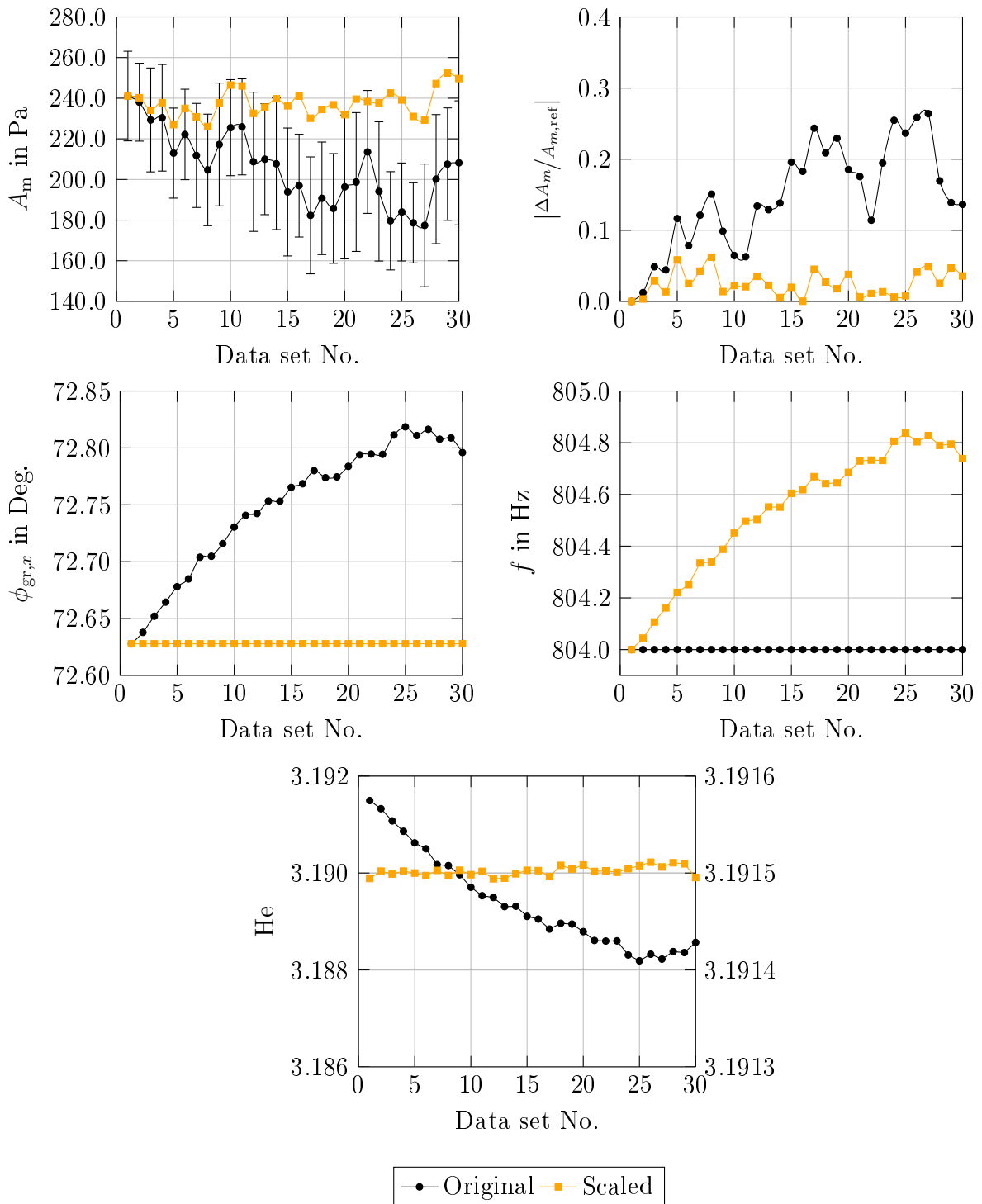


Figure A.35: Results of post-hoc scaling. Top left: Modal amplitude. Top right: Relative change of the modal amplitude with respect to reference data set No.1. Center left: Group velocity angle. Center right: Excitation frequency and calculated reduced frequency. Bottom: Helmholtz number (the lines and markers colored in black and orange refer to the left and the right ordinate, respectively).

[Test Case 2 | design-point operation | $m = 2$ | $f_{exc} = 804$ Hz]

A.10 Results of Post-hoc Scaling for Test Case 2

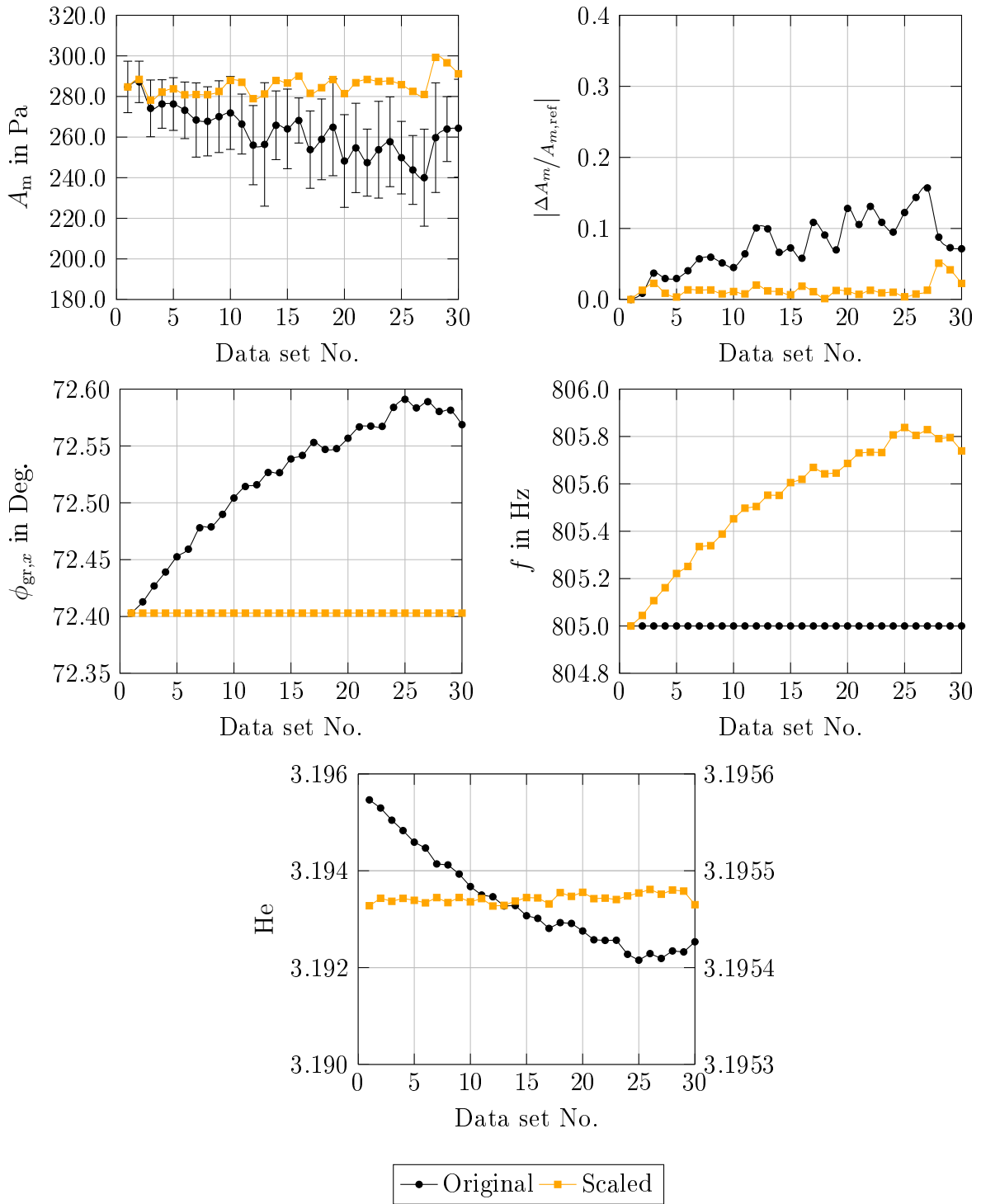


Figure A.36: Results of post-hoc scaling. Top left: Modal amplitude. Top right: Relative change of the modal amplitude with respect to reference data set No.1. Center left: Group velocity angle. Center right: Excitation frequency and calculated reduced frequency. Bottom: Helmholtz number (the lines and markers colored in black and orange refer to the left and the right ordinate, respectively).

[Test Case 2 | design-load operation | $m = 2$ | $f_{exc} = 805$ Hz]

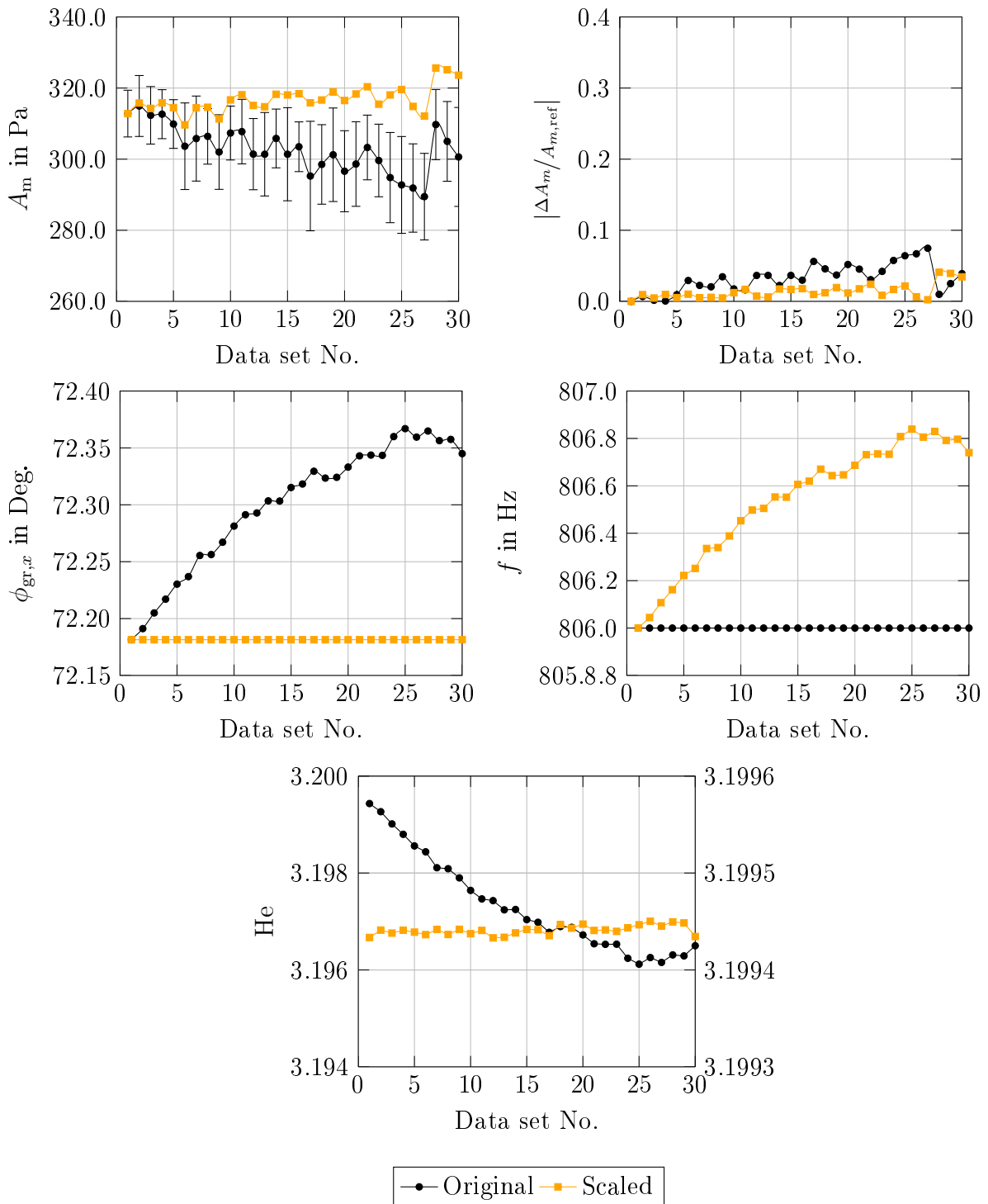


Figure A.37: Results of post-hoc scaling. Top left: Modal amplitude. Top right: Relative change of the modal amplitude with respect to reference data set No.1. Center left: Group velocity angle. Center right: Excitation frequency and calculated reduced frequency. Bottom: Helmholtz number (the lines and markers colored in black and orange refer to the left and the right ordinate, respectively).

[Test Case 2 | design-point operation | $m = 2$ | $f_{exc} = 806$ Hz]

A.10 Results of Post-hoc Scaling for Test Case 2

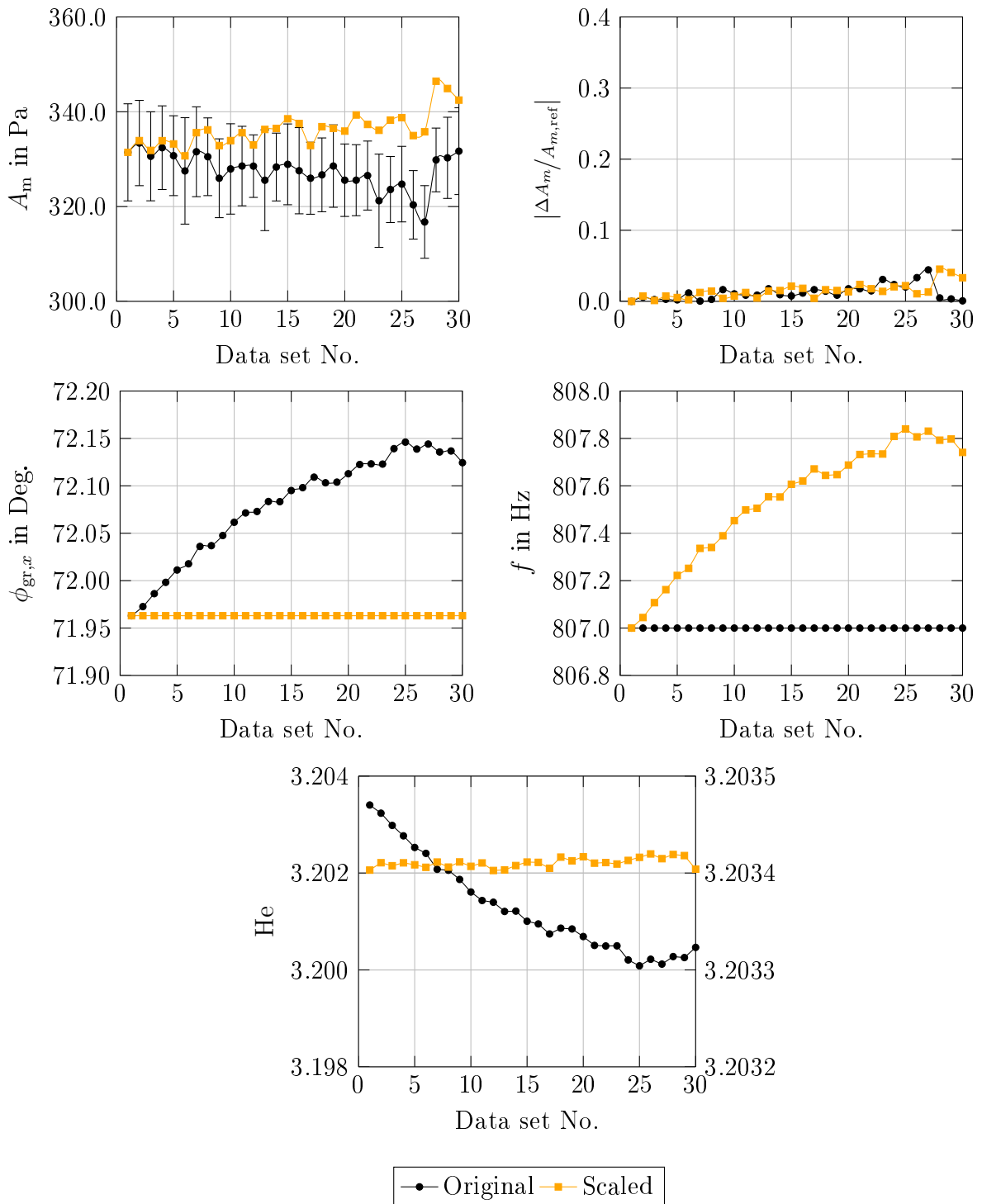


Figure A.38: Results of post-hoc scaling. Top left: Modal amplitude. Top right: Relative change of the modal amplitude with respect to reference data set No.1. Center left: Group velocity angle. Center right: Excitation frequency and calculated reduced frequency. Bottom: Helmholtz number (the lines and markers colored in black and orange refer to the left and the right ordinate, respectively).

[Test Case 2 | design-point operation | $m = 2$ | $f_{exc} = 807$ Hz]

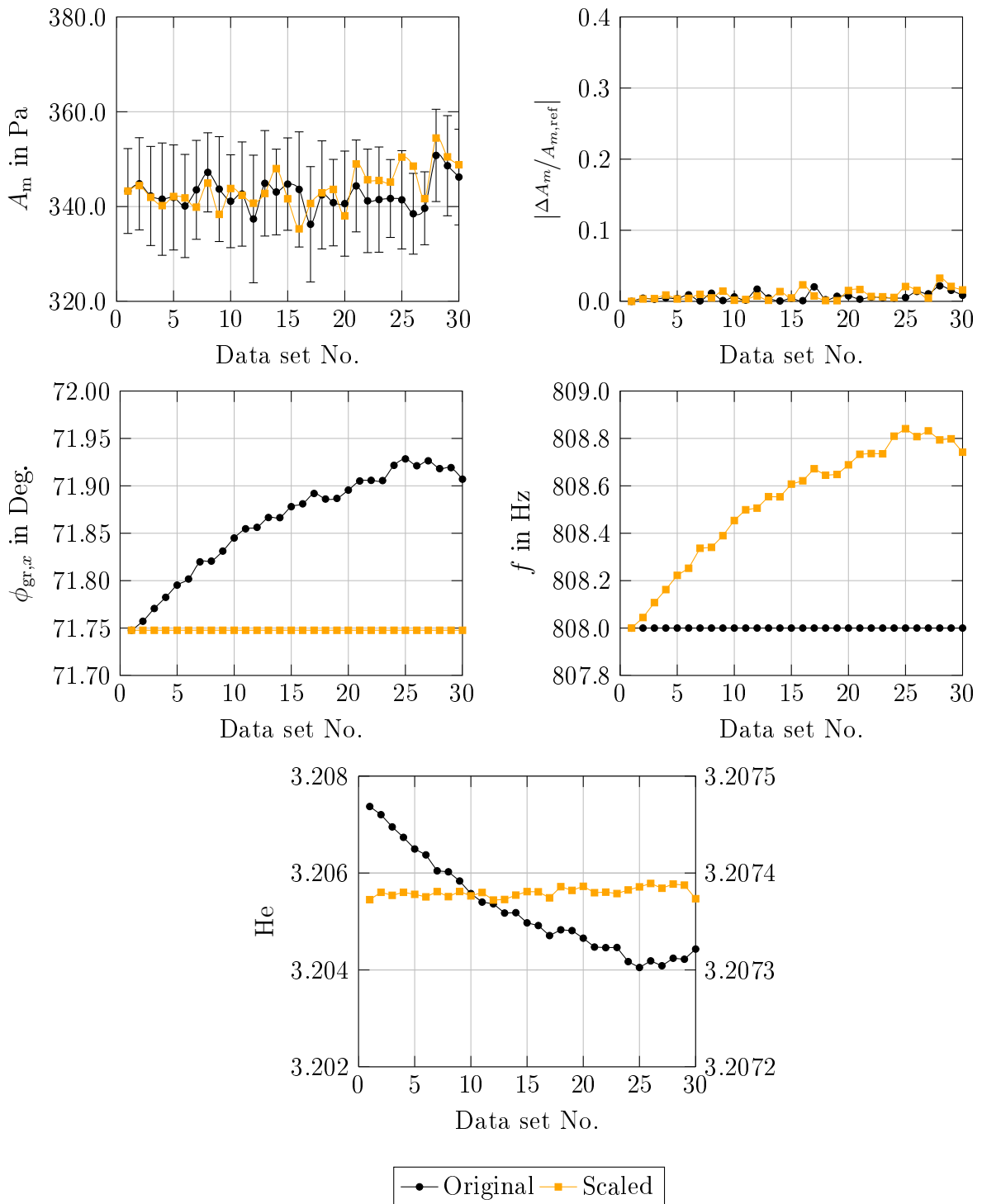


Figure A.39: Results of post-hoc scaling. Top left: Modal amplitude. Top right: Relative change of the modal amplitude with respect to reference data set No.1. Center left: Group velocity angle. Center right: Excitation frequency and calculated reduced frequency. Bottom: Helmholtz number (the lines and markers colored in black and orange refer to the left and the right ordinate, respectively).

[Test Case 2 | design-point operation | $m = 2$ | $f_{exc} = 808$ Hz]

A.10 Results of Post-hoc Scaling for Test Case 2

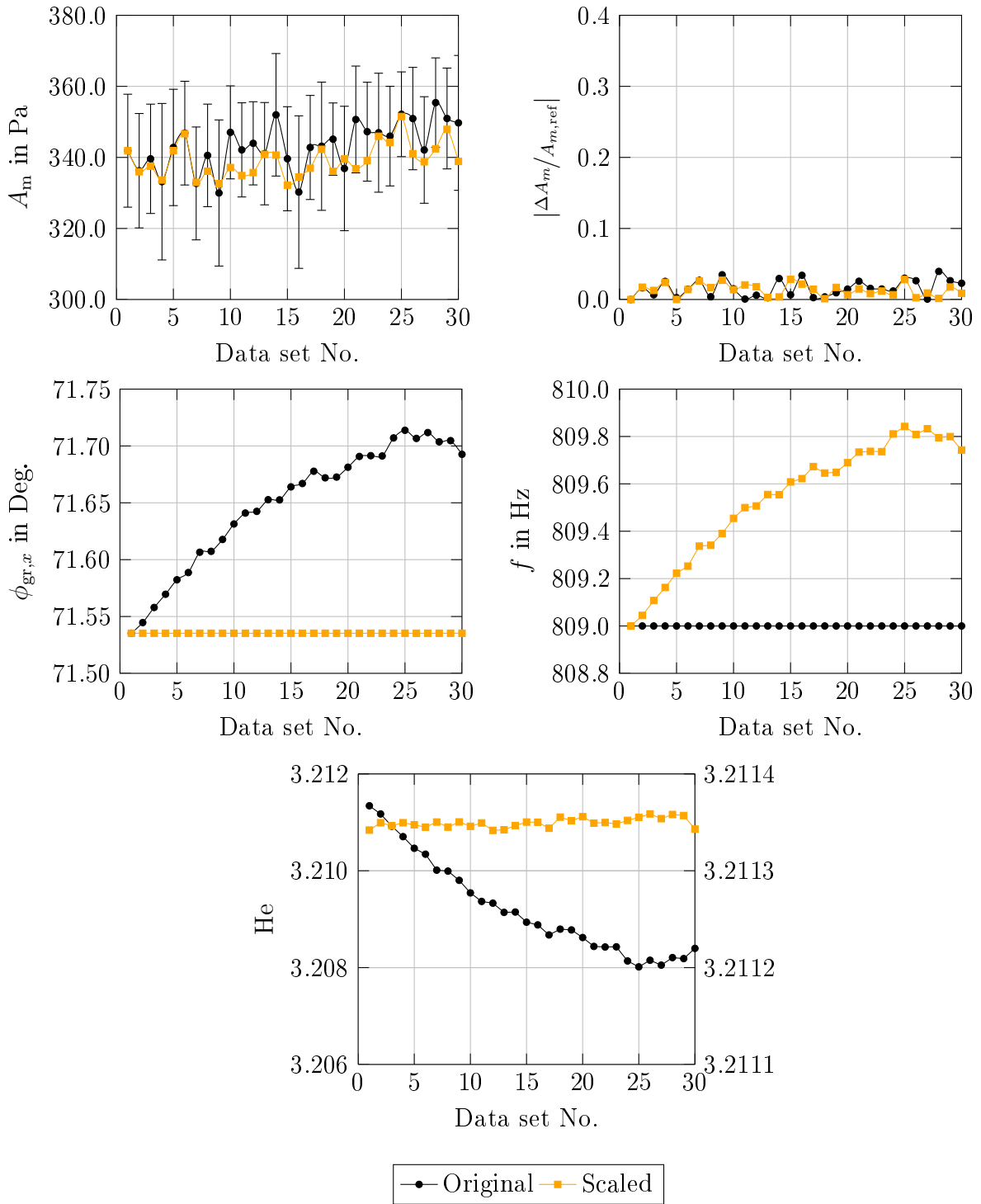


Figure A.40: Results of post-hoc scaling. Top left: Modal amplitude. Top right: Relative change of the modal amplitude with respect to reference data set No.1. Center left: Group velocity angle. Center right: Excitation frequency and calculated reduced frequency. Bottom: Helmholtz number (the lines and markers colored in black and orange refer to the left and the right ordinate, respectively).

[Test Case 2 | design-point operation | $m = 2$ | $f_{exc} = 809$ Hz]

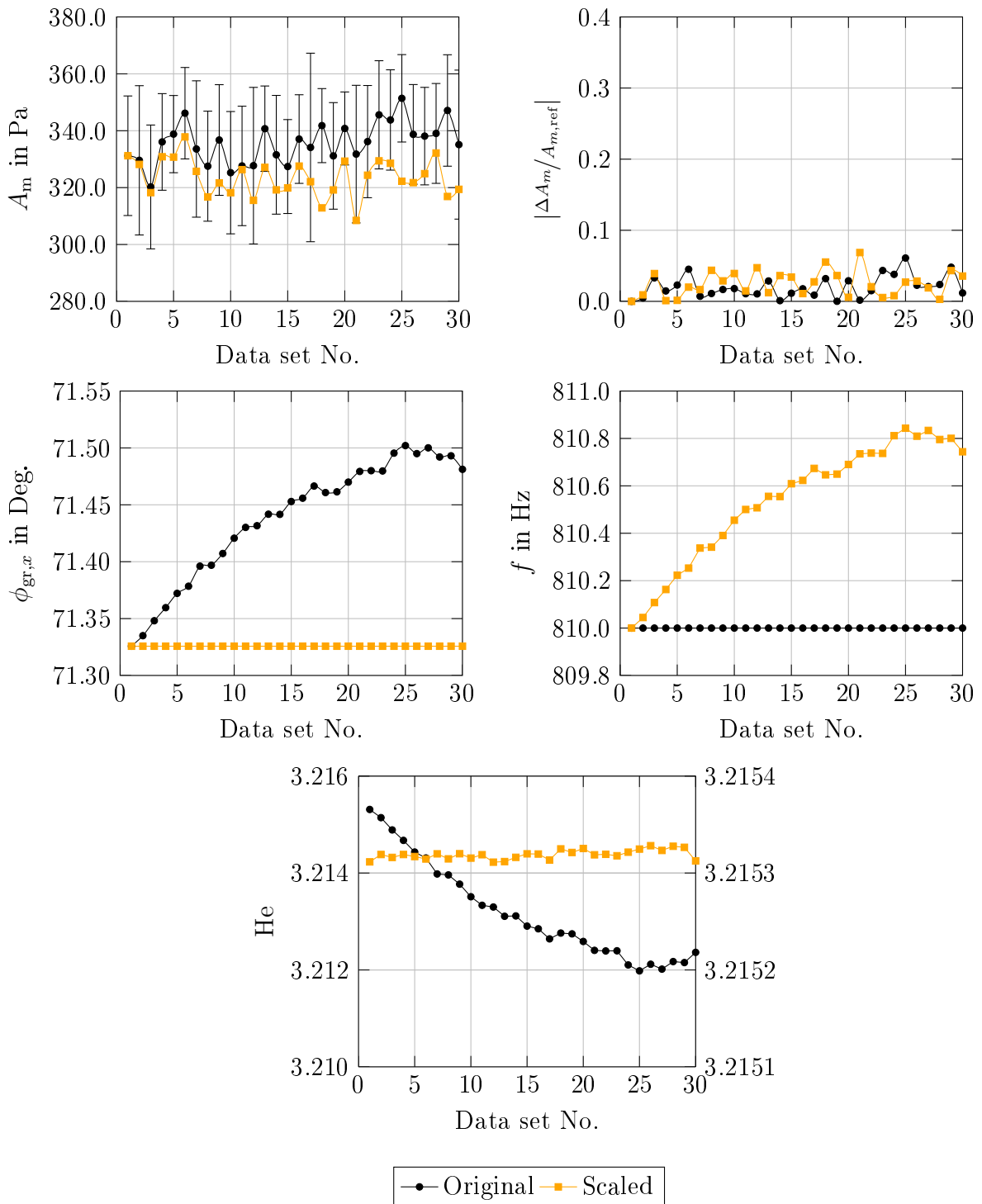


Figure A.41: Results of post-hoc scaling. Top left: Modal amplitude. Top right: Relative change of the modal amplitude with respect to reference data set No.1. Center left: Group velocity angle. Center right: Excitation frequency and calculated reduced frequency. Bottom: Helmholtz number (the lines and markers colored in black and orange refer to the left and the right ordinate, respectively).

[Test Case 2 | design-point operation | $m = 2$ | $f_{exc} = 810$ Hz]

A.10 Results of Post-hoc Scaling for Test Case 2

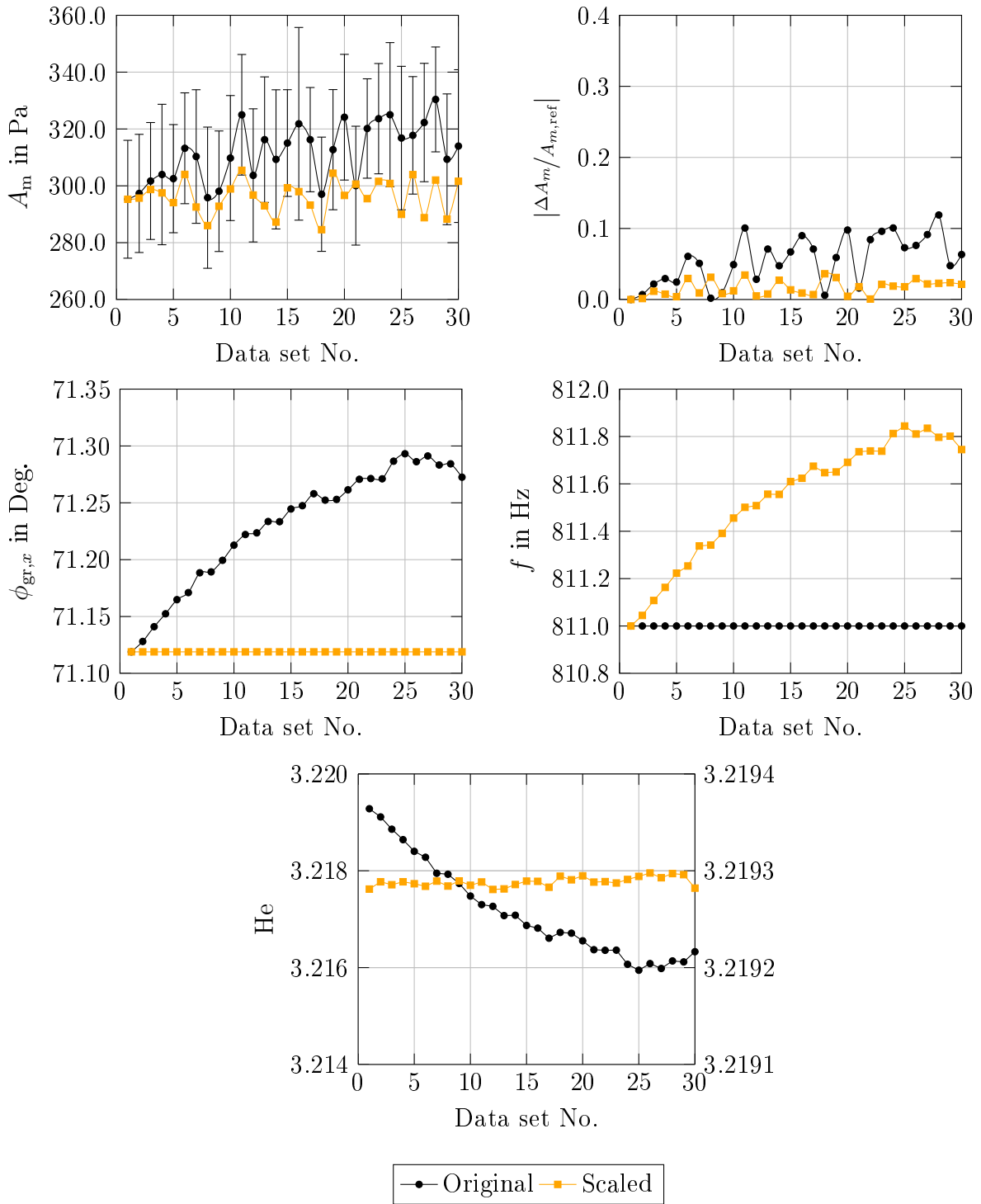


Figure A.42: Results of post-hoc scaling. Top left: Modal amplitude. Top right: Relative change of the modal amplitude with respect to reference data set No.1. Center left: Group velocity angle. Center right: Excitation frequency and calculated reduced frequency. Bottom: Helmholtz number (the lines and markers colored in black and orange refer to the left and the right ordinate, respectively).

[Test Case 2 | design-point operation | $m = 2$ | $f_{exc} = 811$ Hz]

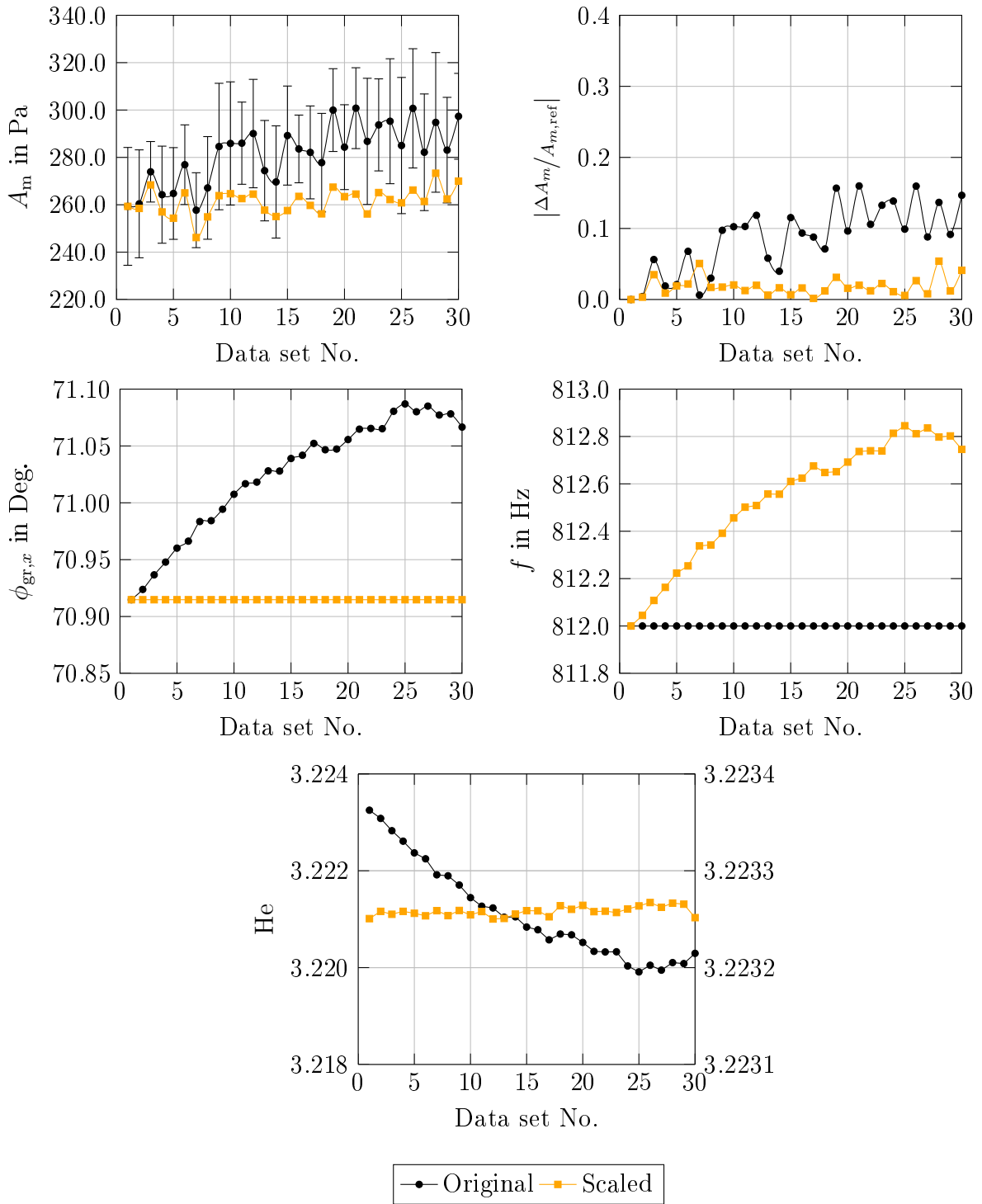


Figure A.43: Results of post-hoc scaling. Top left: Modal amplitude. Top right: Relative change of the modal amplitude with respect to reference data set No.1. Center left: Group velocity angle. Center right: Excitation frequency and calculated reduced frequency. Bottom: Helmholtz number (the lines and markers colored in black and orange refer to the left and the right ordinate, respectively).

[Test Case 2 | design-point operation | $m = 2$ | $f_{exc} = 812$ Hz]

A.10 Results of Post-hoc Scaling for Test Case 2

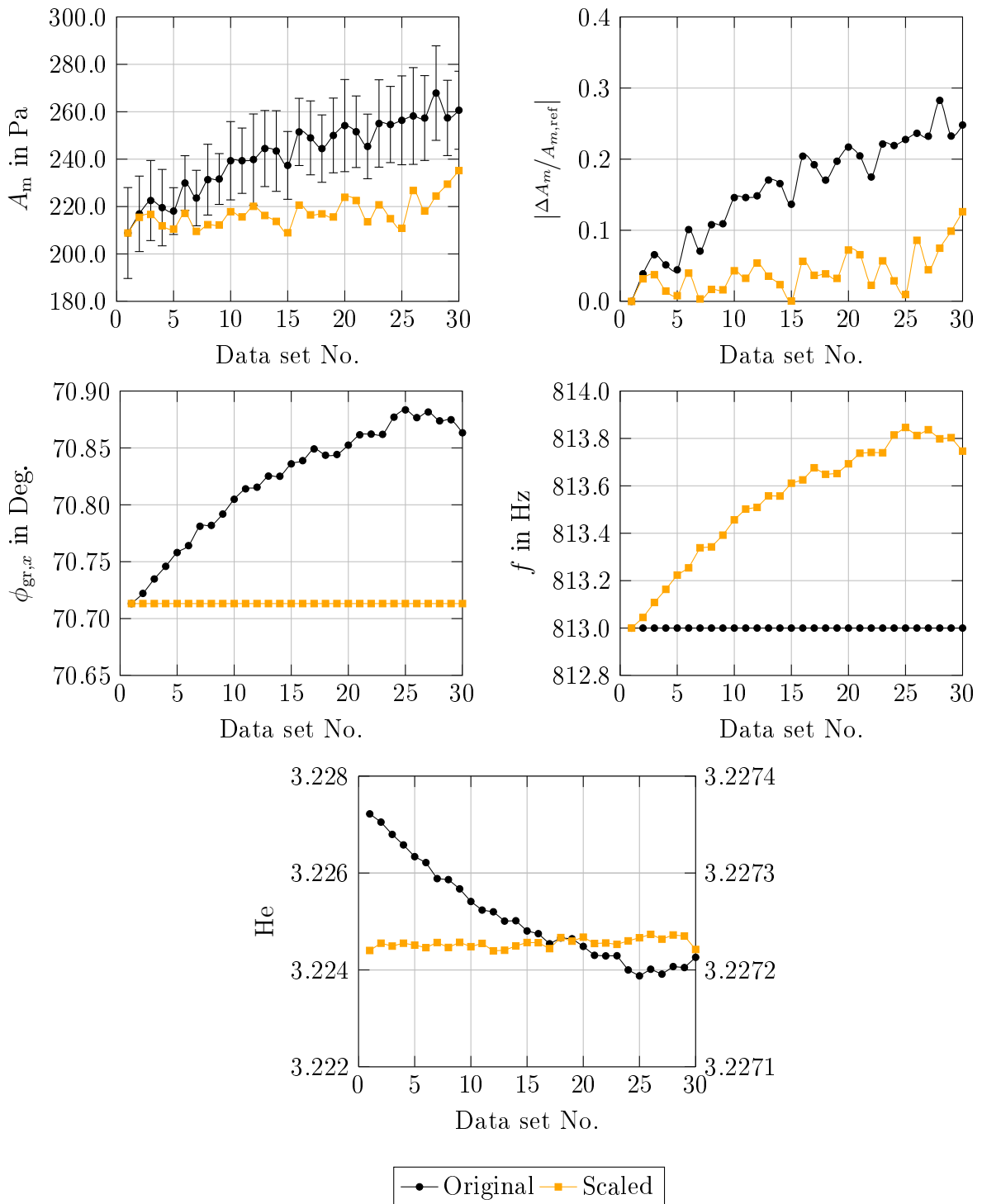


Figure A.44: Results of post-hoc scaling. Top left: Modal amplitude. Top right: Relative change of the modal amplitude with respect to reference data set No.1. Center left: Group velocity angle. Center right: Excitation frequency and calculated reduced frequency. Bottom: Helmholtz number (the lines and markers colored in black and orange refer to the left and the right ordinate, respectively).

[Test Case 2 | design-point operation | $m = 2$ | $f_{exc} = 813$ Hz]

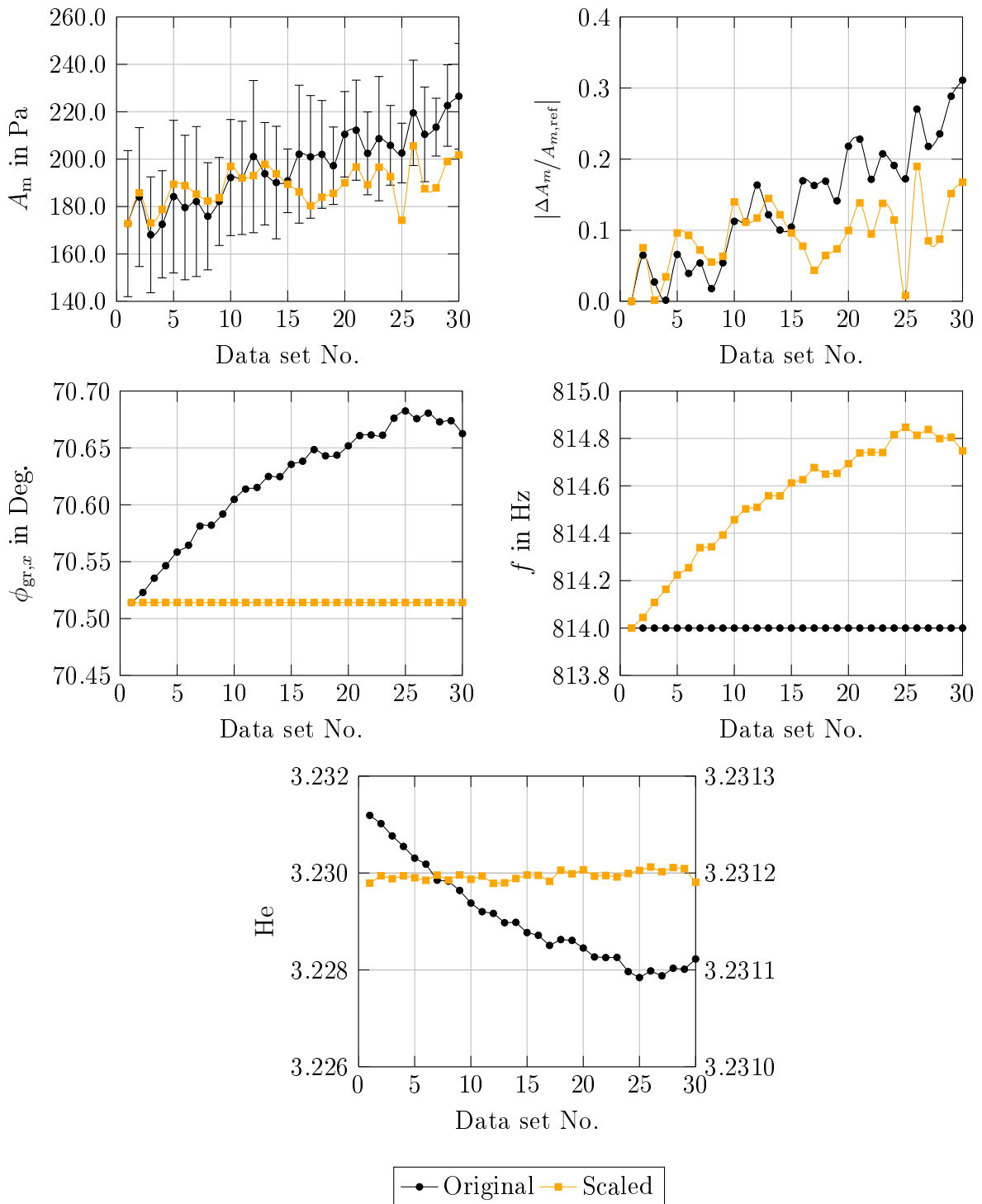


Figure A.45: Results of post-hoc scaling. Top left: Modal amplitude. Top right: Relative change of the modal amplitude with respect to reference data set No.1. Center left: Group velocity angle. Center right: Excitation frequency and calculated reduced frequency. Bottom: Helmholtz number (the lines and markers colored in black and orange refer to the left and the right ordinate, respectively).

[Test Case 2 | design-point operation | $m = 2$ | $f_{exc} = 814$ Hz]

A.10 Results of Post-hoc Scaling for Test Case 2

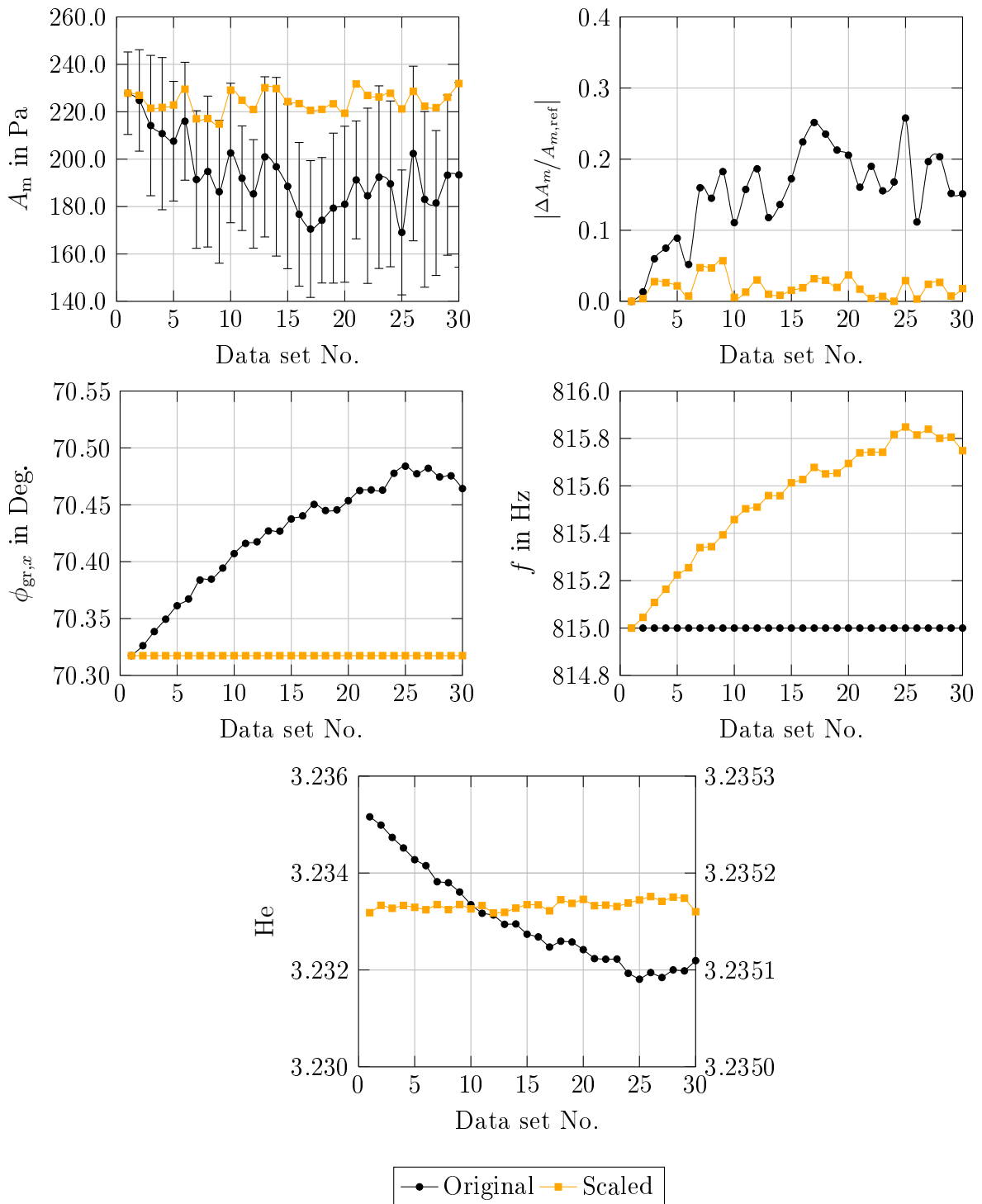


Figure A.46: Results of post-hoc scaling. Top left: Modal amplitude. Top right: Relative change of the modal amplitude with respect to reference data set No.1. Center left: Group velocity angle. Center right: Excitation frequency and calculated reduced frequency. Bottom: Helmholtz number (the lines and markers colored in black and orange refer to the left and the right ordinate, respectively).

[Test Case 2 | design-point operation | $m = 2$ | $f_{exc} = 815$ Hz]

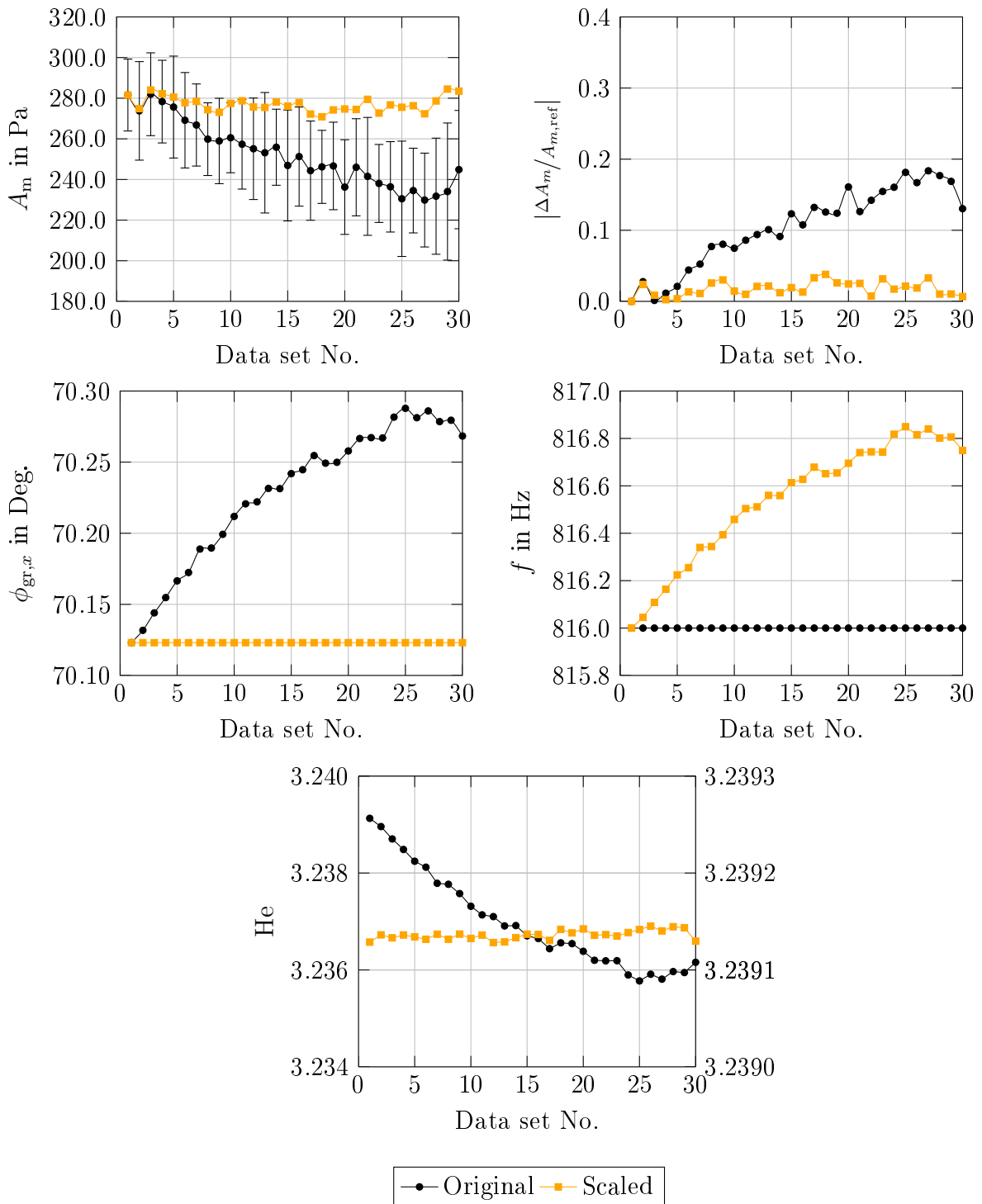


Figure A.47: Results of post-hoc scaling. Top left: Modal amplitude. Top right: Relative change of the modal amplitude with respect to reference data set No.1. Center left: Group velocity angle. Center right: Excitation frequency and calculated reduced frequency. Bottom: Helmholtz number (the lines and markers colored in black and orange refer to the left and the right ordinate, respectively).

[Test Case 2 | design-point operation | $m = 2$ | $f_{exc} = 816$ Hz]

A.10 Results of Post-hoc Scaling for Test Case 2

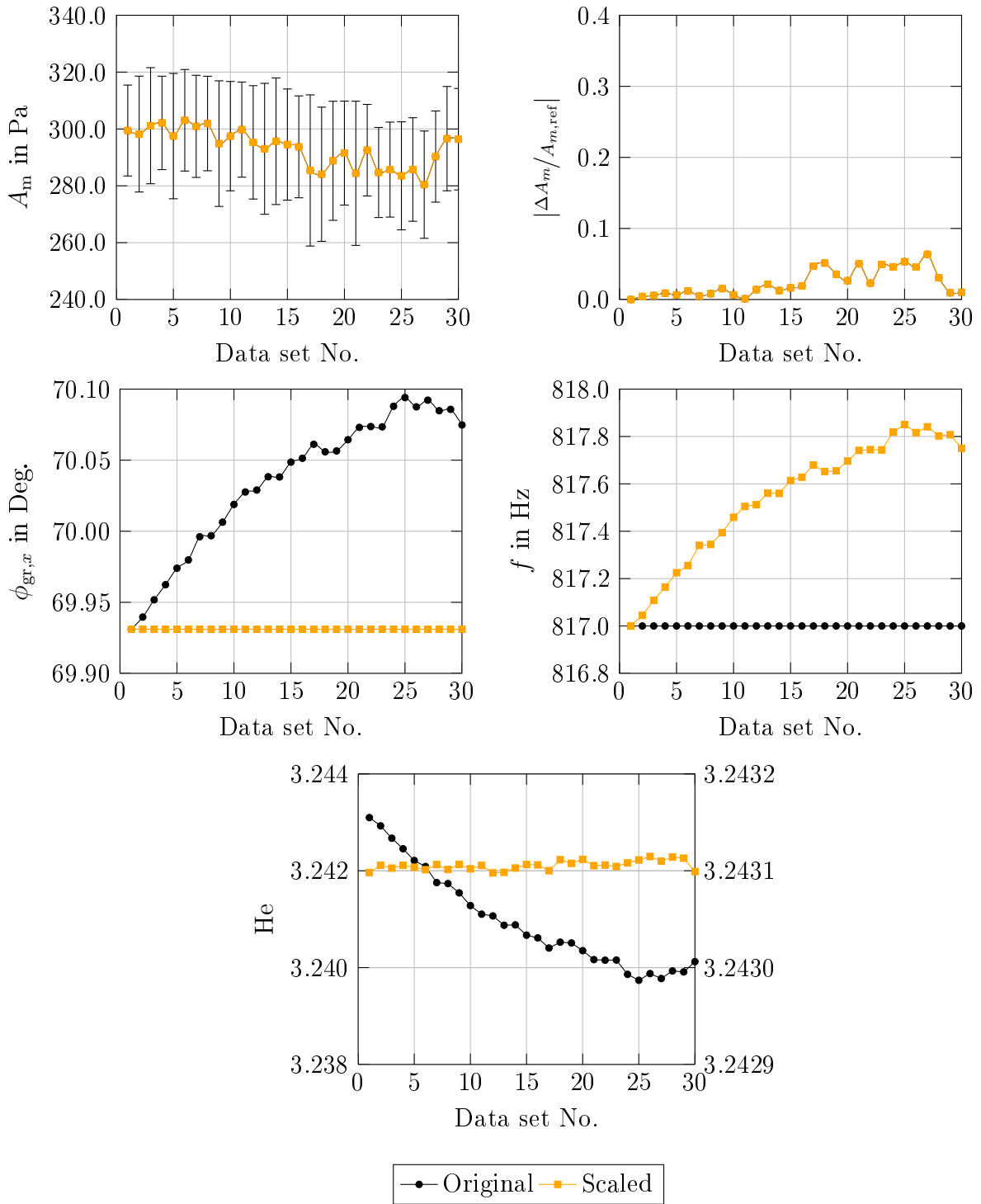


Figure A.48: Results of post-hoc scaling. Top left: Modal amplitude. Top right: Relative change of the modal amplitude with respect to reference data set No.1. Center left: Group velocity angle. Center right: Excitation frequency and calculated reduced frequency. Bottom: Helmholtz number (the lines and markers colored in black and orange refer to the left and the right ordinate, respectively).

[Test Case 2 | design-point operation | $m = 2$ | $f_{exc} = 817$ Hz]

Wissenschaftlicher Werdegang

Persönliche Daten

Name Carolin Mandanna Hurfar
Geburtsdatum 1. Mai 1987
Geburtsort Essen

Schulausbildung

1997 - 2006 Maria-Wächtler Gymnasium, Essen
Abschluss: Allgemeine Hochschulreife

Akademischer Werdegang

2012 - 2016 Wissenschaftliche Mitarbeiterin
Institut für Turbomaschinen und Fluid-Dynamik
Leibniz Universität Hannover, Hannover

2011 - 2012 Leibniz Universität Hannover, Hannover
Abschluss: Master of Science, Wirtschaftsingenieurwesen

2007 - 2011 Leibniz Universität Hannover, Hannover
Abschluss: Bachelor of Science, Wirtschaftsingenieurwesen